UNIVERSITAT POLITÈCNICA
DE CATALUNYA
BARCELONATECH

RFID Multiantenna Systems for Wireless Communications and Sensing

Author
Santiago Capdevila Cascante

Thesis Advisor
Lluís Jofre Roca

A thesis submitted to the Universitat Politècnica de Catalunya (UPC) in partial fulfillment of the requirements for the degree of
DOCTOR OF PHILOSOPHY

Department of Signal
Theory and Communications

PhD. program on Signal Theory and Communications
AntennaLab Group
Barcelona, February 2013

Thesis written by Santiago Capdevila Cascante

RFID Multiantenna Systems for Wireless Communications and Sensing

PhD. program on Signal Theory and Communications

The work presented in this thesis has been supported in part by the Spanish Interministerial Commision on Science and Technology (CICYT) under projects TEC2007-66698-C04-01, TEC2010-20841-C04-02 and CONSOLIDER CSD2008-68 and by the "Ministerio de Educación y Ciencia" through the FPU fellowship program under grant AP2006-02840.

A mi familia

Abstract

Many scientific, industrial and medical applications require the measurement of different physical parameters in order to collect information on the spatially distributed status of some process. Very often this information needs to be collected remotely, either due to the spatial dispersion of the measurement points or due to their inaccessibility. A wireless embedded self-powered sensor may be a convenient solution to be placed at these inaccessible locations.

This thesis is devoted to study the analytical relation governing the electromagnetic coupling between a reader and an embeddable self-powered sensor, based on radio frequency identification (RFID) technology, which is capable of wirelessly retrieving the status of physical parameters at an, in general, remote and inaccessible location by modulating the field it scatters. The physical parameter to be sensed may be the electromagnetic (EM) field existing at that location (primary measurement) or the indirect measurement of other parameters such as the temperature, humidity, etc. (secondary measurement). Given the simplicity of the RFID solution (highly embeddable properties, scavenging capabilities, penetration and radio coverage characteristics, etc.) the measurement can be done at a single location, or it can be extended to a set of measuring locations (an array or grid of sensors). The analytical relation is based on a reciprocity formulation studying the modulated scattered field by the embedded sensor in relation with the incident field, and allows to define a set of quality parameters of interest for the optimum design of the sensors. These parameters are the transfer impedance, which accounts for the propagation path characteristics, the load factor, which relates the transfer of power to the scavenging state, and the modulation efficiency, which accounts for the power of the response of the sensor. Particular attention is given to the scavenging circuitry as well as to the antenna design relevant to the sensing objective.

It will be shown that the communication principle of an RFID probe is similar to what is done in EM-field probes based on the modulated scatterer technique (MST). This technique is mainly used for near-field mapping applications, and it is based on the measurement of the EM-field by modulating the scattering properties of the probe. In RFID tags, the existence of an RF harvesting section is an improvement with respect to conventional MST probes since it removes the need of DC biasing lines or optical fibers to perform the modulation of the field scattered by the probe. However, as will be shown in this thesis, this harvesting section introduces non-linearities in the response of the RFID probe, which will require a proper correction to use them as EM-field probes, although the characterization of the non-linearities of the RFID circuitry cannot be directly done using a conventional vector network analyzer (VNA), because the circuitry needs an excitation

modulated with the RFID protocol. Due to this, this thesis proposes an alternative measurement approach that allows to characterize the different scattering states of the RFID probe and in particular its non-linear behavior. In addition, and taking this characterization as the starting point, this thesis proposes a new measurement setup for EM-field measurements based on the use of multiple tones to increase the dynamic range of the measurement. With this approach the dynamic range, which was originally limited by the harvesting section, is increased and it is now limited by the receiver sensitivity, just like conventional MST probes with DC biasing lines but without giving up on the harvesting module. This is in fact experimentally demonstrated in the measurement of a radiation pattern, as well as for in imaging applications.

The RFID-based sensor response is also electromagnetically sensitive to the dielectric properties of its close environment. This dependence can be used to sense variations of the dielectric properties of the probe's environment. However, the governing formulation for the response of the probe mixes together a set of different contributions, the path-loss, the antenna impedance, the loads impedance, etc. As a consequence, it is not possible to isolate each contribution from the others using only the information available in the modulated scattering of a single loaded probe. This is an intrinsic limitation of conventional MST/RFID probes, which basically arises from a lack of diversity in the scattering states of the probe. In order to improve/enable robust sensing capabilities in the sensor, this thesis mathematically proposes and experimentally develops a modification of the MST scheme to introduce a new set of multi-load scattering states that increases the information available in the response. This additional information makes it possible to differentiate between the different contributions and therefore it enables the use of the RFID sensor for a simultaneous measurement of a field distribution and sensing variations in the dielectric parameters in the neighborhood of the probe. Moreover, this thesis goes a step forward and introduces a new scattering state of the probe sensitive to temperature variations that do not depend on the environment characteristics, thus allowing the retrieval of the temperature even for environments whose permittivity is not temperature dependent. This new configuration enables robust environmental sensing in addition to EM-field measurements, and sensing variations of the dielectric properties of the environment.

Acknowledgments

Aunque éste es un documento básicamente académico, que aporta un conjunto de datos teóricos o empíricamente demostrables, la realización de todo el trabajo que se ha llevado a cabo no sería posible sin la participación de uno u otro modo de la gente que he tenido la suerte de tener a mi alrededor durante todos estos años. Este escrito es un intento de expresar mi agradecimiento hacia todas estas personas.

En primer lugar quiero agradecer a mi director de Tesis, el profesor Lluís Jofre, por haberme dirigido y apoyado durante la realización de esta Tesis doctoral. Su interés por multitud de temas me ha permitido participar en múltiples proyectos durante la realización de esta Tesis, y también me ha dado la oportunidad de asistir a un buen numero de conferencias internacionales, que me han permitido conocer el trabajo de otros grupos de investigación así como diferentes ciudades.

Quiero aprovechar también este espacio para agradecer a los diferentes profesores del departamento su apoyo durante la realización de estas Tesis; en especial al profesor Jordi Romeu por su interés, las fructíferas discusiones y por ser siempre capaz de encontrar esa "s" olvidada en los artículos; y a los profesores Sebastián Blanch y Albert Aguasca que siempre han estado disponibles para cualquier consulta o discusión referente a los experimentos que se han realizado. I would also like to express my most sincere gratitude to professor Jean-Charles Bolomey, for his passion and dedication in all our discussions about MST and RFID sensing. Most of these discussions have led to great improvements in the experimental results shown in this thesis, as shown in the several joint publications.

La realización de los diferentes prototipos o experimentos nunca es una tarea sencilla y Albert, Rubén, Josep o Joaquim siempre han estado disponibles para ayudar en la fabricación de un circuito o una pieza necesaria para un experimento o medida. También Teresa y Aynie me han facilitado enormemente toda la burocracia que ha ido surgiendo durante la realización de la Tesis, ya sea un viaje a una conferencia, un pedido de material, etc. Mi más sincero agradecimiento a todos ellos.

La realización de esta Tesis no habría sido igual sin la presencia del gran grupo de compañeros y amigos con los que he tenido la suerte de compartir todo este tiempo: Dani, Edgar, Edu, Enrique, Gemma, Jordi A., Marc, Maria, Marta y Verónica así como de quellos que ya hace algo más de tiempo que acabaron: Bea, Benji, Javi, Jordi B., Oscar, Pere, Raquel, Txema, y todos aquellos que sin intención me haya podido olvidar en esta lista. Ya sea por las discusiones más o menos técnicas durante el día o por las conversaciones distendidas durante las comidas, por los viajes a conferencias tÃĬcnicas o por las salidas *extra-curriculares*, o por interesantes campañas de medidas (incluyendo una *visita*, a horas algo intempestivas, a los túneles en construcción del metro de Barcelona!),

siempre guardaré un buen recuerdo de todos vosotros y de lo que hemos aprendido los unos de los otros durante todos estos años.

I would also like to express my gratitude to professor Peter Burke for hosting me at the University of California, Irvine during the summer of 2010 and making me feel like one more in his research group during the four months and a half I was there. También quiero agradecer a Javi y a Anna el recibimiento que me dieron durante mi estancia, así como a Rafa y a Salvatore con los que compartimos comidas y excursiones durante la estancia.

Finalmente quiero acabar agradeciendo profundamente su paciencia y comprensión a mi familia y amigos que han sabido *soportarme* durante todos estos años. En especial gracias a mi padres Ramón y Marita, por estar siempre allí e interesarse por todo lo que hago y no cejar en su empeño por obtener respuesta a esa pregunta constante de todo doctorando "¿cuándo presentas?"; a mis hermanos Víctor y Natalia que siempre me demuestran su apoyo sincero y que son una presencia constante en mi vida y a mi tío Pedro que siempre está dispuesto a ofrecer su ayuda cuando se necesita. Gracias también por sorprenderme y por dejaros sorprender.

Contents

1

Chapter 1
Introduction

1.1 Motivation

Sensing the environment is an activity that is linked to the development of technology and the advance of society. By observing and measuring the environment, it has been possible to establish many of the laws of physics and nature, and the relationship between cause and effect of many processes. These measurements can be at a local scale, like measuring the advance of an object when a force impacts on it, or it can be in a distributed system, such as in astronomical measurements. In either case, the availability of information allows to construct a more detailed and accurate model that allows to predict its behavior. A clear example of the latter is the development of weather models, that have benefited a great deal from the use of extensive data coming from different observing sources, as well as the availability of satellite imagery, which introduces a new vector of information (and also the improvement of computational capabilities).

With the advance of the technological processes and the reduction of costs, it is now possible to develop a network of devices (nodes) capable of sensing the state of many different kinds of information, such as traffic data, air pollution, humidity, noise, presence detection, etc., which can be used in a more local scale in many different applications, for instance urban planning and security. The development of these networks requires the creation of an expensive infrastructure to power the sensors and transmit the data towards central processing nodes. Part of the infrastructure can be simplified using wireless transmission, but there is still the requirement of powering the sensors (unless a battery powered system is used). Moreover, with the advent of wireless sensor networks, it is now possible to envision a more pervasive network, with a higher degree of penetrability, so that it amounts a dense grid of information in a local environment. An especially interesting case for such network is when they are used to retrieve information from within an object, either at a single or several testing points. The knowledge of internal information of an object can be used to enhance the available information, for instance of the health of a civil engineering structure, without having to use destructive approaches to get to the internal testing points. These kind of sensors must therefore be able to operate with the required accuracy and with an operating life adequate to the application. For instance wireless sensors in civil engineering structures may rely on batteries, in which case they have to be sufficiently accessible for the adequate maintenance cycle in order to keep the network operating for the whole life of the structure; on the other hand, if they are embedded, they must have an operating life close to the operating life of the structure, or they can use a harvesting technique to obtain the energy from the environment.

This kind of embedded/wireless sensor usually limits to the measurement of a physical quantity, such as the mechanical strain, the temperature, the humidity, etc., but they rarely acquire information from the nearby electromagnetic signal. And the fact that the environment presents a dielectric permittivity implies that the signal reaching the sensor will contain information of the object that is to be sensed, and this can be used along with tomographic imaging algorithms to determine the contains or variations in the area of interest. By enabling the measurement of field distributions with these embeddable sensors, a more detailed information of the interior of host can be achieved which, for instance, could be used for the non destructive evaluation (NDE) of civil engineering structures, or for medical applications.

As a consequence this thesis is devoted to the study of RFID for sensing applications with a special emphasis on the measurement of EM-field distribution. RFID is

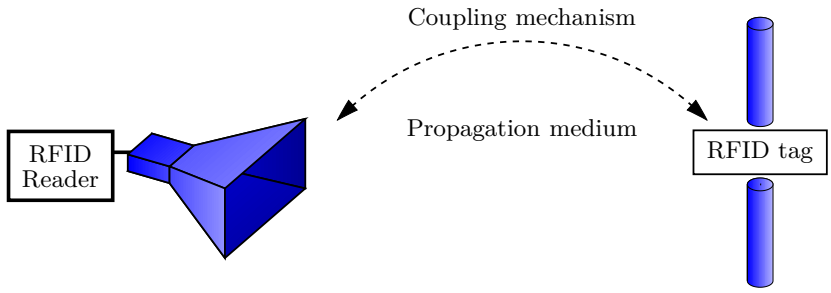

Figure 1.1: Main components of an RFID system, comprising the object (*tag*) whose identity is being challenged by a transmitter (*reader*) by establishing a communication with a given protocol (*medium*)

chosen because it has the self-powering capabilities required for embedded sensors, and its communication principle, as will be analyzed through the thesis is the same as MST, a technique commonly used for field-mapping applications.

1.2 Introduction to RFID

After the initial motivation, this short section briefly introduces the technology that is used in the following chapters, that is RFID technology.

RFID is defined as an automatic identification system that works in a contact-less way (wirelessly) and which uses radio frequency as the support of its communications. As explained in [1], RFID is one of the many different identification systems that are used nowadays, such as barcodes, optical character recognition (OCR), or more complex systems such as biometric or smart card based systems. RFID combines a little of each of the previous systems; it is an electronic identification system, it can be read-only with a small memory, for instance anti-theft RFIDs might present as low as 1 bit of information, or with re-writable memories up to several kbits (similarly to smart cards); and the requirements of line of sight are less restrictive than for optical systems, since it operates at a much lower frequency.

1.2.1 RFID components

There are multiple systems that *fall* under the definition of RFID, with each presenting some distinctive characteristic, such as the frequency, principle of operation and the final applications. However, regardless of these differences, all of them present 3 differentiated components which are schematically presented in Fig. 1.1:

Reader It is the device that is trying to obtain the identification information from the target, it might be composed of a single element (mono-static) or multiple elements (bi-static).

Tag It refers to the transponder located in the object or individual whose identity is challenged by the reader. In this thesis tag and probe are usually used interchangeably.

Medium of transmission Although it is not specifically a component, it is the most important part of the system since it establishes the basis of operation of the given RFID system. By medium of transmission we refer not only to the nature of the medium (dielectric), but also to the frequency of operation, the protocol, etc.

1.2.2 Classification

Classification of RFID systems can be done based on the frequency of operation, which is intrinsically related with the medium of transmission: systems working at frequencies of a few MHz usually work as inductively coupled systems while higher frequencies rely on microwave communications. Table 1.1 presents some of the common frequencies used in different typical applications of RFID systems. The frequency and the operational

Frequency	Sample applications
125-134.2 kHz	Animal identification, Timing chips in sport events, Antitheft systems
13 MHz	Asset Tracking (counterfeiting), Electronic Passport (e-Passport), Baggage tracking
400 MHz	
860-950 MHz	Labeling
2.5 GHz	Toll

Table 1.1: Frequencies were there is defined a standard for RFID applications

principle also determine the range of operation of the system: inductively coupled systems inherently present a limited range in front of microwave which due to the lower attenuation can reach farther distances.

An alternative and complementary classification can be done based on the mechanism used for powering the tag: Purely *passive* RFID tags do not rely in any powering to operate, they basically present a static signature that can be measured remotely and used for identification purposes, [2], in a similar way to surface acoustic wave (SAW) devices. Passive RFID tags still do not rely on any internal power source to operate, but they use a scavenging circuitry to extract the energy from the neighborhood. Finally semi-passive and active RFID system have a battery within the tags that allows their circuitry to operate and even to transmit the RF signal for communications. Passive systems require higher levels of incident power to operate than their active counterparts, but they also present longer lifetimes since they do not rely on a limited internal power supply.

For embedded sensors with self-powering capabilities only purely passive and passive RFID tags make sense, and this last group, in particular UHF passive RFID tags will be the focus of this thesis. In these tags, communication with the external reader is only possible when the scavenged power is above the activation power P_{th}, and then it will communicate using backscattering modulation, which is closely related with MST and consists in the modulation of the scattering of the probe (which will be analyzed in chapter 2). The dependence of this modulation with physical parameters will be the basis that is used for sensing applications as will be shown thourough the thesis.

1.3 State of the art

This section presents a short description of the state of the art in the area that this thesis is focused, that is the remote measurement of EM-field distributions, and the development of wireless battery-less systems that can be used for sensing applications.

1.3.1 Measurement of field distributions: MST

The modulated scatterer technique (MST) is a technique used for the indirect measurement of the electric field distribution introduced in 1955 [3, 4], and which is based on the measurement of the field distribution by observing the scattered field of a probe located at the measurement position. In order to discriminate the field scattered by the probe from others, the scattering properties of the probe are not constant, but modified during the time of the measurement, in such a way that its scattered field is modulated. Originally this modification consisted in a mechanical rotation or displacement of the probe, however that limited the applicability of the technique. An alternative more widely applicable modulation principle is based in loading the probe with some electronic device with two highly differentiated impedance, such as PIN diodes [4] or photodiodes [5].

A single probe has been used in field mapping applications to determine the field distribution at the aperture of an antenna [6] (see Fig. 1.2a), along a microwave circuit, or at specific placements for EMC [7] or SAR measurements [8]. The development of arrays of MST probes [9], drastically reduced the measurement time, enabling the development of fast antenna pattern measurement systems [10] (see Fig. 1.2b) and the development of real-time microwave cameras (see Fig. 1.2c), that can be used in tomography applications [11, 12] or for material characterization [13]. The applicability of MST for general sensing applications, in special in embedded areas, has not been widely researched until recently, when it has started to be used for the detection of dielectric permittivity variations [14–16].

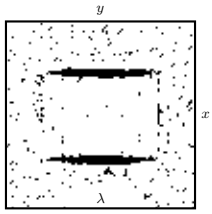

(a) Measurement of the field of a pyramidal horn [6]

(b) Stargate antenna measurement system [10]

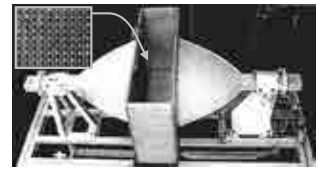

(c) Microwave camera [8]

Figure 1.2: Applications of MST probes for field-mapping.

1.3.2 Wireless sensor networks

A wireless sensor network consists of a set of small nodes distributed in a given region, so that they form a dense grid that is capable of retrieving the physical state of a given parameter ψ in the area and that can communicate this state to a centralized receiver

for processing or reaction. The use of wireless sensor networks is progressively extending to many different areas such as health-care [17], infrastructures monitoring [18, 19], environmental applications [20] or urban services [21, 22] among other.

The requirements for the node are very diverse, and they are quite application specific; for instance in terms of dimensions it is not the same a portable node or one that will remain in a fixed location; similarly in terms of power supply it will greatly depend on the accessibility of the sensor, it may be easily accessible, thus allowing to replace batteries, or it might present a difficult access and such power saving is important to reduce the maintenance cycle; and above all the sensing capabilities will definitely depend on the specific final applications. When these systems are to be deployed in large quantities, its individual cost may be a meaningful parameter that may limit the performance of the system. Moreover the power consumption of the node will limit the operating life of the sensor, and thus will determine the maintenance cycle of the system. To reduce the strong requirements imposed with the battery which greatly define the operating life of the sensor, when the nodes are to be placed in location where ambient energy is available, they might include harvesting modules to capture and store this energy: examples can be the use of solar energy [23, 24], vibrations [25, 26], temperature gradients [27] or electromagnetic RF energy [28].

1.3.3 Passive wireless sensors

Wireless sensor networks as presented earlier are usually composed of some active component that provides the power supply for the communication and operation of the node. With passive wireless sensors we refer to sensors that do not use any active power to communicate and that do not rely on any internal power supply for normal operation. These passive sensors could be divided in two sub-categories:

- Purely passive sensors. These are wireless sensors that do not have any active circuitry at all, also known as chip-less, and whose interaction with the incoming wireless signal (its electromagnetic signature) is dependent on ψ.
- General passive sensors. Those correspond to wireless sensors, that do not contain a battery but that include harvesting modules that provide power to process information and respond to external stimuli to finally transmit the information passively (for instance with backscattering modulation).

Among the first sensors, an important technology is SAW sensors, which will be shortly detailed next. Among the second, there are several examples, depending on the complexity of the circuitry, and therefore on the intelligence of the node, with examples such as RFID, WISP technology among others.

1.3.3.1 SAW and UWB-RFID sensors

SAW sensors are based on SAW transponders and how their response is distorted by variations in ψ [29], usually temperature, strain or mechanical stress. A typical SAW sensor, depicted in Fig. 1.3, consists of an antenna that delivers the incoming RF signal to a SAW transponder which converts it into an acoustic wave. This acoustic wave propagates on the substrate of the SAW device finding a series of parasitic elements as it advances. These parasitic elements reflect part of the wave back to the antenna, conforming an

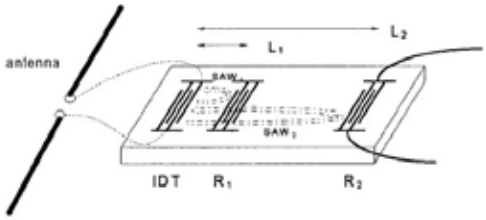

Figure 1.3: Conceptualization of a SAW sensor [29].

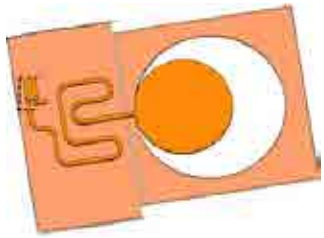

Figure 1.4: Conceptualization of an UWB RFID sensor [30].

electromagnetic signature which is reradiated by the antenna and can be captured by an external receiver. The electromagnetic signature is what contains the information of ψ, encoded in the distance and amplitude of the different reflections (pulses if a broadband frequency is available). Alternatively the SAW sensor may consist of a SAW resonator, and the sensed information is encoded in the variation of the frequency of resonance with ψ. Since the SAW is bounded to the substrate, the delay between reflections (or resonance) will strongly depend on the propagation speed of the acoustic wave in the substrate which can be used to sense variations caused by thermal fluctuations [31–34], mechanical stress [35, 36] and other physical parameters will change the propagating speed in the substrate and thus modifying the electromagnetic signature measured at the receiver.

The electromagnetic signature of each SAW sensor can be different by properly placing the different reflectors, creating an electronic ID that can be used to identify each sensor.

The accuracy of SAW sensors can be very good, and being purely passive solution it can be easily embedded in different materials or in locations where the use of power devices is inadequate. However, since the discrimination is based on the electromagnetic signature, or the variation of the frequency of resonance detected by an external reader in the *echo* to an incident signal, there might be problems when multiple sensors operate or work at the same frequencies due to near-far problems (that is the variation on reflected power for each sensor), which can be solved by using either frequency division (different resonant frequencies) or time division (ensuring the time responses do not overlap), and the use of wavelet filters to detect the variations caused by ψ [29].

Additional sensing capabilities can be achieved by attaching a sensitive load to an additional SAW transponder in the sensor. In this case part of the reflected power will depend on the reflection coefficient of the sensitive load [37].

A similar approach, although it is not based on the same SAW technology, is the so-called UWB-RFID sensor systems [30], depicted in Fig. 1.4 which uses an antenna attached to a transmission line with a sufficiently large delay line terminated in a sensitive load. When an incident UWB pulse impinges on the antenna, part of the energy is coupled to the delay line, reflected at the termination load and reflected back to the antenna and re-radiated. The information of ψ is encoded in the second pulse which depends on the variability of the reflection coefficient of the termination load with ψ.

1.3.3.2 RFID based sensors

The most interesting characteristic of RFID devices (or tags) is that, like SAW devices, they can be interrogated with an electromagnetic wave, and they will respond accordingly

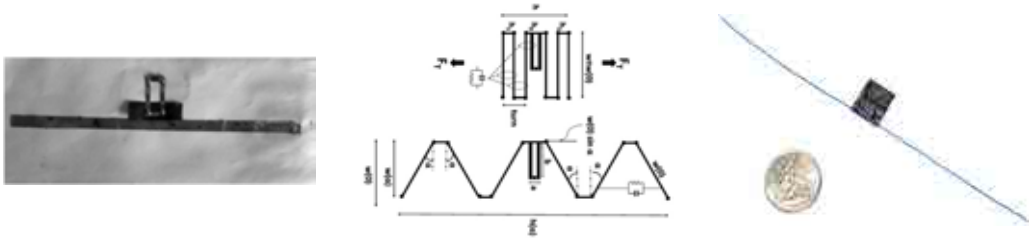

(a) Passive coupled sensing [38]

(b) Changing the antenna structure [39]

(c) Expanding the RFID electronics [40]

Figure 1.5: Different approaches that are followed for sensing capabilities.

with a pre-recorded code or pattern, depending on the specifics of the RFID tag, which allows its identification.

UHF RFID tags due to the principle of operation and the availability of a small logic in the circuitry that operates the tag presents a higher flexibility to develop sensing applications. These kind of tags, in order to power the electronics of the circuitry perform harvesting of ambient energy, basically a rectification of the incoming RF wave, that when it is above the activation threshold allows to properly interrogate the tag.

Currently three approaches are followed in the use of RFID tags for environmental sensing applications, which will be shortly presented.

Passive coupled sensing. This approach, depicted in Fig. 1.5a attaches some material very close to the ports of the RFID antenna. The permittivity or conductivity of the material presents a high dependence with the magnitude ψ to be measured, and since it is placed in a region where the reactive fields of the antenna are very strong, this produces a clear change in the input impedance of the antenna. Due to the principle of operation this strong dependence affect the performance and response of the RFID tag when externally read which allows the detection and measurement of ψ. Examples of this sensing capabilities are the addition of moisture sensitive paint [15], presence detection [41, 42], gas detection [38] and temperature detection [42].

Modification of the RFID antenna structure. In this approach, depicted in Fig. 1.5b the structure of the RFID tag antenna is modified by ψ, in such a way that the response of the RFID is modified in a controlled way, allowing to determine the value of ψ. Examples of this efforts are temperature threshold detection [43, 44], moisture [45] or physical strain [39].

Expanding the RFID electronics. Finally, the approach depicted in Fig. 1.5c consists in the modification of the architecture of the RFID IC to include sensing capabilities while preserving as much as possible the harvesting and power consumption characteristics of the tag. Examples of this are shown in [46] for a moisture sensor and [47] for a temperature sensor. Another possibility that arises with expanding the RFID electronics, which can be very useful during the research states is the development of RFID sensing platforms, that do not necessarily integrate the complete sensors in the electronic itself, but that provide a convenient interface so that different sensors can be plugged in the

RFID IC, including the capabilities to power the external sensors using the scavenged power. An example would be the circuit in [47] which apart from the temperature sensor, includes an external interface, or a more open platform, the Intel's wireless identification and sensing platform (WISP) [40], which for instance has been used for strain measurements [48].

Sometimes there is a mixed approach that combine a bit of several of the previous, such as in [49], where the electronics is expanded to include an additional sensor (with its own power source) which is highly coupled to the RFID tag, modifying its behavior so that it transmits back to the receiver. However this approach, since it relies on a battery could not be properly categorized as passive RFID.

1.4 Objectives of the thesis

The main objective of the thesis is the study of the analytical relationship governing the electromagnetic coupling between a reader and an embeddable self-powered RFID sensor to enable its use as a EM-field probe and sensor which is capable of wirelessly measure physical parameters without the need of using external batteries. As such partial objectives of this thesis can be summarized as follow:

- Development of a general formulation of the response of an RFID tag, and determine how this response can be exploited for sensing purposes.
- Determine and evaluate quality parameters that can be used for the optimum design of the sensor.
- Completely characterize the response of an RFID IC and study the challenges that introduces in the use as a sensor.
- Develop strategies to use RFID probes for field distribution measurements, including tomographic imaging capabilities (large dynamic range measurements).
- Perform sensing of physical parameters in the neighborhood of the antenna using RFID-MST sensors.

1.5 Outline of the thesis

The main contents of this thesis is divided in 4 central chapters and the concluding chapter. Additional information is also distributed in a series of appendices at the end of the thesis. The main contents of each chapter is summarized as follows:

Chapter 2 analyzes the formulation governing the backscattering propagation in RFID sensors with a special emphasis on how it affects the performance of the RFID tag sensing capabilities. A set of quality parameters for the RFID sensors are established.

Chapter 3 characterizes the RFID sensor using the quality parameters introduced in chapter 2. Specifically the antenna design is analyzed in the first part of the chapter, and the non-linearities of the RFID IC are studied in the second part of the chapter before finalizing with a global evaluation of the performance using both components.

Chapter 4 develops strategies to overcome the challenges introduced by the non linearities as shown in chapter 3, and uses the RFID sensor for EM-field measurements. A novel approach to remove the non-linearities in the response of RFID sensors is proposed and experimentally verified in antenna pattern measurements as well as tomographic imaging of a canonical scenario.

Chapter 5 expands the use of RFID sensors, and discusses the challenges that RFID-MST must overcome for measurement of physical parameters of the environment. A new approach to overcome the limitation is proposed based on a multiple loaded RFID sensor.

Chapter 6 presents the main conclusions and contributions of this thesis.

2

Chapter 2

Modulated scattered technique. RFID-MST Formulation

The modulated scatterer technique (MST) is a free-space perturbation technique that is commonly used to remotely measure the electromagnetic field at a given point. As will be shown it is based in the controlled variation of the field scattered by an antenna.
Such simple principle of operation is also the basis of the backscattering modulation that is used by RFID to communicate. For this reason, and because the use of RFID as sensors in this thesis is based in the backscattering modulation, this chapter develops the formulation of MST from the context of passive RFID. Moreover, the formulation developed allows to easily predict the performance of RFID sensor probes in terms of harvesting and backscattered response.
Since RFID sensors are conceived to work in complex scenarios where extraneous scatterers may be present between the reader and the tag, and where the distance from the reader to the tag may vary from a very short range (a few millimeters) to distances as large as a few dozens of wavelengths, the MST formulation is developed in a general way that does not make any assumptions on the scenario except for reciprocity.[1]

[1] The following sections contains portions, sometimes verbatim, of the publication [JA7] of the author.

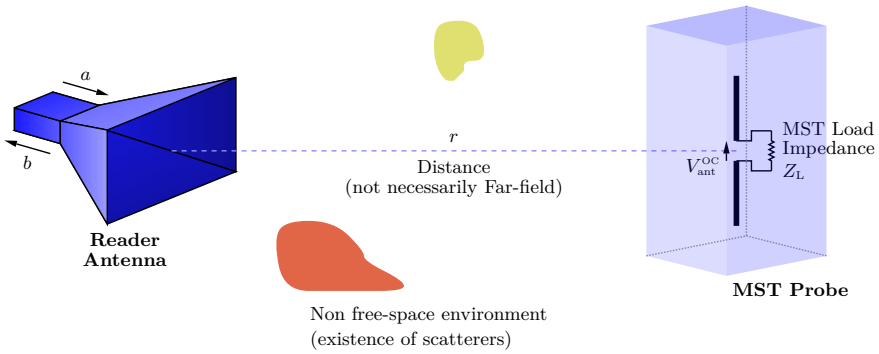

Figure 2.1: General scenario of an RFID system where the RFID tag (or MST probe) is embedded in an object which is located in an environment which, in general, does not have line-of-sight with the reader antenna, and where multiple scatterers might be present.

2.1 Basic definitions for RFID-MST

This section introduces a set definitions that are common in any scenario regardless of the formulation (far-field or reciprocity based) that is being considered. Fig. 2.1 shows a general RFID sensing scenario where a reader is communicating with a tag embedded in a given region. Without any loss of generality, the reader and the tag antenna (the probe) are represented by a horn and a dipole, respectively. The reader horn is fed via a waveguide supporting normalized incident and reflected waves, a and b, respectively. Accordingly, the transmitted and reflected powers are $P_a = \frac{1}{2}|a|^2$ and $P_b = \frac{1}{2}|b|^2$, respectively [50]. The input impedance of the probe antenna in its placement (inside of a box, as the label of a box, embedded in a medium, etc.) is $Z_{\text{ant}} = R_{\text{ant}} + jX_{\text{ant}}$ and its load impedance $Z_{\text{L}} = R_L + jX_L$. For backscattering modulation, the load impedance is switched from $Z_{\text{L}} = Z_{\text{L}_A}$ to $Z_{\text{L}} = Z_{\text{L}_B}$.

Let $V_{\text{ant}}^{\text{OC}}$ denote the open circuit voltage of the probe ($Z_{\text{L}} \to \infty$) and P^{av} the available power ($Z_{\text{L}} = {Z_{\text{ant}}}^*$). In the following, the only restrictions on the propagation medium between the reader and the tag antennas are to be linear, stationary and isotropic in such a way that reciprocity theorem can be applied. Such limitations, which do not imply free-space (FS) nor far-field (FF) assumptions, are usually met in most practical scenarios.

When the reader transmits a signal, part of the energy is reflected back to the reader as power wave b. Indeed, this reflected wave contains various terms: the self-reflection of the reader's antenna $a \cdot S_{11}$ in free-space, reflections coming from the different scatterers in the scenario b_{bgn}, and the specific reflection from the MST probe itself b_{prb}

$$b = a \cdot S_{11} + b_{\text{bgn}} + b_{\text{prb}} \tag{2.1}$$

where higher order interactions (for instance multiple reflections between the reader and the probe) which are much smaller than the rest have been neglected. The probe contribution arises from the radiation of the induced currents in the antenna structure, and can be further divided into the antenna mode (AM) and the structural mode (SM) components:

$$b_{\text{prb}} = b_{\text{AM}} + b_{\text{SM}} \tag{2.2}$$

Although the definition of the AM and the SM is not unique, [51,52], they can be thought as follows: b_{AM} depends on the *radiating currents* of the antenna, those which interact with its feeding port and can be excited directly by feeding the antenna; as a consequence b_{AM} is dependent on the load of the port. On the other hand b_{SM} is the wave that is reflected regardless of the load, that is, the radiation created by induced currents in the structure that do not interact with the feeding port, for instance due to the presence of metallic surfaces. A clear example that shows their difference is a patch antenna and an incident wave with a polarization rotated 45 ° with respect to the patch polarization. The cross-polar component of the incident wave will not excite a voltage at the antenna port, (polarization mismatch), as such the current induced by this wave is independent of the load at the port, and its re-radiation (part of the SM) is the same regardless of the load at the port. On the other hand the co-polar component creates an output voltage and as such the induced current will be dependent of the load (AM); additionally there might be some extra contribution to the SM component. Due to the difficulties of isolating both components, it is usual to define the SM as the scattered field for a reference load (a short circuit [52], a conjugate matched load [51] or an open circuit)and then define the AM as the variation in the scattered field for a different load.

MST relies on modulating (marking) b_{prb} so that it can be isolated from the rest of undesired and non-modulated terms. This modulation is achieved by changing the scattering parameters of the probe, either by a mechanical modification of the probe, such as the displacement or rotation of the probe antenna [8]; or electronically marking the b_{AM} component by using a load which presents highly differentiated impedances, such as the biasing states of a PIN diode [4], a photo-transistor [53], or the variable input impedance of an RFID integrated circuit (IC) [1]. This thesis and the rest of the derivation will focus on the latter modulating case, that is load switching based MST.

In the case of MST based on an electronic load switching, the wave b can be divided in two distinct components:

$$b = b_{\mathrm{AM}} + b_{\mathrm{und}} \tag{2.3}$$

where the first term, b_{AM}, is load-dependent and the second one, b_{und}, groups the rest of the terms $\left(b_{\mathrm{und}} = b_{\mathrm{bgn}} + b_{\mathrm{SM}} + a \cdot S_{11}\right)$ which are load-independent. As a result, when switching the load impedance (between Z_{L_A} to Z_{L_B}), only the first term changes, and by taking the difference between the signals b for each load, the differential reflected wave becomes:

$$\Delta b = b_{\mathrm{AM},A} - b_{\mathrm{AM},B} \tag{2.4}$$

This allows to ignore the load independent response; consequently in the following stages only the tag AM contribution b_{AM} is considered, although the whole expression will be considered once again in chapter 5.

As explained earlier, two possible formulations which converge for the limiting case are possible. The first one consists in following, step by step, the wave radiated by a reader: 1) reader-to-probe propagation; 2) scattering by the probe; and 3) probe-to-reader propagation. Only simple configurations can be treated by such an approach. For instance, the radar equation can be used if both Far-Field and Free-Space assumptions are satisfied. The second approach is global and aims to retrieve the total transfer function between the transmitted and the reflected waves at the reader port. The reader-probe configuration is considered as a black-box, linearly relating relevant quantities at the ports of the reader (incident/reflected waves) and of the tag (voltage/current) antennas.

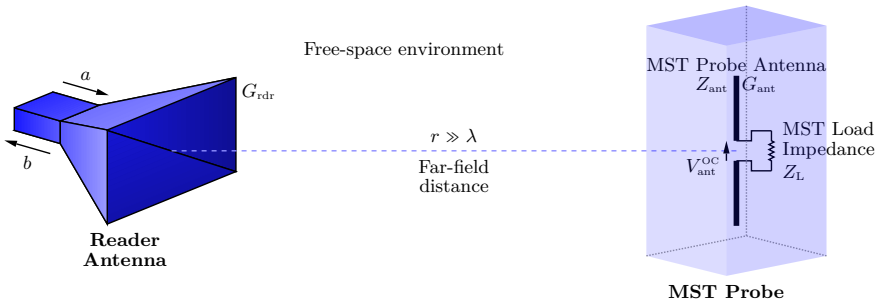

Figure 2.2: RFID scenario for a free-space propagation model where the reader and the tag antennas are in the far-field region.

Reciprocity offers a simple way to obtain the desired transfer function under very general conditions.

2.2 RFID From the Far-Field Viewpoint

The fact that the RFID tag constitutes a target for the reader has naturally inspired to use the radar equation to calculate the tag response. However, the general scenario of Fig. 2.1 must be simplified by assuming that there are no obstacles and that the target is in the Far-Field region of the reader (Fig. 2.2). As part of an RFID system the antenna tag must be characterized as a scatterer, and the Radar Cross-Section (RCS) becomes a relevant parameter [54, 55]. As for the reflected wave, and as shown in (2.3) the scattered field, $\vec{E}_{\text{ant}}$, can be divided in two components, one load dependent (AM) and one load-independent (SM):

$$\vec{E}_{\text{ant}} = \vec{E}_{\text{ant}}^{\text{AM}} + \vec{E}_{\text{ant}}^{\text{SM}} \tag{2.5}$$

Only the first one depends on the load of the tag antenna and is relevant for RFID systems. The radar cross section (RCS) for the antenna mode contribution, $\sigma_{\text{ant}}^{\text{AM}}$, can be easily calculated taking into account the power delivered by the tag to its load as:

$$P_{\text{L}} = P^{\text{av}} \cdot e_{\text{mis}} = S_{\text{rdr}} A_{\text{ant}}^{eff} e_{\text{mis}} \tag{2.6}$$

where S_{rdr} is the power density radiated by the reader on the tag, A_{ant}^{eff} the effective receiving area of the tag antenna and e_{mis} is the impedance mismatch factor, which will be later identified as the *LF* when referring to the scavenging state of the RFID tag:

$$e_{\text{mis}} = \frac{4R_{\text{L}}R_{\text{ant}}}{|Z_{\text{L}} + Z_{\text{ant}}|^2} \tag{2.7}$$

The scattered power (P^{AM}) by the tag antenna is the power that would be radiated by the antenna if used as a transmitter with the same current distribution, and thus:

$$P_{\text{ant}}^{\text{AM}} = |I|^2 R_{\text{ant}} = P_{\text{L}} \frac{R_{\text{ant}}}{R_{\text{L}}} \tag{2.8}$$

Finally and according to the RCS definition:

$$\sigma_{\text{ant}}^{\text{AM}} = \lim_{r\to\infty}\left\{4\pi r^2 \frac{S_{\text{ant}}^{\text{AM}}}{S_{\text{rdr}}}\right\} \tag{2.9}$$

which taking into account the definition of the power density radiated by the tag, $S_{\text{ant}}^{\text{AM}}$:

$$S_{\text{ant}}^{\text{AM}} = \frac{P_{\text{ant}}^{\text{AM}} \cdot G_{\text{ant}}}{4\pi r^2} \tag{2.10}$$

allows to obtain the antenna mode contribution to the tag RCS, [56]:

$$\sigma_{\text{ant}}^{\text{AM}} = \frac{\lambda^2 G_{\text{ant}}^2 R_{\text{ant}}^2}{\pi \left|Z_{\text{ant}} + Z_{\text{L}_2}\right|^2} \tag{2.11}$$

where λ is the wavelength and G_{ant} the gain of the tag antenna. It is then clear that the antenna mode RCS of the tag depends on its load impedance.

The received signal from the RFID tag consists of a succession of bits using two different load impedances $Z_{\text{L}_{A,B}}$. In order to obtain the power of the differential signal, we must consider the coherent subtraction of the scattered field $\Delta\vec{E}_{\text{ant}}^{\text{AM}}$, which can be related to an equivalent differential RCS $\Delta\sigma_{\text{ant}}^{\text{AM}}$, by means of the differential current distributions in the tag antenna [55], to obtain:

$$\Delta\sigma_{\text{ant}}^{\text{AM}} = \frac{\lambda^2 G_{\text{ant}}^2}{4\pi}\Delta\hat{\sigma} \tag{2.12}$$

where $\Delta\hat{\sigma}$ is the normalized RCS, which equals to:

$$\Delta\hat{\sigma} = \left|\frac{2R_{\text{ant}}\left(Z_{\text{L}_B} - Z_{\text{L}_A}\right)}{\left(Z_{\text{ant}} + Z_{\text{L}_A}\right)\left(Z_{\text{ant}} + Z_{\text{L}_B}\right)}\right|^2 \tag{2.13}$$

Introducing the differential RCS in the Radar equation provides the backscattered power (P_{bs}) of the tag received by the reader:

$$\Delta P_{\text{bs}}^{RCS} = \frac{\lambda^2 G_{\text{rdr}}^2 \Delta\sigma_{\text{ant}}^{\text{AM}}}{(4\pi)^3 r^4} P_a \tag{2.14}$$

where G_{rdr}, the gain of the reader antenna, is introduced via the power density S_{rdr}.

The radar approach implicitly assumes that the tag is located in the far-field (FF) of the reader and that the reader radiates in free-Space (FS). Even if such approximations are far from being valid in terms of distance or environmental complexity for the RFID practice, the radar equation is widely used to establish the range of operation of RFID systems.

2.3 General reciprocity Based Formulation

In the previous section a far-field analysis of the power budget of the RFID system has been presented. However such analysis cannot be used in the general scenario of Fig. 2.1, where the probe and the reader may not be isolated, they may not present line of sight conditions or they may be close to each other for far-field quantities to be meaningful, etc. In such situations, the RCS is not an appropriate parameter to describe the tag and a more robust formulation is required. This generalized formulation may be used not only in far-field but also in near-field. Fig. 2.3 shows a more detailed sketch with a definition of all the relevant parameters used throughout this section.

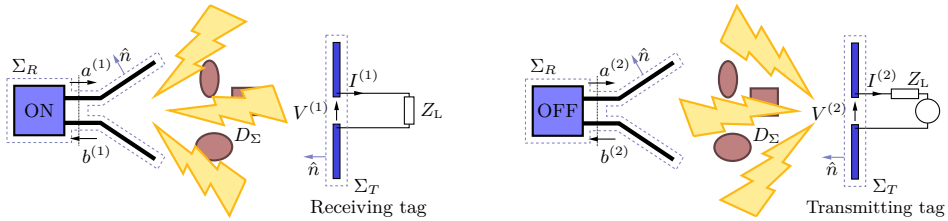

(a) State 1: Reader transmitting

(b) State 2: RFID tag transmitting

Figure 2.3: Diagram for the reciprocity analysis where a pair of antennas in two different situations are analyzed. In every situation, the role of transmitting and receiving antennas is changed for both the reader antenna (the horn) and the tag antenna (the dipole).

2.3.1 Mono-static reciprocity Formulation

Fig. 2.3 is appropriate for illustrating the reciprocity based formulation and for demonstrating its generality. Two situations are considered where, successively the reader and the probe are assumed to be transmitting. The indices $i = 1, 2$ denote each of the states for the incident/reflected waves at the reader $a^{(i)}$, $b^{(i)}$ and the voltages/currents at the tag $V^{(i)}$, $I^{(i)}$, respectively. State 1 is the general MST scenario where the reflected wave $b^{(1)}$ at the reader is composed of various contributions, as shown by equation (2.3). State 2 is introduced to isolate the antenna mode contribution of the tag. Imposing the condition $I^{(2)} = I^{(1)}$ and a matched generator at the reader ($\rho_G = 0$), it results that $b^{(2)} = b_{\mathrm{AM}}$.

Let Σ_{rdr} and Σ_{ant} be two surfaces enclosing the reader and probe antennas and $\hat{n}$ a unit outgoing normal vector, as shown on Fig. 2.3. Thus, if we only assume that Maxwell's equations are verified in the domain D_Σ external to Σ_{rdr} and Σ_{ant}, whether this domain is or not homogeneous, the reciprocity theorem provides the following relationship [8] :

$$\iint_{\Sigma_{\mathrm{rdr}} \cup \Sigma_{\mathrm{ant}}} \left[\vec{E}_1 \times \vec{H}_2 - \vec{E}_2 \times \vec{H}_1 \right] \cdot \hat{n} dS = 0 \tag{2.15}$$

Assuming perfectly conducting boundary conditions on the antennas, each of the surface integrals can be reduced to the excitation area of the antennas and explicitly written in the circuital terms of $a^{(i)}$, $b^{(i)}$ on Σ_{rdr} and $V^{(i)}$, $I^{(i)}$ on Σ_{ant} [8, 57] (see also appendix A.1.2):

$$2(a^{(1)}b^{(2)} - a^{(2)}b^{(1)}) = V^{(1)}I^{(2)} - V^{(2)}I^{(1)} \tag{2.16}$$

and taking into account the condition $I^{(2)} = I^{(1)}$:

$$V^{(1)}I^{(2)} - V^{(2)}I^{(1)} = (Z_{\mathrm{ant}} + Z_{\mathrm{L}})\left(I^{(1)}\right)^2 \tag{2.17}$$

and that

$$I^{(1)} = \frac{V^{\mathrm{OC},(1)}}{Z_{\mathrm{ant}} + Z_{\mathrm{L}}} \tag{2.18}$$

the following equation for the apparent reflection coefficient, $\rho_{\mathrm{rdr}}^{\mathrm{AM}}$, due to the antenna mode contribution of the probe is obtained:

$$\rho_{\mathrm{rdr}}^{\mathrm{AM}} = \frac{b_{\mathrm{AM}}}{a^{(1)}} = \frac{Z_{tr}}{Z_{\mathrm{ant}} + Z_{\mathrm{L}}} \tag{2.19}$$

where the transfer impedance Z_{tr} is introduced [CA24, 58] and expressed in terms of the open circuit voltage at the tag and the radiated power by the reader in state 1. Equivalently in the terms of the original scenario of Fig. 2.1:

$$Z_{tr} = \frac{\left(V^{\mathrm{OC}(1)}\right)^2}{4P_1} = \frac{\left(V^{\mathrm{OC}}\right)^2}{4P_a} \tag{2.20}$$

where $P_a = \frac{1}{2}\left|a^{(1)}\right|^2$ and $a^{(1)}$ is taken purely real. The transfer impedance Z_{tr}, which is more thoroughly discussed in the following section does not imply constraining assumptions on the propagation medium nor on the distance between the reader and the MST probe apart from reciprocity.

2.3.2 Transfer impedance

The switch of the load impedance of the probe antenna between two values causes a change in the apparent antenna mode reflection factor. By coherently subtracting the values obtained for each of these load impedances one obtains the differential reflection coefficient:

$$\Delta\rho_{\mathrm{rdr}} = \rho_{\mathrm{rdr}}\big|_{Z_{\mathrm{L}}=Z_{\mathrm{L}_A}} - \rho_{\mathrm{rdr}}\big|_{Z_{\mathrm{L}}=Z_{\mathrm{L}_B}} = Z_{tr}\frac{Z_{\mathrm{L}_B} - Z_{\mathrm{L}_A}}{\left(Z_{\mathrm{ant}} + Z_{\mathrm{L}_A}\right)\left(Z_{\mathrm{ant}} + Z_{\mathrm{L}_B}\right)} \tag{2.21}$$

It is useful for the following discussion to introduce the complex reflection coefficients of the load impedances defined as [50]:

$$\tilde{\rho}_{\mathrm{L}} = \frac{Z_{\mathrm{L}} - {Z_{\mathrm{ant}}}^*}{Z_{\mathrm{L}} + Z_{\mathrm{ant}}} \tag{2.22}$$

to finally obtain:

$$\Delta\rho_{\mathrm{rdr}} = \frac{Z_{tr}}{2R_{\mathrm{ant}}}\left(\tilde{\rho}_{\mathrm{L}_A} - \tilde{\rho}_{\mathrm{L}_B}\right) = \frac{Z_{tr}}{2R_{\mathrm{ant}}}\Delta\tilde{\rho}_{\mathrm{L}_{A,B}} \tag{2.23}$$

Finally, the backscattered power associated to the differential signal comes as:

$$\Delta P_{\mathrm{bs}}^{MST} = |\Delta\rho_{\mathrm{rdr}}|^2 P_a = \frac{|Z_{tr}|^2}{4R_{\mathrm{ant}}^2}|\Delta\tilde{\rho}_{L}|^2 P_a \tag{2.24}$$

It is worth noting that the transfer impedance is different from the mutual coupling impedance Z_{12}, which is naturally introduced when using an impedance matrix to relate the terminals of both reader and tag antennas [56, 59, 60]. It could be shown that the relationship existing between the transfer and the mutual impedances is: $Z_{21}^2 = Z_{tr}(Z_{11} + Z_{\mathrm{o}})/2Z_{\mathrm{o}}$, where Z_{o} is the characteristic impedance. Thanks to its compact expression in terms of quantities easy to "visualize", namely the open-circuit voltage and the available power, the transfer impedance is probably the simplest way to account for the coupling between antennas, without any limiting assumption on the propagation medium. Of course, the transfer impedance is dependent of the given reader-probe environment scenario. As such changing the distance or the surroundings of reader and probe results in a change of the transfer impedance. However, (2.20) readily shows that the transfer impedance, which is proportional to the square of the open-circuit voltage, is directly related to the square of the field distribution on the tag, since the open-circuit voltage

is proportional to the incident field, being the tag effective length the proportionality constant, which is used in chapter 4 for field measurements.

Equation (2.21) is particularly convenient for discussing the role of various factors on the power budget. Firstly, it appears that most of the environmental impact is due to the transfer impedance, which can be easily deduced from the open circuit voltage at the tag ports. This voltage can be either calculated or measured. Secondly, it appears that the close surroundings of the tag impact its impedance. Of course, this impedance is not the same if the tag antenna is in free-space, placed on a metallic box or embedded in a material. Thirdly, there is a clear separation between the propagation losses and the modulation depth. Indeed, while propagation losses are included in the transfer impedance, the modulation depth is concentrated in the antenna and load impedances, suggesting that there may be some degree of freedom in optimizing the coupling of a probe antenna to the IC chip impedance. All of these will be further analyzed in chapter 5 where RFID-MST probes are used for environmental sensing.

2.3.3 Equivalence Between Reciprocity and Far-Field Formulation

In the RCS approach, the differential Radar Cross Section (RCS), $\Delta\sigma_{\text{ant}}$, is related to the difference of the complex reflection factors of the loads, (2.12). Similarly, in the reciprocity-based formulation, the differential reflection factor $\Delta\rho_{\text{rdr}}$ depends on this difference, (2.23). As a consequence, the differential reflection coefficient can be related to the normalized differential RCS [55], $\Delta\hat{\sigma}$:

$$|\Delta\rho_{\text{rdr}}|^2 = \frac{|Z_{tr}|^2}{4R_{\text{ant}}^2}|\Delta\tilde{\rho}_{\text{L}_2}|^2 = \frac{\lambda^4 G_{\text{rdr}}^2 G_{\text{ant}}^2}{(4\pi r)^4}\Delta\hat{\sigma} \tag{2.25}$$

Introducing (2.25) into (2.24) allows retrieving the usual monostatic radar equation (2.14). Then, as a conclusion, the reciprocity-based formula is fully compliant with the radar equation, as soon as far-field and free-space assumptions are satisfied. Another practical consequence is that modulation depth assessment does not require to be done in plane wave controlled environment such as anechoic chambers, [61, 62] or GTEM cells [63]. For instance, the measurement of the differential reflection coefficient in the near-field, to obtain a better signal to noise ratio, allows retrieving the differential RCS by means of equation (2.25) as soon as the input resistance of the tag antenna and the transfer impedance are known.

2.3.4 Bi-static formulation

The previous formulation considered a mono-static configuration at the reader, however a bi-static setup provides more flexibility in terms of configuration, and increases the chance of detecting responses from far-away (low backscattered power) probes; although in the case of RFID tags, as will be seen in the following sections, the most limiting factor (in terms of reading range) is the scavenged power. Additionally a bi-static configuration increases the available dynamic range of the measurement, since coupling between transmitting and receiving antennas is usually much lower than the self-matching of the reader antenna.

Following a similar procedure as the one used for the mono-static case, which can be seen in appendix A.4, it is possible to derive an expression for the differential transmission coefficient $\Delta\tau_{\mathrm{Rx,Tx}} = \tau^{A}_{\mathrm{Rx,Tx}} - \tau^{B}_{\mathrm{Rx,Tx}}$.

$$\Delta\tau_{\mathrm{Rx,Tx}} = \underbrace{\frac{V^{\mathrm{OC}}_{\mathrm{Tx}} V^{\mathrm{OC}}_{\mathrm{Rx}}}{2a_{\mathrm{Tx}}a_{\mathrm{Rx}}}}_{Z^{\mathrm{bis}}_{tr}} \frac{Z_{\mathrm{L}_A} - Z_{\mathrm{L}_B}}{(Z_{\mathrm{ant}} + Z_{\mathrm{L}_A})(Z_{\mathrm{ant}} + Z_{\mathrm{L}_B})} \tag{2.26}$$

where a bi-static definition of the transfer impedance Z^{bis}_{tr} has naturally developed, which depends on the product of the normalized open circuit voltage (V^{OC}_i/a_i) that the transmitter/receiver antennas would create on the probe antenna. As it can be seen when transmitter and receiver are considered the same, this formulation reverts to the mono-static expression defined in (2.23).

2.4 Probe Antenna Design Optimization

Conventional RFID antenna designs optimize the power scavenged by maximizing the power transfer between the RFID antenna and the scavenging impedance of the RFID IC (Z_{scav}). However, as was shown in the preceding section, the communication with the reader is governed by the relation between the two impedance states of the IC and the probe antenna impedance, so an additional optimization goal can take into account the communication with the reader through the backscattering modulation. The final criteria will be a trade-off between sensitivity (back-scattered power) and coverage of the tag (harvested power).

2.4.1 Quality Parameters

In the previous section it has been shown that the modulated power backscattered by the probe, calculated either from radar or reciprocity, is directly related to the square magnitude of the differential complex reflection factor (2.24). It is straightforward then to consider this quantity as a representative index of an MST system.

In order to obtain a geometrical interpretation of $\Delta\tilde{\rho}_{_L}$ on a Smith chart it is useful to notice that the complex reflection coefficient ($\tilde{\rho}$) can be related to the conventional reflection coefficient (ρ) of a modified load Z'_{L}. This modified load includes the imaginary part of the tag antenna impedance added in series to the load: $Z'_{\mathrm{L}} = Z_{\mathrm{L}} + jX_{\mathrm{ant}}$ [50, 55]:

$$\tilde{\rho}_{\mathrm{L}} = \frac{Z_{\mathrm{L}} - Z^{*}_{\mathrm{ant}}}{Z_{\mathrm{L}} + Z_{\mathrm{ant}}} = \frac{Z_{\mathrm{L}} + jX_{\mathrm{ant}} - R_{\mathrm{ant}}}{Z_{\mathrm{L}} + jX_{\mathrm{ant}} + R_{\mathrm{ant}}} = \rho_{\mathrm{L}}\Big|_{\substack{Z_{\mathrm{L}} = Z_{\mathrm{L}} + jX_{\mathrm{ant}} \\ Z_{\mathrm{o}} = R_{\mathrm{ant}}}} \tag{2.27}$$

Taking this into account, the two impedance states $\tilde{\rho}_{\mathrm{L}_A}$ and $\tilde{\rho}_{\mathrm{L}_B}$ can be located on a Smith chart normalized with respect to the probe antenna resistance R_{ant} [55], at points M_A and M_B respectively, see Fig. 2.4a. In this case $|\Delta\tilde{\rho}_{\mathrm{L}}|^2 = |\overline{M_A M_B}|^2$ is the square of the distance between these points. Then clearly $\Delta\tilde{\rho}_{\mathrm{L}}$ is bounded by 2: $0 \leq |\Delta\tilde{\rho}_{\mathrm{L}_{A,B}}| \leq 2$. The maximum value $|\Delta\tilde{\rho}_{\mathrm{L}_2}| = 2$ (or $+6\,\mathrm{dB}$) is obtained for points located on the outer circle diametrically opposite to each other, see Fig. 2.4b. For the standard load combination assumed for an RFID IC, consisting of Z_{SC} a short-circuit and Z_{scav} as the antenna conjugate matched impedance, $|\Delta\tilde{\rho}_{\mathrm{L}}| = 1$, because $M_A = M_{\mathrm{SC}}$ is located on the

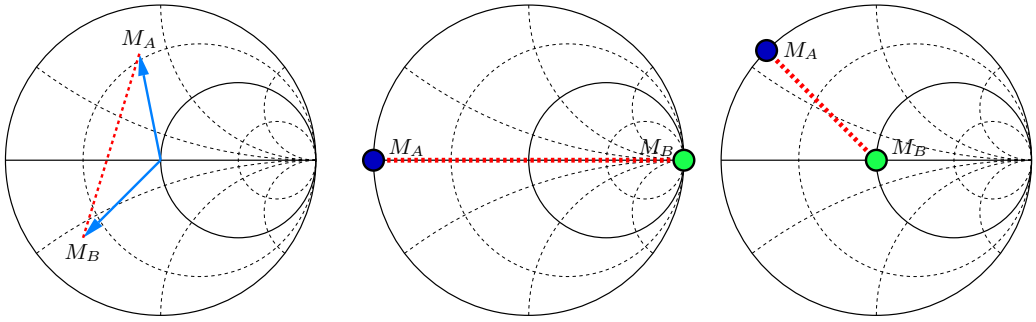

(a) Arbitrary impedances **(b)** $Z_{\mathrm{L}_A} = -jX_{\mathrm{ant}}$, $Z_{\mathrm{L}_B} \to \infty$ **(c)** $Z_{\mathrm{L}_A} = 0$, $Z_{\mathrm{L}_B} = Z^*_{\mathrm{ant}}$

Figure 2.4: If the tag antenna loads are switched between two different states, M_A and M_B, the backscattered power presents a strength proportional to the square of the distance $\overline{M_A M_B}$. It must be noted that the reactance of the antenna impedance makes the short-circuit apparent position on the Smith Chart off-axis.

outer circle (not necessarily on the axis due to the tag antenna reactance) and $M_2 = M_{\mathrm{scav}}$ is at the center of the chart, Fig. 2.4c. From these observations it results that it is impossible to simultaneously maximize the delivered power to the tag and the modulated backscattered power. However it may be anticipated that some optimization might be achieved to meet power scavenging and sensitivity requirements.

For this reason, two quality parameters are introduced. Firstly, the load factor (LF) which provides a measure of how efficient the power scavenging of the RFID IC, and is in fact the impedance mismatch factor for the scavenging mode of the RFID IC (Z_{scav}). Indeed, the load factor relates the power delivered to the load Z_{scav} ($P_{\mathrm{L}_{\mathrm{scav}}}$) and the available power P^{av} at the tag antenna port:

$$P_{\mathrm{L}_{\mathrm{scav}}} = P^{\mathrm{av}} \cdot LF \tag{2.28}$$

The load factor, as defined from equation (2.7), can also be written as:

$$LF = 1 - |\tilde{\rho}_{\mathrm{L}_{\mathrm{scav}}}|^2 \tag{2.29}$$

Note that the available power can be easily related to the transmitted power P_a thanks to the transfer impedance:

$$P^{\mathrm{av}} = P_a \frac{|Z_{tr}|}{2R_{\mathrm{ant}}} \tag{2.30}$$

The Load Factor is bounded as $0 \leq LF \leq 1$ and shows the maximum value $LF = 1$ for the conjugate match. The proper operation of the RFID tag requires that the power $P_{\mathrm{L}_{\mathrm{scav}}}$ delivered to the RFID IC chip is larger than P_{th},or equivalently that $LF > LF_{\mathrm{th}}$ and $|\tilde{\rho}_{\mathrm{L}_{\mathrm{scav}}}| \leq |\tilde{\rho}_{\mathrm{L}_{\mathrm{th}}}|$ for a given transmitted power P_a. Geometrically, this means that on a Smith chart, the point M_{scav} has to be inside of a circle of radius $|\tilde{\rho}_{\mathrm{L}_{\mathrm{th}}}|$.

LF is an important parameter regarding the activation range of the tag. As usual conjugate matching will turn into the best range in terms of power scavenging, but for the whole system operation it is also important to take into account the backscattered power which depends on the Modulation Efficiency (ME).

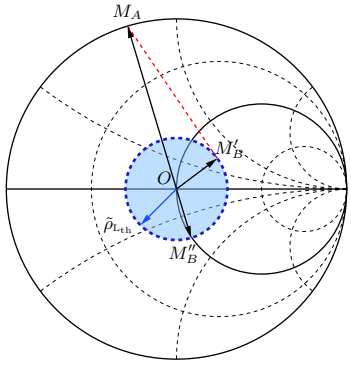

Figure 2.5: The *ME* is clearly affected by the choice of the two loads to be used. For a given *LF*, there is a set of possible values for M_B, all of them presenting the same scavenging efficiency, but only one of them maximizes the strength of the backscattered signal (M''_B).

The aim of the modulation efficiency (*ME*) is to allow the comparison of the backscattered power for a given load combination with respect to the backscattered power obtained with the standard RFID load combination ($Z_{\mathrm{SC}}, Z_{\mathrm{scav}}$). Formally, the *ME* is defined by the following ratio:

$$ME = \frac{P_{\mathrm{bs}}(Z_{\mathrm{L}A}, Z_{\mathrm{L}B})}{P_{\mathrm{bs}}(Z_{\mathrm{SC}}, Z_{\mathrm{scav}})} = \frac{\left|\Delta\tilde{\rho}_{\mathrm{L}_{A,B}}\right|^2}{\left|\Delta\tilde{\rho}_{\mathrm{L_{SC,scav}}}\right|^2} \tag{2.31}$$

and since $|\Delta\tilde{\rho}_{\mathrm{L_{SC,scav}}}| = 1$, *ME* becomes:

$$ME = \left|\Delta\tilde{\rho}_{\mathrm{L}_{A,B}}\right|^2 = \frac{4R_{\mathrm{ant}}^2 \left|Z_{\mathrm{L}B} - Z_{\mathrm{L}A}\right|^2}{\left|Z_{\mathrm{ant}} + Z_{\mathrm{L}A}\right|^2 \left|Z_{\mathrm{ant}} + Z_{\mathrm{L}B}\right|^2} \tag{2.32}$$

It results that the Modulation Efficiency is bounded as $0 \leq ME \leq 4$, or $ME_{\,\mathrm{dB}} \leq 6\,\mathrm{dB}$. Geometrically, the *ME* is simply given by the square of the distance $\overline{M_A M_B}$ on a Smith chart. As an example, consider the case shown in Fig. 2.5 where points M_A and M'_B correspond to the impedance values of the two states. In this case M'_B is within the circle defined by $\tilde{\rho}_{\mathrm{L_{th}}}$ but *ME* is not optimized. By moving to M''_B, *ME* is increased while still preserving the same load factor (*LF*).

2.4.2 Modulation efficiency experimental characterization

To show the importance of the selection of the set of loads/antenna impedance, an experimental measurement is carried out, using three different loads: $Z_{\mathrm{L}A} \approx 50\Omega$, a short-circuit ($Z_{\mathrm{L}B} = 0\Omega$) and open-circuit ($Z_{\mathrm{L}C} \to \infty$), and a resonant (800 MHz) monopole antenna. Fig. 2.6a shows the characterization of the loads at the antenna reference plane, including the electrical length and attenuation added by the small transmission line between the loads and the connector. Alternatively, Fig. 2.6b shows the location of $\tilde{\rho}_{\mathrm{L}}$ using the normalization presented earlier which considers $Z_{\mathrm{o}} = R_{\mathrm{ant}}$.

Using the characterization of the impedances, it is possible to compute $|\Delta\tilde{\rho}_{\mathrm{L}}|^2$, and with that, the expected modulation efficiency, shown in Fig. 2.7a, can be obtained using (2.32). This *ME* presents a large variability depending on the frequency and the set of loads that is considered.

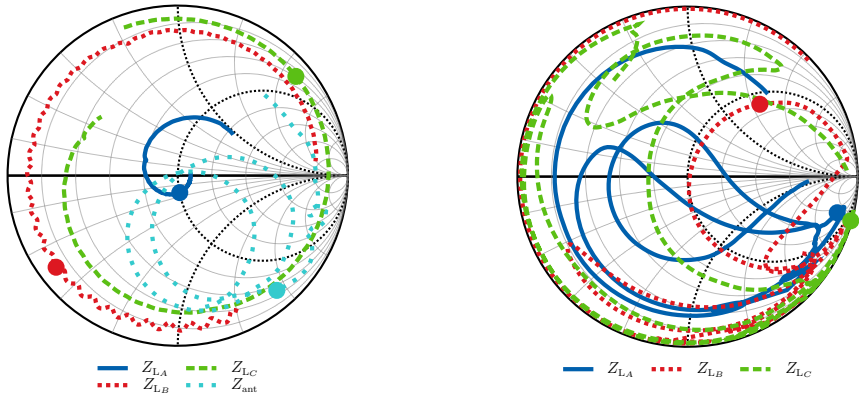

(a) 50Ω as reference

(b) R_{ant} as reference

Figure 2.6: Smith chart representation of the measured input impedance for each of the loads. The dot appears at the frequency 995 MHz where Z_{L_A} is closer to the conjugate matching condition. In (a) a 50 Ω representation is presented; in (b) the reference impedance is the real part of the monopole impedance (R_{ant}) and the distance between the modified loads ($Z'_{\text{L}} = Z_{\text{L}} + jX_{\text{ant}}$) is directly $|\Delta\tilde{\rho}_{L_2}|$.

For the experimental characterization, a ridged horn antenna connected to a VNA is used to illuminate the monopole from 800 MHz to 1800 MHz and ρ_{rdr} is measured for each of the loads at the monopole. It must be noted that in order to directly measure ME , it is required according to (2.31) to measure ρ_{rdr} of the horn antenna with the conjugate of Z_{ant} as well as a purely reactive load (e.g. a perfect short-circuit). Since these loads are not available in the experimental set of loads for the whole range of frequencies, it won't be possible to obtain the normalization required to characterize the ME directly. As an alternative, the pair of loads Z_{L_A} and Z_{L_C} will be taken as a reference to normalize ME $\frac{ME(Z_{\text{L}_i}, Z_{\text{L}_j})}{ME(Z_{\text{L}_A}, Z_{\text{L}_C})}$, as shown in Fig. 2.7b. A good agreement between the prediction and the measured curves is observed, basically because by using this normalization of ME , it is possible to remove the dependence of the transfer impedance (the scenario dependence which is not computed in the prediction).

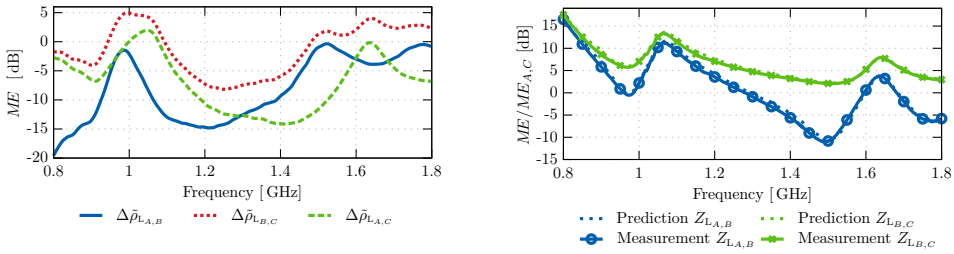

(a) Predicted ME

(b) Normalized ME

Figure 2.7: (a) predicted ME obtained from the characterization of the loads. (b) comparison between the prediction and the experimental response: a normalized ME has been obtained and represented using loads Z_{L_A} and Z_{L_C} as the reference set.

As shown in both plots in Fig. 2.7 the selection of the loads (or alternatively the value of Z_{ant}) has an important impact in the backscattered power.

3

Chapter 3

RFID-MST components. Antenna design and circuitry characterization

The RFID-MST probe is divided in two distinctive components, the antenna and the RFID integrated circuit (IC). This chapter is devoted to the design of the first and the complete dynamic characterization of the latter taking into consideration the quality parameters that were established in the previous chapter and its relationship with the performance of the probe.

Specifically, two antenna designs will be shown that take as an objective the two different goals established by the quality parameters of the previous chapter, namely the optimization of the scavenging of energy, that is the maximization load factor (LF), and the optimization of backscattered power received at the reader, or equivalently the maximization of the modulation efficiency (ME).

As a second step the RFID IC, responsible of the autonomous intelligence and scavenging of the passive RFID tag is described, and the input impedance of the different states that it can support, which is the main parameter to consider regarding backscattering modulation as described in the previous chapter, is characterized. This complete characterization uses a novel approach that allows to measure the dynamic impedance (in terms of power and frequency) of the two states of the RFID IC.

A final discussion of the impact of non-idealities and non-linearities of the RFID IC on the performance of RFID in general is also presented.

3.1 RFID-MST components: Antenna

The antenna of the RFID probe is its largest component and will eventually determine the physical dimensions and properties of the tag. The constraints that the application imposes on the RFID probe therefore will be directly translated to the RFID antenna. These constraints usually fall into one of the following categories:

Dimensions. Depending on the application size requirements change; on one hand some application might need the RFID tag to be as invisible as possible, so that its presence is unnoticed by the end users (for instance counterfeiting). On the other hand, some other applications might be less concerned about the visibility of the tag, so there is no strict requirement on size, but it still must fit the dimensions of the products.

Materials. Similarly to the previous requirements, the material may change with the application. Some application might require bendable tags (RFID for cloth applications) while others require tags with an endurance that makes them capable of being used in harsh environments (RFID in construction environments). Also the materials over which the tag is applied influence the design of the RFID antenna. It is not the same a tag to be placed over cardboard, than for on water bottle, or some tinned product. Additionally the material used to fabricate the antenna can enable further miniaturization processes, or even in the capabilities that the RFID sensor has [38]. Appendix E summarizes some of the research that has been done during the development of this thesis in new materials which present a potential as a building block for small antennas.

Input impedance and bandwidth. UHF RFID in Europe works around 868 MHz, in Japan at 950 MHz and in the USA at 915 MHz. For a single tag to operate in the three regions without any problem, high bandwidths are required. For specific localized applications bandwidth requirements are less restrictive, but fabrication tolerances and also tag placement might require larger bandwidth to ensure proper operation. .

Range. Depending on the application a minimum activation range might be required (in terms of scavenging), this makes maximization of the range of operation the usual optimization goal in the antenna design. Although range is mostly determined by the sensitivity of the IC through P_{th}, the efficiency, radiation pattern and the matching between the antenna and the RFID IC (the load factor (LF)) play an important role towards the final range achieved.

Cost. Common applications of ultra high frequency (UHF) RFID require manufacturing processes that ensure that the final cost of the RFID tag is low. This limits the technological decisions that can be used in the design stage, usually favoring planar structures without vias or interconnection between layers, although it will depend on the specific application.

3.1.1 Common configurations for passive RFID antenna

Usually the most challenging is the combination of a given input impedance with reduced dimensions and a given operation range.

	Z_L [Ω]	Source
A	73.0 − j113	[65]
B	12.0 − j420	[62]
C	15.0 − j151	[66]
D	6.2 − j127	[67]
E	12.0 − j300	[68]

Table 3.1: Input impedance of several RFID IC chips, as obtained from published references.

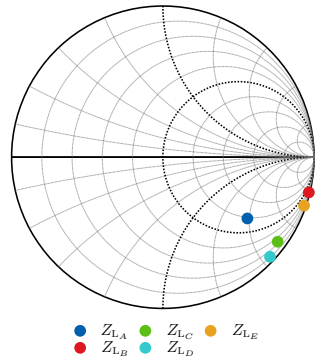

Figure 3.1: Location of the RFID IC from table 3.1 in a Smith Chart normalized to 50 Ω.

In [64] a review of the usual design procedure followed for RFID applications is presented, and it concludes, as expected from conventional antenna applications, that maximization of the read range is achieved for a proper match between the RFID antenna and the RFID IC at the scavenging mode, which implies a load factor (LF) equal to 1.

Since the RFID IC is usually given, or has a limited set of possible values (different manufacturers), this implies that the RFID antenna must be designed to match the IC and not the other way round. Table 3.1 and Fig. 3.1 present values found in the literature for different RFID IC (and in-depth characterization of one of these ICs will be done later in section 3.3). It can be seen that the input impedance of the RFID IC corresponds to a parallel RC circuit, with usually a large negative reactance, as shown in the Smith chart plot. Therefore, the antenna input impedance must be highly inductive with a large ratio between reactance and resistance (Q-factor).

Fig. 3.2 presents some common designs for RFID antennas. The designs rely on different approaches to reduce the antenna size while obtaining a proper inductive behavior of the input impedance at the frequency of operation. However, in the end a combination of the different approaches is commonly used to achieve the design goal [69]. The most common techniques that are used to obtain a high inductance are a T-match configuration and the inductive coupling feeding, that will be shortly introduced next.

3.1.1.1 T-match

One of the most common configurations used for the design of the feeding section of an RFID antenna is the T-match configuration [69, 72], shown in Fig. 3.3a for a dipole. It consists of dipole of length L_1 which instead of being fed at the center, it is fed by a secondary smaller dipole of length L_2 placed at a distance s. Each dipole may present different widths, W_1 and W_2.

The input impedance at the feeding point can be obtained by decomposing the structure in two modes, the antenna (or even) mode and the transmission line (or odd) mode, shown in Fig. 3.4 [73, 74], which combined give the input impedance as:

$$Z_{\text{ant}} = \frac{V}{I} = \frac{V}{I_2^e + I_2^o} \tag{3.1}$$

(a) T-match [70]

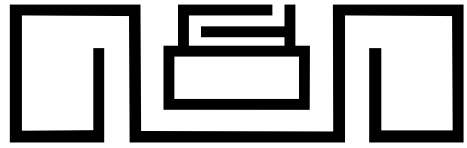

(b) Inductive Coupling [71]

(c) Meander line [64]

Figure 3.2: Example of RFID tags whose design uses different strategies to achieve the desired target impedance

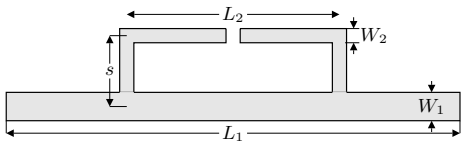

(a) Physical configuration

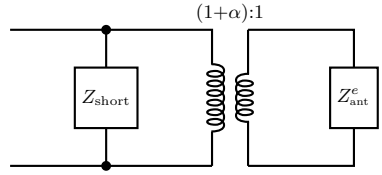

(b) Equivalent circuit

Figure 3.3: T-match feeding configuration: (a) shows the physical disposition; (b) presents the equivalent circuit, with Z_{ant} the impedance of the radiating body, Z_{short} the reactance from the transmission line mode, and α the ratio between the currents in each arm.

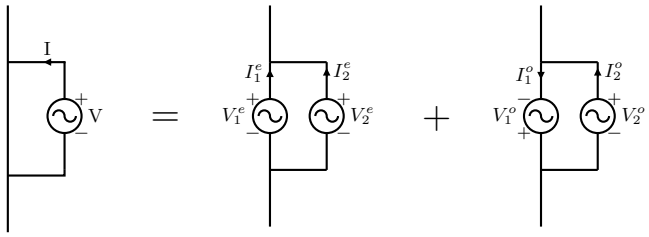

(a) Simple Antenna model **(b)** Even mode **(c)** Odd mode

Figure 3.4: Decomposition of the T-match into the antenna mode (b) and transmission line mode (c).

For the antenna mode (Fig. 3.4b), the feeding voltage is symmetric ($V_1^e = V_2^e = V^e$). It is then possible to apply a circuital analysis to obtain the relationship between the currents in both arms [73] as:

$$\alpha = \frac{I_1^e}{I_2^e} = \frac{Z_{22} - Z_{12}}{Z_{11} - Z_{12}} \tag{3.2}$$

where Z_{ii} refers to the self-impedance of each of the dipoles, and Z_{12} is the mutual impedance. In general $Z_{11} \neq Z_{22}$ because the dipoles have different width and there is a small asymmetry, otherwise $\alpha = 1$. Additionally since the voltage difference between two dipole is 0 for points at the same height, it is electrically equivalent to having a single source supplying the current to both dipoles $I^e = I_1^e + I_2^e$. As shown in [72] the input impedance of this equivalent circuit Z_{ant}^e behaves as a dipole whose radius is a function of W_1, W_2 and s, thus making use of the definition $Z_{\text{ant}}^e = V^e/I^e$ and of (3.2), the current I_2^e becomes:

$$I_2^e = \frac{V^e}{Z_{\text{ant}}^e}(1 + \alpha) \tag{3.3}$$

For the transmission line mode (Fig. 3.4c), the currents at each port are anti-symmetric ($I_1^o = I_2^o = I^o$), and the voltages fulfill the condition [73]:

$$\frac{V_1^o}{V_2^o} = \frac{Z_{11} - Z_{12}}{Z_{22} - Z_{12}} = \frac{1}{\alpha} \tag{3.4}$$

which is the inverse of the ratio of the currents in the antenna mode. Making use of the fact that the sum of both modes result in the circuit of Fig. 3.3a, this uniquely determines the value of the voltages of each mode:

$$V^e = \frac{V}{1+\alpha}, \quad V_1^o = \frac{V}{1+\alpha}, \quad V_2^o = \frac{\alpha V}{1+\alpha} \tag{3.5}$$

Taking into account that the odd mode is composed by 2 transmission lines of length $L_2/2$ terminated with a short-circuit and connected to the sources, the current I^o can be related to the input impedance of the lines Z_{short} as:

$$I^o = \frac{V_1^o + V_2^o}{2Z_{\text{short}}} = \frac{V}{2Z_{\text{short}}} \tag{3.6}$$

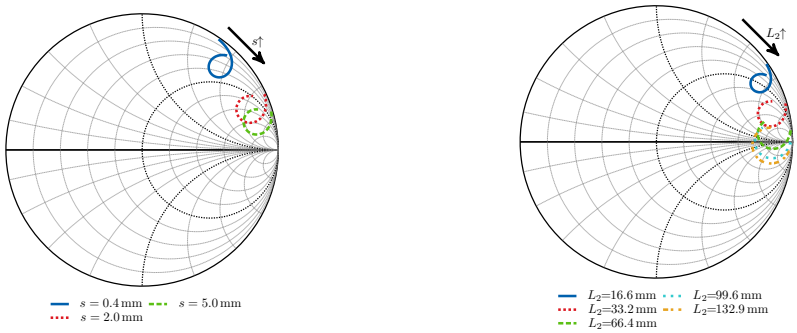

(a) Variation of s **(b)** Variation of L_2

Figure 3.5: Variation of the input impedance of a resonant dipole at 868 MHz using a T-match feeding configuration when the separation s is increased (a) and when the length L_2 is increased (b). The impedance values have been obtained using MoM.

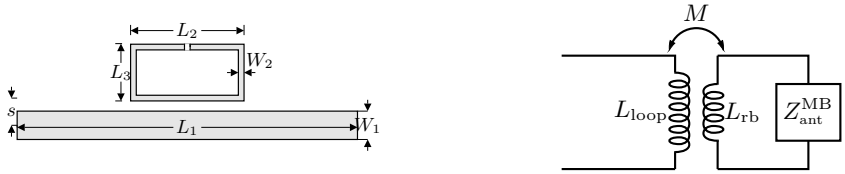

(a) Physical configuration **(b)** Equivalent circuit

Figure 3.6: Inductively coupled feeding configuration: (a) shows the physical disposition; (b) presents the equivalent circuit, with Z_{ant} the impedance of the radiating body, which is coupled to the feeding loop Z_{loop} by means of the mutual inductance M of the loop and the antenna.

Finally the input impedance of the antenna can be obtained as:

$$Y_{\text{ant}} = \frac{1}{Z_{\text{ant}}} = \frac{I_2^e}{V} + \frac{I_2^o}{V} = \frac{Y_{\text{ant}}^e}{(1+\alpha)^2} + \frac{1}{2Z_{\text{short}}} \tag{3.7}$$

$$Z_{\text{ant}} = \frac{2Z_{\text{short}} Z_{\text{ant}}^e (1+\alpha)^2}{2Z_{\text{short}} + Z_{\text{ant}}^e (1+\alpha)^2} \tag{3.8}$$

which corresponds to the equivalent circuit of Fig. 3.3b [69, 72].

Fig. 3.5 shows a comparison of the input impedance that is obtained with variations of the T-match feeding a resonant dipole. Values of L_2 close to the resonant dipole do not add reactive part, and boost the real part (folded dipole-like behavior), on the other hand as L_2 diminishes the reactive part becomes highly inductive.

3.1.1.2 Inductively coupled feeding

The idea of inductively coupled feeding is similar to the T-match feeding, however in this case the feeding element is a small loop instead of a dipole and its separated from the main body of the antenna by a short distance, as shown in Fig.3.6a.

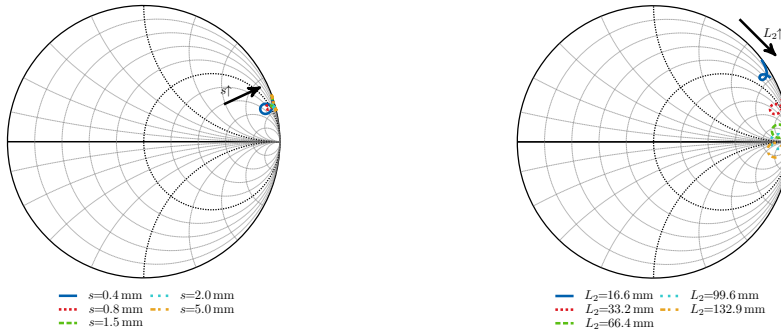

(a) Variation of s with $L_2 = 132.9\,\text{mm}$

(b) Variation of L_2 with $s = 0.4\,\text{mm}$

Figure 3.7: Variation of the input impedance of a resonant dipole at 868 MHz using a inductive coupled feeding when (a) the separation s is increased and (b) when the length of the loop L_2 is increased as obtained using MoM.

An analytical model for the inductively coupled feeding is presented in [75] which is based in the equivalent circuit model shown in Fig. 3.6b. The input impedance then becomes:

$$Z_{\text{ant}} = Z_{\text{loop}} + \frac{(2\pi f M)^2}{Z_{\text{ant}}^{\text{MB}}} \tag{3.9}$$

where Z_{loop} and $Z_{\text{ant}}^{\text{MB}}$ stand for the impedance of the loop and the main body when they are isolated, and M is the mutual coupling between a loop and an infinitely long wire at the main antenna body.

Similarly to the T-match, Fig. 3.7 presents the input impedance of a resonant dipole against different separations and dimensions of the loop. It clearly shows that the inductance is basically controlled with the loop dimensions, while the resistance is modified with the changes in the mutual coupling.

3.1.2 Antenna design for maximum load factor (LF)

The RFID antenna presented in this section [CA21, 76] was designed for the purpose of using it as a field probe, but trying to maximize the dynamic range of operation of the tag, as such the main requirements for the probe are:

- RFID IC matching. To maximize the operating range, the RFID antenna must be well-matched to the IC impedance at P_{th} and with an operating frequency of 868 MHz (Europe band). This implies that the load factor (LF) must be maximized. The RFID IC for which the antenna is designed is the Philips SL3S1001FTT [77], whose input impedance at the frequency of interest is $20 - j404\Omega$ [77], but it is desirable that it can be easily modified to tune it to different ICs.

- Polarization. Since the antenna will be used for field measurements, the antenna should be linearly polarized.

- Dimensions. No specific constraint was imposed here, but the antenna should be as small as possible.

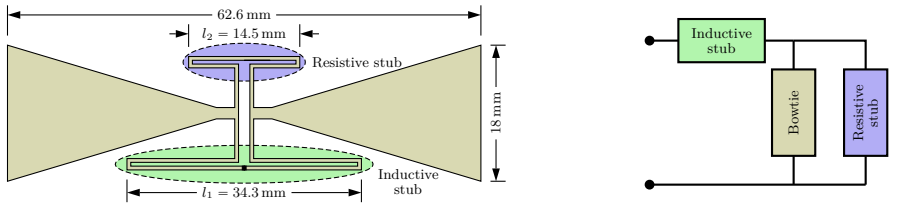

(a) Antenna diagram

(b) Antenna equivalent circuit

Figure 3.8: (a) Final antenna design where the two stubs that can be used to tune the impedance have been shown encircled by a dotted line; (b) presents the equivalent circuit with the effect of the antenna and the stubs.

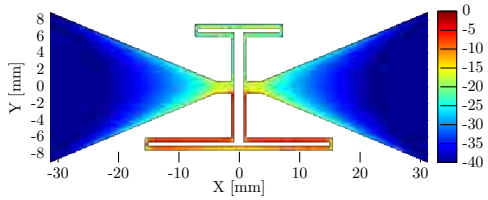

Figure 3.9: Currents excited in the structure of the antenna at a frequency of 868 MHz.

Fig. 3.8 presents the final design of the RFID antenna designed on a substrate of Rogers RO4003C of 1.52 mm of thickness. It is conformed by a central element consisting of a bow-tie antenna with a length approximately equivalent to $\lambda/5$ and a set of stubs in the central part of the antenna. The use of a bow-tie antenna for RFID is not new, [54, 78], but it naturally presents the advantage that it presents a wider bandwidth, and therefore a higher tolerance, due to the *flat* behavior of the input impedance. However it must be observed the lack of either a coupled loop or a T-match feeding configuration, but instead presents a series of metallic strips near the feeding area. The direct consequence of such a decision is that the impedance does not present a resonance (a loop in the smith chart representation) around the IC impedance as it happened in the examples of T-match and coupled loop (see Fig. 3.5 and 3.7). This reduces the final bandwidth at the input port of the antenna (since the impedance goes through the region of interest), and therefore the design would not be suitable for a commercial tag, since it would be highly sensitive to de-tuning; however, the design allows for easy tuning capabilities after fabrication (by modification of the stubs with silver paint), which is interesting for a laboratory prototype that can be used with several ICs.

The high degree of tunability of the antenna is achieved by means of two sets of strips. The currents excited on each of the strips present the same magnitude and opposite direction therefore they operate in a transmission line mode forming two sets of stubs, which do not radiate thus adding an extra reactance to the circuit which can be modified by lengthening and shortening them. The excited currents on the structure and stubs are presented in Fig. 3.9. The so-called inductive stubs, placed at the feeding points of the antenna, offer a high control over the reactance of the antenna, because they are in series to the IC and they can only change the imaginary part of the impedance (neglecting losses); on the other hand the so-called resistive stubs, the ones that are farthest from the

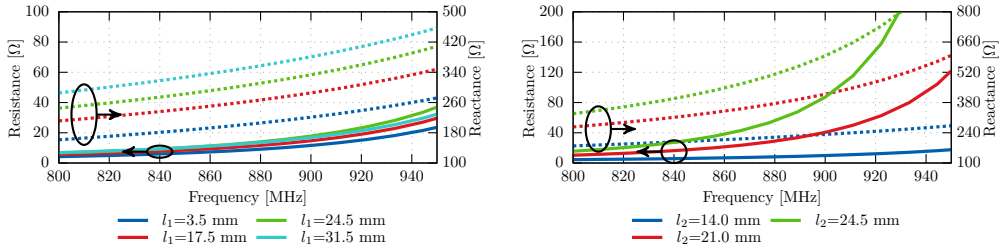

(a) Inductive stub variation for $l_2 = 15\,\text{mm}$ **(b)** Resistive stub variation for $l_1 = 15\,\text{mm}$

Figure 3.10: Impedance results from simulations using HFSS for different lengths of the tuning stubs. The straight line represents the resistance values, and the dashed line the reactance values. It can be observed that the inductive stub (a) has control over the reactance with small effect on the resistance, while the resistive stub (b) modifies the whole impedance.

feeding point, are placed in parallel to the bow-tie antenna. Although the resistive stub impedance is purely imaginary (neglecting losses), the parallel configuration produces a strong variation of the input impedance of the bow-tie, therefore changing simultaneously the resistance and reactance at the terminals of the bow-tie.

Fig. 3.10 shows the effect of the modification of the stubs in the input impedance of the antenna for the range 800 MHz up to 950 MHz. Variations of the length of the inductive stub produce a large variation of the inductance, while keeping the resistance basically constant. Only for an extremely short length (1 mm) there is a noticeable variation of the resistance, which is attributed to the destruction of the transmission line mode in the stubs due to its short length, comparable to the separation between strips, therefore other parasitic effects arise. Similarly for the resistive stub, Fig. 3.10b, a stronger effect in the input impedance is produced, and for any length variation the whole impedance is changed.

The antenna's equivalent circuit is shown in Fig. 3.8b, where the input impedance of the antenna is that of the bow-tie modified by two sets of load; the first one, called resistive stub, is farthest from the feeding and in parallel with the bow-tie impedance, the second pair, inductive stubs, are added in series to the previous parallel combinations.

Measurements The measurement of the input impedance of small antennas is always a complex procedure due to the interaction of the near fields with the measurement structure [79]. Additionally, in a balanced structure like the dipole or the bowtie antenna, the coaxial feeding found in conventional VNA, which is an unbalanced structure, is not appropriate because currents can be excited on the exterior of the cable, creating an artificial asymmetry in the structure, which directly impacts the measured impedance.

Different strategies can be used to reduce these problems, such as the use of external baluns, customized balanced coaxial probes making use of two ports of the network analyzer [80], or even if the structure allows so, the use of balanced on-wafer probes. A different approach has been followed for this antenna which makes use of the symmetry (structural and electrical thanks to it being center-fed) of the antenna across the H-plane which makes it feasible to construct a monopole version of the antenna (as in a conventional dipole). A monopole version has a feeding compatible with the unbalanced coaxial line, and therefore it can be easily measured with a conventional VNA without requiring

(a) Dipole

(b) Monopole

Figure 3.11: Pictures of the fabricated RFID antenna prototypes: (a) shows the dipole version with a RFID chip soldered; (b) shows the monopole version mounted on top of the ground plane.

any external balun.

Both versions of the antenna, dipole and monopole, have been fabricated and are presented in Fig. 3.11. The monopole antenna has been placed on top of a $30\,\text{cm} \times 30\,\text{cm}$ ground plane, with a SMA connector. The measurement of the input impedance with the network analyzer is shown in Fig. 3.12a, where it has been taken into account that the impedance of the monopole is half that of the dipole. Three different curves are presented, two for the measurement and one for the simulation. As shown, one of the curves of the measurement (the dotted green curve, which corresponds to a raw measurement) presents a noticeable rotation with respect to the simulation. This curve is presented to emphasize the importance of setting the correct reference plane when measuring the impedance in RFID applications. In conventional measurements a shift of the reference plane introduced by the connector, or the thickness of the ground plane is usually not critical, since the magnitude of the reflection coefficient to $50\,\Omega$ is the design goal. However, in RFID applications the mismatching factor between Z_{ant} and the complex impedance of the RFID IC Z_{scav} is affected by this rotation of the impedances. Fig. 3.12b presents the *LF* for both measurements and the simulation, which shows good agreement when the measurement has taken the correct reference plane and a complete mismatch above 20 dB when it is not taken into account.

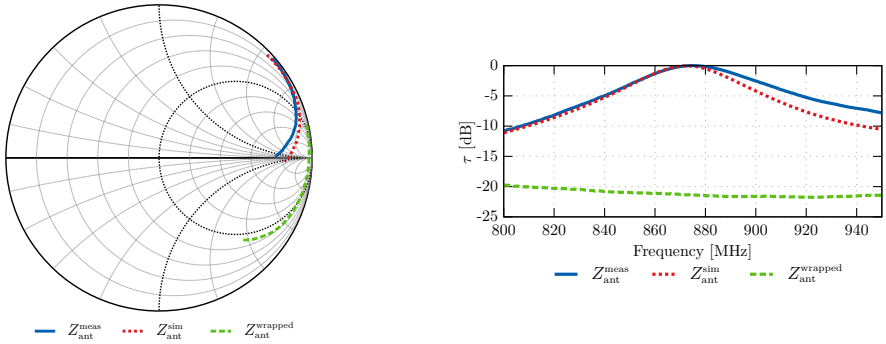

(a) Z_{ant} **(b)** LF

Figure 3.12: Impedance of the monopole as measured with the network analyzer. The green dotted line represents the direct measurement without proper calibration of the reference plane, which, as shown in (b) is important when the reference impedance is complex, as in the current case.

3.1.3 Antenna design for maximum modulation efficiency (ME)

Previously section 3.1.2 presented the design of an antenna which had been matched to the scavenging state of an RFID IC. However, as previously mentioned this might not be the optimum load to maximize the sensitivity in the receiver, which requires maximization of the backscattered power (the ME), or a trade-off between LF and ME .

This section presents a similar design to the previous section towards maximization of the ME of the antenna, where the limitations imposed by the switching loads are also analyzed selecting an optimum load towards maximum ME . In a real RFID-MST application the load would be given or based on a limited choice, but the same criteria for the selection could be applied for every RFID IC. In order to obtain a reasonable comparison of the advantages of a ME oriented design, the antenna will be compared with the backscattered response of an antenna without any optimization (a design with the same size, but without any optimization/tuning regarding its input impedance).

The first step for the maximization of the ME of the probe is to select the best load in terms of maximum achievable ME , taking into account the input impedance of both states. Three different devices have been considered as the two-state load: a PIN diode

	PIN Diode [81] *BAP1321*	Photodiode [53] *PDCS30T*	RFID IC *Alien Higgs 2*
Z_{L_A} [Ω]	$0.85 + j215$	$15.8 - j30$	$16 - j165$
Biasing condition	$I = 100\,\text{mA}$	$P_{\text{light}} = 6\,\text{dBm}$	P_{th}
Z_{L_B} [Ω]	$\sim -j133$	$38.9 - j1315$	$16 - j60$
Biasing condition	$V = 0\text{V}$	no-light	P_{th}
Frequency	2.45 GHz	2.45 GHz	868 MHz

Table 3.2: Parameters of interest for each of the loads under consideration

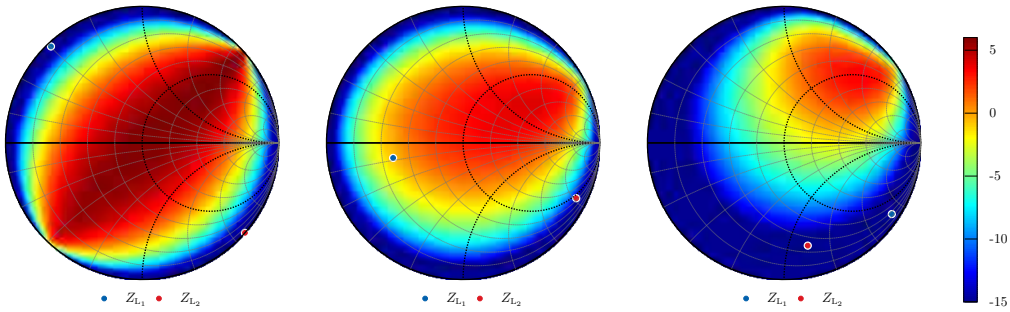

(a) PIN diode $ME_{\max} = 6.0\,\text{dB}$ **(b)** Photodiode $ME_{\max} = 3.9\,\text{dB}$ **(c)** RFID IC $ME_{\max} = 3.32\,\text{dB}$

Figure 3.13: modulation efficiency (ME) computed for each device for every possible Z_{ant} represented on top of a Smith chart for easy identification of the potential impedances that maximize ME .

NXP BAP1321, a photodiode PDCS30T, and an RFID IC Alien Higgs2 [66]. Table 3.2 summarizes the two impedances that each device present, and the biasing conditions that are used to get these values. Fig. 3.13 shows the ME achievable for each of the devices depending on the antenna input impedance. The representation of the ME on a Smith chart plot (normalized to $50\,\Omega$) allows to easily see the potential that each device has towards a maximization of the modulation efficiency. For instance it can be observed that the PIN diode presents a larger range of impedances that present a large ME , whilst the RFID IC is much more concentrated in areas of a higher Q-factor. Also the maximum ME achievable by the PIN diode is between 2 and 3 dB larger than the other two, due to the reduced losses that the PIN diode presents in forward and reverse states. As a consequence the MST probe antenna designed in this section will consider a PIN diode as the operating load.

The antenna will operate at 2.45 GHz and the size should be small ($\leq \lambda/5$). From Fig. 3.13a it shows that a good compromise for Z_{ant} that guarantees $ME \geq 5.5\,\text{dB}$ at 2.45 GHz is approximately:

$$Z_{\text{ant}} = \begin{cases} 50 \leq R_{\text{ant}} \leq 100 \\ 0 \leq X_{\text{ant}} \leq 150 \end{cases} \tag{3.10}$$

although the exact region in rectangular coordinates (resistance versus reactance) would have a crescent moon shape.

The starting point for the antenna will be a scaled version of the bowtie antenna designed in section 3.1.2.

Since the scaled version will be smaller, the tolerance to errors in the fabrication must be higher than before, so it is desirable a larger bandwidth than the previous design. To improve the bandwidth, the inductive stub is substituted with an inductive coupled feeding. The schematics of the designed antenna and the main dimensions are shown in Fig. 3.14 and table 3.3 respectively. Notice the presence of two small gaps in the inductive feeding of the antenna. One of them is to attach the PIN diode, while the second is to place a DC-block capacitor, to ensure that the loop is not short-circuited and thus allowing a proper DC biasing of the structure.

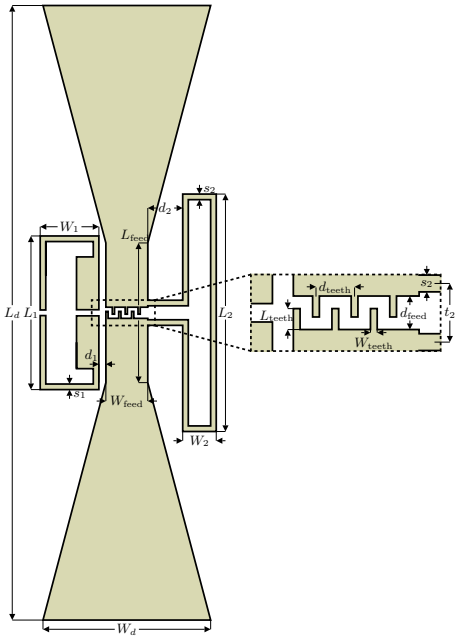

Figure 3.14: Sketch of the antenna design consisting of a bowtie antenna with an inductive coupled feeding and a set of stubs near the central (feeding) region.

Parameter	Value 1st design [mm]	Value 2nd design [mm]
Bowtie Dipole		
L_d	22	22
W_d	6	6
L_{feed}	5	5
W_{feed}	1.5	1.5
d_{feed}	0.4	0.4
Inductive stub		
L_1	5.5	5.5
W_1	2.1	2.1
d_1	0.25	0.25
s_1	0.2	0.2
Resistive stub		
L_2	8.25	8.5
W_2	1.2	1.6
d_2	1.25	1.25
s_2	0.2	0.4
Capacitive fingers		
L_{teeth}	0.25	0.25
W_{teeth}	0.08	0.15
d_{teeth}	0.38	0.45
N_{teeth}	6	4

Table 3.3: Main dimensions of the final design for the antenna

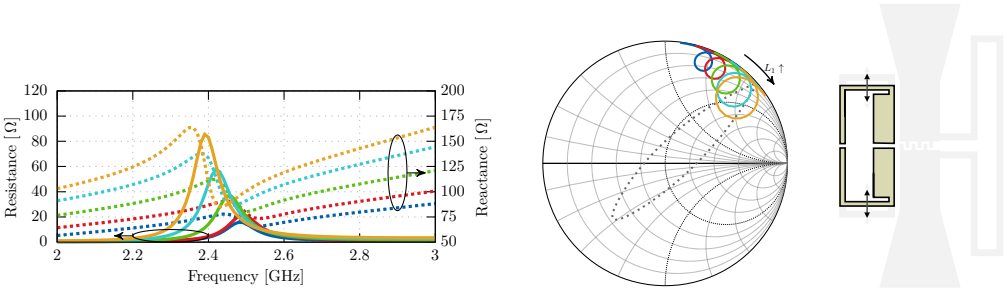

(a) L_1

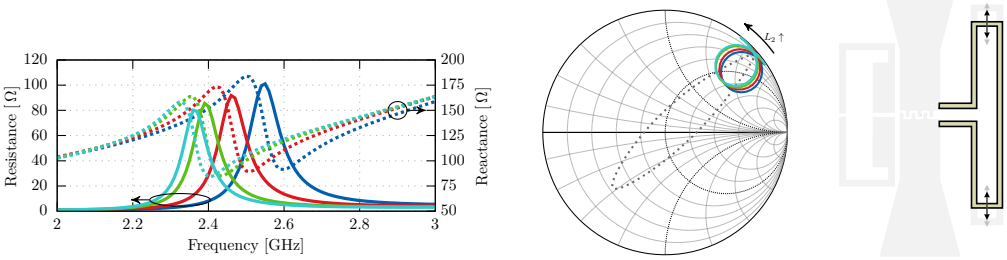

(b) L_2

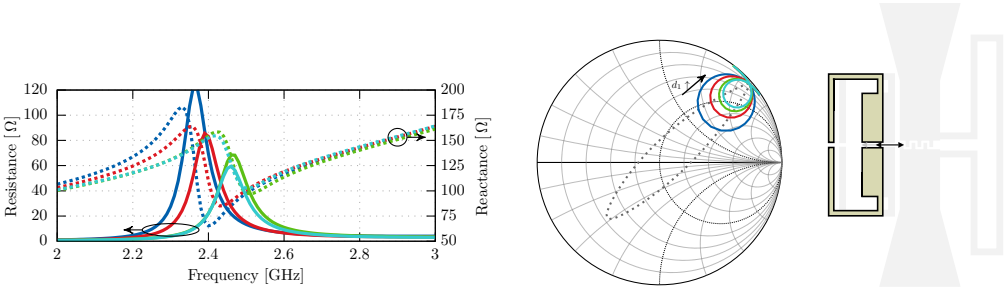

(c) d_1

Figure 3.15: Parametric analysis of the antenna structure. Impedance plot is shown on the left and the Smith chart equivalent (50 Ω) on the right.

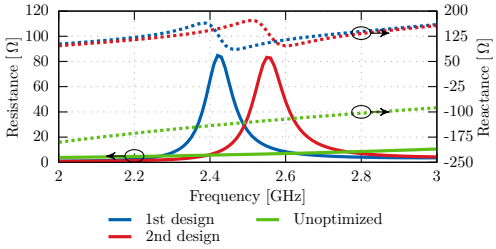

(a) Input impedance

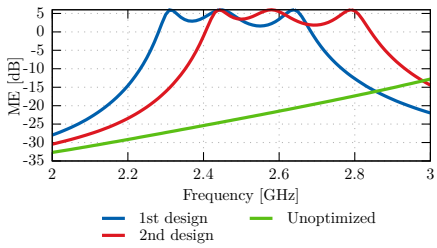

(b) Modulation efficiency

Figure 3.16: (a) Input ipmedance and (b) modulation efficiency (ME) for the designed bowtie antennas. The figures present the optimized designs and an additional curve which shows the expected behavior of a non-optimized design (a bowtie dipole of the same dimensions, but without any matching feeding) which results in extremely lower ME . An alternative sub-optimized design that used $Z_{\text{ant}} = Z^*_{\text{L}_B}$ would still have had a performance 3 dB below the optimized design.

(a) 1st Optimized

(b) Non-optimized (1st diode)

(c) 2nd Optimized

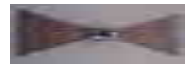

(d) Non-optimized (2nd diode)

Figure 3.17: (a) and (c) shows the prototypes of the two antennas designed with the optimization goal that maximizes ME for the 2 diode models. (b) and (d) shows the respective reference dipoles that do not have any feeding network

A short parametric analysis of the structure allows to determine which parameters allow more easily to fine-tune the impedance response of the antenna, without modifying the overall dimension, as shown in Fig. 3.15. The amount of reactance of the antenna is highly controlled by the dimensions of the loop, as expected from the inductive feeding, as well as the distance to the main body of the antenna, which controls the sharpness of the resonance. Figure 3.16 presents the expected impedance Z_{ant} and modulation efficiency (ME) for the final design of the antenna. Several things can be observed from this plot: the operating frequency presents a ME above 5.5 dB; the existence of a resonance around 2.45 GHz ensures a large bandwidth, although since Z_{ant} is not always within the bound given in (3.10), there is a ripple of 3 dB. After this small region of large ME , it goes down to almost -30 dB at 2 and 3 GHz. In the same figure, the backscattered power for a unoptimized dipole, consisting exclusively on the bowtie dipole without any inductive coupling or feeding optimization (thus a capacitive input impedance) is presented. It can be shown that the proper tuning of Z_{ant} allows to improve the backscattered response of the MST probe on the order of 35 dB for the frequency of interest.

With this design in mind, two sets of antennas have been fabricated, as shown in Fig. 3.17. The first set uses a BAP1321-04 PIN diode, which uses a three pin encapsulate SOT23, and contains two diodes in series (the original design). From the results of this set, which will be shortly shown, a second set was fabricated with minor modifications, and using a slightly different diode encapsulate BAP1321-02, which uses a smaller two

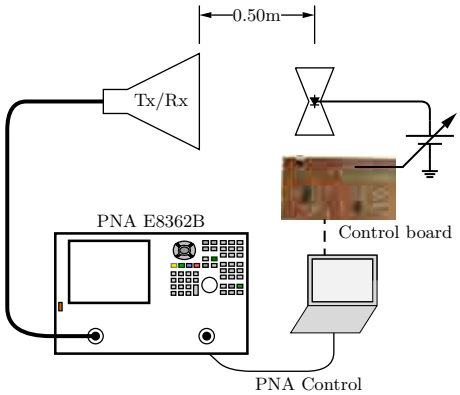

(a) Measurement sketch

(b) Experimental measurement

Figure 3.18: Experimental setup to evaluate the designs of the designed antennas. It consists of a PC connected to a control board that turns a DC voltage on and off to properly bias the diodes of the antennas. A network analyzer connected to a ridged horn antenna measure $\Delta\rho_{\text{rdr}}$.

pin package (SOD-523).[1] Fig. 3.18 presents the experimental setup that has been used to carry the measurements of the *ME* for the different antennas, which is similar to what was done in section 2.4.2. A horn antenna connected to an Agilent N5242A VNA measures ρ_{rdr}, the MST probe is placed at a distance of 50 cm of the horn, and is biased by a programmable DC power supply. The measurement is carried out for forward and reverse biasing of the diode, to obtain $\Delta\rho_{\text{rdr}}$ which is plotted in Fig. 3.19. Here it must be taken into account that as in chapter 2, since no reference measurements with a short-circuit and a matched load are available, it is not feasible to obtain the absolute value of the *ME* , but the measurement allows to retrieve the backscattered power and compare the results for the optimized dipole with the non-optimized dipole. As can be appreciated from Fig. 3.19a, there was an initial downshift of the frequency of maximum *ME* from the designed 2.45 GHz to about 2 GHz caused by the dimensions of the packaging of the first dipole that are affecting the region of the inductive feeding of the dipole. This led to some small modifications in the structure of the antenna used with the smaller diode, while at the same time widening some of the metallic strips to relax the requirement during fabrication. The results for this second set of antennas is shown in Fig. 3.19b.

It can be noticed in the measurement that there is a reduction of the available bandwidth between the simulated results and the experimental characterization, however due to the asymmetry of the structure (in the capacitive fingers near the center of the antenna), it is not possible to perform a monopole version of the antenna as in the previous chapter to measure the input impedance. An alternative measurement using a differential probe made of two semi-rigid coaxial cables was carried out. However, still with this setup the relative position of the differential probe and the antenna affected noticeably the measured Z_{ant}, thus not allowing to retrieve meaningful values. Nevertheless, the

[1] It must be noted that due to the difference in the encapsulate, this model presents a slightly smaller capacitance, from 425 fF to 400 fF, and an inductance that goes from 1.4 nH to 0.6 nH. With that Z_{L_1} is increased in $j20\,\Omega$ and Z_{L_2} is reduced in $-j10\,\Omega$. This has an important impact on the reactance of the forward biasing of the diode which is now bounded as $10 \leq X_{\text{ant}} \leq 170$.

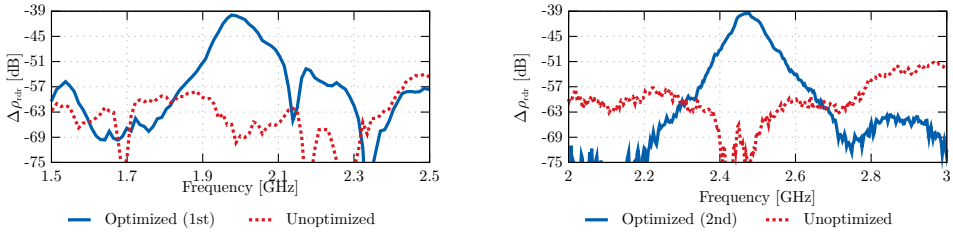

(a) First prototype **(b)** Second prototype

Figure 3.19: $\Delta\rho_{\text{rdr}}$ measured at the ridged horn antenna for each prototype and the unoptimized reference antennas. The blue solid line represent the results for the optimized designs, which show a backscattered response 20-30 dB above the response obtained by dipoles of the same physical length, but without any feeding network design (dashed red lines).

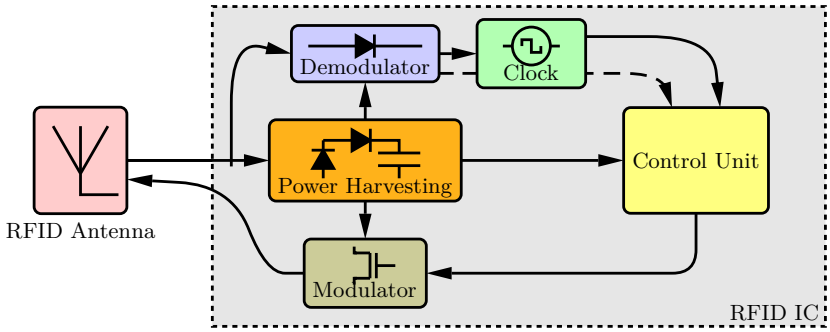

Figure 3.20: The RFID IC block diagram can be divided in several functional blocks: the *scavenging* section provides power to the rest of the blocks, the *demodulator* provides the incoming stream of bits to the *control unit* that uses the *modulator* to respond back if necessary.

measurement has shown how the proper design of the antenna input impedance can increase P_{bs} up to 20 dB with respect to a design which does not take into account the MST loads to be used.

3.2 RFID-MST components: Integrated Circuitry

This section presents the main components of an RFID IC making special emphasis on the blocks that are responsible of the two states used for backscattering modulation, and thus with the performance of the RFID probe.

Fig. 3.20 presents the block diagram of the RFID IC, with is composed mainly of 4 different blocks [77, 82–84] :

Power section. Consists of the power harvesting block, the circuit that rectifies the incoming RF signal to generate a regulated stable voltage to supply the rest of modules of the IC.

Demodulator. This block includes an envelope detector for demodulation of the incoming signal and outputs the digital stream of data received by the RFID tag to the

control subsystem.

Control subsystem. This block contain the *intelligence* of the IC, decoding the input data stream and generating the proper response, if any, that is sent towards the modulator. This module also contains the memory of the RFID IC.

Modulator. This block performs the modulation of the data stream to be sent to the reader. It uses backscattering modulation, which basically changes the input impedance observed by the RFID tag. Depending on the way it is implemented the modulation will be ASK, PSK or a mix between them.

3.2.1 Power harvesting section

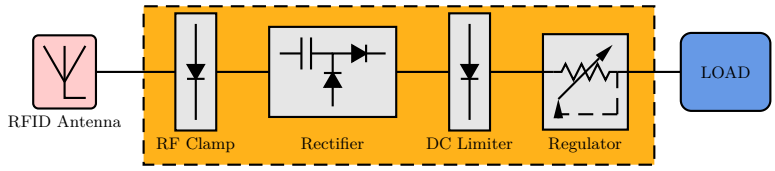

Figure 3.21: Block diagram for the power section of an RFID tag; it consists of a set of power/voltage limiters for protection and a rectifier and regulator to provide a stable voltage to the rest of stages of the RFID IC.

The harvesting module is composed of the blocks shown in Fig. 3.21:

RF Clamp. Limits the power that passes to other blocks in the chain for protection against sudden bursts of input power.

Rectifier. One of the main stages in the power harvesting section. It rectifiers the input alternating current (AC) signal in direct current (DC) voltage that can be used to feed the rest of the circuitry. Due to the transformation of frequencies (from radio frequency (RF) to DC), it is a highly non-linear circuit, and presents a non-linear RF input impedance. The most common non-linear elements are Schottky diode[2] or MOSFET transistor diode connected [85][3] in a charge pump configuration based on a Dickson multi-stage rectifier [84, 86]. Appendix C analyzes the power dependence of the input impedance for a diode-based rectifier. The efficiency and voltage multiplier factor of the rectifier determine the minimum power P_{th} required to activate the rest of the circuitry.

DC Limiter. Similar to the RF clamp, the DC limiter ensures that large DC output voltages are not passed to the rest of the circuitry (high voltage might appear due to variation of the propagation conditions even if they do not go above the limits of the RF clamp. [87]). Such high voltages could damage not only the logic circuitry of the RFID IC, but also the rectifier itself.

Regulator. A voltage regulator is needed between the rectifier and the logic circuitry to cope with smaller voltage variations that those prevented by the DC limiter in order

[2] Citation for the diode

[3] Maybe some other more relevant. Also maybe I should explicit which are the advantages of each one

to supply a stable voltage. The regulator must be transparent to avoid penalization of the efficiency of the harvesting section. Different architectures are available for voltage regulation; the most efficient, are switching regulators [88] but the requirements for voltage transformation (high inductance, or high clock frequency) are usually not suitable for RFID applications. The most common alternative is the use of linear regulators, which introduce a variable load (a controlled current sink for a shunt regulator, or a controlled voltage source for a series regulator) which is modified according to the output voltage. A common choice for series regulator is the low-drop out (LDO) regulator as it presents the minimum dropout voltage between input and output pins for low input voltages [87, 89], thus improving the sensitivity of the system.

3.2.2 Demodulation circuitry

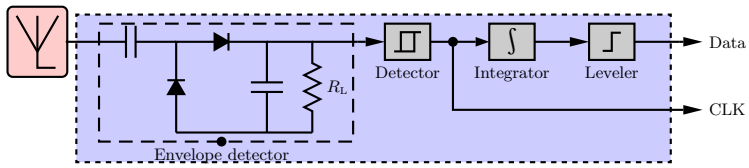

Figure 3.22: Block diagram of an RFID demodulator [90]. The data bits are discriminated according to the length of the pulses, which is obtained integrating the envelope of the transmitted data after going through a pulse reshaper stage.

The reader uses amplitude modulation to transmit the data encoded with pulse-interval encoding (PIE), which implies that bits 0 and 1 are formed by a sequence of high and low transmitted power with different duration (see Fig. B.1) Hence, proper demodulation of the received signal must be able to detect the level as well as the duration of the received pulses, to identify the bits and generate the proper frequency to modulate the response. The demodulation circuit used to detect the stream of bits as well as measure their duration is shown in Fig. 3.22; it consists of an envelope detector and a leveler to regenerate the received signal into a proper digital square signal. The discrimination of bit 0 and 1 is done with an integrator and a comparator. At the same time the signal received from the reader is used to generate the system clock of the RFID control unit.

3.2.3 Modulation circuitry

The communication from the tag to the reader uses either an amplitude shift keying (ASK), a phase shift keying (PSK) modulation or a combination of both.

Data transmission is based on backscattering modulation (explained in detail in chapter 2), which consist in the variation of the reflected signal by a change of the impedance of the load. In the absence of this block, the input impedance of the RFID IC is basically defined by the impedance of the rectifier. Therefore, an additional load must be added, usually in parallel to the rectifier, able to significantly modify the overall input impedance, without reducing the efficiency of the rectifier (see Fig. 3.23a). This is commonly done with a tunable load, implemented either as a tunable capacitance or resistance [1] (although the use of a resistive load might decrease the efficiency of the rectifier section due

to higher losses [90]). A typical implementation is presented in Fig. 3.23b which consists

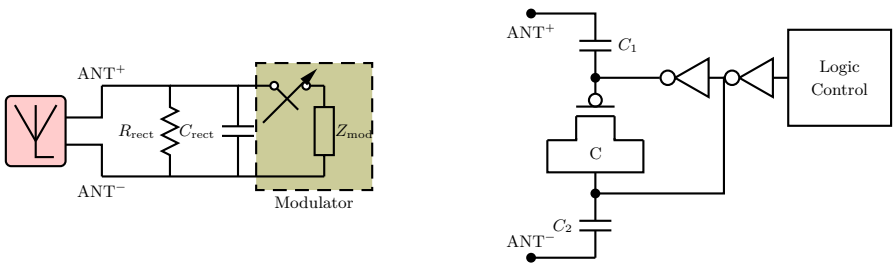

(a) General idea **(b)** MOS Varactor implementation

Figure 3.23: Example of a typical backscattering modulator used in RFID applications, when the voltage of the varactor (b) is changed the capacitance seen by the antenna changes and modifies $\Delta\tilde{\rho}_{\text{L}}$.

in the addition in parallel to the antenna and rectifier of two capacitors in series to a central varactor. By properly biasing the varactor (for instance swapping the polarity of the DC voltage at its terminals, there is a variation of the capacitance (ΔC). Assuming a constant impedance for the rectifier for both states of the varactor, the input admittance of the IC becomes:

$$\begin{aligned} Y_{\text{in}}^{A} &= Y_{\text{rect}} + j2\pi f\,(C_1 + C_2 + C) \\ Y_{\text{in}}^{B} &= Y_{\text{rect}} + j2\pi f\,(C_1 + C_2 + C + \Delta C) = Y_{\text{in}}^{A} + j2\pi f \Delta C \end{aligned} \tag{3.11}$$

3.2.4 RFID Control unit

This block controls the different RFID subsystems and the communication with the reader using the appropriate RFID protocol (some details of the protocol are explained in appendix B). The most important part, apart from the *intelligence* unit, is the EEPROM which contains the information to perform the identification of the tag, and parts of which can be reprogrammed through specific commands by the reader. The control unit is responsible of decoding the commands and data received through the demodulator from the reader and acting according to its inner state and the received command.

Some of the actions that can be taken are [91]:

- If the command was sent to another tag, do nothing.
- If the reader request information, it reads the EEPROM and sends the reading back through backscattering modulation
- If some new information is requested to be written, it activates the writing circuitry and stores the data in the EEPROM

3.3 RFID Integrated circuitry input impedance

As introduced earlier in chapter 2 the RFID input impedance is switched back and forth between two differentiated states when answering to an interrogating command, the *scav-*

enging impedance and the *short-circuited* impedance (usually assumed as a perfect short-circuit or open-circuit). However, as will be shown in this section, the input impedance of the RFID IC is neither static, nor ideal, thus presenting non-linear effects in both states and non-idealities in the short-circuited state, which must be properly characterized to use them in sensing applications.

The following sections deal with the characterization of the two states of the RFID IC and the solution proposed in this thesis to measure the input impedance of the IC.[4]

3.3.1 Dynamic input impedance characterization

The characterization of the RFID IC input impedance using a conventional VNA is not directly possible because the RFID protocol (see Appendix B) establishes that the RFID IC only initiates a data transaction (backscattering modulation) as a response to a properly modulated signal from a reader, for instance the issuance of a QUERY command, remaining otherwise silent and harvesting RF energy (scavenging state). As a consequence, since a conventional VNA cannot modulate the outgoing RF signal with this QUERY command, the VNA can only measure the input impedance of the scavenging state Z_{scav} of the RFID IC, as in [92] where the power dependence of Z_{scav} is measured with a VNA, and P_{th} is determined in a second measurement using an external reader, but no measurement of Z_{SC} is done. To determine Z_{SC}, only two methodologies have been proposed. In [93] the RFID IC input impedance of both states is measured using a specialized VNA that allows the use of modulated signals; similarly in [94] a vector signal generator and a spectrum analyzer are used to determine the input impedance in both states.

In this section, the characterization is done using a transparent modulator introduced in the RF path between the VNA and the RFID IC. This modulator must be capable of modulating the signal in the forward direction and allowing to go through undisturbed the signal coming back into the VNA. Although this could be implemented using a circulator and a 2-port configuration of the VNA, an alternative and simpler approach is proposed in this thesis which uses the circuit of Fig. 3.24 as the transparent modulator. It consists of a single pole double throw (SPDT) device interconnecting the VNA at the common port and the RFID IC and a 50Ω load at the output ports. This allows to electronically connect (thru) and disconnect (isolate) the VNA to the RFID IC, achieving full ASK modulation of the RF signal between the common and the RFID IC ports (during the modulation of the forward signal), as well as a direct connection between the ports (when measuring the modulated backscattering of the RFID IC), which occur in different time slots.

A programmable integrated circuit (PIC) microcontroller governs the SPDT and generates the proper sequence of bits to modulate the RF signal with the *QUERY* sequence stored in its internal memory (see Fig. 3.25 (a)). For the current measurements, and to ensure the slowest possible response of the RFID IC, the symbol length (TARI) and the tag-to-interrogator calibration symbol (TRcal) have been set to its maximum values: 25 µs and 225 µs respectively. Finally, two general purpose pins of the PIC are used to synchronize the IC response with the VNA (trigger) and to externally set the modulator in a thru state, used during the calibration stage.

[4] The following sections contains portions, sometimes verbatim, of the publication [JA3] of the author.

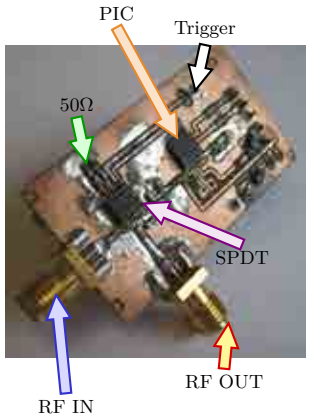

(a) Circuit

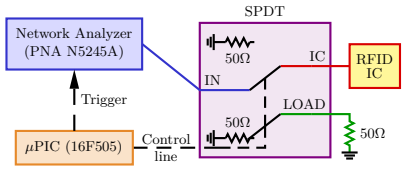

(b) Circuit diagram

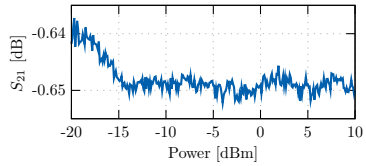

(c) Linearity [dB]

Figure 3.24: (a), (b) The modulator consists of an SPDT connecting the VNA to the RFID IC and a 50 Ω. A PIC microcontroller governs the SPDT and triggers the network analyzer. (c) The characterization of the S_{21} of the modulator with respect to power at 868 MHz, shows low losses and high linearity with variations below 0.01 dB for the whole range of power swept.

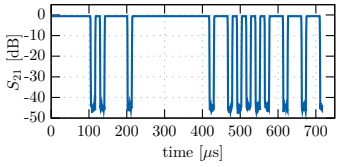

(a) S_{21} Modulation [dB]

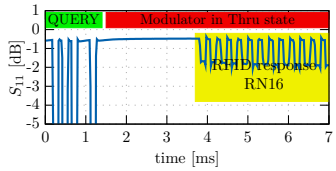

(b) S_{11} IC response [dB]

Figure 3.25: (a) Shows the S_{21} between input and output port of the modulator while generating a *QUERY* sequence; an isolation above 40 dB, ensures a 100% ASK modulation. (b) Presents the S_{11} when the RFID IC is connected showing the last part of the *QUERY* sequence and the response of the RFID IC.

Since the modulator does not implement a complete reader, only the RN16 from the tag is measured, but this sequence is sufficient to measure the values of Z_{SC} and Z_{scav}, as shown in Fig. 3.25 (b) where the response of the RFID IC is shown as captured by the VNA, and where the change of input impedance between the two impedance is clearly identified.

3.3.2 Experimental results and discussion

The RFID IC characterized is an Alien Higgs 2 with strap connector [66]. It is mounted at the end of a short grounded coplanar waveguide (GCPW) 50Ω transmission line with an SMA connector at the opposite end (see Fig. 3.26a). To remove the effect of the connector, a thru-reflect-line (TRL) (see Fig. 3.26b) calibration is performed after the modulator. During the calibration, the modulator is forced to remain in the thru configuration using the external pin. This ensures a correct calibration of the thru mode of the modulator

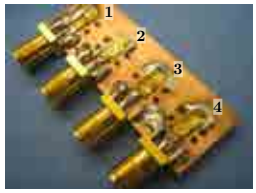

(a) IC fixture

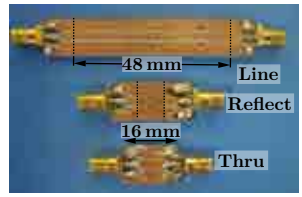

(b) TRL Calibration kit

Figure 3.26: (a) Grounded CPW (on a 1.52mm RO4003C substrate) are used to connect the RFID IC to an SMA connector. (b) A TRL calibration kit establishes the proper reference plane.

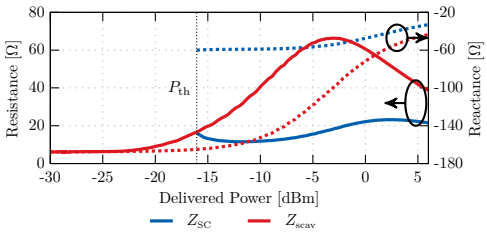

(a) Measured impedance

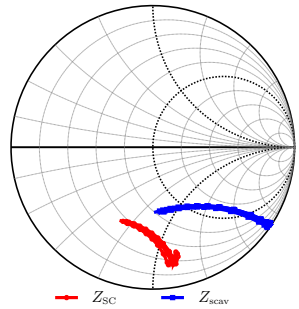

(b) Multiple RFID IC

Figure 3.27: Input impedance of Alien Higgs 2 RFID IC at 868 MHz as measured by the experimental setup introduced in this paper. Z_{SC} can only be measured after P_{th} is reached, which is around −16 dBm.

used during the measurement of the two impedance states of the RFID IC. Here it must be noted that since the RFID IC continuously changes the impedance, a time-domain measurement at a fixed frequency and power must be used, so the VNA is set to a continuous wave mode at a fixed frequency of 868 MHz; likewise since the response of the RFID IC is modulated at 36 kHz (established by the timings of the *QUERY* sequence), the IF bandwidth (IFBW) of the VNA must be larger than that to avoid filtering the response out. For the current measurements the IFBW has been established at 360 kHz.

The measurement of the input impedance of the RFID IC with respect to power is shown in Fig. 3.27. When the delivered power is below P_{th}, only Z_{scav} can be measured and it remains basically constant; as power increases, around −20 dBm Z_{scav} starts showing variation. Once the delivered power level reaches P_{th}, the IC activates and responds, allowing to measure Z_{SC}, see Fig. 3.25b. From then on, the non-linear dependence of both states with respect to power can be measured. It can be observed that the short-circuit state is in reality much different than the ideal value (a short-circuit or a open-circuit), and this will directly impact the performance of the RFID tag in terms of modulation efficiency (*ME*), as will be shown in the following section.

A total of 5 RFID IC have been measured at 868 MHz for P_{av} ranging from −20 dBm up to 10 dBm and are shown in a Smith chart in Fig. 3.27b. The retrieved values of Z_{scav},

Parameter	1	2	3	4	5	[66]
P_{th} [dBm]	-16.1	-16.2	-16.6	-16.5	-16.9	-14.0
$R_{\text{scav}}^{\text{parallel}}$ [kΩ]	1.64	1.62	1.76	1.69	1.82	1.50
$C_{\text{scav}}^{\text{parallel}}$ [pF]	1.10	1.09	1.12	1.15	1.10	1.20
$R_{\text{SC}}^{\text{parallel}}$ [kΩ]	0.24	0.26	0.24	0.24	0.22	N/A
$C_{\text{SC}}^{\text{parallel}}$ [pF]	2.84	2.85	2.87	3.02	2.85	N/A

Table 3.4: Measured impedance for the 5 samples of Alien Higgs 2 RFID IC. It must be noted that the values do not directly correspond to the values of Fig. 3.27, because here they have been expressed as a parallel RC circuit, which is the conventional representation in RFID IC datasheets.

Z_{SC} and P_{th} present high repeatability between samples, where the differences can be attributed to parasitic effects introduced during manipulation and soldering, as well as the intrinsic variation of the IC. Table 3.4 summarizes the most relevant results for each sample.

3.4 RFID-MST - Performance evaluation

In chapter 2 the formulation governing MST was presented and a set of quality parameters that can be used to evaluate its performance were introduced; this section presents a study case of the predicted performance of RFID tags depending on the optimization goals at the design stage.

The performance is evaluated in terms of how the load factor (LF) and the modulation efficiency (ME) are affected by the design goals and what does that imply from the point of view of the reader and the tag. Additionally and to obtain a realistic behavior of the tag, the impedance states of the RFID IC includes its non-linear behavior and non-ideality, making use of the characterization of the RFID IC of the preceding section.

The non-linear behavior of Z_{scav} does not change LF since this depends on Z_{scav} at P_{th} and this is a value provided in the datasheet. However, the backscattered power, directly depends on the variation of ME with respect to power, as well as the presence of non-idealities, such as how much Z_{SC} differs from a short-circuit.

For the analysis three different tag antennas are considered fulfilling three different decisions at the design stage regarding their impedance[5]:

Antenna A considers a conventional RFID application where LF is maximized to maximize the activation range, leading to $Z_{\text{ant}} = Z_{\text{scav}}^{*}$ at P_{th}.

Antenna B does not follow a specific optimization goal, and Z_{ant} is taken as the conjugate of Z_{scav} for a delivered power of $P_{\text{th}} + 5\,\text{dB}$.

Antenna C considers a sensing application and maximizes ME for the minimum operating power (P_{th}).

Table 3.5 shows the respective antenna impedances, as well as the evolution of the quality parameters. Since antenna A maximizes the activation range it presents a $LF =$

[5]The following sections contains portions, sometimes verbatim, of the publication [JA3] of the author.

Antenna	Z_{ant} [Ω]	$LF(P_{\text{th}})$ [dB]	ME [dB]
A	$16 + j165$	0	-0.4
B	$35 + j156$	-1.4	2.2
C	$55 + j112$	-3.4	3.3

Table 3.5: Performance parameters for two antenna impedances.

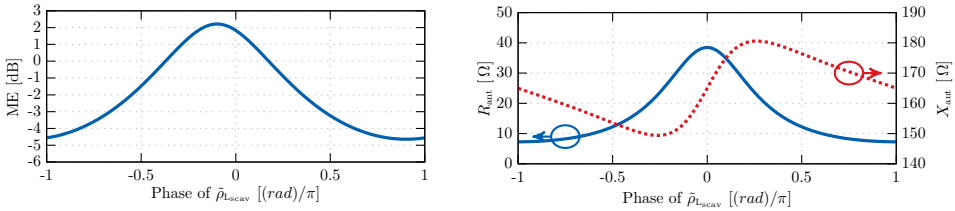

(a) ME with respect to the phase of $\tilde{\rho}_{\text{Lscav}}$.

(b) Z_{ant} for the different phases of $\tilde{\rho}_{\text{Lscav}}$.

Figure 3.28: (a) Prediction of the performance of the RFID tag when the LF is fixed at 0.7 dB (like antenna B), but the phase of $\tilde{\rho}_{\text{Lscav}}$ is not fixed. (b) The allowed Z_{ant} values correspond to a circle in the Smith chart representation, and the ME changes 7 dB.

0 dB, on the other hand antenna B has an additional 1.4 dB of mismatch losses and antenna C a total of 3.4 dB. This reduction in the load factor (LF) implies that the activation range is reduced, and for instance in a free-space environment, it would be about 85% and 70% of the activation range of antenna A respectively.

On the contrary, the backscattered power which is proportional to ME does not follow the same trend. In this case, ME for antenna A is 2.6 dB below that of antenna B and 3.7 dB below that of antenna C. Moreover due to the non-ideality of Z_{SC}, the maximum ME of this RFID IC at P_{th} is almost 3 dB below the maximum possible (6 dB). This is caused by the losses present in Z_{SC} and it emphasizes the importance of a proper characterization of the second impedance state to obtain an accurate prediction of the performance, and to define the optimization goal for the maximization of ME.

Both antennas A and C have a maximization goal of LF or ME respectively, as such the impedance goal is unique. On the contrary, antenna B has no such goal. If for instance we want to ensure that $LF = -1.4$ dB, we are just imposing a condition on the magnitude of $\tilde{\rho}_{\text{L}}$, but the phase, $\angle\tilde{\rho}_{\text{Lscav}}$, can be chosen arbitrarily. However a proper selection of $\angle\tilde{\rho}_{\text{Lscav}}$ can improve (or worsen) the performance of antenna B in terms of ME . This is shown in Fig. 3.28a where the magnitude of $\tilde{\rho}_{\text{Lscav}}$ is maintained to ensure a constant $LF = -1.4$ dB (the value obtained for antenna B), but the phase of $\tilde{\rho}_{\text{Lscav}}$ is swept between 0 ° and 360 ° in order to compute the ME . It can be seen that the ME presents a swing of 7 dB depending on the relative phase of the antenna and the load (the values of Z_{ant} corresponding to each phase of $\tilde{\rho}_{\text{Lscav}}$ are shown in Fig. 3.28b).

Additionally, not only does the non-ideality reduce the available modulation efficiency (ME), but the non-linearities introduce a power dependence on it. In contrast with conventional backscattered devices, where the scattering is proportional to the incident power (that is a constant ME), the RFID IC presents a ME which decays with increasing power levels, as shown in Fig. 3.29a for each antenna. In particular, since the

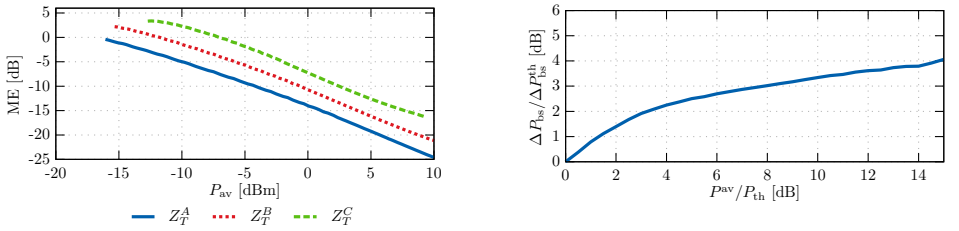

(a) *ME* [dB] **(b)** Normalized P_{bs} [dB]

Figure 3.29: (a) Predicted modulation efficiency for the three different antenna impedances of table 3.5 with the RFID IC Higgs 2. (b) Shows the variation of the backscattered power by an ALN-9529 RFID tag at a fixed distance when the transmitted power is increased 15 dB starting at P_{th}. It readily shows that the increment is not linear with the transmitted power due to the changes in the *ME* .

backscattered power P_{bs} is proportional to $\left(ME{\cdot}P^{\text{av}}\right)$ and *ME* decays with approximately the same rate at which P_{av} increases, then P_{bs} becomes less sensitive to variations of the incident power. As an example, Fig. 3.29 (b) shows the measured P_{bs} of an ALN-9529 RFID tag as the incident power is increased by the reader (details on the measurement setup will be given in the next chapter). It must be appreciated how in spite of a variation of almost 15 dB in the transmitted power, P_{bs} increases only in about 4 dB.

As a direct consequence, in a free-space far-field scenario where the incident power upon the tag decays with distance at a rate of r^2, the backscattered power remains almost constant, and the received power at the reader decays only as the return path loss factor, r^2, instead of the conventional mono-static rate of r^4. This also implies that although the reading range for a bad *LF* can be achieved increasing the transmitted power P_a, the backscattered power won't be benefiting in the same way due to the non-linearities of the IC, since the increment of incident power will diminish the *ME* in a similar factor, thus maintaining the signal to noise ratio (SNR).

Finally, table 3.6 presents *LF* and *ME* for different combination of antennas and chips reported in the literature. As expected, it is clear that not every antenna can be used with every RFID IC. When the antenna and IC present an almost conjugate matching, *ME* is basically 0 dB, that is the case of the combination of Z_{ant_1} and Z_{C1}. On the other hand, the combination of the tag with impedance Z_{ant_4} with the IC chips with impedances Z_{C1} and Z_{C6} have similar *LF* , but the *ME* is 15 dB worse for the Z_{C1} impedance than for the Z_{C6}. In consequence it is a much better choice Z_{C6} for that antenna as it will maximize the SNR at the reader for the same activation range (*LF*) A similar behavior is observed with the combination of Z_{ant_2} and Z_{C1} and Z_{C6}.

3.5 Concluding remarks

This chapter has presented the different components of the RFID tag, focusing in the antenna design goals and the RFID IC characterization. The design of the antenna must ensure that the capabilities of scavenging of the RFID IC are not compromised, whilst at the same time ensuring that backscattered power is as large as possible, to obtain the highest possible SNR of the measurement. It has been shown, through the quality parameters defined in the previous chapter, that once the requirements in terms

		Chip Impedances Z_C [Ω]													
		Z_{C1} [65]		Z_{C2} [62]		Z_{C3} [a]		Z_{C3*} [b]		Z_{C4} [66]		Z_{C5} [67]		Z_{C6} [68]	
		$73 - j113$		$12 - j420$		$16.7 - j165$		$16.7 - j165$		$15 - j151$		$6.2 - j127$		$12 - j300$	
	Antenna Impedances [Ω]	*LF* [dB]	*ME* [dB]	*LF* [dB]	*ME* [dB]	*LF* [dB]	*ME* [dB]	*LF* [dB]	*ME* [dB]	*LF* [dB]	*ME* [dB]	*LF* [dB]	*ME* [dB]	*LF* [dB]	*ME* [dB]
Z_{ant_1} [65]	$49 + j106$	-0.2	-0.7	-16.4	0.8	-3.8	3.9	-3.8	3.3	-3.2	4.2	-4.6	5.1	-12.5	1.9
Z_{ant_2} [62]	$70 + j400$	-7.0	-16.8	-3.3	4.7	-11.3	-12.8	-11.3	-15.5	-12.2	-14.0	-16.7	-16.2	-7.0	-1.9
Z_{ant_3} [68]	$166 + j160$	-0.9	-2.0	-11.0	5.7	-4.8	2.3	-4.8	-0.8	-5.2	1.6	-8.7	0.4	-8.1	5.6
Z_{ant_4} [68]	$90 + j313$	-4.0	-10.8	-7.0	3.9	-7.4	-6.0	-7.4	-8.5	-8.4	-7.2	-12.9	-9.5	-3.9	4.2
Z_{ant_5} [c]	$6 + j151$	-6.3	-18.0	-23.8	-17.8	-2.4	-5.9	-2.4	-5.7	-0.8	-4.6	-6.7	-8.2	-18.8	-15.6

[a] Measured value for the Alien Higgs 2 chip at P_{th}

[b] Same as Z_{C3} but considering the measured Z_{SC} instead of a perfect short-circuit for the computation of *ME*

[c] Alien ALN-9540 Squiggle antenna simulated with the Method of Moments

Table 3.6: Modulation efficiency and Load factor in dB for a set of known RFID antennas and IC chips. Due to the unavailability of the value of Z_{SC} for the majority of the chips, it has been assumed an ideal short-circuit for the computation of *ME* (with the exception of sample Z_{C3*}.

of *LF* have been established for the operating conditions of the sensor and the value of Z_{scav}, the impedance of the antenna is not uniquely determined, but rather a wide range of choices are available which present a different performance in terms of modulation efficiency (*ME*). An example has been provided that shows a variability in *ME* around 7 dB of power for a fixed *LF* of −1.4 dB.

It has also been shown how *LF* can be easily predicted using available information readily available in the RFID IC datasheet (the value of Z_{scav}), or with a direct measurement using a VNA; on the other hand the prediction of *ME* is not so easy, since it is strongly dependent on the value of Z_{SC}, which depends on the internal architecture of the RFID IC and is not necessarily known beforehand. Since Z_{SC} cannot be measured directly with the VNA, an alternative measurement procedure was developed using a transparent modulator introduced in the RF path between the RFID IC and the VNA, which was capable of characterizing both impedance states of the RFID IC. This characterization showed that the losses in Z_{SC} were far greater than the usual consideration, and this reduces the maximum *ME* that can be obtained from this specific RFID IC in optimum conditions (almost 3 dB below the ideal).

With the characterization of the impedance of the two states of the RFID IC it was possible to determine the power dependence of both impedance and predict the performance of the RFID sensor for a changing incident power. In particular, it was shown that contrary to conventional MST scatterers, where the backscattered power increases linearly with the incident power, in an RFID tag the non-linearities in *ME* reduce the rate at which this backscattered power increases. This has two direct consequences:

- If the transmitted power is increased, the *ME* decreases with a similar rate, and the total backscattered power reaching the receiver remain almost the same (it increases slightly since the rate at which *ME* decreases does not fully compensate the increasing rate in transmitted power).
- Similarly, if the scenario increases the propagation losses reducing the power reaching the RFID tag in a factor α, the *ME* will increase almost in the same factor (compared to the original *ME*). This implies that the backscattered power at the receiver will have only decreased in a factor α, instead of the factor α^2 of conventional MST (or radar) scenarios.

The effect of this non-linearities in sensing applications will be fully shown in the following chapters, where they will have a direct impact on the measurement of an EM-field distribution.

4

Chapter 4

RFID-MST based EM-field measurements and Imaging

This chapter is devoted to the measurement of near or far fields distributions using RFID-MST probes, and it strongly focuses in the challenges brought in by the introduction of RFID as an MST probe. The first part focuses in the analysis of coupling effects when arrays of multiples probes are used for the measurement under the loading conditions of RFID tag. Afterwards several measurements of aperture field distributions with different arrangements of RFID probes are presented. The final part introduces an alternative approach to the use of RFID tags for EM-field measurements to enhance its applicability as EM-sensors in applications such as antenna pattern characterization and imaging tomography. Additionally the benefits of multi-frequency approaches in a MST tomography application are also analyzed.

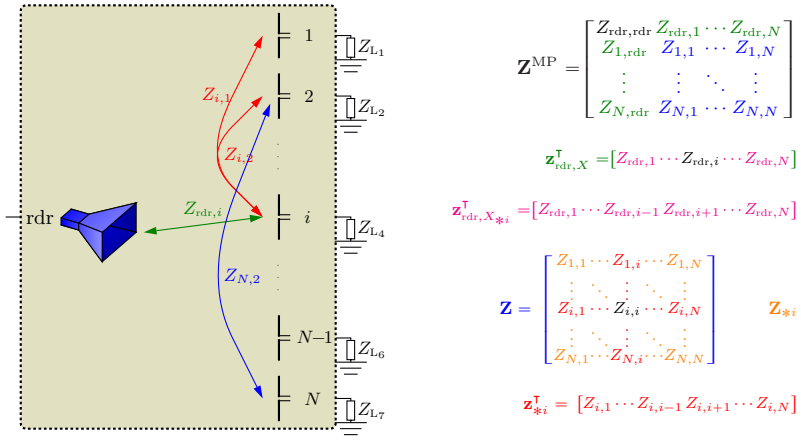

Figure 4.1: Block diagram for the measurement using an array of MST probes. The scenario/field distribution is characterized by the Z-parameters matrix. This matrix can be divided in a set of sub-matrices and vectors ($\mathbf{Z}_{*i}$, $\mathbf{z}_{\mathrm{rdr},X}$ and $\vec{Z}_{*i}$) useful for computations. The corresponding for each of them is presented in the figure with a color code to help with the associations.

4.1 Introduction

Many applications rely on the knowledge of a field distribution to obtain some information of the environment that is being measured, or some device under test, such as in antenna characterization [6], imaging applications [12], non-destructive evaluations of structures [13], etc.

When performing field measurements there are basically two options: a direct measurement and an indirect measurement. While direct measurement provide better dynamical range and sensitivity in the measurement, they require direct access to the measurement points, in order to bring the receiver (transmitter) to this specific point. This implies the use of multiple RF headers for each measurement point, which adds complexity and cost to the measuring system, or the use of a mechanical positioning system, which is not always compatible with the scenario. Conversely, indirect measurement rely on the measurement of an alternative parameter that allows to infer the field distribution, as is the case of MST, which allows to measure the existing field at the probe location by observing the scattered field by the probe. This is possible because the scattered field is proportional to the square of the incident field upon the probe from (2.20). However, this technique reduces the dynamic range of the system and also reduces the complexity of the system, since the probes do not require bulky (and expensive) RF equipment, but rather low-frequency modulation schemes. Moreover, with the use of self-powered probes, such as RFID, it is possible to have measurement points located in inaccessible points, where a conventional direct measurement/MST measurement would not be possible.

4.2 MST array field measurement

In field mapping applications it is reasonable to expect a regular grid of sensors sampling the electromagnetic field distribution. In these cases the formulation developed in section 2 although accurate for a single element response is somewhat incomplete, since it lacks the consideration of the mutual coupling effects, which will affect the measurement, and therefore it must be taken into account in the design of the grid. Specifically, as will be shown in the following derivation, if the coupling is too large, the signal that is excited in the neighbor elements of the array couples with the specific probe that is being modulated and the scattered field (and the measurement) will be an inaccurate representation of the field distribution, consisting of a filtered field distribution with contributions leaked from the nearby non-modulated elements.

4.2.1 MST Array Formulation

A common quantity that is used in diversity application to evaluate the coupling or correlation between multiport antennas, is the envelope correlation, however it is only adequate for Rayleigh distribution of the incoming signal on the antennas; moreover it can only evaluate 2 ports of the array at once, which limits the range of operation. The expression for the overall error in the measurement using an MST array (see Fig.4.1) due to the coupling of the nearby antennas has been developed in the appendix A.5 and is:

$$\begin{aligned} \Delta Z_{\mathrm{in_{rdr}}} =& Z_{\mathrm{in_{rdr},A}} - Z_{\mathrm{in_{rdr},B}} = \left(Z_{\mathrm{rdr},i} + C_i^Z\right)^2 \frac{\left(Z_{\mathrm{L}_B} - Z_{\mathrm{L}_A}\right)}{\left(Z_{\mathrm{L}_A} + Z_{\mathrm{ant_i}}\right)\left(Z_{\mathrm{L}_B} + Z_{\mathrm{ant_i}}\right)} \\ C_i^Z =& - \mathbf{z}_{\mathrm{rdr},X_{*i}}^T \left(\mathbf{Z}_{*i} + \mathbf{Z}_{\mathrm{L}*i}\right)^{-1} \mathbf{z}_{*i} \end{aligned} \tag{4.1}$$

where $Z_{\mathrm{rdr},i}$ accounts for the coupling between the reader and the current MST probe and C_i^Z represents the error due to the coupling of the nearby probes; $\mathbf{z}_{\mathrm{rdr},X_{*i}}$ is a vector representing the mutual coupling between the reader and the rest of the MST probes, therefore its elements are $Z_{\mathrm{rdr},j}\big|_{j\neq i}$; $\mathbf{Z}_{\mathrm{L}*i}$ is a diagonal matrix which contains the termination load of the rest of the MST probes; and finally $\mathbf{z}_{*i}$ is a vector whose elements represent the mutual coupling between the probe i and the rest of the proves, Z_{ij}.

If $\Delta Z_{\mathrm{in_{rdr}}} \ll Z_{\mathrm{in_{rdr}}}$ which is reasonable in an MST scenario, $\Delta\rho_{\mathrm{rdr}}$ becomes:

$$\Delta\rho_{\mathrm{rdr}} = \frac{2Z_{\mathrm{o}}}{\left(Z_{\mathrm{in_{rdr}}} + Z_{\mathrm{o}}\right)^2} \Delta Z_{\mathrm{in_{rdr}}} \tag{4.2}$$

which is basically the same as for a single MST probe, but with the introduction of the coupling term C_i^Z.

4.2.2 Effect of the loads of the array in the field distribution

From (4.2) it is observed that the received signal when the probe i is being modulated depends on the coupling between the elements of the array, as well as their specific loads. For instance if the loads attached to the array tend to an open circuit ($Z_{\mathrm{L}} \to \infty$), the parameter C_i^Z tends to 0, and $\Delta\rho_{\mathrm{rdr}}$ is proportional to $Z_{\mathrm{rdr},i}^2$, as in the case of a single probe. In this case, if the currents excited in the rest of elements of the array when they

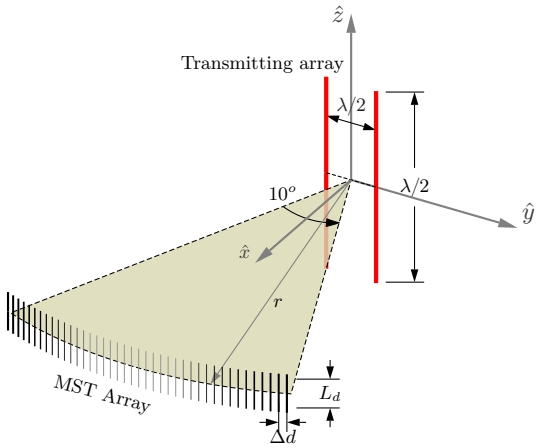

Figure 4.2: Configuration that will be used for the simulations to show the effect of the mutual coupling between elements. To create comparable scenarios, a polar distribution of the dipoles along an 10 ° arc is created in the direction of the null of a transmitting array formed by two dipoles with opposite current.

are left in open circuit are negligible, the incident field E_{inc} will be proportional to $Z_{\text{rdr},i}$[1]. Under a different loading condition the currents excited on the other elements of the array increase and the coupling modifies $\Delta\rho_{\text{rdr}}$ so that it no longer is directly proportional to the square of the field distribution; in this case $\Delta\rho_{\text{rdr}}$ corresponds to a filtered version of the field distribution by the overall array. As long as coupling is low, this effect is negligible, or can be corrected by deconvoluting the impulse response of the array. However, if the coupling is large enough, the information of the field distribution might be completely distorted.

This section shows a simulation carried out in order to observe first-hand the effects of the inter-element coupling, and to determine some criteria regarding maximum admissible coupling between elements. The scenario of Fig. 4.2 will be used to generate the field distribution measured by the MST array. It consists of a transmitting array of two dipoles separated $\lambda/2$ on the Y-axis, and fed with a phase difference of 180 °. The array creates a null in the X-axis and a maximum in the Y-axis. An MST array composed of 40 small dipoles (length L_d) is distributed along a 10 ° arc of radius r from the center of the transmitting array to measure the field distribution generated around the null.

In order to modify the coupling between the elements of the MST array without changing the field distribution to be measured, the radius r at which the measurement is taken is increased while keeping the angular distribution being scanned. This modifies the separation between elements of the MST array and thus modifies the coupling, but the field distribution is maintained, differing only in a proportionality factor of e^{-jkr}/r.

A MoM simulation for an inter-element distance Δd going from $\lambda/100$ to 3λ was done to obtain the Z-parameters matrix $\mathbf{Z}$ to evaluate (4.2). The simulations were done for two different MST arrays, consisting of different basic elements: the dipoles of MST array 1 have a length $L_{d_1} = \lambda/10$, whilst for the MST array 2 $L_{d_2} = \lambda/2$. An additional

[1]For other antennas, for instance slots, C^Z would not be a true measure of the coupling error, and an equivalent expression based on Y-parameters should be developed

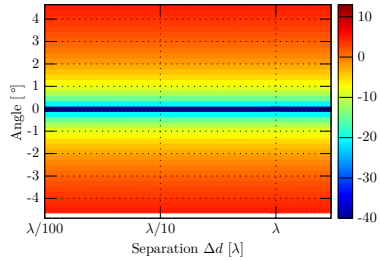

Figure 4.3: Field distribution generated by the transmitting array for different distances (r), evaluated at the positions of the MST array (not present for the simulation) and which correspond to different inter-element distance (X-axis). The measurement has been normalized with the factor e^{-jkr}/r to remove the distance dependence. Although the plot is basically constant, it has been shown like this to allow quick comparison between the expected result and the results obtained by different configurations of MST array in the following paragraphs.

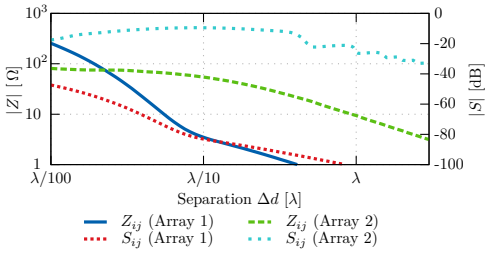

(a) Coupling from S_{ij} and (4.1)

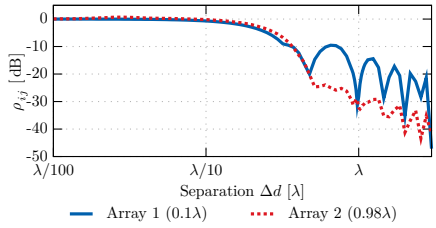

(b) Envelope correlation ρ_{ij}

Figure 4.4: Evolution of the mutual coupling between adjacent elements of the array as their separation is increased. (a) shows the coupling based on the Z/S-parameters; (b) shows the envelope correlation (ρ_{ij}) for the array (loaded with 50 Ω). It can be seen that the coupling analyzed from Z_{ij} or S_{ij} is not conclusive, because it does not take into account the accepted power nor the current loading conditions. On the other hand, the envelope correlation ρ_{ij} takes into account the accepted power and present a more comparable result.

simulation has been carried out without any element of the MST array to plot the exact field distribution to be expected, shown in Fig. 4.3 (the dependence with r has been removed through a normalization).

Fig. 4.4a presents the S_{ij} between the central elements of the MST array. Similarly Fig. 4.4b presents the maximum envelope correlation for each Δd. If only the S-parameters are considered, which are referred to a $Z_o = 50\,\Omega$, array 1 clearly presents a lower coupling than array 2; and both arrays have a clear decaying coupling as the separation increases. However it must be noted that this is not a fair comparison, since the dipoles of both arrays present highly differentiated input impedance (array 1 has a highly capacitive Z_{ii}, whilst array 2 is almost real). As such the mismatch between $Z_o = 50\,\Omega$ and the antenna input impedance for each of the MST arrays is not taken into account, therefore the interpretation does not fully explain the coupling effects. This is partially compensated using the envelope correlation, that shows a similar behavior for small separation between elements. Contrarily, the envelope correlation normalizes the coupled power to the accepted power by the array, and as such is somehow much more insensitive to the

	L_d	Z_{ii}	$\tilde{\rho}_{\mathrm{L}_i}$		
			$Z_{\mathrm{L}_i} \to \infty$	$Z_{\mathrm{L}_i} = 50\,\Omega$	$Z_{\mathrm{L}_i} = Z_{ii}^*$
Array 1	0.1λ	3.5 - j2220	1	$1\angle -0.18\,^\circ$	0
Array 2	0.96λ	72 -j 15	1	$0.21\angle -138\,^\circ$	0

Table 4.1: Self-impedance values for the dipoles of both arrays, along with the complex reflection coefficient for each of the cases under study

mismatch between the antenna and the reference load. It must be noted that to have an exact value of the coupling, the specific loads that are to be used in the MST array should be considered through (4.2). Nevertheless using a reference impedance, such as Z_{o} allows to obtain a first idea of the goodness of the array in terms of coupling. From the results observed in Fig. 4.4b it follows that the coupling should be expected to be large until a separation of approximately $\lambda/10$.

As previously stated and seen in equation (4.1) $\Delta\rho_{\mathrm{rdr}}$ depends on the load that is used in the different elements of the array. This is shown in the received signal shown in Figs. 4.5 and 4.6, which have considered three different loading conditions: in **case A** the non-modulated load for the elements of the array are open circuits, $Z_{\mathrm{L}_i} \to \infty$; in **case B** they are a conventional $Z_{\mathrm{L}_i} = 50\,\Omega$ load, and in **case C** they are the conjugate matched of the self-impedance (at the farthest separation) which would be the case corresponding to a conventional RFID design, $Z_{\mathrm{L}_i} = Z_{ii}^*$. As expected the field retrieved when the dipoles are left open circuited (case A) is perfect, which is reasonable since the currents excited on small wires is small; on the other hand, when the dipoles are loaded with Z_{ii}^* (case C), the retrieved field is inaccurate due to the high coupling between the different elements when the separation between elements is small. In this case, when the separation is around $\lambda/10$, the measured $\Delta\rho_{\mathrm{rdr}}$ is a more accurate representation of the field distribution. Finally for case B ($Z_{\mathrm{L}_i} = 50\,\Omega$) both arrays show a different behavior. For array 1 the performance is similar to case A, whereas for array 2 the performance is similar to case C. This can be explained looking at table 4.1 where the self-impedance and the complex reflection coefficient for the different loads are presented. It can be observed how array 1 is highly capacitive, as such the load impedance for cases A and B have basically the same complex reflection coefficient; on the other hand for array 2, which is almost resonant, cases A and B present two highly differentiated reflection coefficients, opposite to cases B and C which are very similar.

As a conclusion, it shows that for an MST array of small dipoles which use a matched load as the non-modulated load, as in the case of RFID, the resonance that arises induces a large current in the elements of the array, which can couple with the modulating element of the MST array, depending on the coupling levels of the array. As such, any RFID array will need to be analyzed using the formulation developed in (4.1) to evaluate the level of error in the measurement.

4.3 RFID field measurements

As previously introduced, the knowledge of a near(far) field distribution is important for applications such as imaging or antenna characterization. Although MST is a common

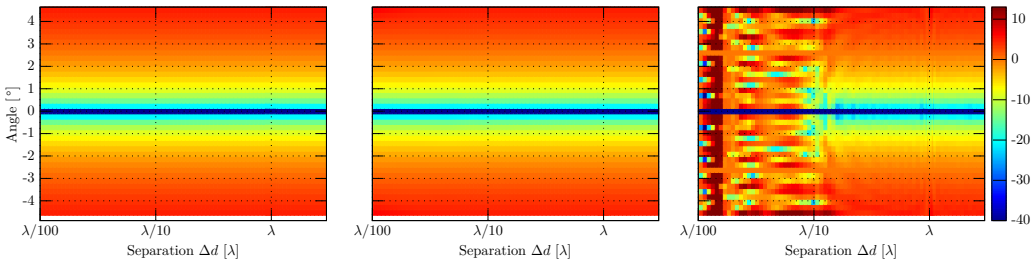

(a) Case A. $Z_{\mathrm{L}} \to \infty$ **(b)** Case B. $Z_{\mathrm{L}} = 50\,\Omega$ **(c)** Case C. $Z_{\mathrm{L}} = Z_{ii}^{*}$

Figure 4.5: Results of the simulation of $\Delta\rho_{\mathrm{rdr}}$ for 3 different loading conditions of the MST array 1 (length of the elements $L_d = \lambda/10$). When compared with the expected field of Fig. 4.3, cases A and B show similar results with no apparent coupling error, while case C presents errors in the measurement. This can be explained because the high capacitance of the self-impedance of the MST elements makes cases A and B very similar in terms of excited currents; on the other hand, case C considers a matched load having a resonant behavior which increases the error of coupling.

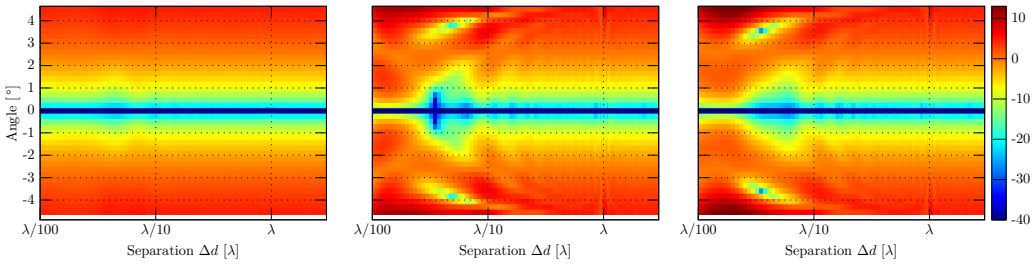

(a) Case A. $Z_{\mathrm{L}} \to \infty$ **(b)** Case B. $Z_{\mathrm{L}} = 50\,\Omega$ **(c)** Case C. $Z_{\mathrm{L}} = Z_{ii}^{*}$

Figure 4.6: Results of the simulation of $\Delta\rho_{\mathrm{rdr}}$ for 3 different loading conditions of the MST array 1 (length of the elements $L_d = \lambda/2$). When compared with the expected field of Fig. 4.3, case A presents a minimum error in the measurement, whilst cases B and C show similar results with the same level of error. In this case, the Z_{L_B} and Z_{L_C} present a similar value, thus showing a similar behavior in terms of excited currents, whiles the open-circuit of Z_{L_A} reduces the coupled current, minimizing the coupling errors.

technique used for indirect measurement, it still requires the use of external wiring to perform the modulation. Usually low frequency cabling [8] is used to bias and modulate positive-intrinsic-negative (PIN) diodes used as loads in the MST probe, alternatively, there optical fibers and photodiodes [5, 53] have also been used as the modulation signal and the MST loads. Of this solutions, the former requires physical access to the modulating probes, whilst for the latter there is a need of a line of sight (LOS) between the photodiode and the actual modulation source. These requirements pose a great challenge for embedded applications where the field to be measured is within an inaccessible medium, for instance within a human body, or a concrete structure; where it might be unacceptable to have such biasing cables going out of the medium.

In this context RFID rises as a possible solution for EM-field measurement, because the principle of operation is based on MST, and they do not need any external power, apart from the power associated to the incident wave, to operate. Also the modulation is triggered externally. Thus becoming a natural evolution for MST probes.

4.3.1 RFID intrinsic limitations as MST probe

As introduced in section 3.2.1, the input impedance of an RFID IC is basically the input impedance of the harvesting section with an equivalent circuit of an parallel RC load. However, as experimentally observed in 3.3 and 3.4, the non-linearities introduced by the harvesting circuitry are reflected in a variation of the scattering parameters of the RFID probe, showing a non-linear behavior. This needs to be taken into account when using the RFID tag as the MST probe becoming the first challenge of RFID EM-field probes. A second limitation arises from the minimum power required by the IC to operate P_{th}, which limits the dynamic range of the measurements, as well as the ability to detect low-power field distributions. This section deals with the first limitation, while the following sections enhance the dynamic range of the measurement as well as improving the non-linearities behavior of the probe.

As previously introduced in (2.23), the differential reflection coefficient in a monostatic configuration is:

$$\Delta\rho_{\mathrm{rdr}} = \frac{Z_{tr}}{2R_{\mathrm{ant}}}\Delta\tilde{\rho}_{\mathrm{L_2}} = \frac{\left(V^{\mathrm{OC}}\right)^2}{8P_a R_{\mathrm{ant}}}\Delta\tilde{\rho}_{\mathrm{L_2}} = \frac{h_{\mathrm{eff}}^2}{8R_{\mathrm{ant}}}\cdot\frac{E_{\mathrm{inc}}^2}{P_a}\cdot\Delta\tilde{\rho}_{\mathrm{L_2}} \tag{4.3}$$

which presents three differentiated terms. For an RFID probe, the first one is intrinsic from the probe antenna parameters therefore it is assumed constant thorough this chapter; the second term corresponds to the parameter of interest, as the square of the normalized electric field distribution $L_{\mathrm{inc}}(r) = {}^{E_{\mathrm{inc}}}/_{\sqrt{P_a}}$; finally the last term depends on the IC and the probe antenna and, as shown in the previous chapter, on the available power $P^{\mathrm{av}} \propto P_a \cdot \left|L_{\mathrm{inc}}(r)\right|^2$ at the probe antenna.

Since the last two terms in (4.3) are linked together, in order to obtain $E_{\mathrm{inc}}(r)$, it is necessary to remove the effect of $\Delta\tilde{\rho}_{\mathrm{L}}$

4.3.1.1 Calibration procedure

The power dependence of the different parameters in (4.3) with respect to power or position is explicitly shown as:

$$\Delta\rho_{\mathrm{rdr}}\big(P_a, r\big) = \frac{h_{\mathrm{eff}}^2}{8R_{\mathrm{ant}}} \cdot L_{\mathrm{inc}}^2\big(r\big) \cdot \Delta\tilde{\rho}_{\mathrm{L_2}}\left(P^{\mathrm{av}}\big(P_a, r\big)\right) \tag{4.4}$$

To remove the constant terms, equation (4.4) can be normalized with respect to a reference measurement, taken at a reference position r^{ref} and at a given transmitted power P_a^{ref}, becoming:

$$\overline{\Delta\rho}_{\mathrm{rdr}}(P_a, r) = \frac{\Delta\rho_{\mathrm{rdr}}\big(P_a, r\big)}{\Delta\rho_{\mathrm{rdr}}\big(P_a^{\mathrm{ref}}, r^{\mathrm{ref}}\big)} = \frac{L_{\mathrm{inc}}^2\big(r\big)}{L_{\mathrm{inc}}^2\big(r^{\mathrm{ref}}\big)} \frac{\Delta\tilde{\rho}_{\mathrm{L_2}}\left(P^{\mathrm{av}}\big(P_a, r\big)\right)}{\Delta\tilde{\rho}_{\mathrm{L_2}}\left(P^{\mathrm{av}}\big(P_a^{\mathrm{ref}}, r^{\mathrm{ref}}\big)\right)} \tag{4.5}$$

Additionally the variation in the last right hand term of (4.5) only depends on the variation of the available power, P^{av}, regardless of the source of this variation; as such it is possible to define a curve S which only depends on the relative variation of power levels:

$$S\left(\frac{P}{P^{\mathrm{ref}}}\right) = \frac{\Delta\tilde{\rho}_{\mathrm{L_2}}\big(P\big)}{\Delta\tilde{\rho}_{\mathrm{L_2}}\big(P^{\mathrm{ref}}\big)} = \frac{\Delta\tilde{\rho}_{\mathrm{L_2}}\big(P^{\mathrm{ref}}\frac{P}{P^{\mathrm{ref}}}\big)}{\Delta\tilde{\rho}_{\mathrm{L_2}}\big(P^{\mathrm{ref}}\big)} \tag{4.6}$$

Curve S is equivalent to the modulation efficiency (ME) as defined in section 2.4.1, where the reference measurement is taken at a given power level instead of for a specific set of loads. When (4.6) is introduced into (4.5):

$$\overline{\Delta\rho}_{\mathrm{rdr}}(P_a, r) = \left(\frac{L_{\mathrm{inc}}\big(r\big)}{L_{\mathrm{inc}}\big(r^{\mathrm{ref}}\big)}\right)^2 S\left(\frac{P_a}{P_a^{\mathrm{ref}}}\left|\frac{L_{\mathrm{inc}}(r)}{L_{\mathrm{inc}}(r^{\mathrm{ref}})}\right|^2\right) \tag{4.7}$$

From this equation it is seen that when the field distribution has a variation of α with respect to the reference position, the measured $\overline{\Delta\rho_{\mathrm{rdr}}}$ will change according to $\alpha^2 \cdot S(|\alpha|^2)$. To remove this non-linear behavior, it is required to characterize S for the given RFID probe, for instance by sweeping P_a at the reference position. Once the power dependence of S is known, the value of $S(\alpha)$ can be obtained by solving the roots of the implicit equation:

$$\left|\overline{\Delta\rho}_{\mathrm{rdr}}(P_a, r)\right| - \left|\frac{L_{\mathrm{inc}}\big(r\big)}{L_{\mathrm{inc}}\big(r^{\mathrm{ref}}\big)}\right|^2 \cdot \left|S\left(\left|\frac{L_{\mathrm{inc}}(r)}{L_{\mathrm{inc}}(r^{\mathrm{ref}})}\right|^2\right)\right| = 0 \tag{4.8}$$

And the field distribution is obtained as:

$$\overline{E}_{\mathrm{inc}}(r) = \sqrt{\frac{\overline{\Delta\rho}_{\mathrm{rdr}}(P_a, r)}{S(\alpha)}} \tag{4.9}$$

4.3.2 Single element RFID field measurement

This section presents the measurement of the field distribution of a ridged horn antenna using a single moving RFID element for its measurement. The experimental setup

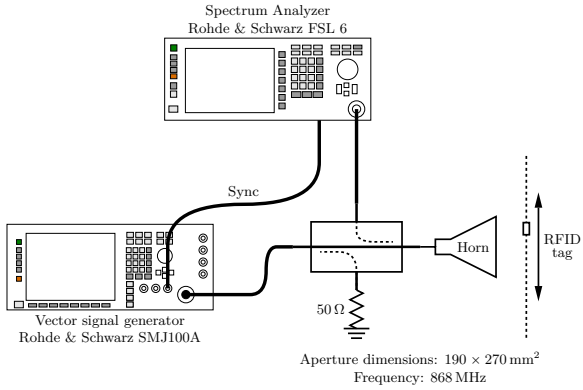

(a) Block diagram

(b) Measurement setup

Figure 4.7: Experimental setup for the measurement of RFID MST probe. The vector signal generator creates the proper code for activation of the RFID tags; the response of the RFID tag is captured by the spectrum analyzer.

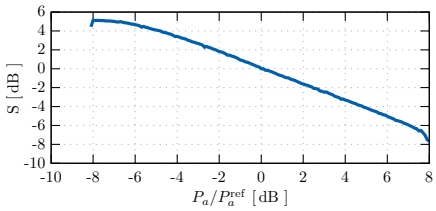

(c) Magnitude

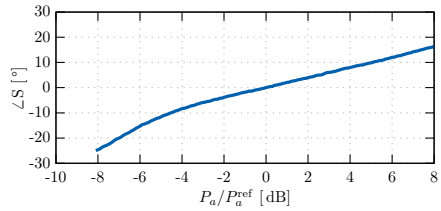

(d) Phase

Figure 4.8: Characterization of the power dependence of the S-curve ($^{\Delta\tilde{\rho}_{\text{L}}}/_{\Delta\tilde{\rho}_{\text{L}}(P_a^{\text{ref}})}$) obtained for a fixed position of the RFID tag (r^{ref}) and changing the transmitted power (P_a) by the vector signal generator. Non-linearities are shown as a slope of the S-curve, which would have a fixed value of 0 dB if the response were linear.

used in this measurements is shown in Fig. 4.7, and consists of a Rohde & Schwarz (R&S) SMJ100A vector signal generator to generate the proper wake-up RFID signal at the frequency of operation (868 MHz); a directional coupler which feeds the RF signal to the reader antenna; the reflected signal is then received through the coupler by a R&S FSL6 spectrum analyzer which is synchronized with the signal generator; finally a linear stage is used to perform the movement of the RFID probe along the aperture of the horn antenna. The RFID probe that was used for this experiment consisted of the bowtie antenna designed in section 3.1.2.

It must be noted that in this measurement the network analyzer used in section 3.3.1, and which presented the capability of large IFBW necessary for the measurement, was unavailable thus an alternative setup with conventional equipment from a microwave laboratory was used. The main implication for the measurement is that the magnitude that will be measured is Δb instead of $\Delta\rho_{\mathrm{rdr}}$, although since per the calibration of the previous section a normalization is performed, all the previous formulation still remains valid, hence for clarity in the exposition the measurements will be referred to as $\Delta\rho_{\mathrm{rdr}}$.

Fig. 4.8 presents the characterization of the curve S when the RFID probe is centered at the aperture of the ridge when the generator power is swept. Although the power was swept over a range of 30 dB, the curve can only be characterized for 16 dB, corresponding to power levels above the activation power P_{th}, thus the dynamic range is limited to 16 dB. Observing the figure, it must be noted that the behavior predicted from the measurements of the input impedance of the RFID IC in section 3.3.1 (see Fig. 3.29a) is experimentally corroborated with the current measurement: as the incident power upon the tag is increased, the magnitude of $\Delta\rho_{\mathrm{rdr}}$ is decreased in almost the same magnitude. The physical consequence of this non-linear behavior translates in that although the measured $|\Delta\rho_{\mathrm{rdr}}|$ should be proportional to the $|E_{\mathrm{inc}}|^2$, it is almost proportional to $|E_{\mathrm{inc}}|$, although since S is not a straight line the exponent changes with the actual power. From Fig. 4.8 it follows that when the E_{inc} changes -4 dB, the non-linearities modify $\Delta\tilde{\rho}_{\mathrm{L}}$ increasing it almost 3.5 dB, and thus $\Delta\rho_{\mathrm{rdr}}$ changes only -4.5 dB instead of -8 dB, which would result in an erroneous estimation of the variation of E_{inc} of -2.2 dB.

Fig. 4.9 presents the measured field distributions for the two principal planes of the horn aperture; three different curves present the expected field distribution: as obtained with a simulation based on the MoM, the estimation of E_{inc} neglecting the non-linearities (without performing calibration); and the result after applying the calibration. Several things can be said about the different curves: on the one hand the uncalibrated field distribution presents the behavior predicted in the previous paragraph due to the non-linearities, being always *above* the other two curves; additionally the calibrated field and the expected distribution present a very good matching, where the difference can be attributed to inaccurate modeling of the reader antenna as well as misalignment in the measurement line of the RFID probe, which is noticeable in the phase of the H-plane distribution, which translates in a slight shift between the curves.

Here it must be pointed out that the relative phase of the field distribution can be measured with an uncertainty of 180 ° introduced by the square root (in a bi-static configuration with a known relationship between the probe and the field, this uncertainty is completely removed). The fact that the RFID circuitry has a small (random) delay between the end of the QUERY command from the reader and the moment it starts answering, does not affect the capabilities to measure the carrier phase, because the measurement setup uses a coherent setup.

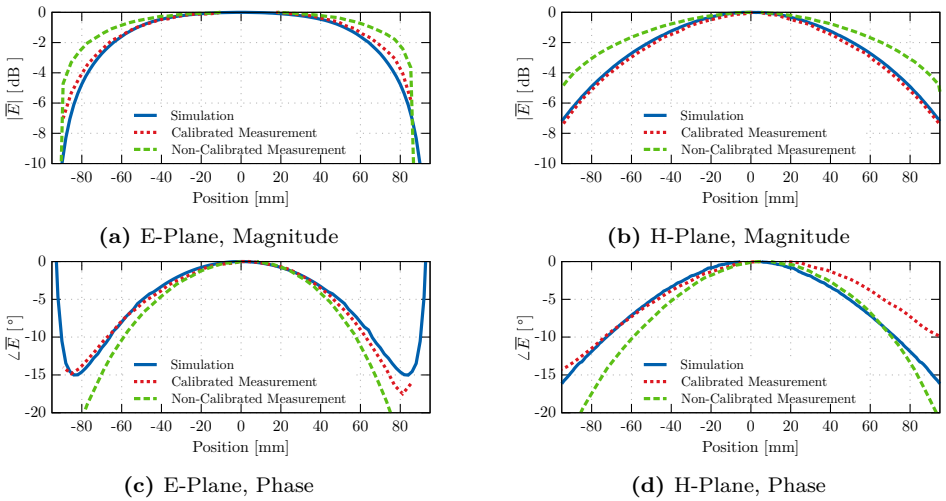

(a) E-Plane, Magnitude

(b) H-Plane, Magnitude

(c) E-Plane, Phase

(d) H-Plane, Phase

Figure 4.9: Comparison between the normalized field distribution at the two principal planes of the aperture. Three different curves are being shown, the first corresponds to the expected field distribution obtained using MoM, the second is the calibrated measurement, and the third is the raw measurement, where non-linearities have not been taken into account.

4.3.3 RFID array field measurement

The previous section has shown the capability to fully retrieve the field distribution by a single RFID probe despite the non-linear effects; nevertheless with only a single element, the sampling of the field requires external movement to be able to obtain the field distribution. This section presents the performance using arrays of several RFID tags.

Thorough this section the RFID probes used correspond to a commercial RFID tag, Alien Technologies ALN9529 Squiggle SQ [95], which has dimensions of 2 cm × 2 cm or equivalently approximately $\lambda/15 \times \lambda/15$ at 900 MHz. The use of such an RFID tag is based on its commercial availability, which emphasizes two of the advantages of the RFID MST probes: on the one hand its basic usage, unoptimized, only requires of a working RFID tag, without any specific design for the field measurement; on the other hand, the cost of the MST is reduced when compared with custom made, and low-scale production. Although the small dimensions of the RFID tag allow to create a dense array, with sampling below Nyquist, it reduces the dynamic range of the probe, since the efficiency of the antenna is smaller requiring more power to overcome P_{th}.

The RFID array measures the same field distribution of the ridged horn antenna aperture with two different configurations: in the first one a linear array (1D) is used, while in the second a bidimensional (2D) array is used.

4.3.3.1 1D array

The experimental setup is similar to that of the previous section and is presented in Fig. 4.10. A total of 4 different tags were placed on a foam support with a separation between centers of 60 mm. Although the RFID tags are placed along their H-plane (direction of maximum radiation), simulations applying (4.1) show that the coupling error

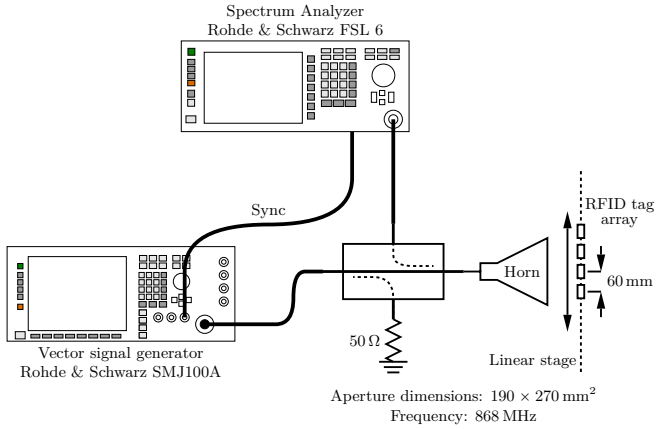

(a) Experimental setup block diagram

(b) Detail of the experimental setup.

Figure 4.10: Experimental setup for the measurement with a 1D array.

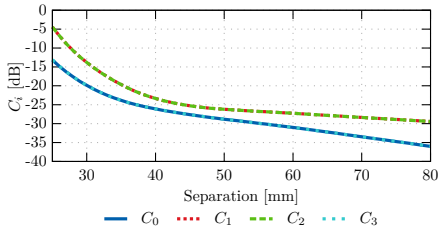

Figure 4.11: Dependence of the error introduced in the measurement due to coupling between the elements of the array with respect to their separation.

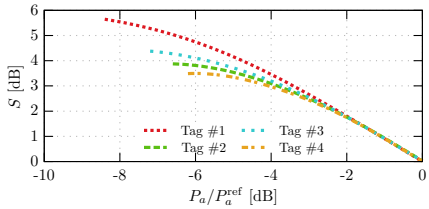

Figure 4.12: Characterization of the non-linearities of the different tags. Due to difference in the manufacturing, each tag presents a slightly different response, basically in terms of threshold. Due to this different the calibration must be performed for every tag individually.

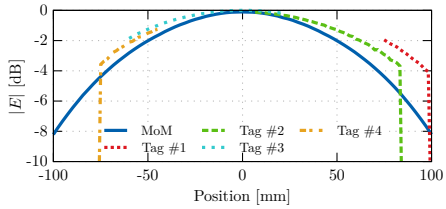

Figure 4.13: Normalized field distribution as retrieved by the 1D RFID array without applying any calibration. The non-linear error, as well as the differences between the tags shown in a disagreement with respect to the expected field.

in the measurement is of the order of $-25\,\text{dB}$, as shown in Fig. 4.11. For the calculation of the error, it has been assumed a uniform field distribution for the rest of the elements of the array, with a $\mathbf{\Gamma}_\text{L}$ corresponding to the RFID IC of the datasheet: $Z_\text{L} = 15 - j150\,\Omega$.

The array has been placed on top of the same linear stage than in the previous section and a measurement along the H-plane of the aperture. Thanks to the movement capabilities of the linear stage, the calibration procedure is as follows:

- The linear stage element i of the array to the reference position, the center of the aperture
- The signal vector generator interrogates the RFID probe for different power levels to obtain an individual calibration curve S.
- Optionally if the measurement power level is not included in the previous, it can be measured to use as a reference, although as introduced in section 4.3.1.1 it is not necessary that the reference power is the same as the measurement power.

The characterization of S curve for each of the elements of the array is presented in Fig. 4.12, where differences in the P_th of the different probe elements can be noticed, which effectively move the S-curve left or right. As a consequence, the raw measurement (Fig. 4.13) presents important variations between each probe. Nonetheless this variation can be corrected after calibrating the non-linearities of the RFID probe (see Fig. 4.14).

It must be emphasized that in the measurement the array was displaced for about 80 mm ensuring that for every two tags there was an overlapping area of each of the tags; as shown in Fig. 4.14 where the curves coming from each of the tags present an almost perfect match between each other.

4.3.3.2 2D array

For the 2D array a total of 25 tag elements have been arranged in a rectangular grid, see Fig. 4.15, with a separation $\Delta = 70\,\text{mm}$, which corresponds to a coupling error below 20 dB for the worse case, the central element (see Fig. 4.16). The array, which has been placed on top of a foam, is placed on a 2D linear stage in order to ease the calibration steps, which follow the same routine than for the 1D array. Fig. 4.17 presents

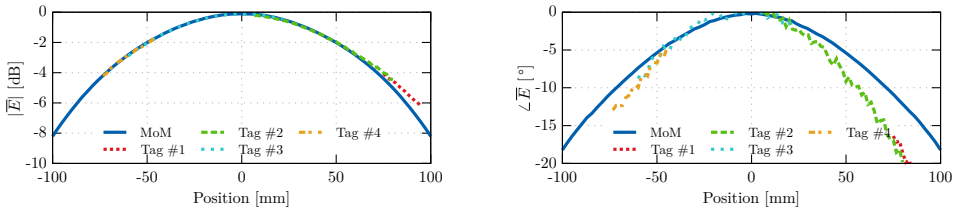

(a) Magnitude **(b)** Phase

Figure 4.14: Calibrated field distribution as retrieved by the 4-element array. Once the non-linear effects of the RFID IC have been corrected using the previous characterization, the field retrieved by the RFID-MST array presents a good agreement between the measurement and the expected field.

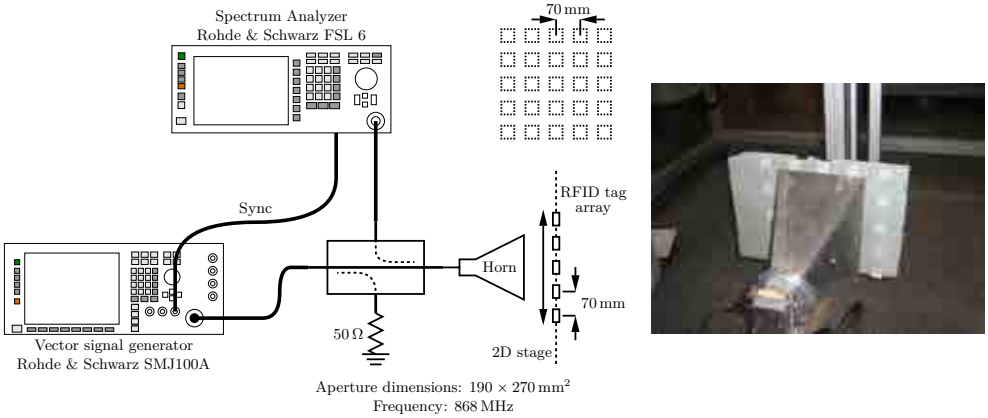

(a) Experimental setup block diagram **(b)** Detail of the experimental setup, frontal view

Figure 4.15: Experimental setup for the measurement with a 2D array, using in this case a 2D stage for the movement of the array.

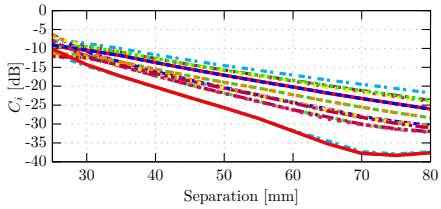

Figure 4.16: Dependence of the error introduced in the measurement due to coupling between elements with respect to the separation between centers. Depending on the position of the element in the array, the coupling error will be larger (for the central elements) or smaller (for the external elements).

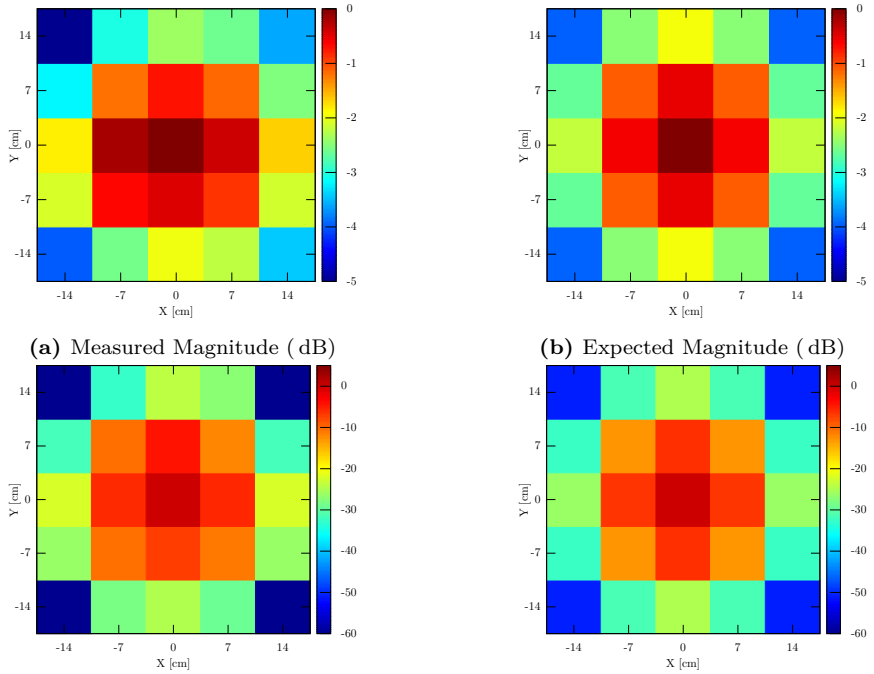

(a) Measured Magnitude (dB)

(b) Expected Magnitude (dB)

(c) Measured Phase (°)

(d) Expected Phase (°)

Figure 4.17: Field distribution obtained from the measurements of the 2D field distribution of a horn antenna using the 2D RFID array.

a 2-dimensional plot with the calibrated results of the measurement, compared to the expected field distribution as obtained from the simulation. In this case the measurement has been taken at a single position thus obtaining a total of 25 pixels.

4.4 Extending RFID capabilities: dual frequency configuration

The previous sections have shown the capabilities of RFID technologies as MST field sensors and although the measured field is accurate and matches the expected field distributions, the non-linear effects and the scavenging nature of RFID limits its applicability, since the dynamic range is much more limited than conventional MST systems.

In this section, an alternative and novel approach is taken for RFID MST field measurements that although this approach does not completely remove the non-linear effects in the response, and thus the need of calibration, it reduces its impact in the response, and at the same time, it increases the dynamic range of the sensor, making it comparable to conventional MST sensors, which are limited by the receiver's sensitivity.

The idea behind this alternative approach is the same of a biased amplifier and it is sketched in Fig. 4.18. In a biased amplifier, a DC signal establishes the operating point and then a small RF signal can be linearly amplified, provided it is sufficiently small. In

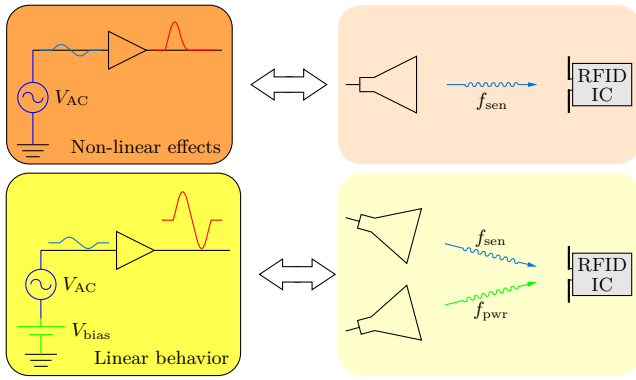

Figure 4.18: Principle of operation of the dual frequency configuration proposed to extend the capabilities of RFID tags as field sensors. As in an RF amplifier, the biasing of the harvesting section will ensure a more linear response of the RFID IC. In this case the biasing is proposed using a second RF signal (tone) operating at a different frequency.

this approach we want to establish a similar behavior, with a feeding signal that power the RFID probe, and a second signal for the measurement that will see a reflection coefficient independent to the power of this signal.

The proposal of using an alternative signal to power the RFID tag resembles a semi-passive tag, in which a internal battery ensure that the harvesting section is no longer needed (powering signal is a DC voltage) and therefore the non-linearities can be avoided. However, although this would be a valid solution to the non-linear problem, this approach would lead to costly sensors which require maintenance to keep them operative, which is not always possible if they are embedded. Conversely, what is proposed in this section does not modify the architecture of the RFID-based sensor, and therefore it keeps the harvesting section, and makes use of a combination of two incident signals to operate the sensor. The first signal, at a frequency f_{pwr} carries enough power to activate the RFID probe, while the second signal, at a different frequency f_{sen}, carries lower power and performs the sensing measurements.

4.4.1 Variation of the input impedance of a charge pump rectifier with power for a incident signal consisting of two tones

The following summarizes the analysis on the input impedance of a rectifier circuit when two input tones are used at the input port of the rectifier (the whole analysis is in appendix C). It focuses mainly on the behavior of a single diode although it is extensible to the behavior of the whole rectifier. In this part only an ideal diode (no parasitic junction capacitance) will be considered.

The incident signal consists of the sum of two tones with different amplitudes and relative phases:

$$v_g = V_{g_{\text{pwr}}} \cos(2\pi f_{\text{pwr}} t + \phi_{\text{pwr}}) + V_{g_{\text{sen}}} \cos(2\pi f_{\text{sen}} t + \phi_{\text{sen}}) \tag{4.10}$$

Due to the non-linearities of the diode, the current will present a series of mixed harmonics between f_{pwr} and f_{sen}, whose amplitude will generally depend on both $V_{g_{\text{pwr}}}$

and $V_{\mathrm{g_{sen}}}$. Developing the expression of the harmonics for the frequencies of interest f_{pwr} and f_{sen}, the current phasors become:

$$I(f_{\mathrm{pwr}}) = 2 \cdot I_s \cdot e^{-\frac{V_o}{2N \cdot nV_T}} \cdot B_1\left(\beta_{\mathrm{pwr}}\right) B_0\left(\beta_{\mathrm{sen}}\right) e^{j\phi_{\mathrm{pwr}}} \tag{4.11}$$

$$I(f_{\mathrm{sen}}) = 2 \cdot I_s \cdot e^{-\frac{V_o}{2N \cdot nV_T}} \cdot B_0\left(\beta_{\mathrm{pwr}}\right) B_1\left(\beta_{\mathrm{sen}}\right) e^{j\phi_{\mathrm{sen}}} \tag{4.12}$$

where B_i stands for the modified Bessel function of the first kind and $\beta_i = {}^{V_{\mathrm{g}_i}}/_{nV_T}$; which results in a dynamic resistance ($R_j(f)$) of the diode as:

$$R_j(f_{\mathrm{pwr}}) = \frac{V_{\mathrm{g_{pwr}}}}{2\left(I_s + I_L\right)} \frac{B_0\left(\frac{V_{\mathrm{g_{pwr}}}}{nV_T}\right)}{B_1\left(\frac{V_{\mathrm{g_{pwr}}}}{nV_T}\right)} \tag{4.13}$$

$$R_j(f_{\mathrm{sen}}) = \frac{V_{\mathrm{g_{sen}}}}{2\left(I_s + I_L\right)} \frac{B_0\left(\frac{V_{\mathrm{g_{sen}}}}{nV_T}\right)}{B_1\left(\frac{V_{\mathrm{g_{sen}}}}{nV_T}\right)} \tag{4.14}$$

where I_L is the load DC current that goes through the diode.

Focusing in the behavior at f_{sen}, it is shown that for small incident power, or equivalently $\frac{V_{\mathrm{g_{sen}}}}{nV_T} \ll 1$ the quotient of Bessel functions in (4.14) becomes $1/V_{\mathrm{g_{sen}}}$ and therefore the dynamic resistance becomes

$$R_j(f_{\mathrm{sen}}) = \frac{nV_T}{I_s + I_L} \tag{4.15}$$

Which only depends on intrinsic parameters of the diode and the current load conditions (requirements of current) of the rectifier, and becomes insensitive to the incident power at f_{pwr}. In fact this is the small signal model of the diode when it is biased with a output current I_L, which in this case is generated thanks to the rectified signal at the frequency f_{pwr}. However, the input impedance at f_{sen} for real diodes will not remain independent of P_{pwr} because parasitic effects, for instance in the junction capacitance, depend of the biasing conditions (V_o and I_L) and as such, variations of P_{pwr} will change $Z_{\mathrm{scav}}(f_{\mathrm{sen}})$.

4.4.2 Experimental characterization of the variation of the input impedance of an RFID IC for a signal consisting of two tones

Although the previous analysis shows the potential of dual frequency excitation to increase the dynamic range, it is based on a diode charge pump configuration of the RFID IC harvesting section, and therefore it must be validated experimentally for the RFID IC, since its exact internal architecture is not known. The characterization of the impedance of the RFID IC when two tones are applied follows a similar procedure as that shown in section 3.3.1. However, in this case since the characterization and the activation are at different frequencies, f_{sen} and f_{pwr} respectively, the external modulating circuit presented in 3.3.1 is not required. The measurement setup is presented in Fig. 4.19, where the vector signal generator generates the modulated signal at f_{pwr} and the VNA operates at f_{sen}. Both signals are combined with a Wilkinson divider [57] with the RFID IC being placed at the output port of the divider. The experimental setup is calibrated in power for both

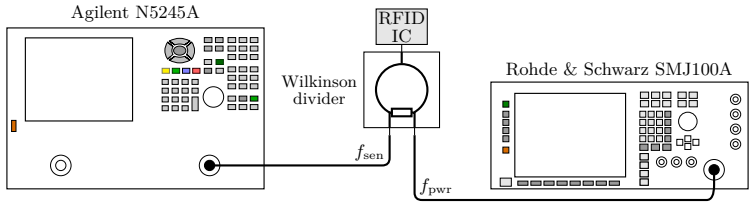

Figure 4.19: Experimental setup for the characterization of the input impedance of the RFID IC for an incoming signal composed of two differentiated tones; a vector signal generator operating at f_{pwr} generates the feeding RFID signal which is combined with a second signal generated by a network analyzer operating at f_{sen} with lower power. The calibration of the reference plane is performed using the calibration kit used in chapter 3 (see Fig. 3.26b).

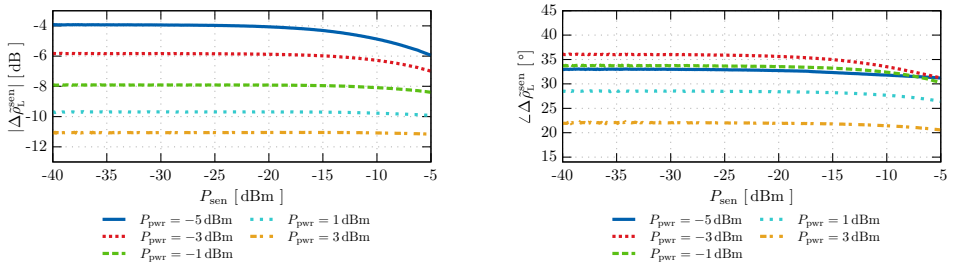

(a) Magnitude **(b)** Phase

Figure 4.20: Measured $\Delta\rho_{rdr}^{sen}$ at the frequency f_{sen} =950 MHz for a feeding frequency of f_{pwr} =868 MHz. The response of the RFID IC remains constant for low values of P_{sen} regardless of the power of the feeding frequency P_{pwr}. When P_{sen} increases to reach values comparable to P_{pwr}, $\Delta\rho_{rdr}^{sen}$ starts changing.

devices, and an additional TRL calibration of the VNA, as done in section 3.3.1, ensures that the effects of the divider are corrected.

Without loss of generality, the characterization has been taken for two sets of frequencies; f_{pwr} = 868 MHz and f_{sen} = 950 MHz and f_{pwr} = 1 GHz and f_{sen} = 868 MHz. For each set the VNA output power has been swept from −40 dBm up to 5 dBm and P_{pwr} has been established at different power levels: −5 dBm, −3 dBm, −1 dBm, 1 dBm and 3 dBm.

Figs. 4.20 and 4.21 present the measurement of the differential reflection coefficient $\Delta\tilde{\rho}_L^{sen}$ at f_{sen} for each value of P_{pwr} for f_{sen} = 868 MHz and f_{sen} = 1 GHz respectively. They show a constant behavior of $\Delta\tilde{\rho}_L^{sen}$ when P_{sen} is small, until it becomes comparable to P_{pwr} when $\Delta\tilde{\rho}_L^{sen}$ starts changing and decreasing in value. Moreover, as expected, the value of $\Delta\tilde{\rho}_L^{sen}$ depends on the actual P_{pwr} (the biasing conditions) as shown by the non-overlapping curves for each value of P_{pwr}.

Table 4.2 presents the value of P_{sen} for each frequency at which the change in $\Delta\tilde{\rho}_L^{sen}$ begin to be larger than 0.1 dB. It can be seen that this threshold is not constant and directly depends in P_{pwr}, showing a variation of 16 dB for a variation in the feeding power P_{pwr} of 8 dB. Additionally, it can be noted a similar effect that was detected on the single frequency characterization of section 3.3: $\Delta\tilde{\rho}_L^{sen}$ decreases as P_{pwr} increases, and as P_{sen} increases, and with a similar trend, that is when P_{pwr} increases 8 dB, $\Delta\tilde{\rho}_L^{sen}$ has decreased approximately 7 dB.

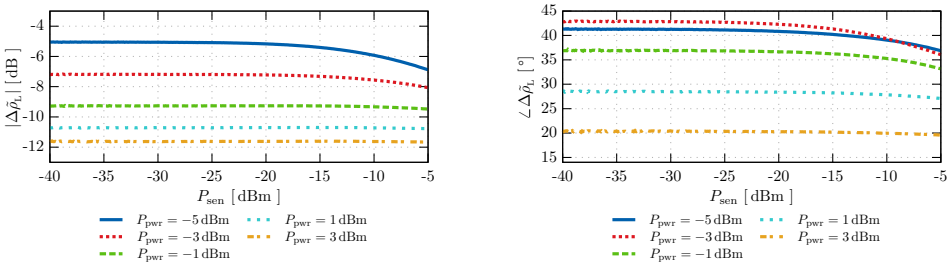

(a) Magnitude **(b)** Phase

Figure 4.21: Measured $\Delta\rho_{rdr}^{sen}$ at the frequency f_{sen} =868 MHz for a feeding frequency of f_{pwr} =1 GHz. A similar behavior to the previous figure can be appreciated, with the response of the RFID IC remaining basically constant (with respect to P_{sen}) for low values of power, and starts changing when P_{sen} becomes comparable to P_{pwr}.

	$f_{sen} = 950$ MHz			$f_{sen} = 868$ MHz		
P_{pwr} [dBm]	P_{sen} [dBm]	$\Delta\rho_T$ [dB]	P_{bs}^{sen} [dBm]	P_{sen} [dBm]	$\Delta\rho_T$ [dB]	P_{bs}^{sen} [dBm]
-5	-21.0	-3.9	-24.9	-20.2	-5.0	-25.2
-3	-17.0	-5.8	-22.8	-16.1	-7.2	-23.3
-1	-12.3	-7.9	-20.2	-8.7	-9.3	-18
1	-9.6	-9.7	-19.3	-5.0	-10.7	-15.7
3	-5.1	-11.1	-16.2	-5.0	-11.6	-16.6

Table 4.2: Maximum power that can be used in the dual frequency scheme for a variation of the reflection coefficient below 0.1 dB

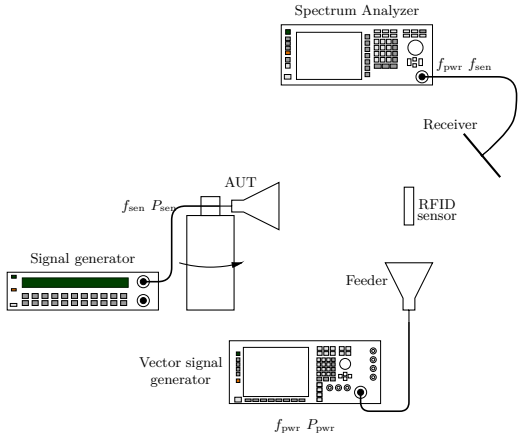

(a) Block diagram

(b) Experimental setup

Figure 4.22: Experimental setup for the measurement of the radiation pattern of the horn antenna. The horn antenna is placed on top of a rotary stage in order to measure the radiation patter from $-75\,°$ to $75\,°$.

Therefore two conclusions can be drawn from the results: (1) an increase of P_{pwr} increases the available dynamic range of the measurement since P_{sen} can reach higher values; secondly, $\Delta\tilde{\rho}_{\text{L}}^{\text{sen}}$ diminishes as P_{pwr} increases, thus reducing the backscattered power at f_{sen} for a fixed transmitted P_{sen}. However, since the dynamic range of P_{sen} increases more rapidly than $\Delta\tilde{\rho}_{\text{L}}^{\text{sen}}$ decreases with P_{pwr}, the overall SNR of the measurement improves, as seen in Table 4.2 where the maximum *linear* backscattered power at f_{sen}, $P_{\text{bs}}^{\text{sen}}$, goes from $-25\,\text{dBm}$ to $-16\,\text{dBm}$.

4.4.3 Experimental measurements with a dual frequency setup: radiation pattern

Previously the assessment of the field distribution measurements has been done by measuring the aperture field distribution of a horn antenna by moving a single probe, or an array, in front of the horn antenna. Although it would be desirable to repeat such measurement, the requirements for the enhanced RFID tag demand that the power reaching the tag at f_{pwr} remains constant in the measurement, because the response at f_{sen} it is not entirely independent of P_{pwr}. A way to solve this would be to have an additional antenna illuminating the probe at f_{pwr}, and instead of moving the RFID tag in front of the horn, the latter is moved in front of the RFID tag. However, due to the proximity of the horn antenna, there is still a strong reflection in its metallic regions that modify the total incident power at f_{pwr} reaching the RFID tag, and therefore $\Delta\tilde{\rho}_{\text{L}}^{\text{sen}}$ will be modified (due to the change in the biasing as seen in Fig. 4.20. A possible solution, not followed in this thesis, is to determine for every location/tag the required P_{pwr} to activate the tag. Once this value is known, a common power offset of P_{pwr} can be applied for every location in such a way that the feeding power is the same for every location/tag and with that the variation of $\Delta\tilde{\rho}_{\text{L}}^{\text{sen}}$ due to biasing conditions introduced by f_{pwr} are completely removed.

As an alternative experimental setup, what is proposed is the measurement of a cut of

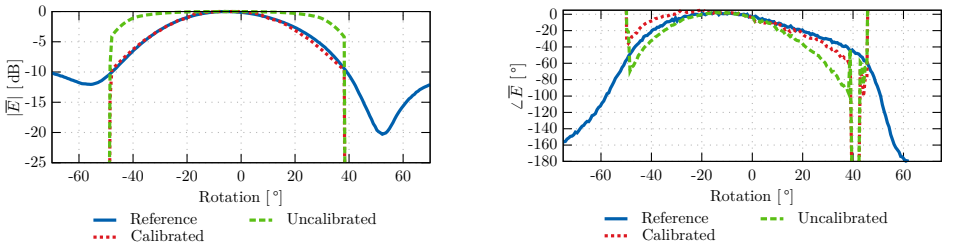

(a) Magnitude **(b)** Phase

Figure 4.23: Retrieved radiation pattern for the conventional operating mode of the RFID tag. Due to the presence of non-linearities it is required to properly calibrate the measured signal with respect to power variations, and in spite of the calibration the dynamic range is limited by P_{th}, which does not allow for a full measurement of the radiation pattern.

the H-plane of the near field radiation pattern of the horn antenna, in such a way that the reflections on the horn of feeding signal at f_{pwr} can be minimized. Fig. 4.22 represents the configuration of the measurements. Which uses a bi-static setup to allow amplification of the received signal. The instrumentation consists of a CW signal generator working at $f_{\mathrm{sen}} = 1\,\mathrm{GHz}$ which is connected to the antenna under test (AUT), the horn antenna, which has been placed on top of a rotary stage which moves from $-75\,^{\circ}$ to $75\,^{\circ}$; a signal vector generator is connected to another horn antenna (the feeder) which illuminates the RFID tag that is used as a probe; this antenna is placed in such a way that reflections from the antenna under test are minimized. The vector signal generator operates at $f_{\mathrm{pwr}} = 905\,\mathrm{MHz}$ and generates the protocol to trigger the RFID tag while providing sufficient power to activate the tag. A third antenna (the receiver) is used to received the reflected signal with the spectrum analyzer which performs the measurement. This third antenna is also used for taking the reference measurement for the same H-plane of the horn antenna. To do so it is placed slightly behind the RFID tag.

For comparison of performance, the measurement is divided in two stages. In the first one, the vector signal vector generator creating the RFID protocol is directly connected to the AUT working at f_{sen}; this provides a reference measurement using a conventional RFID setup; additionally the configuration of the receiver antenna allows to obtain a direct measurement of the field pattern. In the second stage, the configuration that is used is the previously defined and presented in Fig. 4.22, which allows to obtain the measurement for the dual frequency approach.

Fig. 4.23 shows the results of the conventional RFID field measurement as well as the direct measurement obtained with the receiver antenna. Here it must be noted that although the reference measurement is a direct measurement, and thus does not require the use of a dual frequency approach, the measurement has been done with the feeding signal active. The reason behind this is that since the RFID tag and the folded dipole are close to each other, variations of the input impedance of the RFID IC due to changes in the incident power would couple to the receiver antenna and the measured signal would be inaccurate.

From the curves, it is clear that the conventional measurement presents the effects of the non-linearities (direct estimation above the actual field), which can be calibrated as in the previous section to obtain a good agreement with the direct measurement. However,

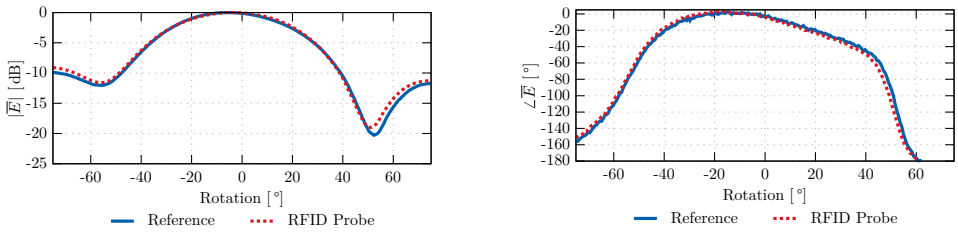

(a) Magnitude **(b)** Phase

Figure 4.24: Retrieved radiation pattern for the RFID tag operated in a dual-frequency mode. The only required calibration for this measurement is the normalization of the RFID probe response which can be easily removed.

it is unable to measure the whole pattern of interest since the tag stops working when the signal is 10 dB below the maximum. The results for the dual frequency are presented in Fig. 4.24, where it must be noted that no extra calibration has been required in the measurement (apart from the normalization of the maximum). The differences observed in the minimum of the radiation pattern are produced by the slightly different location of the RFID tag and the receiver antenna, which although close are not physically in the exact same location. However, it must be emphasized the extremely good agreement between both curves in magnitude and phase, with the whole dynamic range required of the measurement being measured correctly, which is one of the main advantages of the dual frequency setup.

4.4.4 Experimental measurements with a dual frequency setup: tomographic imaging using an array of multiple elements

This section presents a second dual frequency experimental measurement where an array 8 RFID elements measures the scattered field generated by a metallic cylinder in order detect its position by means of tomographic imaging [JA6, 96]. The experimental setup is shown in Fig. 4.25; it consists of an array of 8 RFID tags (ALN-9540) placed at a height of 50 cm and with a inter-element separation of 14 cm ($0.47\lambda_{\text{sen}}$), and as in the previous section three different antennas are used to generate and capture the required signals. The first one, the transmitter antenna, is at a height of 55 cm and connected to a continuous wave (CW) signal generator operating at $f_{\text{sen}} = 1$ GHz creates the incident field illuminating the scenario; the second one, the feeder antenna, is connected to the vector signal generator operating at $f_{\text{pwr}} = 905$ MHz and is placed orthogonal to the RFID array to minimize the reflections coming from the scenario. As with the previous section this antenna is in charge of feeding the RFID array and generating the RFID protocol. The third antenna, the receiver antenna, is located at the opposite end of the MST array and is connected to the spectrum analyzer to capture the scattered field by the array. Finally, a small metallic cylinder of diameter 1 cm is placed in different positions (A−D) of the region between the RFID array and the illuminating antenna (see Fig. 4.25).

The scattered field required for the imaging algorithm is obtained as the subtraction of two consecutive measurement $E^{\text{scat}} = E^{\text{diff}} - E^{\text{inc}}$, where E^{diff} corresponds to the measurement of the scene with the cylinder present, and E^{inc} corresponds to the scenario

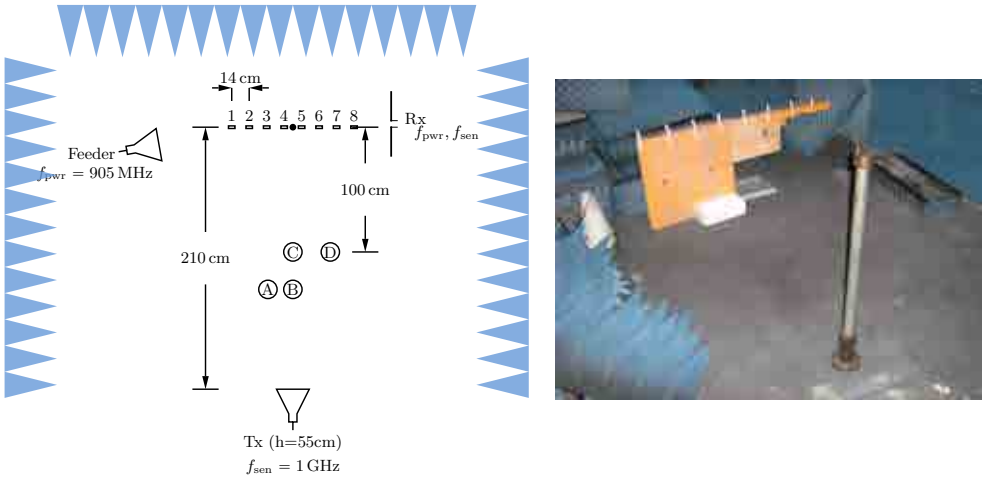

(a) Sketch **(b)** Experimental setup

Figure 4.25: Scenario for the measurement of the diffracted field by a set of cylinders in different locations (A,B,C,D)

without the cylinder.

Since 8 different RFID tags are used as MST probes and the elements of the array are not identical (fabrication tolerances, chip differences, different power reaching each RFID IC, etc.), it is to be expected that the MST response (see eq. (2.23)) and more specifically $\Delta\tilde{\rho}_{\mathrm{L}_i}$ is not necessarily the same for each tag, as opposed to a virtual array using a moving tag. It is required to calibrate the response of each of the RFID tags so that the variation in the measured $\Delta\rho_{\mathrm{T}}$ corresponds to variations in the field distribution. Since the non-linearities of the RFID IC circuitry are removed by the dual operation mode, as shown in the previous section, the calibration that is required to perform is independent of power, and it is the conventional calibration scheme used in MST arrays [8]. It basically consists in using a known incident field distribution as a reference field (E^{ref}) so that a calibration factor (α) can be obtained for each element of the array:

$$\alpha_i = \frac{E^{\mathrm{scat}}}{E^{\mathrm{ref}}} \tag{4.16}$$

Although measuring a uniform field distribution, an incident plane wave, would directly measure the correction factor from the measurement, this is not possible in the current scenario due to the large distances required to obtain such plane wave. An alternative solution is to use a canonical scatterer (such as a metallic cylinder) in a known position (such as position C in Fig. 4.25), which generates a field distribution whose solution is well-known and can be easily obtained [97]. This is the solution that is implemented in this section as the calibration procedure.

Fig. 4.26 presents the tomographic reconstruction of each measurement of the different scenarios. The theoretical reconstruction uses the analytical scattered field by a metallic cylinder [97] and present good agreement with the experimental reconstruction, albeit with larger background noise in the measurement, which probably arise from a small disturbance in the feeding signal E_{pwr} between the empty and diffracted measurements.

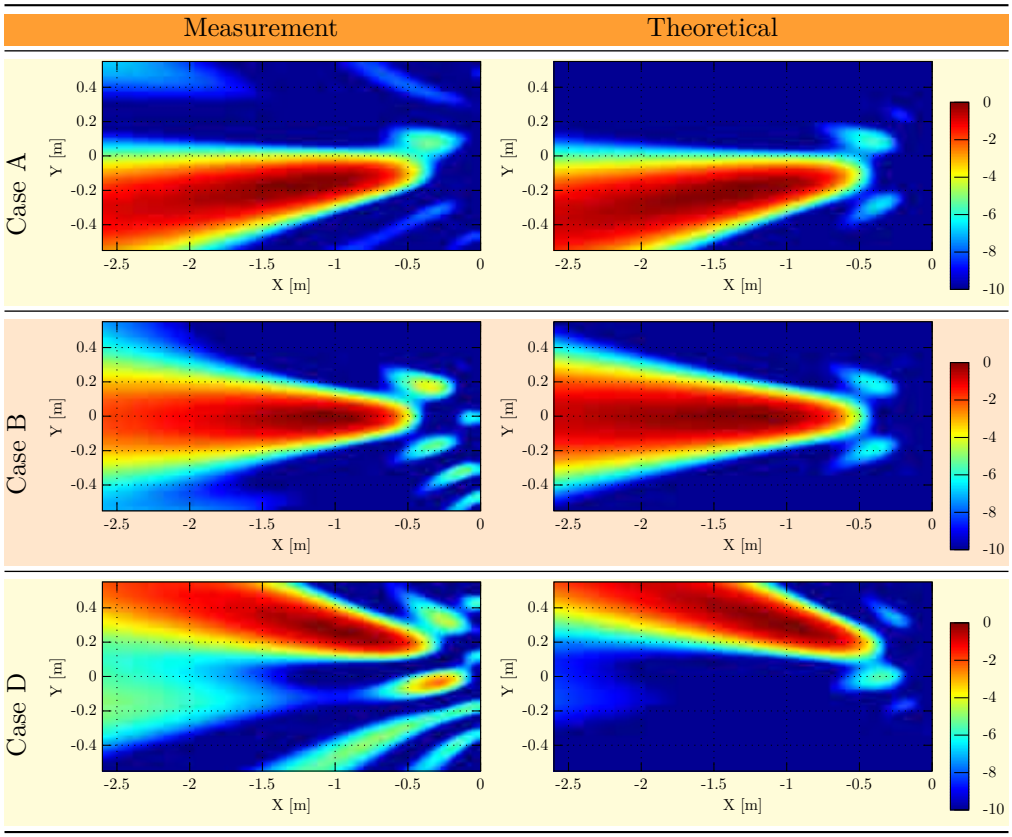

Figure 4.26: Comparison of the reconstructed images of the scenario for the different positions of the cylinder. The reconstructed image is capable of detecting the position of the cylinder with similar accuracy to what would be ideally retrieved. Improvement of the resolution could be achieved using a longer array, or a multi-frequency approach (see next section).

Also, it must be noted that the low resolution of the reconstruction is due to the reduced angle of vision of the cylinder by the array, given by the size of the array and the distance to the cylinder. This could have been improved either with a larger array, or a closer distance between the cylinder and the array, however the latter would not have been possible with the current experimental setup, because the feeding field E^{pwr} would have been different for the empty and the non-empty scenes (reflections from the scene), thus changing the values of $\Delta\bar{\rho}_{\text{L}}^{\text{sen}}$ between scenes.

4.5 UWB MST Imaging

In the previous section it was shown how RFID-MST probes could be used to measure EM-field distributions, and how eventually these could be used to perform tomographic imaging of a given scenario to determine the location of scatterers. This section focuses more specifically in tomographic imaging using MST probes and how the use of a multi-frequency approach can improve the tomographic reconstruction. Although this section considers a conventional MST probes to perform the analysis it could, in the end, be combined with RFID-MST probes using a similar approach to the dual frequency setup with a larger bandwidth of operation.

In tomographic applications, if instead of a single frequency, a set of frequencies are used, there will be a series of benefits:

Redundancy. Since constitutive parameters, such as permittivity and conductivity, do not usually present strong variations in frequency, the combination of information at close frequencies, increases the signal to noise ratio of the retrieved image.

Resolution. By taking measurements at different frequencies, it is possible to obtain images at different resolutions. Moreover by combining them, although the overall resolution is reduced when compared to the highest frequency, the quality of the reconstruction is much more solid [98].

Aliasing. When working at a single frequency, sub-sampling of the measured electric field, that is a separation between probes larger than Nyquist limit, reduces the area of proper reconstructions, by introducing aliasing in the reconstructed image. When operating in a multi-frequency environment, and since Nyquist conditions are frequency dependent, the aliasing introduced at each frequency is located in a different position, and does not add constructively, so the combined image does not require such a dense grid of points, although the quality will be improved if it is enforced.

In order to use MST in an efficient way for imaging applications in multi-frequency applications, there are three different aspect that should be designed.

Transmitter. Imaging algorithms rely in a known incident field distributions, which usually consist of a plane wave distributions. As such the transmitter must be able to generate a field distributions as close as possible to a plane wave (to avoid complex noisy calibration procedures).

Receiver or collector. Since the field scattered by each probe is received or collected by this antenna, it is important that the attenuation to each of the probes is as uniform as possible.

	C_{UP} [fF]	R_s [Ω]	L_s [pH]
Rockwell Scientific DC-Contact MEMS (M1)	2	2	60
Motorola DC-Contact MEMS Series (M2)	2	2	20
HRL DC (M3)	3	2	60
NorthEastern University/Radant MEMS (M4)	4	1.5	30
Lincoln Laboratory Inline and Capacitive (M5)	6	2	0
Omron DC-Contact MEMS (M6)	5	0.5	0

Table 4.3: Equivalent circuit parameters of different MEMS switches [99].

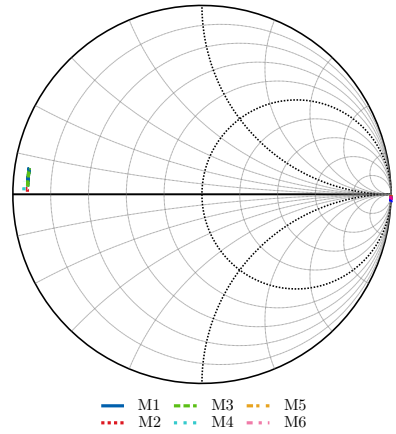

Figure 4.27: Smith chart representation of the different MEMS switches shown in table 4.3.

MST probe. As previously shown, the MST probe design must maximize the *ME* of the measurement; this is specially challenging in a multi-frequency environment due to the possible frequency dependent response of the loads.

4.5.1 UWB Probe

4.5.1.1 Requirements for the probe

In order to design an ultra wideband (UWB) MST probe, it is required a load that presents two highly differentiated states, and that is as constant in frequency as possible. PIN diodes and micro electromechanical systems (MEMS) switches are two possible choices of switching devices that can act as the load. With MEMS offering higher isolation and lower conduction losses, thus emulating a short-circuit and an open circuit for the whole UWB frequency range. In the following, it has been assumed that a MEMS switch is being used as the switching device for these systems.

To maximize the SNR of the signal, the input impedance of the probe must maximize its *ME* , thus the input impedance of the loads of the MEMS switch must be known beforehand. Although the specific parameters of the MEMS switch that were to be used were not fully known at the design stage, it is known that they should present low losses and high bandwidth, thus low capacitance. As a starting reference point, Table 4.3 presents the equivalent circuit of different MEMS switches fabricated at different research centers. Using these parameters, it is possible to compute the ON and OFF impedance of the switches, which are represented in Fig. 4.27. For the OFF state, since the capacitance is extremely small all MEMS present basically an open circuit impedance. On the other hand, for the ON state, the MEMS switches become basically RL circuit, and the difference between each MEMS is more noticeable in the displacement from the short-circuit.

With this knowledge, it is possible to establish that $Z_{L_2} \to \infty$ is the impedance of the OFF state for any MEMS switch that we could use at the fabrication stage; on the other

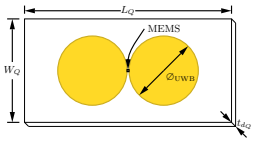

Figure 4.28: UWB dipole disc antenna designed to serve as the MST probe antenna.

Parameter	Value
Substrate	Quartz ($\epsilon_r \approx 3.78$)
$\varnothing_{\mathrm{UWB}}$	17 mm
W_Q	25.4 mm
L_Q	50.8 mm
t_{dQ}	1.8 mm

Table 4.4: Design parameters for the UWB MST probe.

hand, the value of Z_{L_1} is close to a short-circuit, but with a small reactive part which will strongly depend on the specific MEMS. As previously shown in section 2.4.1, *ME* can be viewed as the square of the distance between $Z_{\mathrm{L}_1} + jX_{\mathrm{ant}}$ and $Z_{\mathrm{L}_2} + jX_{\mathrm{ant}}$ when represented in a Smith chart normalized with R_{ant}, thus having a maximum value of 4. If we look back again to Fig. 4.27 it is clear that for a Smith chart normalized to 50 Ω, the distance between Z_{L_1} and Z_{L_2} is almost 2. In fact for a combination of loads $Z_{\mathrm{L}_1} = 0$ and $Z_{\mathrm{L}_2} \to \infty$ it can be shown that the optimum Z_{ant} must be purely real, without any restriction on the value of the resistance.

Taking this into account, and the uncertainty of the small reactance of Z_{L_1}, the design goal for the probe antenna is taken as if it was an ideal short-circuit, thus the design goal is to have a resistive antenna for the whole UWB frequency band.

4.5.1.2 Antenna probe

The antenna that has been used as the antenna probe is an UWB dipole disc antenna [100, 101], which presents a good response for UWB communications. Since the antenna should be integrated with MEMS technology fabrication procedure, the antenna will be fabricated with the same process: the metallization is made of gold and the substrate is a wafer of quartz. The initial antenna was simulated with high frequency structural simulator (HFSS) and fine-tuned in order to obtain a good response for the whole frequency band, leading to the final design shown in Fig. 4.28, with the main dimensions shown in Table 4.4. The total size of the antenna is roughly 34mm, and it presents a good reflection coefficient for the whole band below -6 to -10 dB for the whole frequency band. Similarly, the linear polarization remains constant for the whole range of frequencies, although due to the disparate dimensions, from $\lambda/3$ at 3 GHz to roughly λ at 10 GHz, there is a shift of the main lobe direction which reduces the directivity in approximately 10 dB for the broadside direction at 10 GHz.

In order to measure the antenna performance, basically the input S-parameters, as in section 3.1.2, a monopole version of the antenna was fabricated consisting of half the antenna. This antenna with the proper separation was placed on top of a ground plane to conform a monopole version of the UWB MST probe antenna. Fig. 4.29 presents measured S-parameters of the antenna (converted to the dipole impedance by doubling its value).

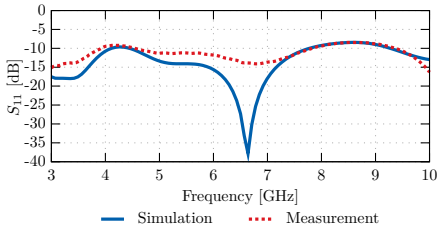

Figure 4.29: S-Parameters of the UWB dipole disc antenna. Measurement corresponds to the monopole version of the dipole, which has been converted to the equivalent dipole antenna by doubling its value.

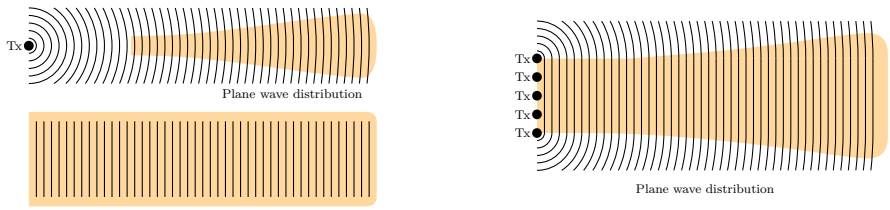

(a) Source placed far from the system

(b) Uniformly spaced sources

Figure 4.30: Generation of plane waves for the imaging system, they can be created by a far-away source (a) or by a uniform current distribution (b)

4.5.2 Collector Antenna: Conformal UWB Antenna for uniform phase generation

As previously introduced when doing tomographic imaging it is usually required to have a plane-wave distribution incident on the scene of interest, this plane-wave can be obtained by placing the transmitter far away from the scene of interest, so that the spherical wave behaves locally as a plane wave. Nevertheless this requires of an extra space that is not always available, but more importantly wastes a lot of energy thus reducing the final SNR of the system. An alternative way is to introduce a set of transmitters uniformly located in a plane, so that they all transmit simultaneously in-phase, see Fig. 4.30. The spherical waves generated by each of the sources add constructively generating a plane wave. For a practical realization the array will have finite dimensions, and the truncation will imply that the resulting wave, will only present a quasi plane wave distribution in the inner region of the array.

By the equivalence theorem an array of uniformly distributed transmitters is equivalent to a uniform aperture field distribution, thus the collector antenna must generate a uniform field distribution at the aperture.

Therefore, the requirements for the collector antennas are two-fold: on the one hand, a uniform field distribution at the edge of the antenna both in magnitude and phase; on the other hand to ensure a similar SNR for the different frequencies of interest, the frequency response must be as uniform as possible.

In order to have a planar configuration, a Vivaldi geometry is chosen as the starting point.A Vivaldi antenna consists of a tapered slot line that opens up to match the free-space wave impedance η to the impedance of the transmission line. The use of a tapered

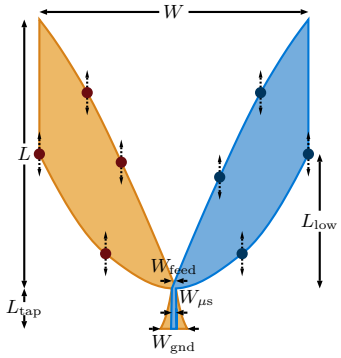

Figure 4.31: Basic geometry of the vivaldi antenna that is optimized for uniform field distribution. The dots represent points of the spline which have free movement in the PSO.

	Value [mm]	Description
W	200	Width of the antenna (*)
L	200	Length of the antenna (*)
$W_{\mu s}$	3.5	Width of the input microstrip (*)
W_{gnd}	31.5	Width of the input microstrip ground plane (*)
W_{feed}	3	Width of the central feeding strip
L_{tap}	30	Length of the feeding taper
L_{low}	100	Length of the lower curve

Table 4.5: Parameters used in the vivaldi geometry. The asterisk marks the parameters that are left to optimize by the algorithm.

profile ensures a large bandwidth of operation, and also by shaping it, it is possible to modify both the frequency response and the field distribution at the edge.

The optimization of the profile of the Vivaldi antenna has been achieved by means of a particle swarm optimization (PSO), where the shape of the antenna is continuously modified. The cost function that is used for ranking the different antennas consist of a weighted combination of the S_{11} response and the overall field distribution:

$$c = \frac{1}{N_f}\sum_f \left(|S_{11}(f)|^2 + \text{std}\angle E_x(f) + \frac{1}{4}(\max|E_x(f)| - \min|E_x(f)|)\right) \tag{4.17}$$

The basic geometry is shown in Fig. 4.31, which consists in an antenna with outer dimensions of 20 cm × 20 cm and a bottom and top symmetrical planes. The profile of the element is formed by a spline that goes through the different points, which present almost free movement under the PSO algorithm. The main parameters of the antenna are in Table 4.5, where an asterisks marks the parameters which are not changed by the PSO algorithm. In order to obtain the electromagnetic response of the antenna, it is solved using the MoM code FIESTA [102], developed at the AntennaLab group.

Fig. 4.32 presents the measurement of the magnitude and phase of the field distribution along the aperture of the antenna for the whole frequency band. It must be noted that for representation purposes a delay has been removed from the phase representation in order to establish the reference plane at the measuring point.

4.5.3 Experimental results

The UWB probe antenna with integrated MEMS switches was fabricated at the clean room facilities of the Univesity of California, Irvine (UCI), and is shown in Fig. 4.33 where the detail of placement of the MEMS switch has been highlighted. Due to low yield of the fabrication process, the MEMS switches in the fabricated samples did not work properly and remained at dummy states, that is either shorted or open circuited, and thus it was impossible to use the MEMS switched version for the MST measurements;

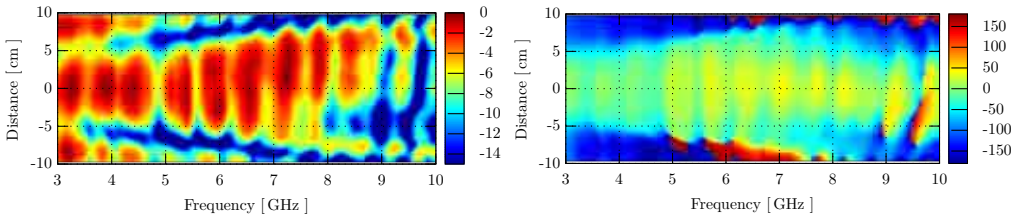

(a) Magnitude [dB] **(b)** Phase [°]

Figure 4.32: Measured field distribution for the collector antenna. The extra delay due to the length of the antenna and the measuring probe has been remove to establish the reference plane at the edge of the aperture.

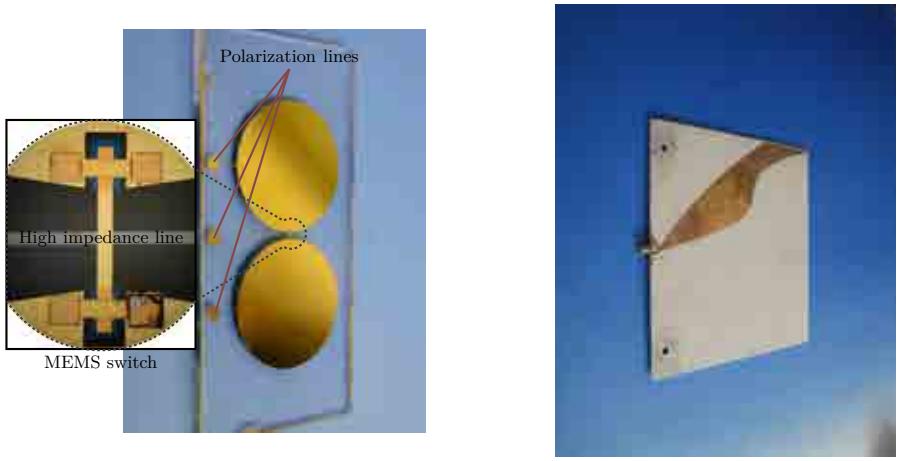

(a) UWB probe **(b)** Collector antenna

Figure 4.33: Fabricated components for the UWB MST imaging experiment. (a) the sensor which is fabricated with a deposition of gold on top of a substrate of quartz, the MEMS switch should go in the central feeding area as presented. (b) one of the profile-optimized Vivaldi antennas

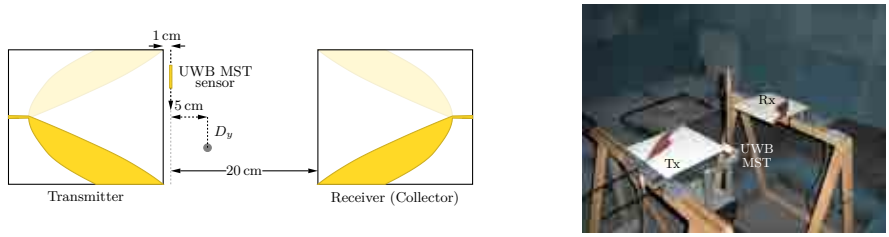

(a) Diagram **(b)** Actual setup

Figure 4.34: Experimental setup used for the UWB imaging measurement. Two of the designed collector antennas are located in front of each other, and a linear stage is used to move the UWB-MST probe in front of the collector antenna. A cylinder is placed in the central region between the collector and transmitter antennas.

instead a dummy version of the probe without any device in the feeding area of the probe was used for the measurement. The two differentiated states were obtained by using silver paint to short circuit the antenna. An alternative option, which was not followed at the time would have been the use of a PIN diode for the switching capabilities, although due to the capacitance it could have introduced different requisites in the design of the sensor, similar to the design carried out at a single frequency in section 3.1.3, where a PIN diode is used in the design of an MST probe.

The measurement setup configuration used for the measurements is shown in Fig. 4.34. The two Vivaldi antennas, acting as the transmitter (plane wave generation) and the collector antenna are placed in front of each other with a separation of 20 cm. The UWB MST sensor is placed in front of the collector at a distance of 1 cm. To simulate an array of sensors, a single sensor is mounted on top of a linear stage moving it along the edge of the collector, thus creating a virtual array. The obstacle to be imaged consists of a metallic vertical bar with a diameter of 1.5 cm, located at 5 cm from the sensor array which is displaced along the direction of the edge a distance of D_Y depending of the scenarios. The measurements are taken with a calibrated network analyzer working from 3 GHz to 10 GHz, for each position of the linear array, as it moves the sensor along the edge of the collector, taking a total of 7 samples (with a separation of $\Delta y = 34$ mm).

Two different positions for the cylinder have been studied: the first one has the cylinder centered, $D_\mathrm{Y} = 0$, and the second with the cylinder displaced to $D_\mathrm{Y} \approx 5$ cm. Fig. 4.35 presents the reconstructed image obtained for both scenarios, compared with the expected reconstruction obtained by simulation of the same scenario. It must be noted that in the simulation, the effect of the sensor and the collector are not taken into account (nor any frequency dependence), and only the effect of the object under test is simulated: the incident field is not an ideal plane wave but the field generated by an uniform line of current placed at the edge of the transmitting antenna, thus simulating the optimization goal for the collector antenna. Similarly, the field scattered by the cylinder is evaluated at the sensors' position, but without any receiving antenna. From the comparison of the different results, it can be concluded that the UWB imaging system is capable of properly discriminating the location of the object being imaged, since it is sensitive to the change of location of the cylinder; also the resolution of the system is the expected, although the simulation behaves slightly better that the measurement. The benefit of

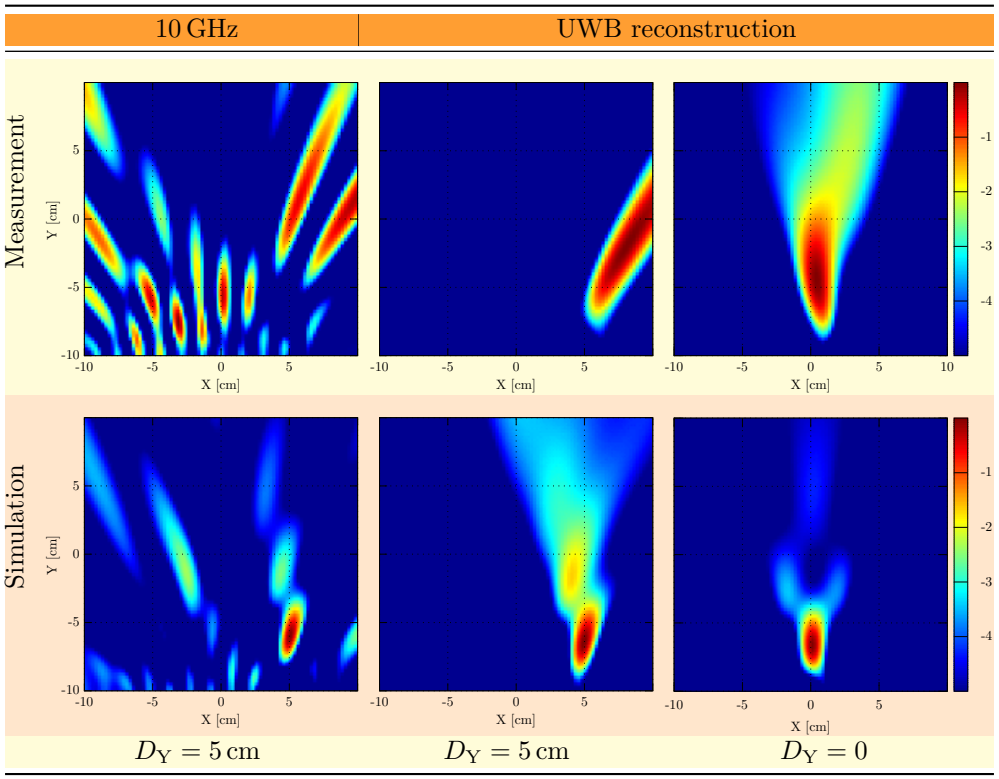

Figure 4.35: UWB images for the different scenarios under study. Top row presents the results for the simulation of the scenarios, where the bottom row shows the images obtained from the current measurements using the MST probe.

using an UWB frequency range is clearly manifested in the results: the dimensions of the sensor probe do not allow to perform a proper sampling for the whole frequency band, for instance at 10 GHz, the sampling is approximately 1.13λ, much larger than Nyquist limit of 0.5λ. Due to this sub-sampling, alias is expected to appear in the reconstructions of such frequencies, as observed on the right column of Fig. 4.35. However, as previously mentioned, UWB imaging is capable of dealing with the sub-sampling, since the alias position is frequency dependent, at the expense of a reduced resolution image for the overall reconstruction, but still better than what would be possible to obtain at a single frequency.

4.6 Concluding remarks

This chapter has presented experimental results showing the capabilities of RFID-MST sensors to measure a EM-field distribution. The chapter has analyzed the error in the measurement that occurs when different RFID sensors are distributed to conform an array. It has been shown that error does not only depend on the coupling between the different antennas, but also in the value of the load that is attached to the rest of the elements of the array that are not switching. As such it is reasonable to compute the coupling error term to evaluate the performance of the array at the design stage using the characterization of Z_{scav} as the load of the elements of the array.

It has also been shown that the non-linearities in the RFID IC that were previously characterized in the previous chapter, become a problem when trying to measure a field distribution, since they disturb the response in such a way that $\Delta\rho_{\text{rdr}}$ is not directly proportional to E_{inc}^2 as desired, but in fact it has been affected by the power dependence of $\Delta\tilde{\rho}_{\text{L}}$. Moreover, the scavenging and the activation threshold of the tag limit the dynamic range of the measurement.

Two alternatives have been implemented as a solution: the first one consists in the characterization of the non-linear response of each tag in order to use this calibration curve to remove the non-linear effect from the measurements. This procedure allows to obtain the field distribution but it still presents the limitation of the dynamic range. The second solution that has been implemented consists in a modification of the measuring scheme in order to introduce an additional signal so that two tones with different power are used in the measurement. Using this scheme, the tone with highest power activates the RFID sensor and establishes the value of $\Delta\tilde{\rho}_{\text{L}}$ for the second tone, which remains constant as long as this second tone has a sufficiently low power. This guarantees that the field distribution can be measured with this tone without introducing non-linear effects, and without the limitations in the dynamic range imposed by the scavenging when the same tone measures and activates the tag.

Moreover, this chapter has also explored the capabilities of MST sensors to operate in a wide frequency range, showing how the use of a multi-frequency scheme can relax the requirements for tomographic imaging and the quality of the reconstructed images.

5

Chapter 5
Robust RFID-MST environmental sensing: multi-load MST sensor

After introducing the capabilities of MST-RFID sensors to accurately measure a field distribution presented in the previous chapter, this chapter focuses on its use to retrieve information of the environment where the sensor has been placed, and more specifically on the challenges that are involved and which solutions are available.
In this chapter the behavior of a generic MST probe will be tested in scenarios where the close environment does not necessarily remain constant or it cannot be assumed constant as was the case in the previous chapter; in such a way that the different terms in the formulation that governs the communication between reader and probes are mixed. This represents a more realistic environment for an embedded sensor, since it is not always possible to guarantee that it will remain isolated unless it is during a very controlled experiment. In order to overcome this limitation for environmental sensing using the Electromagnetic signature of the MST probe, a modification of the modulation scattering is proposed to enhance its capabilities and to be able to experimentally measure a physical parameter such as the temperature of the environment.

5.1 Introduction

The use of MST for environmental sensing applications is quite recent, although it is being investigated by several groups [14,15,103]. It usually relies in the study of the variation of the signal backscattered by the sensor, and how this signal can be related to a known, or assumed propagation model. Afterwards the variations of the signal are correlated with the variation of a physical parameter ψ, such as humidity, temperature, level of corrosion, etc. This type of sensing will be analyzed in the first part of the chapter, which will focus in the *conventional* MST sensing.

When the scenario is less canonical, and cannot be fully modeled beforehand, this conventional sensing is usually not sufficiently accurate, since the backscattered signal might be the same for two different conditions of ψ (due to the additional variations of the scenario). Many of the previous research groups that have been working on sensing MST have been focusing lately in devising ways to overcome this limitation, with the study of multi-port MST sensors to obtain a richer data-set that can be used to either detect that the response of the conventional MST is being perturbed in an unexpected way by the scenario, or by combining the information of each port to obtain a better general understanding.

In this chapter an alternative approach for MST sensors is proposed consisting in the development of an enhanced MST sensor that presents a set of multiples loads that are switched to obtain a higher number of backscattering states. The formulation for this multi-load sensor is detailed in the chapter, as well as the criteria that can be used to optimize its behavior in a given scenario, and it is experimentally validated in three different tests.

Additionally in the final part of the chapter an experimental validation of the operation of the sensor in a fully embedded and remote mode (albeit battery powered) is presented, as an example of the wireless capabilities of the multi-load sensor.[1]

5.2 Conventional MST-based environmental sensing

Sensing the local environment with an MST probe relies on the variation of $\Delta\rho_{\text{rdr}}$ with the physical parameter ψ that is being measured. Recalling (2.21) from chapter 2,

$$\Delta\rho_{\text{rdr}} = Z_{tr}\frac{Z_{\text{L}_B} - Z_{\text{L}_A}}{\left(Z_{\text{ant}} + Z_{\text{L}_A}\right)\left(Z_{\text{ant}} + Z_{\text{L}_B}\right)} \tag{5.1}$$

it can be observed that $\Delta\rho_{\text{rdr}}$ may change due to variation in each of its components, which may have a very different origin and thus sensing capability. Specifically Z_{ant} depends on the electromagnetic conditions in the neighborhood of the probe (permittivity, permeability, conductivity), as well as in variations of the antenna structure caused by the environment (stretching, compression, bending, dilation, etc.); the loads $Z_{\text{L}_{A,B}}$ can be affected by the local conditions in the neighborhood (temperature, humidity, etc.) and Z_{tr} depends on the variation in the propagating medium (including but not limited to distance, polarization mismatch, permittivity, etc.) as well as changes in the antenna parameters (effective length, gain, etc.).

[1] The following sections contains portions, sometimes verbatim, of the publications [JA8, JA2] of the author.

Although the dependence of Z_{tr} and $Z_{\mathrm{L}_{A,B}}$ with the environment is very scenario specific, the variations that the environment electromagnetic parameters have on Z_{ant} can be known beforehand.

5.2.1 Z_{ant} dependence with the medium

It is well known [104] that the medium in which an antenna is located modifies its input impedance according to:

$$Z_{\mathrm{ant}}\left(f, \epsilon_r^{\mathrm{II}}\right) = \sqrt{\frac{\epsilon_r^{\mathrm{I}}}{\epsilon_r^{\mathrm{II}}}} Z_{\mathrm{ant}}\left(\sqrt{\frac{\epsilon_r^{\mathrm{II}}}{\epsilon_r^{\mathrm{I}}}} f, \epsilon_r^{\mathrm{I}}\right) \tag{5.2}$$

where f is the frequency of operation, and ϵ_r represents the relative permittivity of the environment in which the antenna is embedded. The super-indices I and II identify two different conditions of the scenarios where ψ has changed (for instance the temperature has changed). As such (5.2) states that when the external medium changes from state I with permittivity ϵ_r^{I} to state II with a larger (smaller) permittivity ϵ_r^{II}, the input impedance will be simultaneously compressed (expanded) in frequency and value.

Equation (5.2) is in principle valid only for an homogeneous external medium. However, even in inhomogeneous media, the input impedance of the antenna is strongly dependent on the nearby region around the antenna (a radiansphere [105]), where the near fields are contained. Consequently, equation (5.2) can still be used if the permittivity in the reactive field region is constant; in other cases, an effective permittivity of this region can be used, but the relationship will not hold completely, since resonances could arise in the external inhomogeneous medium.

In spite of this, assuming homogeneity in the near region of the antenna, we observe that Z_{ant} is indeed sensitive to variations of permittivity in this close region. This is in fact commonly used in material characterization with the use of a slot ring antenna (open coaxial cable) [106] to determine the permittivity of an attached material through the changes in the input impedance/reactance of the coaxial, and has also been presented for the measurement of the variation in the permittivity of the host medium of embedded probes [JA8, 107, 108].

As an example, if we consider a host whose permittivity changes with temperature (such as water), it is possible to relate the compression (expansion) of Z_{ant} with the variation of temperature of the host medium; in the case of water, and given the variation of ϵ_r with temperature [109], the compression of the impedance of Z_{ant} corresponds to a shift of around 7% of the resonant frequency when the temperature changes from 25 °C to 65 °C.

As previously stated, an alternative mechanism through which Z_{ant} might change is the physical modification of the antenna, either its structure [39] or the electrical properties of the conducting or dielectric materials [38], however these changes cannot be directly predicted in a single equation as done for the changes in the permittivity of the environment, because they strongly depend on the antenna shape as well as the nature of the structural modification, much like the variations of Z_{L} or Z_{tr}.

5.2.2 Current usage of conventional MST for sensing applications

Although the use of $\Delta\rho_{\text{rdr}}$ for sensing applications (other than EM-field mapping) has not been extensive, there has been a growing interest recently, with different groups using them in several ways for sensing applications. The different approaches that have been used can be classified mainly in two groups:

Discrete sensing. This kind of sensing does not provide a detailed sensing, but operates in a binary mode, in such a way that it is possible to detect that a sensing condition (or threshold) has been achieved according to the existence of response of the MST probe. In many occasions this relies on RFID probes, by ensuring that the harvested power changes greatly with variations of ψ. [42, 45, 110].

Calibration curve. This method is based on the construction/measurement of the response of the MST probe in a controlled scenario where the conditions of sensing are reproduced in order to obtain a profile of the backscattered response versus ψ, so that it can be inverted afterwards. [39, 42].

Within the development of this thesis, several sensing experiments have been carried out using conventional MST, which fall under the previous categories. The following section presents two of them, which help to detect some of the limitations of conventional MST sensing.

5.2.2.1 Water level detection: discrete sensing

The first experiment that was used was based on the simplest sensing approach using RFID, that is, making use of the limited available power to sense the condition in the probe location. To do so, the parameter ψ to detect was the presence of water in the neighborhood of the RFID. As previously introduced, the presence of water in the neighborhood of an antenna will change its input impedance; when the antenna is matched to a given load, this change in Z_{ant} introduces additional mismatching losses, which in the case of an RFID tag reduce the incident power below P_{th}. When this happens the RFID tag becomes unresponsive thus indicating the presence of water.

Six RFID tags were placed on a container of 8 L which was filled with water (see Fig. 5.1). The reader consisted of a ridged horn antenna at a distance of approximately 40 cm connected to a vector signal generator and a spectrum analyzer through a directional coupler, to create the RFID interrogating signal and measure the response from the tags respectively. Fig. 5.2 presents the measured backscattered power from each tag while the water tank is progressively emptied. For each tag, there is an instant, when the water is near the height of the specific tag, when this tag start answering. This marks the threshold point indicating the presence of water. Thus it is possible to determine the current level of water by noticing the sequence of RFID tags that answer. However, it is important to notice that the response of the RFID tags after activation is not constant, but rather the backscattered power changes as the level of water continues to descend. This is explained because Z_{ant} continuously change when there are changes in the nearby region of the tag, as such, although here 6 tags have been used to determine the level, by properly detecting the variation on the backscattered power, it would be possible to get information on the level of water with just one single tag after activation has been achieved. Alternatively when using several tags, the combined use of the variation of their

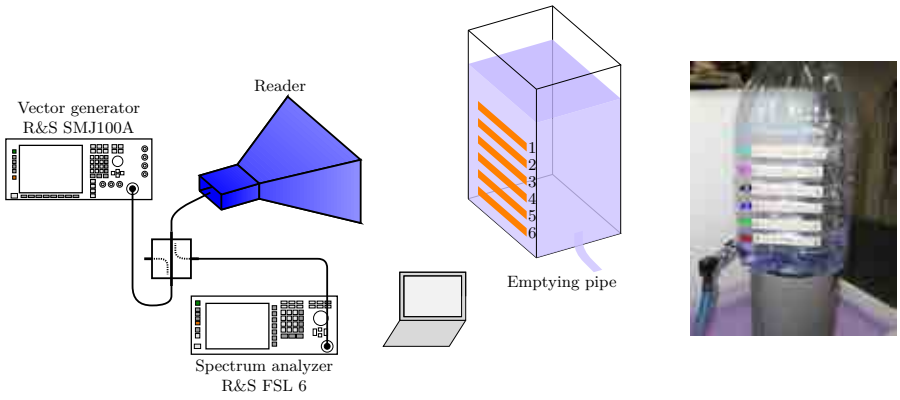

(a) Block diagram **(b)** Measurement

Figure 5.1: Experimental setup for the detection of water level using RFID tags. A vector signal generator and spectrum analyzer generate the RFID signal and capture the response of the tags that have been located on the front side of a water container.

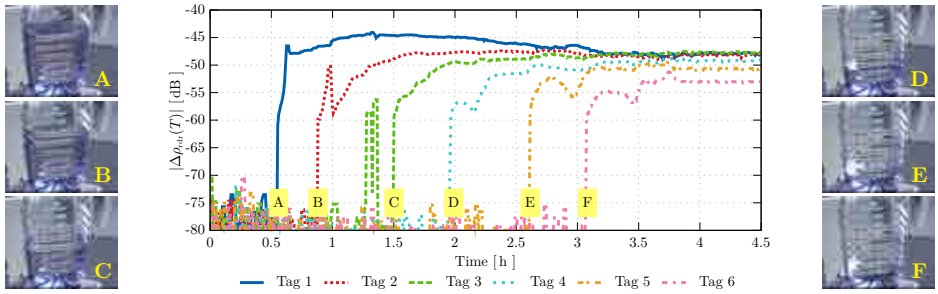

Figure 5.2: Measured backscattered power as the level of water decreases. Each of the tags is sequentially activated as the level of water reaches the height of the tag. It can also be noticed once the tag starts answering, the response of the RFID tag does not remain constant, but is still affected by the level of water.

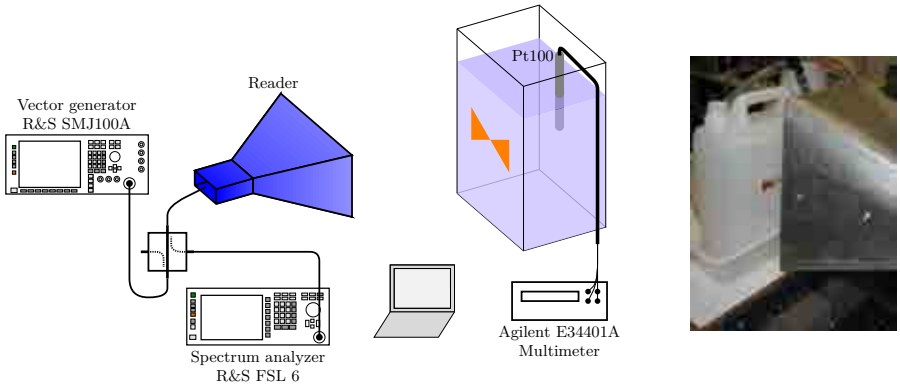

(a) Block diagram **(b)** Measurement

Figure 5.3: Experimental setup for the monitoring of the backscattered response of an RFID tag as water cools down. A vector signal generator and spectrum analyzer generate the RFID signal and capture the response of an RFID tag located on the front side of a water container. The container is heated up to 80 °C and the response is captured as the water cools down. A Pt100 sensor probe is used to capture the actual temperature of the water.

backscattered responses can provide with a much finer detail in the level of water, using a calibration curve as in the following section.

5.2.2.2 Water temperature sensing: Continuous variation

In the previous experiment ψ was the presence or level of water and was measured using a discrete array of RFID tags. However it was observed that the study of the variation of $\Delta\rho_{\text{rdr}}$ after activation could provide finer information on the level of water, by properly capturing the profile of the backscattered response with the level of water. This is what will be done in this experiment, although instead of the level of water, the parameter ψ to sense is the variation of the temperature of water. This allows to have a more controlled scenario which remains static with only the permittivity of water changing. The experimental setup is shown in Fig. 5.3, and as in the previous experiments uses a ridged horn antenna, a signal vector generator and spectrum analyzer as the reader. The RFID tag was placed on the external side of a water container which was placed in front of the horn antenna. The RFID tag used in this experiment was the RFID tag designed in 3.1.2 which was experimentally tuned using silver paint to shorten the stubs, so that it responded properly when attached to the water container. The temperature of the water was measured at the same time using a temperature sensor Pt100 [111] and a digital multimeter.

The water in the container was heated up to 70 °C and the tag was continuously interrogated as the water in the container was cooled down. Fig. 5.4 presents the measured $\Delta\rho_{\text{rdr}}$ against the temperature of water. Here it must be pointed out that since $\Delta\rho_{\text{rdr}}$ is the differential reflection coefficient it has filtered out the reflection at the interface of the container, which also changes with the temperature of water.From Fig. 5.4a it shows that the magnitude is not sufficient to determine the temperature of the water, but the

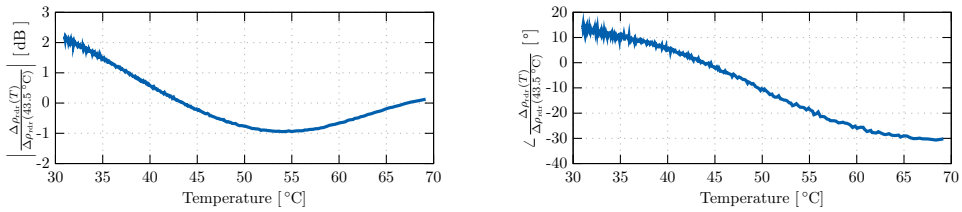

(a) Magnitude **(b)** Phase

Figure 5.4: (a) Magnitude and (b) phase of the backscattered signal by the RFID tag as water cools down. The magnitude presents a non-monotonic behavior, which introduces an uncertainty in the determination of the temperature of water unless the information contained in the phase is incorporated.

complete complex response is required if we want to use this curve as a calibration curve.

Since the phase is much more sensitive to the relative position between reader and tag, it will be important that the calibration curve is taken at the measurement position when using this kind of sensing, or some approach be used to control the change in the phase due to the measurement conditions (for instance the distance), rather than the variation of ψ.

5.2.3 Limitations inherent to conventional MST for robust sensing.

The preceding sections have shown experimental examples of exploiting MST for sensing applications, relying either on $\Delta\rho_{\text{rdr}}$ or the activation power (the the MST probe must forcibly be an RFID) to determine the current conditions of ψ. However, the variation of either one of them cannot be guaranteed to be linked to a variation of ψ unless some assumptions are made on the scenario.

Let's take for instance a discrete scenario, where the power required to activate the RFID probe determine the current conditions, such as the presence of water. There are two conditions that will change the power reaching the RFID IC. On the one hand, the channel between the reader and the probe might be blocked/unblocked by external scatterers, or the relative orientation between sensor and reader might change, thus changing the incident power on the tag. This will directly reduce/increase the available power at the tag (through Z_{tr}), and as such the delivered power (even if water is not present), thus it may create a false positive. On the other hand, the variation of ψ nearby the probe's antenna modifies Z_{ant}, as previously shown, and accordingly the load factor (LF) with the RFID IC is modified which finally changes the delivered power to the RFID IC. Therefore when a single tag is used for digital sensing, there is an ambiguity to whether the change occurred due to ψ or by an external agent.

This can be partially solved by using diversity in the sensing, using two tags tuned to a different condition of ψ, as done in [43], so that one or the other is activated depending on ψ, in such a way that if none answers, it means that there is some unexpected change in the propagation channel. However, in spite of this, discrete sensing as introduced here requires that the probe is placed in a very controlled scenario, since unexpected changes

in Z_{ant} produced by a nearby scatterer cannot be directly detected, and could lead to false positives.

In the case of continuous sensing with the use of a calibration curve, there is a similar problematic. The use of MST removes the uncertainty which arises from undesired scattering of the scenario, thus obtaining the response of the probe, but as in the discrete sensing, there is the ambiguity to which, Z_{tr} or Z_{ant}, is the cause of this variation. In [112] an interesting approach is presented to remove the effect of Z_{tr} from $\Delta\rho_{\text{rdr}}$ for RFID tags, making use of the power activation threshold P_{th}. Since according to (2.28) and (2.30) when the tag is activated the delivered power P_{Lscav} is equal to P_{th}, thus:

$$P_{\text{Lscav}} = P_a \cdot \frac{|Z_{tr}|}{2R_{\text{ant}}} \cdot LF = P_{\text{th}} \tag{5.3}$$

and in this conditions, the backscattered power is:

$$\Delta P_{\text{bs}} = P_a \cdot |\Delta\rho_{\text{rdr}}|^2 = P_a \cdot \frac{|Z_{tr}|^2}{4R_{\text{ant}}^2} \cdot ME = P_a \cdot \left(\frac{P_{\text{th}}}{P_a \cdot LF}\right)^2 \cdot ME = \frac{P_{\text{th}}^2 \cdot ME}{P_a \cdot LF^2} \tag{5.4}$$

Since P_{th} is known (datasheet or measurement), in [112] an adimensional parameter F_n is defined as the ratio of the previous quantities:

$$F_n = \frac{P_{\text{th}}}{\sqrt{\Delta P_{\text{bs}} \cdot P_a}} = \frac{P_{\text{th}}}{P_a|\Delta\rho_{\text{rdr}}|} = \frac{LF}{\sqrt{ME}} = \frac{2R_{\text{scav}}}{|Z_{\text{scav}} - Z_{\text{SC}}|} \cdot \left|\frac{Z_{\text{SC}} + Z_{\text{ant}}}{Z_{\text{scav}} + Z_{\text{ant}}}\right| \tag{5.5}$$

This normalized F_n can therefore be used for sensing purposes since it removes the dependence of the measured quantity with the propagating channel Z_{tr} (for instance the attenuation due to distance), and the strong dependence with the relative orientation and position.

However, in order to ensure the viability of F_n as a sensing parameter for a given application, we must ensure that it will be a bijective function with respect to ψ. For instance, the parameter as defined in [112] only considers the normalization of $|\Delta\rho_{\text{rdr}}|$ without considering the phase, and in the experiment shown in the previous section, $|\Delta\rho_{\text{rdr}}|$ presented the same value for different temperatures (for instance between 43 °C and 70 °C), as such it would not be a suitable parameter. In fact even if the phase of $\Delta\rho_{\text{rdr}}$ in (5.5) is preserved, there is still the ambiguity of the phase of the numerator, since the only knowledge is that the power arriving is P_{th} but not the phase, so only the magnitude of Z_{tr} is removed and not its phase.

In spite of this, this parameter provides a good tool when the only expected variation in Z_{ant} will be due to ψ (that is the antenna is sufficiently isolated so that extraneous scatterers cannot be around it) during the operating life of the sensor, and it is also very easy to implement since it only requires the knowledge of P_{th} for the RFID IC that is being used, which can be easily measured as presented in 3.3.1. For scenarios where this condition cannot be ensured, a more detailed knowledge of Z_{ant} (real and imaginary parts) is required to ensure that its variation is within the expected variation with ψ, and as such being able to recognize a false positive in ψ due to the presence of an undesired object near the antenna.

5.3 Multi-load MST based sensing

The preceding section has presented some of the strategies that are followed to use (5.1) for sensing application, and it is clear that the problem is that Z_{tr}, Z_{ant} and Z_{L} are mixed together in a single equation. Although sometimes a priori information [JA8] can be used to estimate the behavior of some of them in order to isolate the rest, this is not always possible. In these cases to isolate Z_{ant} or Z_{tr} it is required to enrich the available information.

Some research groups have decided to enhance the MST probes by creating multi-port MST probes, where a conventional MST load, such as a PIN diode [16] or an RFID IC [41, 110] is connected to each port. Using this strategy, the amount of available information at the reader is larger, since the variability of scattering states of the MST probe is larger. However, as can be seen from the equation governing multi-port MST arrays in appendix A.5 the number of unknowns in a multi-port MST probe is increased, since it has a Z_{tr} for each port, as well as the mutual coupling between each pair of ports (which will also change along with Z_{ant}). As such, the number of available equations is still lower that the unknowns, and as with the conventional MST probe, it could lead to an erroneous estimation of ψ.

This section presents an alternative approach developed during the course of this thesis, which instead of using a multi-port antenna, relies in a single port MST probe antenna, which uses several known loads at the antenna port. This creates a larger diversity in the backscattered response that allows to increase the available information and thus isolate the different propagation conditions, as detailed next.

5.3.1 Multi-load MST formulation

From equations (2.3) and (2.19) it can be seen that before obtaining $\Delta\rho_{\text{rdr}}$ there are 3 different unknown terms in ρ_{rdr} (or equivalently the power wave b), namely the undesired term ρ_{und} which groups the background reflections, the structural scattering of the probe antenna and the self-reflection of the reader antenna; the transfer impedance Z_{tr} and the antenna probe's impedance Z_{ant}, and they are linked along with Z_{L} as:

$$\rho_{\text{rdr}} = \rho_{\text{und}} + \frac{Z_{tr}}{Z_{\text{ant}} + Z_{\text{L}}} \tag{5.6}$$

In order to isolate Z_{tr} and Z_{ant} from (5.6), at least three different equations are required to solve the system. These equations can be obtained using three different loads ($Z_{\text{L}_{A,B,C}}$) [113–115]. After re-arranging and grouping in terms of unknowns, (5.6) becomes,

$$\rho^i_{\text{rdr}} Z_{\text{L}_i} = Z_{tr} + \rho_{\text{und}} Z_{\text{ant}} + \rho_{\text{und}} Z_{\text{L}_i} - Z_{\text{ant}} \rho^i_{\text{rdr}} = \begin{bmatrix} 1 & Z_{\text{L}_i} & -\rho^i_{\text{rdr}} \end{bmatrix} \begin{bmatrix} Z_{tr} + \rho_{\text{und}} Z_{\text{ant}} \\ \rho_{\text{und}} \\ Z_{\text{ant}} \end{bmatrix} \tag{5.7}$$

and finally in matrix form:

$$\underbrace{\begin{bmatrix} 1 & Z_{\text{L}_A} & -\rho^A_{\text{rdr}} \\ 1 & Z_{\text{L}_B} & -\rho^B_{\text{rdr}} \\ 1 & Z_{\text{L}_C} & -\rho^C_{\text{rdr}} \end{bmatrix}}_{\mathbf{N}} \begin{bmatrix} Z_{tr} + \rho_{\text{und}} Z_{\text{ant}} \\ \\ \rho_{\text{und}} \\ Z_{\text{ant}} \end{bmatrix} = \begin{bmatrix} \rho^A_{\text{rdr}} Z_{\text{L}_A} \\ \rho^B_{\text{rdr}} Z_{\text{L}_B} \\ \rho^C_{\text{rdr}} Z_{\text{L}_C} \end{bmatrix} \tag{5.8}$$

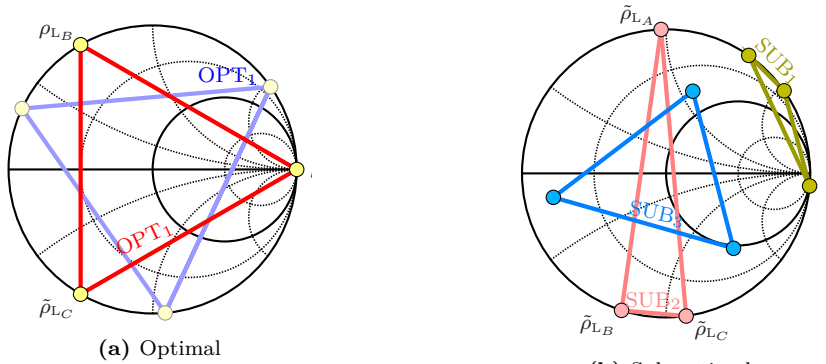

(a) Optimal

(b) Sub-optimal

Figure 5.5: Representation of the loads in a Smith chart normalized to R_{ant}. The optimal loads Z_{L_i} are such that when representing $Z_i = Z_{\text{L}_i} + jX_{\text{ant}}$ they have the same distance between each other, as in (a). When the distance between the loads is not the same, as in (b), the quality of the estimation will deteriorate.

which by inversion of $\mathbf{N}$ leads to the simultaneous retrieval of Z_{ant}, Z_{tr}, and ρ_{und}.

The accuracy of the estimation directly depends, as usual, on the noise of the measurement, however since ρ_{rdr} is in both sides of the equation, the uncertainty of the measured ρ_{rdr} will be amplified by matrix $\mathbf{N}$. Appendix D develops the expression for the uncertainty of the estimated Z_{ant}, which finally becomes:

$$\sigma^2_{Z_{\text{ant}}} = \sigma^2_N \frac{16R^4_{\text{ant}}}{|Z_{tr}|^2} \cdot \frac{|\Delta\tilde{\rho}_{\text{L}_{B,C}}|^2 + |\Delta\tilde{\rho}_{\text{L}_{B,A}}|^2 + |\Delta\tilde{\rho}_{\text{L}_{A,B}}|^2}{\left|\Delta\tilde{\rho}_{\text{L}_{A,B}}\Delta\tilde{\rho}_{\text{L}_{B,A}}\Delta\tilde{\rho}_{\text{L}_{B,C}}\right|^2} \tag{5.9}$$

As expected the expression shows that the accuracy in the estimation of Z_{ant} directly depends on the noise of the measurement (σ^2_N) and the propagation losses between reader and MST sensor (through Z^{-1}_{tr}). The most interesting part is the last term, which is the one that can be controlled at the design stage of the sensor, and it shows that a proper selection of the loads Z_{L} can improve (or worsen) the accuracy. As shown in the appendix, the condition that minimizes $\sigma_{Z_{\text{ant}}}$ is to ensure that $|\Delta\tilde{\rho}_{\text{L}_{i,j}}| = \sqrt{3}$, which leads to an inaccuracy of:

$$\sigma^2_{Z_{\text{ant}}} = \sigma^2_N \frac{16R^4_{\text{ant}}}{3|Z_{tr}|^2}. \tag{5.10}$$

Therefore the design criteria for the MST probe antenna and the loads used is that when the loads are represented in a Smith chart normalized with Z_{ant} (as presented in chapter 2 for complex Z_{ant}), their mutual distance is maximized Fig. 5.5, presents sets of configurations for the loads $Z_{\text{L}_{A,B,C}}$, in Fig. 5.5a the loads have a mutual distance of $\sqrt{3}$ and as such become optimum loads in terms of accuracy, while the configurations in Fig. 5.5b have a varying accuracy. Table 5.1 presents the value of the accuracy for each of the different load combinations presented in Fig. 5.5. It can be noted how the combination SUB$_3$ in spite of consisting of lossy loads it is better than the others sub-optimal configurations because the distance between the loads is more balanced. To obtain Z_{L_i} from $\tilde{\rho}_{\text{L}_i}$ a two step de-normalization must be done: first the value Z_i is obtained

Configuration	$\tilde{\rho}_{L_A}$	$\tilde{\rho}_{L_B}$	$\tilde{\rho}_{L_C}$	$\overline{\sigma_{\mathbf{Z}_{ant}}}$
OPT_1	$1\angle 0\,°$	$1\angle 120\,°$	$1\angle -120\,°$	0.58
OPT_2	$1\angle 35\,°$	$1\angle 155\,°$	$1\angle -85\,°$	0.58
SUB_1	$1\angle 35\,°$	$1\angle 55\,°$	$1\angle -5\,°$	5.3
SUB_2	$1\angle 92\,°$	$1\angle -108\,°$	$1\angle -82\,°$	1.6
SUB_3	$0.8\angle -168\,°$	$0.7\angle -48\,°$	$0.6\angle 72\,°$	1.2

Table 5.1: Estimated performance for the configurations of Fig. 5.5. As it can be observed, although configuration SUB_3 corresponds to resistive loads, since it is well distributed, the normalized accuracy is much better than the other sub-optimal configurations.

using $Z_o = R_{ant}$; the second step is incorporating the reactive part of the antenna to obtain Z_{L_i} as $Z_{L_i} = Z_i - jX_{ant}$.

This de-normalization implies that for some Z_{ant}, loads that seem quite apart in the Smith chart might be much closer (due to the subtraction of X_{ant}), so even if a set of loads behaves better in terms of uncertainty, if they are too close once de-normalized, they might not be adequate, since they could become too sensitive to variations in Z_{ant}.

5.3.2 Multi-load MST circuit prototype

The preceding section has shown the formulation that governs sensing via a multi-load configuration of the MST probe, as well as the criteria that should be used to enhance the accuracy of the sensor, by properly choosing the loads used in the sensor. This section presents the circuitry capable of presenting this multiple loads states so that it can be used in experimental validations of the multi-load MST sensor concept.

To be able to switch between at least 3 different loads, it is required to have a switch which sequentially interconnects one of the loads with the probe antenna. A single pole four throw (SP4T) from Hittite (HMC241QS16) has been selected as the switch for the prototype circuitry due to its low insertion losses and the adequate control interface, which can be easily connected to a PIC microcontroller. Fig. 5.6 presents a block diagram and a picture of the fabricated circuit. It consists of the SP4T switch with a CPW line from the common port to an SMA connector. The SP4T has 4 different switchable ports, which allows to connect up to 4 different loads. For this specific prototype, optimization of the sensor is not the primary goal in front of demonstration of the capabilities, as such the selected loads are not optimized for a specific Z_{ant}. The loads attached to the ports are:

- Z_{L_A} corresponds to an inductor $L = 10\,\text{nH}$ (Q=15 at 100 MHz and SRF=5.3 GHz)
- Z_{L_B} is a resistive load of $51\,\Omega$
- Z_{L_C} corresponds to an inductor $L = 2.2\,\text{nH}$ (Q=10 at 100 MHz and SRF=6 GHz)
- Z_{L_D} is a short circuit

The control of the SP4T is made on-board by a PIC micro-controller (PIC18F2550), which can also communicate with the computer through the universal serial bus (USB) port. In the PIC, two modes of operation have been implemented: the first one is the *slave-mode*, where the PIC just acts as a relay, requiring a computer connected to the

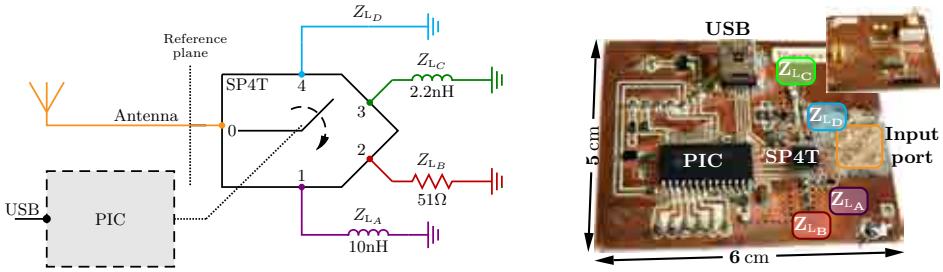

(a) Block diagram **(b)** Fabricated circuit

Figure 5.6: The multi-load circuit (a) and (b) consists of two differentiated sections: the RF section, composed by an SP4T switch connected to an SMA port at the common pin, and 4 different loads at the switchable pins; the control section is basically composed of a PIC micro-controller which can operate autonomously or remotely controlled by a computer using the built-in USB port.

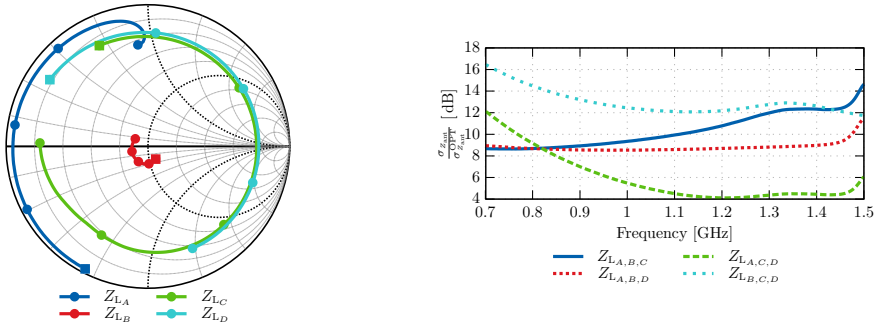

(a) Reflection coefficient ($Z_o = 50\,\Omega$) **(b)** Uncertainty factor for $Z_{\text{ant}} = 50\,\Omega$

Figure 5.7: (a) Characterization from 700 MHz to 1.5 GHz of the loads of the circuit shown in Fig. 5.6 measured at the SMA port. The square marks the lowest frequency (700 MHz) of the characterization range. (b) Uncertainty that the different choices can achieve for an antenna of impedance $Z_{\text{ant}} = 50\,\Omega$.

USB port to trigger the switching of the loads at every instant; the second mode, *master-mode*, is completely autonomous and switches the loads back and forth according to a pre-programmed code or pattern, in such a way that each load can be identified. This mode allows a complete remote measurement when direct access to the MST probe is not possible. More details on the code programmed in this mode will be presented in section 5.5 when the autonomous-mode is presented. Until then the slave-mode will be used.

Fig. 5.7a shows the characterization of the different states presented by the circuit for a frequency range from 700 MHz to 1.5 GHz. The characterization presents the loads in a 50 Ω Smith chart representation. Additionally Fig. 5.7b shows the normalized accuracy $\sigma_{Z_{\text{ant}}}$ depending on which subset of the loads is chosen. And it can be seen that the sets formed by $Z_{L_{A,B,D}}$ and $Z_{L_{A,C,D}}$ present the best behavior in terms of accuracy (when $Z_{\text{ant}} = 50\,\Omega$). From these, the set A, C, D has been selected as the primary set of loads for the following experiments, because the behavior of $Z_{L_{A,B,D}}$ shows an almost constant

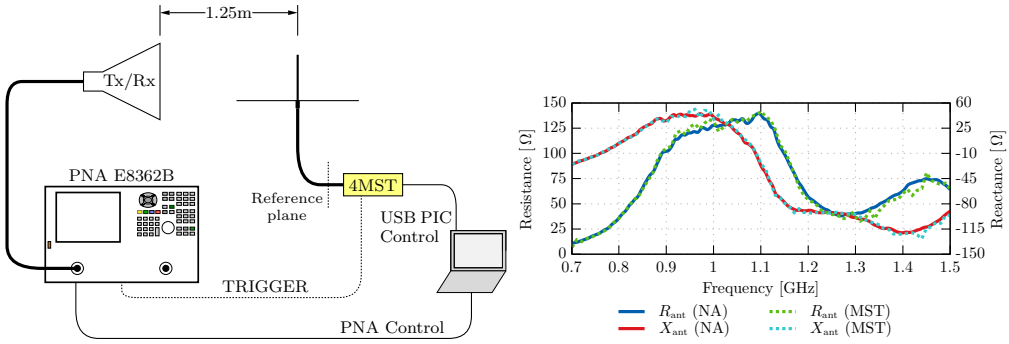

(a) Experimental setup

(b) Input impedance (Z_{ant})

Figure 5.8: The 4 loads MST circuit is connected to a 800 MHz quarter wavelength monopole and it is remotely measured switching between 3 different states. As observed the retrieved input impedance $(\hat{R}, \hat{X})$ presents excellent agreement with the direct measurement in the VNA (R, X).

behavior over the whole frequency range.

A first test is carried out to retrieve the input impedance of an 800 MHz quarter wavelength monopole using the multi-load MST circuit. Fig. 5.8a presents the experimental setup that has been used for the measurement, which consists of the VNA to measure the reflection coefficient ρ_{rdr} of a ridged horn antenna acting as the reader antenna. The reader antenna is located at a distance of approximately 1 m from the monopole antenna. A PC simultaneously controls the VNA and the multi-load MST circuit. Fig. 5.8b presents the measured input impedance of the monopole directly with the VNA compared to the estimated impedance obtained using (5.8), showing a good agreement between them.

This agreement shows that it is possible to use this technique to successfully retrieve Z_{ant} and as such it can be used for sensing applications that measure variations in Z_{ant}.

5.3.3 Sensing through Z_{ant}

As shown in the previous section, the multi-load MST circuit is capable of successfully retrieving the probe's antenna impedance Z_{ant}. The knowledge of Z_{ant} can be used to estimate variations on the electromagnetic conditions of the environment, through a permittivity dependence with ψ, and can also be used to detect changes in the antenna structure, produced for instance due to modification of the antenna structure, or by the presence of nearby scatterers which affect the current distribution in the antenna structure. This section will focus on the former, while the latter will be explored in the following sections.

The scenario that will be used to explore the sensing capabilities through Z_{ant} consists of an antenna surrounded by water, and the physical parameter to measure is the temperature of the water $\psi = T_{\text{water}}$. Water has been chosen because its permittivity presents a known and large dependence with the temperature and the change will be homogeneously distributed around the probe. The measurement setup is depicted in Fig. 5.9 and consists of a bi-static configuration with two ridged horn antennas forming an angle of 90° with the water tank at the vertex. The VNA measures the S_{21} of the

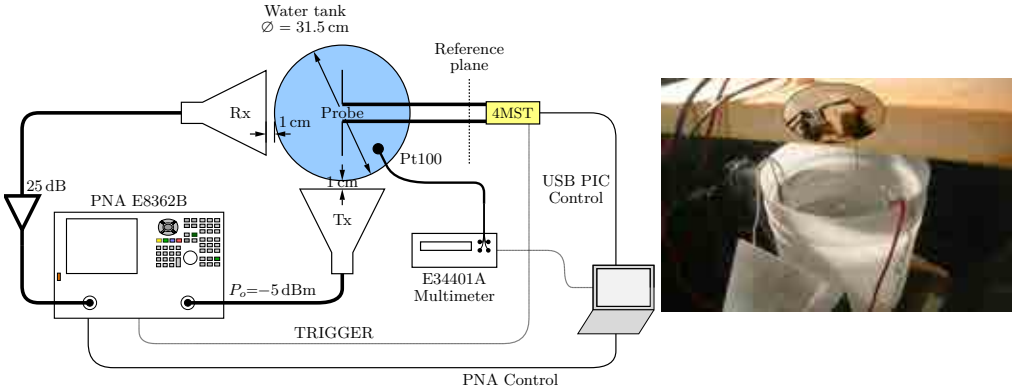

(a) Diagram of the setup **(b)** Detail of the setup

Figure 5.9: The experimental setup for the measurement through Z_{ant} uses a folded dipole submerged in a tank filled with water which has been previously heated up to 60 °C; a semi-rigid coaxial cable allows to connect the dipole from the outside, where the multi-loaded MST circuit is connected. Two ridged horn antennas are set up in a 90^o bi-static configuration allowing to measure the scattered signal with a VNA. The temperature is simultaneously measured by a Pt100 sensor introduced in the water tank with a multi-meter.

signal going through the water tank; this allows to use an amplifier at the receiver to improve the SNR which will be strongly diminished due to the losses in water and at the interface between air and water. The temperature of the water is continuously measured with a digital multimeter connected to a Pt100 temperature sensor.

The MST probe antenna that is used consists of a 17 mm folded dipole antenna placed in the center water tank. The input port of the antenna is accessible from the outside through a semi-rigid coaxial cable, where the MST multi-load circuit is attached. Although the formulation introduced in 5.3.1 considered a mono-static approach, the use of a bi-static configuration (measuring S_{21}) has no impact in the formulation, where now the term ρ^{und} would include the coupling between transmitter and receiver antennas and Z_{tr} would account for the coupling between transmitter-probe and probe-receiver, as shown in appendix A.4 for a conventional 2-loaded MST.

Two measurement cycles have been performed. The first one is the reference measurement which connects the VNA directly to the MST probe antenna to directly measure the reflection coefficient from 700 MHz to 1.5 GHz as the water cools. In the second measurement, the VNA is connected to the horn antennas, and the MST circuit is connected to the coaxial cable of the MST probe antenna; the S_{21} between the two horn antennas is measured sequentially for each load of the MST circuit. Fig. 5.10 shows the differential responses ΔS_{21} (equivalent to $\Delta\rho_{\text{rdr}}$ for a bi-static configuration) for the different combinations of loads ($Z_{\text{L}_{A,B,D}}$) when the water is at a temperature of 40 °C. Here it must be noted the presence of nulls common in all the combinations (most notably at 700 MHz and around 930 MHz) which implies that its origin is in a null in Z_{tr}, which probably arises from a destructive interference coming from reflections at the walls of the water tank. This implies that at these frequencies $\sigma_{Z_{\text{ant}}}$ is larger, making the estimation at these frequencies much less reliable. Similarly the differential signal above 1.1 GHz has a larger attenuation with respect to the range below 1.1 GHz; as such the data in this

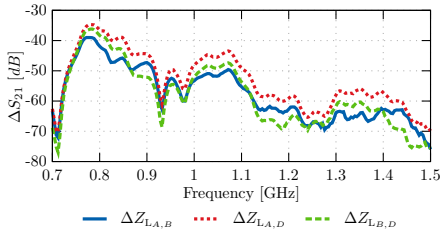

Figure 5.10: Differential response (ΔS_{21}) between the transmitting and receiving antenna for the different loads combinations of the MST sensor for a temperature of the water of 40 °C.

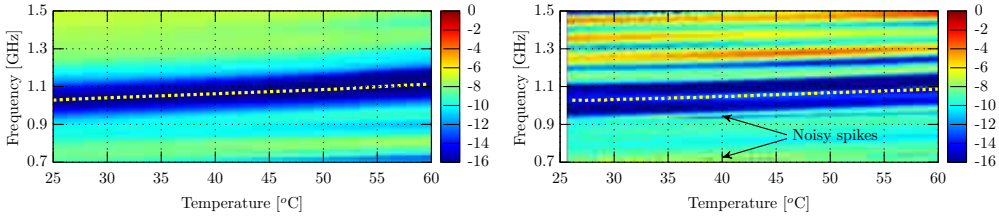

(a) PNA **(b)** MST

Figure 5.11: Magnitude of the reflection coefficient of the probe antenna (folded dipole) when measured directly (a) or remotely using the multi-load MST sensor (b). The yellow dotted line marks the resonant frequency, and the arrows point the unreliable lines due to nulls in Z_{tr}.

frequency range will also be noisier.

The measured Z_{ant}, either directly or through the multi-load MST, will present an important wrapping due to the presence of the coaxial line which shifts the reference plane away from the antenna input port. Since Deschamps equation (5.2) predicts the evolution of Z_{ant} at its port, this evolution will be masked by the wrapping introduced by the coaxial line, and as such its effect must be removed if the exact input impedance variation is to be obtained. This would not happen in a final prototype where the MST circuit is located directly at the port of the antenna.

In this experimental setup, instead of unwrapping the coaxial's effect, the magnitude of the ρ_{ant} is used, since it is also affected by the temperature variations (for instance through a shift of the resonant frequency), while not being affected by the displacement of the reference plane.

Fig. 5.11 presents the magnitude of the reflection coefficient as a 2D plot versus frequency and water temperature. First of all, it can be shown that both plots present a similar shape, and how for both plots, the behavior for the resonance is the expected and predicted by (5.2): as the temperature increases, the permittivity of water decreases, and the resonant frequency increases. This has been highlighted in the figures by showing the resonant frequency by a dotted yellow line. By a closer look at the results obtained using the multi-load MST technique it can be shown that as predicted from the differential ΔS_{21} of Fig. 5.10, the frequency range above 1.1 GHz is noisier than the rest of the measurement. Similarly, the null in Z_{tr} detected from the same figure at the frequencies

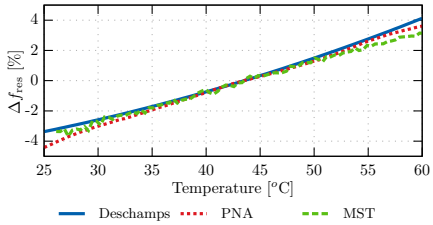

Figure 5.12: Relative variation of the frequency of resonance of the dipole antenna as predicted by (5.2), the direct measurement of the folded dipole antenna, and the remote MST measurement. The reference temperature has been taken at 43.5 °C.

of 700 MHz and 930 MHz (at 40 °C) produce two noisy lines in the retrieved reflection coefficient (marked with two arrows in the figure). These nulls arise from destructive reflection coming from the relative position of the probe and the walls of the water tank, and as such they also present a dependence with the temperature of water, following a similar trend with temperature as the resonant frequency.

Fig. 5.12 plots the shift in the resonant frequency of the folded dipole for both measurements, as well as the expected behavior predicted by Deschamps equation (5.2). A similar behavior is shown between the direct measurement and the MST measurement which agrees quite well with the expected theoretical response. However a slope difference between the reference and the MST measurement can be appreciated, which might lead to an estimation error below 3 °C when the temperature is 60 °C (the estimated temperature would be around 57 °C).

5.4 Enhanced multi-load MST sensor: Sensitive loads

The multi-load MST sensor presented in the previous sections is capable of doing sensing by measuring variations in Z_{ant} which can then be related to ψ. However, the influence that the environment has on Z_{ant} makes this kind of sensor unsuitable when it cannot be guaranteed that the antenna will remain isolated; for instance, due to the presence of scatterers the resonant frequency might change in unpredictable ways, leading to a bad estimation of the permittivity. Moreover, in order to detect a change in ψ it is a requirement that the permittivity of external medium to the antenna has a dependence with ψ, and this is not always the case for instance the example presented in the previous section would not be possible if the probe was surrounded by air, since the permittivity of air does not change appreciably for the same range of temperatures.

In these scenarios sensing cannot rely on Z_{ant}, and the multi-load MST sensor must be improved. To do so, we can start by considering a scenario where Z_{ant} is completely independent of ψ, and can be considered as a well known quantity. If Z_{ant} is well-known, one of the loads of the MST multi-load sensor, for instance Z_{L_C}, can be changed with a sensitive load $Z_{\text{L}_C}(\psi)$, whose impedance depends with ψ. Since the hypothesis considers Z_{ant} a known quantity, it can act as a third known quantity, and with the other known

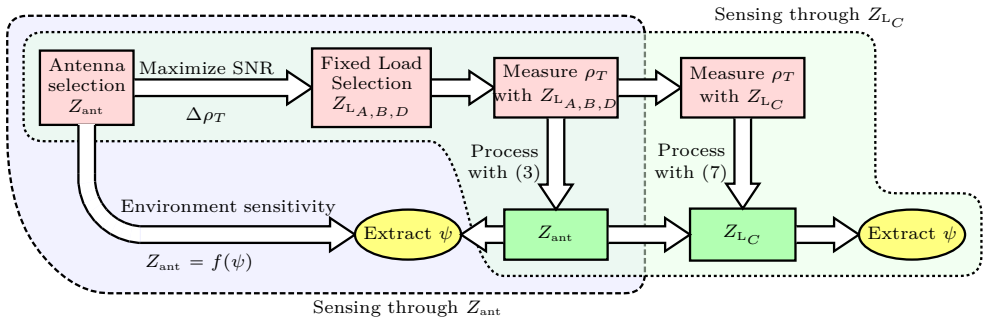

Figure 5.13: Block diagram of the steps that are done for retrieval of the sensed quantity ψ using the multi-loaded MST load. Sensing through Z_{ant} extracts ψ from the study of the variation in Z_{ant}. Sensing through Z_{L} requires first to compute Z_{ant} using 3 fixed loads and then estimates Z_{L_C} to compute ψ.

fixed loads $Z_{\mathrm{L}_{A,B}}$, the unknown value of $Z_{\mathrm{L}_C}(\psi)$ can be estimated as:

$$\begin{bmatrix} \rho^{\mathrm{und}} \\ Z_{tr} \end{bmatrix} = \begin{bmatrix} 1 & \frac{1}{Z_{\mathrm{ant}}+Z_{\mathrm{L}_A}} \\ 1 & \frac{1}{Z_{\mathrm{ant}}+Z_{\mathrm{L}_B}} \end{bmatrix}^{-1} \cdot \begin{bmatrix} \rho^A_{\mathrm{rdr}} \\ \rho^B_{\mathrm{rdr}} \end{bmatrix} \tag{5.11}$$

$$Z_{\mathrm{L}_C} = \frac{Z_{tr}}{\rho^C_{\mathrm{rdr}} - \rho^{\mathrm{und}}} - Z_{\mathrm{ant}} \tag{5.12}$$

In a practical implementation Z_{ant} is affected by nearby scatterers and cannot be known beforehand to solve (5.12). However, as shown in the previous sections, Z_{ant} can be effectively measured by using the multi-load sensor when it has 3 known loads (with ψ-dependence). Consequently the number of loads in the multi-load sensor will need to be increased, so that at least 3 known fix loads can be used to estimate Z_{ant} using (5.8), and then Z_{ant} can be used to estimate any $Z_{\mathrm{L}_C}(\psi)$ present in the multi-load sensor using (5.12). The whole process is summarized in the block diagram of Fig. 5.13.

5.4.1 Sensing through Z_{L_C}. Robust sensing of the local temperature of the sensor.

The experimental validation of the enhanced sensor uses a thermistor as the sensitive load $Z_{\mathrm{L}_C}(\psi)$, allowing it to detect variations of temperature even if the environment's permittivity does not change appreciably with temperature. Specifically the load corresponds to a negative temperature coefficient (NTC) thermistor (model EPCOS B57236S500M) with a nominal resistance of $R_o = 50\Omega$ at $T_o = 293\mathrm{K}(25^{\mathrm{o}}\mathrm{C})$ and a material constant (β) of 3165K. At DC frequencies the resistance of the temperature presents a dependence with temperature as:

$$R(T) = R_o e^{\beta\left(\frac{1}{T}-\frac{1}{T_o}\right)} \tag{5.13}$$

Although this dependence is only valid at DC it will be used later on to estimate the temperature of the measurement by measuring the DC resistance of the thermistor simultaneously to the MST measurement.

As a preliminary step to performing the measurement, extra care must be taken when placing and measuring this specific thermistor because, due to its size and encapsulate,

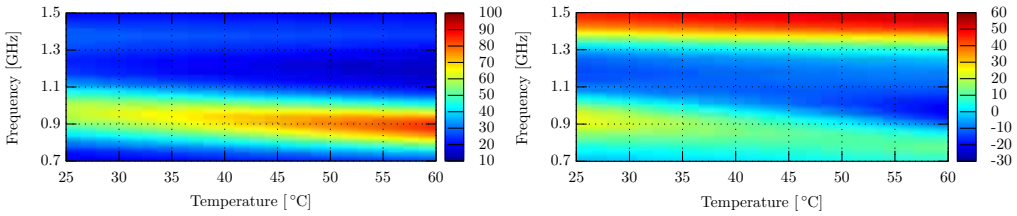

(a) Resistance **(b)** Reactance

Figure 5.14: Characterization of the thermistor input impedance at the input port of the 4 load MST circuit measured with a VNA.

it presents large parasitic reactances, as well as some losses due to radiative effects that depend on its placement. To ensure repeatability for the measurements the thermistor was isolated by covering it with RF absorbing material, after placing a 10 Ω ceramic resistor on top of the thermistor to remotely increase its temperature and a coaxial cable to access the SMA port without disturbing the absorbing material position.

For the characterization of the thermistor impedance, the multi-load MST circuit was directly connected to the VNA and the 10 Ω ceramic resistor was turned on to heat the thermistor from 30 °C to 60 °C. Fig. 5.14 shows the resulting impedance as a 2D plot for the frequency range from 700 MHz to 1500 MHz at the SMA port (the coaxial cable was measured at 1.03 ns of electrical length). The actual temperature of the thermistor is determined directly using eq. (5.13) with the DC resistance of the thermistor. The DC resistance has been measured indirectly by the PIC through an RF choke, and transmitted to the computer through the USB port. The characterization readily shows that there is an important variation of both real and imaginary part of the RF impedance of the thermistor with the temperature, which can be clearly noticed at frequencies such as 880 MHz or 1.2 GHz with a variation around 25% of the resistance with respect to the value at a temperature of 43.5 °C.

The experimental setup, depicted in Fig. 5.15, is similar to the measurement within the water tank. In this case the MST probe antenna is the same 800 MHz monopole antenna that was used in section 5.3.2 with an additional coaxial cable connected to the SMA port (with an electrical length of 1.12 ns), and the reader is in a mono-static configuration at a distance of 1.25 m from the monopole. To simulate a scenario where the antenna input impedance could change due to nearby scatterers, two sets of measurements were done. The first one, shown in Fig. 5.16a, corresponds to the monopole isolated and the second one, shown in Fig. 5.16b, has scatterers placed nearby the monopole antenna that modify its input impedance. Fig. 5.17 presents the estimated input impedance of the monopole Z_{ant} (at the SMA port reference plane) for both scenarios using the multi-load MST circuit and the three known fixed loads $Z_{\text{L}A,B,D}$. Z_{ant} was correctly obtained for the whole range of temperatures that were measured, and Fig. 5.17a shows the average impedance that was obtained. Since multiple measurements of ρ_{rdr} where taken (for the different temperatures), it is possible to compute the experimental uncertainty in the estimation of Z_{ant} which is shown in Fig. 5.17b along with the predicted accuracy. Which was obtained using (5.9) and the set of parameters ρ_{und} and Z_{tr} obtained after solving (5.11). Both sets of curves agree well when the noise power of the measurement is taken as $\sigma_N = 0.25 \cdot 10^{-4}$.

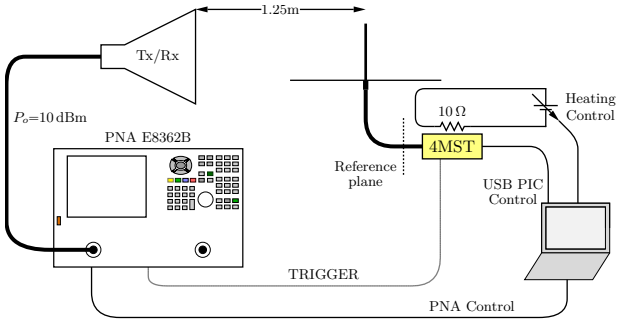

(a) Diagram of the setup

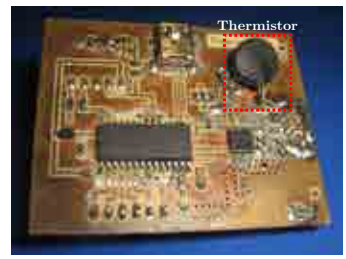

(b) Detail of the circuit with the thermistor soldered into Z_{L_C}

Figure 5.15: The experimental setup for the validation of the sensing through Z_{L_C} uses a monopole antenna as the probe antenna, and a thermistor as the sensing load. A 10 Ω ceramic resistor is placed on top of the circuit to have a controlled heating during the measurement. A single ridged horn antenna transmits and receives the reflected signal which is captured by the VNA.

(a) Isolated

(b) Scatterers

Figure 5.16: Two scenarios have been considered in the measurement of the thermistor, (a) considers the monopole isolated, while (b) considers two scatterers near the monopole affecting its input impedance.

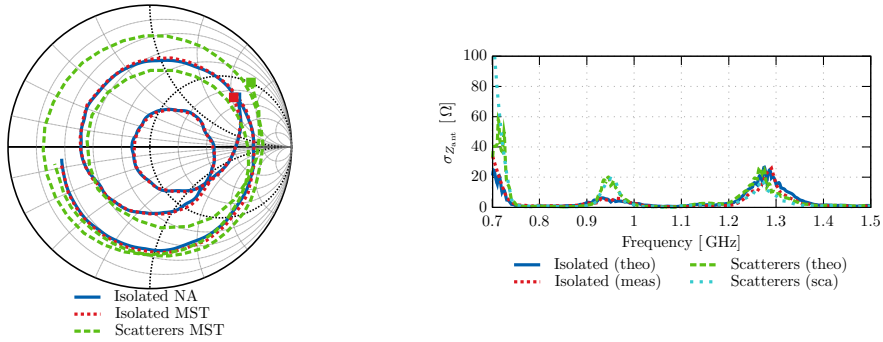

(a) Impedance **(b)** Accuracy

Figure 5.17: (a) input impedance estimated for the scenarios depicted in Fig. 5.16. The filled region represents the uncertainty of the measured (one standard deviation) computed with the whole set of measurements at the different temperatures. (b) shows the accuracy of the measurement and compares it with the values obtained using the theoretical expression (5.9).

Using the estimated Z_{ant} in (5.12) the value of $Z_{\text{L}C}$ is estimated, see Fig. 5.18, which independently of the variation in Z_{ant} (isolated or with scatterers) shows very good agreement with the characterization previously presented in Fig. 5.14. Fig. 5.19 shows a single cut of the impedance at the frequency of 880 MHz, which according to the characterization showed the maximum sensitivity in terms of $\Omega/\,°\text{C}$, and where the different sets of curves overlap each other. This plot highlights how the enhanced multi-load MST sensor is capable of dealing with variations in the scenario that affect the input impedance of the antenna, allowing to measure the thermistor impedance regardless of these variations, and showing a good agreement with the actual characterization.

Finally Fig. 5.20 presents an estimation of the temperature using the characterization of the thermistor as the calibration curve (since a theoretical behavior $Z_{\text{L}C}(T)$ is not know at this frequency), showing that the temperature is correctly estimated. If the standard deviation of the estimation is computed, it is approximately 0.7 °C for the whole range of temperatures at the current measurement conditions, although this will depend on the actual thermistor being used and the SNR of the measurement.

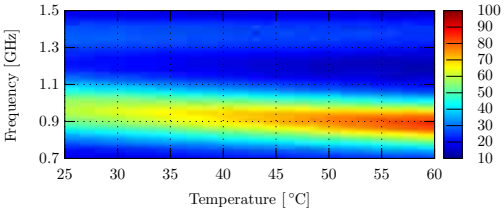

(a) R_{L} Remote Isolated

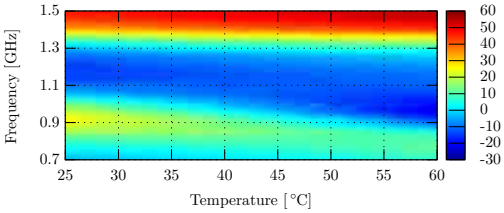

(b) X_{L} Remote Isolated

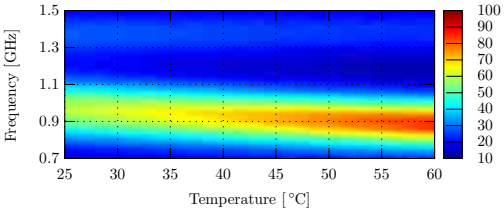

(c) R_{L} Remote Scatterers

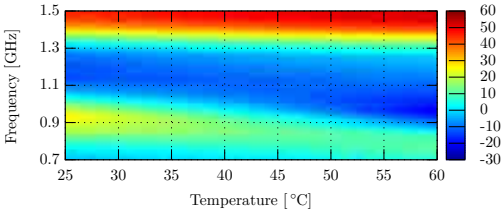

(d) X_{L} Remote Scatterers

Figure 5.18: Remote MST estimation of the impedance for the thermistor Z_{L_C} using the retrieved input impedance of the monopole. This case considers the monopole with the nearby scatterers. Similar results are obtained for the case without scatterers.

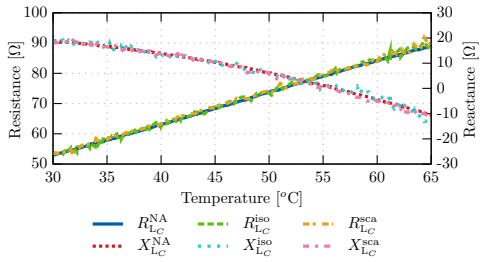

Figure 5.19: Cut of Fig. 5.18 at 880 MHz, showing very good agreement for both scenarios.

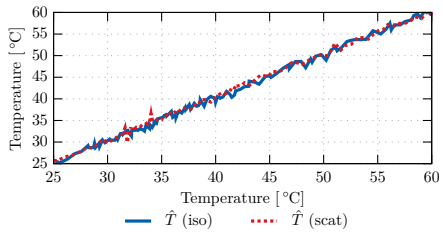

Figure 5.20: Estimated temperature from the wireless measurements using the impedance of the characterization as the pattern. The estimation presents a standard deviation of 0.7 °C with respect to the actual temperature.

5.5 Completely wireless multi-load MST operation mode. Combined sensing

The previous section, used the multi-load MST sensor operating always in the slave-mode, that is with the sensor always connected to the computer that was making the measurements. In this section a completely wireless measurement is carried out with the fabricated circuit, using the master-mode of operation. This operation mode allows to synchronize the signal that has been measured at the post-processing stage, so that the instant at which each load is being switched can be detected. A more efficient operating mode would integrate demodulating capabilities in the sensor, in such a way that a trigger sequence could be transmitted by the reader to start the measurement, as with RFID tags.

5.5.1 Master operation mode for the multi-load MST sensor

When the master-mode is used, the synchronization and location of each state is done in the post-processing of the received signal. To this end, the circuitry does not simply switch between each load alternatively, but uses a more complex sequence (S), shown in Fig. 5.21. The sequence consists of a header (H), which is used for synchronization of the measured signal; and the sensing information section (I) of the measurements, where the whole set of loads is swept consecutively at a much slower rate than the synchronization sequence to improve the SNR. The header is generated by switching a pair of loads sequentially according to a Gold code of 31 bits [116]. A locally generated header is then used at the computer to synchronize the signals, thanks to the properties of auto correlation of the Gold code. However, since the signal coming back from the MST probe is composed of 4 different levels with noise, depending on which two are used for the header, the auto correlation peak might be masked by the correlation of the locally generated header and the sequence I of the received signal (similar to the near-far problem in CDMA). To avoid this, the sequence S is repeated 3 times, and each time H is generated by a different pair of loads: Z_{L_A} and Z_{L_B}, Z_{L_B} and Z_{L_C} and Z_{L_C} and Z_{L_D}. This guarantees that by capturing a signal with a length of at least 3 periods of the sequence S, the maximum of correlation will correspond to one of the headers, and the information stream will be properly located. This can be seen when the signal from Fig. 5.21 is correlated with the Gold code to obtain the curve of Fig. 5.22: the correlation peak of the first two headers is easily discernible but the third one is completely masked by the correlation with sequences I before and after the header, which would lead to a wrong synchronization and an error in the estimation of Z_{ant} if only this sequence S had been used for the measurement.

5.5.2 Experimental measurement

The experimental setup will combine the experiments carried out in the previous measurements in a single measurement, using simultaneously the changes in Z_{ant} and Z_{L_C} (the thermistor) to detect variations of the temperature of water. In order to do this, the complete MST circuit needs to be introduced in the same tank of heated water. To avoid damaging the circuitry and the battery that powers the MST circuit, they are introduced in a protective case with ingress protection degree IP67 [117], which is able to withstand immersion in water without internal leaking. Here it must be noted that this changes the isolation conditions of the thermistor, which was previously protected with absorbing

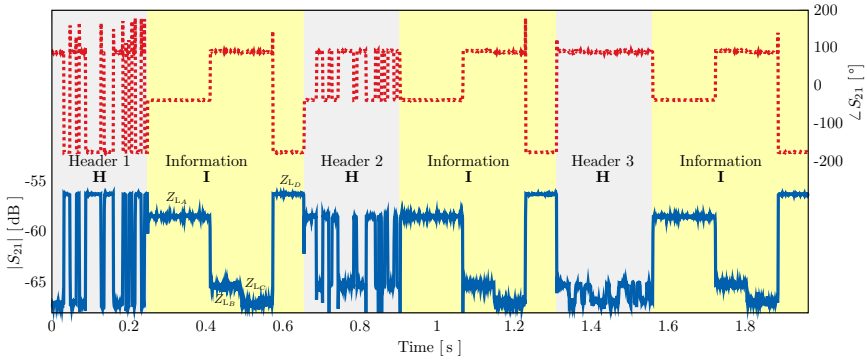

Figure 5.21: Graphical representation of the sequence (S) used for the synchronization of the signal in the autonomous measurement. It consists of a header (H), obtained by switching two loads according to a Gold code, followed by a slower sequence (I) that goes through all the loads. The sequence S is repeated 3 times, changing the pair of loads used to modulate H between $Z_{L_{A,B}}$, $Z_{L_{B,C}}$ and $Z_{L_{C,D}}$, as observed by the difference in the header at the beginning and at the end of the plot.

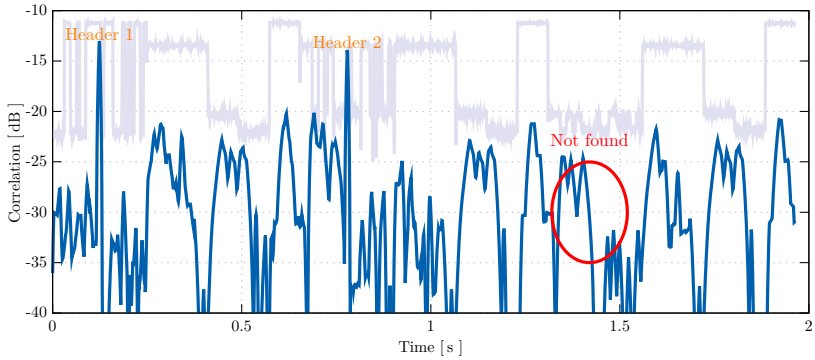

Figure 5.22: Correlation of the signal in Fig. 5.21 with the Gold code used in the header. As can be observed, the first two headers are perfectly identified by the correlation peaks, but the third header, which used a improper combination of loads cannot be located.

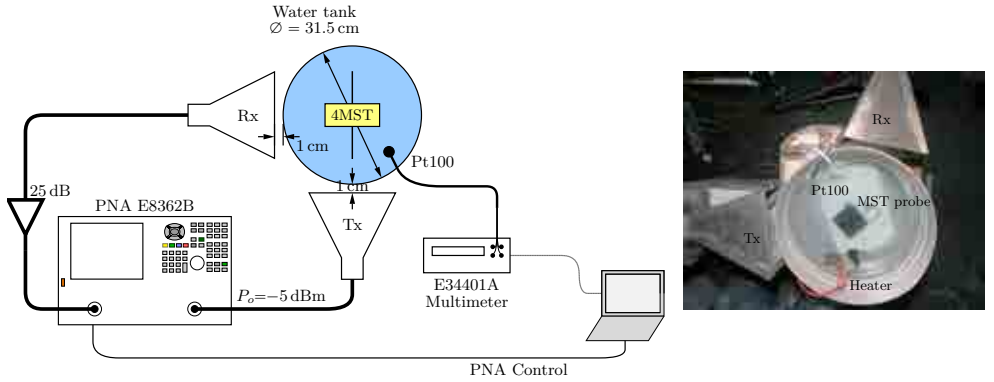

(a) Diagram of the setup **(b)** Detail of the setup

Figure 5.23: For the dual measurement, the experimental setup is like in section 5.3.3. However the MST circuit is placed within an IP67 protective case inside of the water tank, and any control signal to/from the MST circuit are removed.

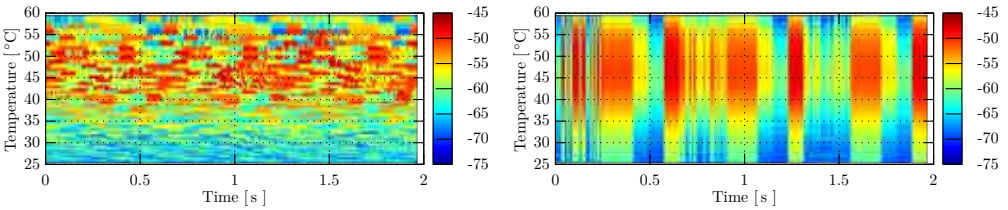

(a) Measured signal at 1.1 GHz **(b)** Measured signal at 1.1 GHz

Figure 5.24: (a) presents the raw measurement (without the mean value so that changes are noticeable in the figure) for the completely wireless measurement, it can be seen that for each temperature the position of the header and the information (data) is completely random; after correlation with the header (b) allows to easily identify each load state according to Fig. 5.21.

material, and as such the thermistor impedance will change unpredictably with respect to the previous measurement and Z_{L_C} cannot be compared with the previous results. The experimental setup, shown in Fig. 5.23, is similar to the one in section 5.3.3 but with the MST circuit operating completely autonomously and with the thermistor acting as load Z_{L_C}.

Fig. 5.24 presents the measured signal in a CW time for 1 GHz for a set of temperatures before and after synchronization has been carried out at the computer, and how each state can be easily identified after synchronization. After properly synchronizing the time slots corresponding to each load state, Z_{ant} can be obtained at the reference plane of the MST circuit. Fig. 5.25 presents the reflection coefficient, where the shift in the resonant frequency, highlighted by a yellow dotted line on the figure, presents the same behavior than the results obtained in section 5.3.3, and with a similar sensitivity (see Fig. 5.27a).

Once Z_{ant} is obtained, the value of Z_{L_C} of the thermistor can be estimated using (5.12) as shown in Fig. 5.26. Although in this case it cannot be directly compared to the impedance obtained in section 5.4.1, due to the changes in the conditions of the measure-

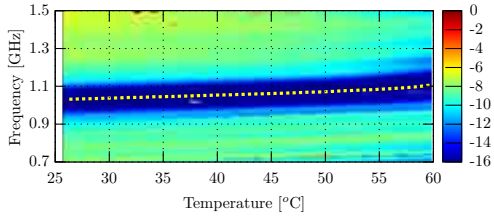

Figure 5.25: Estimated reflected coefficient after identification of each load, showing a similar shape and trend as previous results; the yellow dotted line highlights the resonant frequency evolution with temperature.

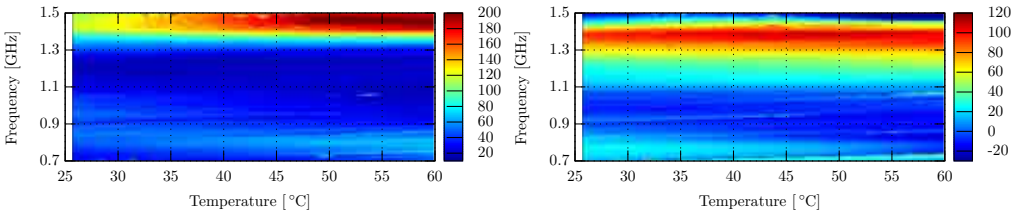

(a) Resistance **(b)** Reactance

Figure 5.26: Retrieved impedance of the thermistor, Z_{L_C}, for the complete wireless measurement inside the tank of heated water. It must be noted that since the isolating conditions of the thermistor have changed the impedance response will not be as in Fig. 5.14

ment, it can be observed that the dependence of Z_{L_C} with temperature can be remotely measured. Moreover, it can be seen that the sensitivity of the thermistor impedance, shown in Fig. 5.27b, is comparable to the one obtained in section 5.4.1 when the thermistor was surrounded by air, therefore, in spite of the variations on the impedance, the thermistor could still be used to retrieve temperature using this curve as a calibration curve.

5.6 Concluding remarks

This chapter has shown the viability of using RFID-MST probes as sensors, in order to measure parameters (ψ) that are not the conventional field distribution that is normally associated with MST scenarios. The parameters measured in this chapter consisted basically in the temperature of some medium (water or air), but the scheme could also be used for other parameters such as humidity, pH levels, etc. Moreover, the limitations associated with conventional MST probes for sensing applications, have been analyzed and a solution based on a multi-load MST probe has been proposed and successfully developed. The multi-load MST probe allows to fully determine the complete set of parameters involved in the communication between a reader and the MST probe, thus being able to detect the term that caused a variation in the measured $\Delta\rho_{\mathrm{rdr}}$, thus enabling the direct use of information such as Z_{ant} to estimate ψ. This methodology has been experimentally validated using a prototype of a multi-load MST sensor to measure the temperature variations of a heated water tank, giving a good estimation of the temperature of water.

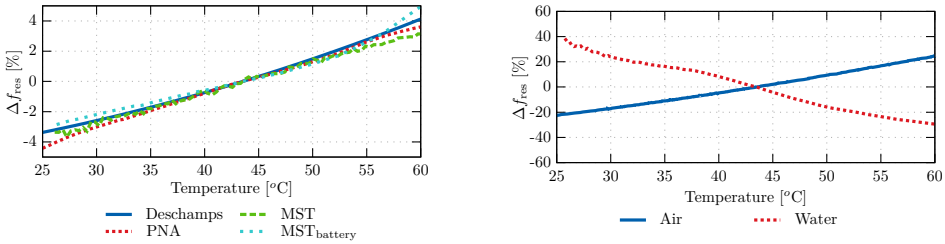

(a) Z_{ant} resonance **(b)** Thermistor

Figure 5.27: Sensitivity of the autonomous MST measurement: (a) shows a comparison of the theoretical expected sensitivity, and the one obtained using both measurements approaches, PC triggered and completely remote. (b) shows the sensitivity of the measurement of temperature from the thermistor when located in air, or for the fully remote measurement while immersed in water.

Table 5.2: Comparison of the results when using the multi-load sensor to measure the temperature remotely using the approaches presented in this chapter.

Experimental conditions	$\mathbf{Z}_{\text{ant}}$	$\mathbf{Z}_{\mathbf{L_C}}$
Dielectric	Water	Air
Temperature-range	25 – 60 °C	25 – 60 °C
Tx. power	−5 dBm	10 dBm
Rx. amplification	25 dB	0 dB
Distance to the sensor	∼ 17 cm	∼ 1.25 m
Tx/Rx (reader) far-field antenna gain	7.5 dB	7.5 dB
Parameter	$\mathbf{Z}_{\text{ant}}$	$\mathbf{Z}_{\mathbf{L_C}}$
Experimental temperature sensitivity	$\Delta f = 0.2\%/°\text{C}$	$\Delta\lvert Z\rvert = 1.15\Omega/°\text{C}$
Error (σ)	±1 °C	±0.7 °C
Bias	max 3 °C	0 °C
General temperature sensitivity	Medium dependent	Load dependent
Robustness to changes in the environment	Low	High
Applicability	Particular	General

However sensing through variations in Z_{ant} has its own limitations due to the high dependence of the antenna impedance with the nearby environment, such as the introduction of nearby scatterers to the sensor. To avoid this problem, the multi-load MST sensor has been further extended to allow the inclusion of sensitive loads in the sensor, whose impedance depends on the parameter ψ. This approach makes the sensor robust to variations of the impedance due to the scenario, and allows the measurement in environments whose permittivity is not ψ-dependent. This has also been experimentally validated using a thermistor as the sensitive load, but could be extended to other physical parameters using loads that change with humidity [118], pH levels [119], glucose [120], etc.

An important conclusion that was observed from the selected thermistor, is that although the method by itself is robust to changes in the environment, if the load is not properly designed for working at RF frequencies, such as the thermistor used in this chapter, it could be badly shielded at RF frequencies and this introduce an undesired dependence with the external environment. This can be overcome by adequately shielding them as part of the sensor design, or using adequate RF alternatives of the load if they are available.

Table 5.2 summarizes the results observed for each validation. In terms of accuracy, it must be taken into account that since the sensor is based on MST, the SNR of the received signal decays with distance as r^4 (in free space), and this will affect the available SNR. However the direct impact that this variation of the SNR has on the accuracy will greatly depend on the temperature profile (sensitivity) of the sensing impedance (Z_{ant} or $Z_{\text{L}C}$).

When comparing both methodologies, there are a set of differences which can make each better suited in different situations. For instance, although the thermistor approach is more generally applicable since it does not rely in permittivity variations, it gives a local (point) knowledge of the temperature (at the thermistor). On the other hand, the variation of the input impedance of Z_{ant} gives a temperature-related information averaged over the antenna neighborhood. However, if the parameter of interest (for instance the temperature) is continuous in the neighborhood of the antenna, they will be practically equivalent. Furthermore, in terms of robustness, the existence of scatterers might affect the position of the resonance of the antenna leading to an error in the estimation of the temperature, therefore the method based on Z_{ant} requires that the antenna is properly isolated from scatterers or that the changes introduced by the scatterers can be detected to reject the measurement. On the contrary, and as previously shown, the final estimation of the temperature with the thermistor is not affected by the presence of scatterers provided that the antenna still operates correctly.

The sensitivity of the measurement is different for each configuration. The sensitivity for $Z_{\text{L}C}$-based measurement is established by the sensitivity of the load itself, that is the variation of the impedance with ψ (temperature in the experimental validation); for the measurement through the antenna input impedance, the sensitivity is linked simultaneously with the variation of the permittivity of the surrounding medium with ψ, and the frequency variation of Z_{ant}.

In spite of their differences, both methodologies are complementary and can be combined to enhance the sensing capabilities by measuring two different physical parameters, such as for instance temperature and humidity, in a similar configuration as presented in the final experimental validation of 5.5.

Finally and although the validation has been conducted making use of a battery-assisted temperature sensor, the principle of operation is applicable for non-wired applications. For instance, the same principle could be envisioned for an embeddable *enhanced* RFID sensor, where 1) instead of a battery, a harvesting section is used to power it up, and 2) a *passive* sensitive load would allow to remotely monitor a quantity of practical relevance, such as, for instance, patient acidity or glucose levels in implanted devices inside of human bodies, or the detection of water leakages within civil engineering structures.

6

Chapter 6
Conclusions

6.1 Main conclusions

This PhD thesis has devoted to the study of the RFID-MST sensor with a special emphasis in the electromagnetic capabilities that these sensor have, and what can be done in order to fully exploit them. The main conclusions can be summarized as follows:

- *Performance of the RFID tag as a sensor.* A complete characterization of the formulation governing the propagation and communication with an RFID tag has been developed and studied, in order to evaluate the goals for a proper design of an RFID tag in terms of objective input impedance. It has been shown that there are two main goals. On the first hand there is the optimization of the power transfer to the scavenging state of the RFID which result in the optimization of the reading distance, and therefore on the dynamic range of the sensor. On the other hand the optimization might take into account not only the scavenging mode, but at the same time make use of the short-circuiting mode (the alternative impedance used for modulation) in order to improve the backscattered response. It has also been shown that although the variation in the backscattered power will be of 3 dB for an optimization of the RFID tag in an ideal (not-lossy) RFID IC, this difference will widen as both the matching or the losses in the RFID IC increase.

- *Non-linearities of the backscattered response of the RFID tag.* While characterizing the performance of the RFID tag, a methodology for the complete characterization of the RFID IC tag has been proposed using conventional laboratory equipment, which relies in the modulation of the signal measuring the RFID IC with the VNA. This complete characterization of the two states of the RFID IC allows to perform a characterization of the dynamic response of the RFID IC allowing to change either frequency or power and obtaining the dependence of both states of the RFID IC. The knowledge of the non-linear response of the RFID IC allows to predict the behavior of the RFID tag with changes in the incident power. It has been shown that the *ME* of the RFID tag increases when the incident power diminishes in a similar factor, and this effectively translates in that the backscattered power received at the external of the antenna diminishes with a slower rate than the conventional mono-static radar response of r^{-4}.

- *Field measurements with RFID tags.* Although initial measurements using an RFID tag as an MST probe shows a high difference between the expected field distribution and the actual measurement, this can be attributed to the non-linear response of the RFID tag. Once the cause of the dissimilitude is located it is possible to define a calibration method that enables its use as a EM field sensor. However due to the dynamic range limitation of the RFID tag, basically the requirement of an activation power above a given threshold, it is not possible to directly measure a strongly variant field, because when these variations go below the activation threshold, the RFID tag becomes silent. The knowledge acquired with the characterization of the RFID tag response allowed to devise an alternative approach for the measurement of the RFID field measurement which consists in the use of two different interrogating signals; the first one must turn the RFID tag on, establishing the impedances that will be operated with the RFID tag, and the second one, which uses a lower power will measure the field distribution. Although this second signal will be affected by the power associated to the first, it is possible to always use the same level of

the powering signal (thanks to the activation threshold which acts as a beacon), thus removing the limitation imposed by the activation threshold and increasing the dynamic range which is now limited by the receiver sensitivity.

- *Environmental EM sensing with RFID tags.* RFID tags can act as passive electromagnetic sensors, thanks to the dependence of their behavior with the environment, due to the variation of input impedance and propagating characteristics of the backscattered response with a (slowly) changing environment. However this direct sensing is strongly restricted to controlled environments or dispositions because the backscattered response is interdependent of several components which may change for a variety of causes. In fact this same limitation will affect measurement of field distribution, which will be affected by a change in the RFID tag antenna input impedance, if it is not properly identified. In spite of the previous limitation, it has been shown that the addition of a small level of complexity to the design of the tag, basically the addition of at least one additional modulation state allows to completely dissociate the backscattered response into its many components. In this case the different components: field distribution, antenna impedance, and even the *undesired* (clutter) response can be identified. This identification enables the use of each of these parameters to sense variation of electromagnetic parameters of the scene, and can also be used to detect false positives that would go unnoticed in a conventional configuration.

- *General sensing with enhanced RFID tags.* The EM sensing capabilities that can be obtained with the enhanced RFID sensor can be further improved with an additional sensitive impedance as part of the set of impedance used in the backscattered modulation. This sensitive load, may be dependent on the acidity, glucose levels, temperature, moisture, etc., of the environment where the RFID sensor is embedded, and when used in combination with the rest of the loads of the enhanced RFID sensor in backscattered modulation, can be fully retrieved using a similar formulation that was used for enhanced RFID tags. Which makes it compatible with the environmental EM sensing thus allowing to diversify the sensing capabilities of the RFID tag.

  In a completely wireless sensor, the use of a diverse synchronization sequence for the enhanced RFID tag is important in order to properly discriminate the instant at which each state changes. However, alternatives using triggering events already available in the RFID protocol can be implemented, such as the issuance of a specific interrogation code for every different load state.

It must be noted that although the research developed thorough this thesis has used only passive RFID to sense through passive probing of the environments, it can be also used in other kind of sensors that do some active probing of the environment. In such a way, solutions such as wireless identification and sensing platform (WISP), which can use part of the harvested power to operate external sensors, can be further improved by adding the capabilities of passive sensing that has been presented and demonstrated in this thesis.

6.2 Future research lines

Several research lines can be thought of as a continuation of the work developed during this PhD. Thesis that make use of some or several of the conclusions drawn from it.

Use of *ME* maximization in MST applications Improve the response of MST arrays for EM-field sensing making use of the concept of modulation efficiency (*ME*). In such a way the backscattered power can be improved increasing the dynamic range of the array and at the same time reducing the noise of the system.

Development of RFID arrays for bio-medical applications. In bio-medical applications, in special for imaging applications, the availability of low-cost arrays of autonomous sensors capable of measuring a scattered field distribution will allow the implementation of fast scanning systems. Moreover, the use of a bi-frequency approach can be used for large dynamic range measurements.

Extension of RFID sensors for large bandwidth sensing. The design of an RFID sensor for maximum modulation efficiency (*ME*) or load factor (*LF*) optimizes the response of the RFID sensor at the harvesting frequency. However, this may limit the response of the sensor when used in a multi-frequency approach in order to obtain a field distribution along a large bandwidth. For such operation, the design of the RFID antenna will have to simultaneously maximize the harvesting at the *feeding* frequency, while also ensuring an adequate backscattering response (*ME*) of the sensor at the different frequencies where the EM-field is being sensed.

Integration of a third load state in a complete RFID IC. As shown in the last chapter, the integration of a 3rd load in the RFID circuitry allows to fully decouple the elements involved in the communication between the RFID sensor and the external reader. This will fully enable the use of RFID sensors as embedded devices capable of retrieving meaningful and trustworthy information from within the body in which they are embedded. Moreover, the intelligence of the RFID sensor will allow the controlled selection of the load used for the backscattered response, thus allowing faster measurements.

Exploitation of the non-linear response of an RFID IC for enhanced sensing. As shown in the last chapter, the use of a third load enhances the capabilities of the RFID sensor. For a conventional, 2 states, RFID IC, the existence of non-linearities in the RFID IC automatically introduces a varying input impedance of the RFID IC, and this can be considered as a different load that could be used for sensing. However, the use of such approach will reduce the accuracy of the sensing, since the distance between the impedance states is not maximized as shown in the corresponding chapter.

A

Appendix A

Reciprocity and transfer impedance formulation

This appendix presents details on the development of the expressions for $\Delta\rho_{\text{rdr}}$ and Z_{tr} used thorough the thesis, especially in chapters 2 and 4. In the appendix the expression for the transfer impedance is obtained using different formulations, as well as for different experimental configurations (mono-static, bi-static, multi-port)

A.1 Reciprocity formulation

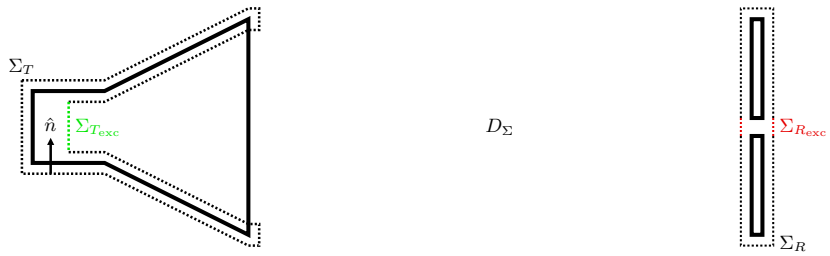

Figure A.1: A horn and a dipole antennas are generating the fields $\vec{E}$ and $\vec{H}$ upon the volume D_Σ limited by the surfaces Σ_i.

For a linear, isotropic medium in a given volume (D_Σ) and limited by the surfaces Σ_i, the Lorentz reciprocity theorem states the relationship between 2 pairs of sources and the

electromagnetic fields each produces is:

$$\oiint_{\Sigma}\left(\vec{E}_1\times\vec{H}_2-\vec{E}_2\times\vec{H}_1\right)\cdot\hat{n}dS+\iiint_{D_\Sigma}\left(\vec{E}_1\cdot\vec{J}_2+\vec{H}_2\cdot\vec{M}_1-\vec{E}_2\cdot\vec{J}_1-\vec{H}_1\cdot\vec{M}_2\right)dV=0 \tag{A.1}$$

with $\hat{n}$ the vector normal to the surface Σ and outward to volume D_Σ.
Considering the scenario depicted in Fig. A.1, D_Σ is the volume external to the antennas and limited by $\Sigma=\Sigma_T\cup\Sigma_R\cup\Sigma_\infty$, that is, the surface enclosing the antennas (Σ_T and Σ_R) and the surface at infinite (Σ_∞). As each surface Σ_i is disjoint from the others, the surface integral can be separated and each surface can be integrated individually. Since the fields are produced by real sources, the field vanishes at infinity, and thus the integral $\oiint_{\Sigma_\infty}$ goes to zero. Similarly, due to the lack of sources within volume D_Σ, the volume integral vanishes. Equation (A.1) then becomes the sum of the surface integrals at each antenna:

$$\oiint_{\Sigma_T}\left(\vec{E}_1\times\vec{H}_2-\vec{E}_2\times\vec{H}_1\right)\cdot\hat{n}dS+\oiint_{\Sigma_R}\left(\vec{E}_1\times\vec{H}_2-\vec{E}_2\times\vec{H}_1\right)\cdot\hat{n}dS=0 \tag{A.2}$$

By properly choosing the surfaces $\Sigma_{T,R}$ as parallel to the metallic parts of the antenna, and assuming perfectly conducting boundary conditions on them (tangential $\vec{E}$ to the surface vanishing), each of the closed surface integrals is reduced to the surface integral of the excitation area of the antennas:

$$\iint_{\Sigma_{T_{exc}}}\left(\vec{E}_1\times\vec{H}_2-\vec{E}_2\times\vec{H}_1\right)\cdot\hat{n}dS+\iint_{\Sigma_{R_{exc}}}\left(\vec{E}_1\times\vec{H}_2-\vec{E}_2\times\vec{H}_1\right)\cdot\hat{n}dS=0 \tag{A.3}$$

The final expression depends on the type of excitation that is considered [57, 121]. In the following paragraphs the procedure is expanded for an antenna excited by a waveguide and for a delta gap.

A.1.1 Waveguide excitation

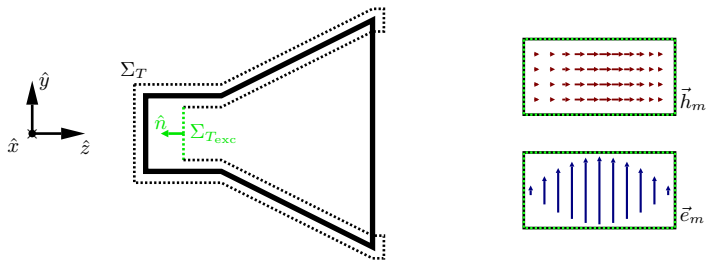

Figure A.2: Detail of the excitation area of the horn antenna, with the distribution corresponding to the fundamental modes TE_{10}.

Assuming a waveguide excitation of an antenna, the field within the waveguide can be expressed as the sum of a set of orthogonal traveling waves [57] propagating along the

waveguide. Without loss of generality, particularizing z as the direction of propagation:

$$\vec{E}_t = \sum_m \left(\alpha(m)e^{-j\beta_m z} + \kappa(m)e^{j\beta_m z}\right)\vec{e}_m \tag{A.4}$$

$$\vec{H}_t = \sum_m \left(\alpha(m)e^{-j\beta_m z} - \kappa(m)e^{j\beta_m z}\right)\vec{h}_m \tag{A.5}$$

where $\alpha(m), \kappa(m)$ are the amplitudes of the forward and backwards traveling waves, and $\vec{e}_m$ and $\vec{h}_m$ are real field distributions of mode m with unitary power, which comply with the following conditions:

$$\vec{e}_m = \eta_m \vec{h}_m \times \hat{z} \tag{A.6}$$

$$\iint_\Sigma (\vec{e}_m \cdot \vec{e}_n)\, dS = \eta_m \cdot \delta_{mn} \tag{A.7}$$

with η_m is the wave impedance of mode m, $\hat{z} = -\hat{n}$, and δ_{mn} is the Kronecker delta. Using this definition, (A.3) becomes:

$$\iint_{\Sigma_{iexc}} \left(\vec{E}_1 \times \vec{H}_2 - \vec{E}_2 \times \vec{H}_1\right) \cdot \hat{n} dS = -2 \sum_m \left[\kappa_1(m)\alpha_2(m) - \alpha_1(m)\kappa_2(m)\right] \tag{A.8}$$

For a single-mode waveguide, α and κ can be directly related to the power waves a and b, by using the associated power with both nomenclatures:

$$\frac{1}{2}|\alpha(1)|^2 = \frac{1}{2}|a|^2 \tag{A.9}$$

$$\frac{1}{2}|\kappa(1)|^2 = \frac{1}{2}|b|^2 \tag{A.10}$$

So finally for a single-mode waveguide the integral can be expressed in terms of power waves a and b as:

$$\iint_{\Sigma_{iexc}} \left(\vec{E}_1 \times \vec{H}_2 - \vec{E}_2 \times \vec{H}_1\right) \cdot \hat{n} dS = 2\left(a_1 b_2 - a_2 b_1\right) \tag{A.11}$$

A.1.2 Delta gap excitation

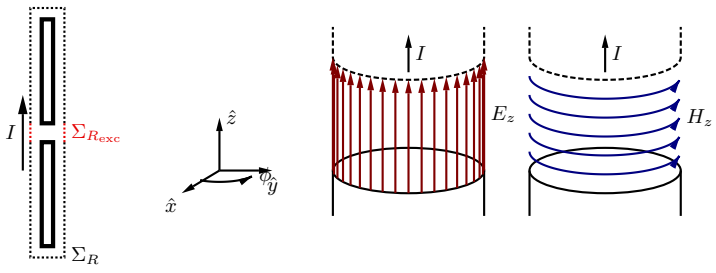

Figure A.3: Detail of the excitation area of a dipole antenna using a delta gap excitation, with the field distribution assumed at the delta gap.

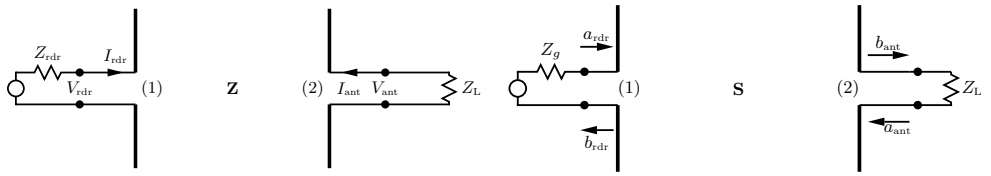

(a) Z-parameters **(b)** S-parameters

Figure A.4: Circuital representation used for the mono-static configuration either with Z or S-parameters.

Similarly to the waveguide excitation, a delta gap can be assumed as the excitation of the antenna. This is a good approximation of, for instance, the excitation of a dipole antenna. Fig. A.3 shows a sketch of the surface that must be integrated.
A delta gap assumes the following excitation at the boundary Σ_R:

$$\vec{E} = E \cdot \hat{z} \tag{A.12}$$

$$\vec{H} = H \cdot \hat{\phi} \tag{A.13}$$

which allows to define circuital parameter V and I as:

$$V = -\int_{\Delta z} \vec{E} \cdot d\vec{z} \tag{A.14}$$

$$I = \int_{2\pi} \vec{H} \cdot a d\vec{\phi} \tag{A.15}$$

Taking the previous into account, the integral becomes:

$$\iint_{\Sigma_{i_{exc}}} \left(\vec{E}_1 \times \vec{H}_2 - \vec{E}_2 \times \vec{H}_1 \right) \cdot \hat{n} dS = V_2 I_1 - V_1 I_2 \tag{A.16}$$

A.2 Transfer impedance formulation based in impedance parameters for a mono-static approach

In chapter 2 the formulation for a mono-static MST measurement has been obtained directly applying reciprocity, using the expressions shown in the previous section of the appendix. However it is possible to obtain the same parameters using the conventional Z or S-parameters. This section, and the following presents the development of the expression using respectively Z and S-parameters, and the following sections will deal with more complex scenarios using bi-static or multi-probe configuration. Using Z-parameters it is possible to relate the voltage and currents at each port (antenna) [57], according to the following matrix formulation:

$$\mathbf{v} = \begin{pmatrix} V_{\text{rdr}} \\ V_{\text{ant}} \end{pmatrix} = \begin{pmatrix} Z_{11} & Z_{12} \\ Z_{21} & Z_{22} \end{pmatrix} \cdot \begin{pmatrix} I_{\text{rdr}} \\ I_{\text{ant}} \end{pmatrix} = \mathbf{Z} \cdot \mathbf{i} \tag{A.17}$$

where V_i is the voltage at the input port of antenna i and I_i is the current going into the antenna, as shown in Fig. A.4a. When the antenna i is loaded with impedance Z_{L}, I_i and

V_i are related through Ohms' Law as $V_i = -I_i \cdot Z_{\mathrm{L}_i}$. Accordingly the input impedance of each of antenna i in the presence of antenna j becomes:

$$Z_{\mathrm{in}_i} = Z_{ii} - \frac{Z_{ji}^2}{Z_{\mathrm{L}_j} + Z_{jj}} \tag{A.18}$$

Taking into account the definition of the input reflection coefficient $\rho_{\mathrm{rdr}} = \frac{Z_{\mathrm{in}_{\mathrm{rdr}}} - Z_{\mathrm{o}}}{Z_{\mathrm{in}_{\mathrm{rdr}}} + Z_{\mathrm{o}}}$, the differential reflection coefficient can be obtained as:

$$\Delta\rho_{\mathrm{rdr}} = 2Z_{\mathrm{o}} \frac{Z^A_{\mathrm{in}_{\mathrm{rdr}}} - Z^B_{\mathrm{in}_{\mathrm{rdr}}}}{\left(Z^A_{\mathrm{in}_{\mathrm{rdr}}} + Z_{\mathrm{o}}\right)\left(Z^B_{\mathrm{in}_{\mathrm{rdr}}} + Z_{\mathrm{o}}\right)} = \frac{Z_{21}^2}{Z_{11} + Z_{\mathrm{o}}} \frac{Z_{\mathrm{L}_A} - Z_{\mathrm{L}_B}}{\left[Z_{22} - \frac{Z_{12}^2}{Z_{11}+Z_{\mathrm{o}}} + Z_{\mathrm{L}_A}\right]\left[Z_{22} - \frac{Z_{12}^2}{Z_{11}+Z_{\mathrm{o}}} + Z_{\mathrm{L}_B}\right]} \tag{A.19}$$

which can be further simplified if we apply the expression (A.18) for port 2 assuming a load of $Z_g = Z_{\mathrm{o}}$ at the reader antenna (a canonical generator) and introducing $Z_{\mathrm{in}_{\mathrm{ant}}} = Z_{\mathrm{ant}}$:

$$\Delta\rho_{\mathrm{rdr}} = \underbrace{\frac{2Z_{\mathrm{o}}Z_{21}^2}{\left(Z_{11} + Z_{\mathrm{o}}\right)^2}}_{Z_{tr}} \frac{Z_{\mathrm{L}_A} - Z_{\mathrm{L}_B}}{\left(Z_{\mathrm{ant}} + Z_{\mathrm{L}_A}\right)\left(Z_{\mathrm{ant}} + Z_{\mathrm{L}_B}\right)} \tag{A.20}$$

Although at first glance it might look as a different definition of Z_{tr} compared to (2.20), it is nevertheless an equivalent formulation, as can be shown when we take into consideration the definition of $Z_{21} = \frac{V_2^{\mathrm{OC}}}{I_1^{\mathrm{OC}}}$, and noting that $I_1^{\mathrm{OC}} = a_1 - b_1^{\mathrm{OC}}/\sqrt{Z_{\mathrm{o}}}$

$$Z_{tr} = \frac{2Z_{\mathrm{o}}\left(V_2^{\mathrm{OC}}\right)^2}{I_1^{\mathrm{OC}}\left(Z_{11} + Z_{\mathrm{o}}\right)^2} = \frac{2Z_{\mathrm{o}}^2\left(V_2^{\mathrm{OC}}\right)^2}{\left(a_1^{\mathrm{OC}} - b_1^{\mathrm{OC}}\right)^2\left(Z_{11} + Z_{\mathrm{o}}\right)^2} \tag{A.21}$$

and knowing that $b_1^{\mathrm{OC}} = a_1\rho_{\mathrm{in}_1}^{\mathrm{OC}}$ and $Z_{\mathrm{in}_1}^{\mathrm{OC}} = Z_{11}$, the transfer impedance becomes:

$$Z_{tr} = \frac{2Z_{\mathrm{o}}^2\left(V_2^{\mathrm{OC}}\right)^2}{a_1^2\left(\frac{2Z_{\mathrm{o}}}{Z_{11}+Z_{\mathrm{o}}}\right)^2\left(Z_{11} + Z_{\mathrm{o}}\right)^2} = \frac{\left(V_2^{\mathrm{OC}}\right)^2}{2a_1^2} \tag{A.22}$$

which corresponds with the definition in (2.20)

A.3 Transfer impedance formulation based in scattering parameters for a mono-static approach

Following a similar procedure to the preceding section, it is possible to obtain a similar expression based exclusively on the full 2-port S-parameters (refer to Fig. A.4b for definition of the ports).

$$\rho_{\mathrm{rdr}} = \frac{b_{\mathrm{rdr}}}{a_{\mathrm{rdr}}} = S_{11} + \frac{S_{12}S_{21}\rho_{\mathrm{L}}}{1 - S_{22}\rho_{\mathrm{L}}} \tag{A.23}$$

Assuming reciprocity ($S_{21} = S_{12}$):

$$\Delta\rho_{\mathrm{rdr}} = S_{21}^2 \frac{\rho_{\mathrm{L}_A} - \rho_{\mathrm{L}_B}}{\left(1 - S_{22}\rho_{\mathrm{L}_A}\right)\left(1 - S_{22}\rho_{\mathrm{L}_B}\right)} \tag{A.24}$$

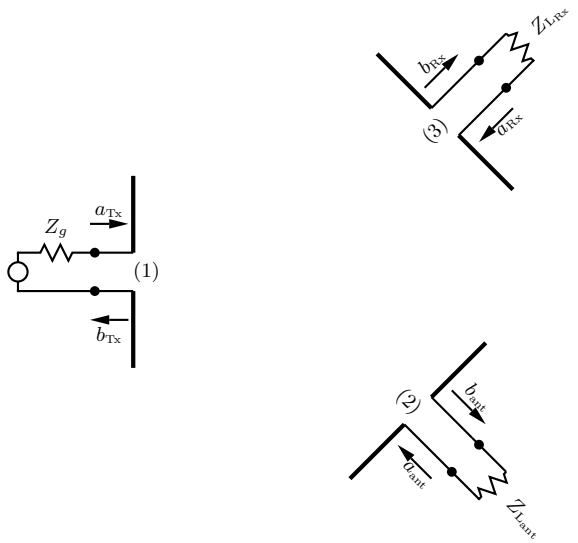

Figure A.5: Circuital representation using power waves of the bi-static measurement.

Similarly to the previous section, by definition $S_{22} = \rho_{\mathrm{in_{ant}}}|_{Z_g=Z_{\mathrm{o}}} = \frac{Z_{\mathrm{ant}}-Z_{\mathrm{o}}}{Z_{\mathrm{ant}}+Z_{\mathrm{o}}}$ finally obtaining:

$$\Delta\rho_{\mathrm{rdr}} = S_{21}^2 \frac{\rho_{\mathrm{L}_A} - \rho_{\mathrm{L}_B}}{\left(1-\rho_{\mathrm{in}_2}\rho_{\mathrm{L}_A}\right)\left(1-\rho_{\mathrm{in}_2}\rho_{\mathrm{L}_B}\right)} = \underbrace{S_{21}^2 \frac{\left(Z_{\mathrm{ant}}+Z_{\mathrm{o}}\right)^2}{2Z_{\mathrm{o}}}}_{Z_{tr}} \frac{Z_{\mathrm{L}_A} - Z_{\mathrm{L}_B}}{\left(Z_{\mathrm{ant}}+Z_{\mathrm{L}_A}\right)\left(Z_{\mathrm{ant}}+Z_{\mathrm{L}_B}\right)} \tag{A.25}$$

Which provides an alternative definition of the transfer impedance based on the S-parameters S_{21}.

A.4 Transfer impedance formulation based in scattering parameters for a bi-static approach

It is possible to obtain a similar expression for a bi-static configuration [122]. In this case a 3-port block must be considered and the transmission parameter $\Delta\tau_{\mathrm{Rx,Tx}}$ is the parameter of interest (refer to Fig. A.5 for definition of ports and sensors.

$$\mathbf{b} = \begin{pmatrix} b_{\mathrm{Tx}} \\ b_{\mathrm{ant}} \\ b_{\mathrm{Rx}} \end{pmatrix} = \begin{pmatrix} S_{11} & S_{12} & S_{13} \\ S_{21} & S_{22} & S_{23} \\ S_{31} & S_{32} & S_{33} \end{pmatrix} \cdot \begin{pmatrix} a_{\mathrm{Tx}} \\ a_{\mathrm{ant}} \\ a_{\mathrm{Rx}} \end{pmatrix} = \mathbf{S} \cdot \mathbf{a} \tag{A.26}$$

Assuming a matched transmitter at port 1 ($Z_g = Z_{\mathrm{o}}$), a matched receiver at port 3 ($Z_{\mathrm{L_{Rx}}} = Z_{\mathrm{o}}$), and a loaded port 2 ($Z_{\mathrm{L_{ant}}} = Z_{\mathrm{L}_{A,B}}$), the parameter $\tau_{31} = \frac{b_{\mathrm{Rx}}}{a_{\mathrm{Tx}}}$ is obtained from:

$$\mathbf{b} = \left(\mathbf{I} - \mathbf{S} \cdot \mathrm{diag}\begin{pmatrix} 0 & \rho_{\mathrm{L}} & 0 \end{pmatrix}\right)^{-1} \cdot \mathbf{S} \cdot \begin{pmatrix} a_{\mathrm{Tx}} \\ 0 \\ 0 \end{pmatrix} \tag{A.27}$$

Finally after developing the two sets of loads and taking the difference::

$$\Delta\tau_{\mathrm{Rx,Tx}} = S_{21}S_{31}\frac{(\rho_{\mathrm{L}_A}-\rho_{\mathrm{L}_B})}{(1-S_{22}\rho_{\mathrm{L}_A})\,(1-S_{22}\rho_{\mathrm{L}_B})} = \underbrace{S_{21}S_{32}\frac{(Z_{\mathrm{ant}}+Z_{\mathrm{o}})^2}{2Z_{\mathrm{o}}}}_{Z_{tr}^{\mathrm{bis}}}\frac{Z_{\mathrm{L}_A}-Z_{\mathrm{L}_B}}{(Z_{\mathrm{ant}}+Z_{\mathrm{L}_A})\,(Z_{\mathrm{ant}}+Z_{\mathrm{L}_B})} \tag{A.28}$$

Developing the product $S_{21}S_{32}$ or equivalently $S_{21}S_{23}$:

$$S_{21}S_{32} = S_{21}S_{23} = \frac{V_{\mathrm{ant,Tx}}^{\mathrm{OC}}\cdot V_{\mathrm{ant,Rx}}^{\mathrm{OC}}}{a_{\mathrm{Tx}}a_{\mathrm{Rx}}}\frac{Z_o}{(Z_{\mathrm{ant}}+Z_{\mathrm{o}})^2} \tag{A.29}$$

where $V_{i,j}^{\mathrm{OC}}$ represents the open circuit voltage in port i when the excitation is at port j and the third port is loaded with Z_{o}. And finally:

$$\Delta\tau_{\mathrm{Rx,Tx}} = \frac{V_{\mathrm{ant,Tx}}^{\mathrm{OC}}\cdot V_{\mathrm{ant,Rx}}^{\mathrm{OC}}}{2a_{\mathrm{Tx}}a_{\mathrm{Rx}}}\frac{Z_{\mathrm{L}_A}-Z_{\mathrm{L}_B}}{(Z_{\mathrm{ant}}+Z_{\mathrm{L}_A})\,(Z_{\mathrm{ant}}+Z_{\mathrm{L}_B})} \tag{A.30}$$

It is readily observed that $\frac{V_{\mathrm{ant,Tx}}^{\mathrm{OC}}}{a_{\mathrm{Tx}}}$ represents the normalized open circuit voltage at the probe antenna when port 1 acts as a transmitter and port 3 is loaded and similarly for the term $\frac{V_{\mathrm{ant,Rx}}^{\mathrm{OC}}}{a_{\mathrm{Rx}}}$ with port 3 acting as the transmitter and port 1 loaded. It must be noted that (A.30) becomes (A.20) or (2.23) when port 3 and port 1 become the same.

A.5 Multiple MST probes

The previous sections have shown the common formulation where there is a transmitter and an MST probe. Nevertheless the scenarios might be much more complex than that, with several MST probes close to each others. Under this scenario, the following would be the general formulation governing the differential response, and the previous formulation would be a particularization for the case of a single element array.

A.5.1 S-Parameter formulation

To determine the influence of the multi-port configuration in the backscattering response of a single element, the mutual coupling between the different elements of the array must be taken into account. Fig. A.6a presents the sketch of the multi port network, which consists of a transmitting/receiving antenna (identified with the index 0), the N elements of the MST array, and the N termination loads ρ_{L_i} of the array elements. In the following the transmitter is assumed to be connected to a canonical generator ($Z_g = Z_{\mathrm{o}}$).
Fig. A.6b presents the scattering matrix $\mathbf{S}^{\mathrm{MP}}$ for the whole multi-port. For compactness of the following discussion, the matrix is divided in 4 sub-matrices: element $S_{\mathrm{rdr,rdr}}$ represents the self-scattering of the transmitter, vectors $\mathbf{s}_{\mathrm{rdr},X}$ and $\mathbf{s}_{\mathrm{rdr}X}^{\intercal}$ represent the coupling between the transmitter and each element of the array and $\mathbf{S}$ refers to the scattering between elements of the array. The latter would be the same as the scattering matrix of the array when isolated, provided that the effect of the transmitting antenna can be neglected (low scattering reader, or large distance). Similarly the wave vectors $\mathbf{b}^{\mathrm{MP}}$, $\mathbf{a}^{\mathrm{MP}}$ are subdivided into b_{rdr}, a_{rdr} and $\mathbf{b}$, $\mathbf{a}$.

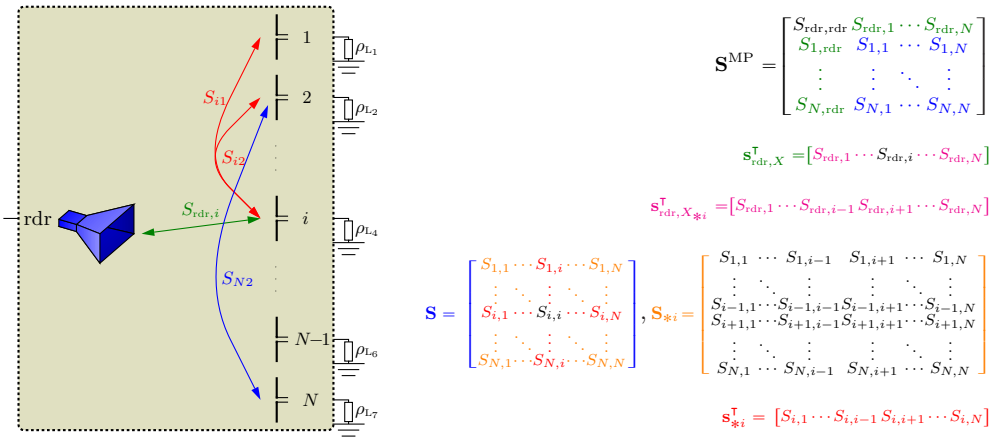

(a) Diagram **(b)** S-parameters matrices

Figure A.6: (a) S-parameters of the MST array. (b) presents the nomenclature and subdivisions of the matrix S^{MP}, the sub-index in $\mathbf{A}_{*i}$ ($\mathbf{a}_{*i}$) refers to the sub-matrix (sub-vector) without the elements corresponding to the i-column and row (i-element).

Taking into account this notation, and making use of the relation $\mathbf{b}^{\mathrm{MP}} = \mathbf{S}^{\mathrm{MP}}\mathbf{a}^{\mathrm{MP}}$:

$$b_{\mathrm{rdr}} = S_{\mathrm{rdr,rdr}} \cdot a_{\mathrm{rdr}} + \mathbf{s}^{\intercal}_{\mathrm{rdr},X} \cdot \mathbf{a} = S_{\mathrm{rdr,rdr}} a_{\mathrm{rdr}} + \mathbf{s}^{\intercal}_{\mathrm{rdr},X} \cdot \mathbf{\Gamma}_{\mathrm{L}} \cdot \mathbf{b} \tag{A.31}$$

$$\mathbf{b} = \mathbf{s}_{\mathrm{rdr},X} \cdot a_{\mathrm{rdr}} + \mathbf{S} \cdot \mathbf{a} = \mathbf{s}_{\mathrm{rdr},X} a_{\mathrm{rdr}} + \mathbf{S} \cdot \mathbf{\Gamma}_{\mathrm{L}} \cdot \mathbf{b} \tag{A.32}$$

where $\mathbf{\Gamma}_{\mathrm{L}}$ is a diagonal matrix where each element i of the diagonal corresponds to the reflection coefficient of the termination load (ρ_{L_i}) at the array element i. Finally the input reflection coefficient at the transmitter is:

$$\begin{aligned} \rho_{\mathrm{rdr}} &= S_{\mathrm{rdr,rdr}} + \mathbf{s}^{\intercal}_{\mathrm{rdr},X} \cdot \mathbf{\Gamma}_{\mathrm{L}} \cdot (\mathbf{I} - \mathbf{\Gamma}_{\mathrm{L}} \cdot \mathbf{S})^{-1} \mathbf{s}_{\mathrm{rdr},X} = \\ &= S_{\mathrm{rdr,rdr}} + \mathbf{s}^{\intercal}_{\mathrm{rdr},X} \cdot \left(\mathbf{\Gamma}_{\mathrm{L}}^{-1} - \mathbf{S}\right)^{-1} \mathbf{s}_{\mathrm{rdr},X} \end{aligned} \tag{A.33}$$

Similarly, it is possible to obtain the input reflection coefficient for each port of the elements of the array as:

$$\rho_{\mathrm{in}_i} = S_{ii} + \mathbf{s}^{\intercal}_{*i} \cdot \left(\mathbf{\Gamma}^{-1}_{\mathrm{L}_{*i}} - \mathbf{S}_{*i}\right)^{-1} \mathbf{s}_{*i} \tag{A.34}$$

where $\mathbf{S}_{*i}$ refers to the sub-matrix obtained after removing the i-row and i-column from matrix $\mathbf{S}$, and $\mathbf{s}_{*i}$ refers to the vector resulting from the i-column of $\mathbf{S}$ without the ith-element (see Fig. A.6 for a sketch of both of them).
When an MST measurement is carried out, only the element i of the array changes its termination load from ρ_{L_A} to ρ_{L_B}, therefore the termination matrix Γ_{L} will have its i diagonal element modified by $\Delta\rho_{\mathrm{L}} = \rho_{\mathrm{L}_A} - \rho_{\mathrm{L}_B}$. In the following, and without loss of generality but to simplify the notation, the element i is considered the last element of the matrix. Accordingly matrix $\mathbf{\Gamma}^{-1}_{\mathrm{L}_B}$ is expressed as:

$$\mathbf{\Gamma}^{-1}_{\mathrm{L}_B} = \mathbf{\Gamma}^{-1}_{\mathrm{L}_A} + diag\left(0, \cdots, \frac{\Delta\rho_{\mathrm{L}}}{\rho_{\mathrm{L}_A}\rho_{\mathrm{L}_B}}, \cdots, 0\right) \tag{A.35}$$

Let $\mathbf{D}_{A,B} = \left(\mathbf{\Gamma}_{\mathrm{L}_{A,B}}^{-1} - \mathbf{S}\right)^{-1}$, then matrix $\mathbf{D}_B$ can be obtained as a function of $\mathbf{D}_A$ (see appendix F.1):

$$\mathbf{D}_B = \mathbf{D}_A + \begin{bmatrix} \mathbf{d}_{A_{*i}} \\ D_{A_{ii}} \end{bmatrix} \begin{bmatrix} \mathbf{d}_{A_{*i}}^{\intercal} & D_{A_{ii}} \end{bmatrix} \frac{\Delta\rho_{\mathrm{L}} \left(1 - \rho_{\mathrm{L}_A}\Gamma_{\mathrm{in}_i}\right)}{\rho_{\mathrm{L}_A}^2 \left(1 - \rho_{\mathrm{L}_B}\Gamma_{\mathrm{in}_i}\right)} \tag{A.36}$$

where the values of $D_{A_{ii}}$ and $\mathbf{d}_{A_{*i}}$ can be found applying the inversion of a partitioned matrix, see appendix F.2:

$$\mathbf{d}_{A_{*i}} = \left(\mathbf{\Gamma}_{\mathrm{L}_{*i}}^{-1} - \mathbf{S}_{*i}\right)^{-1} \mathbf{s}_{*i} \cdot \left(\rho_{\mathrm{L}_A}^{-1} - \rho_{\mathrm{in}_i}\right)^{-1} \tag{A.37}$$

$$D_{A_{ii}} = \left(\rho_{\mathrm{L}_A}^{-1} - \rho_{\mathrm{in}_i}\right)^{-1} \tag{A.38}$$

Finally, Introducing (A.36) into (A.33) and developing:

$$\Delta\rho_{\mathrm{rdr}} = \rho_{\mathrm{rdr}}^{A} - \rho_{\mathrm{rdr}}^{B} = -\left(S_{0i} + \mathbf{s}_{0X_{*i}}^{\intercal} \cdot \left(\mathbf{\Gamma}_{\mathrm{L}_{*i}}^{-1} - \mathbf{S}_{*i}\right)^{-1} \mathbf{s}_{*i}\right)^2 \frac{\Delta\rho_{\mathrm{L}_i}}{\left(1 - \rho_{\mathrm{L}_A}\rho_{\mathrm{in}_i}\right)\left(1 - \rho_{\mathrm{L}_B}\rho_{\mathrm{in}_i}\right)} \tag{A.39}$$

which can be developed to obtain the common formulation:

$$\Delta\rho_{\mathrm{rdr}} = \underbrace{\left(S_{\mathrm{rdr},i} + \mathbf{s}_{\mathrm{rdr},X_{*i}}^{\intercal} \cdot \left(\mathbf{\Gamma}_{\mathrm{L}_{*i}}^{-1} - \mathbf{S}_{*i}\right)^{-1} \mathbf{s}_{*i}\right)^2}_{Z_{tr_{\mathrm{i}}}^{\mathrm{MP}}} \frac{\left(Z_{\mathrm{ant_i}} + Z_o\right)^2}{2Z_o} \frac{\left(Z_{\mathrm{L}_A} - Z_{\mathrm{L}_B}\right)}{\left(Z_{\mathrm{L}_A} + Z_{\mathrm{ant_i}}\right)\left(Z_{\mathrm{L}_B} + Z_{\mathrm{ant_i}}\right)} \tag{A.40}$$

A.5.2 Z-Parameters formulation

Similarly to the previous procedure it is possible to obtain a formulation for the differential input impedance of the transmitter as a function of the Z-parameters:

$$Z_{\mathrm{in}_{\mathrm{rdr}}} = Z_{\mathrm{rdr,rdr}} - \mathbf{z}_{\mathrm{rdr},X}^{\intercal} \left(\mathbf{Z} + \mathbf{Z}_{\mathrm{L}}\right)^{-1} \mathbf{z}_{\mathrm{rdr},X} \tag{A.41}$$

$$Z_{\mathrm{ant_i}} = Z_{ii} - \mathbf{z}_{*i}^{\intercal} \left(\mathbf{Z}_{*i} + \mathbf{Z}_{\mathrm{L}*i}\right)^{-1} \mathbf{z}_{*i} \tag{A.42}$$

where the contribution of the reader impedance in Z_{in_i} has been neglected assuming it is much smaller than the rest. Further developing the expression, the differential input impedance becomes:

$$\Delta Z_{\mathrm{in}_{\mathrm{rdr}}} = Z_{\mathrm{in}_{\mathrm{rdr}}}^{A} - Z_{\mathrm{in}_{\mathrm{rdr}}}^{B} = \left(Z_{\mathrm{rdr},i} - \mathbf{z}_{\mathrm{rdr},X_{*i}}^{\intercal} \left(\mathbf{Z}_{*i} + \mathbf{Z}_{\mathrm{L}*i}\right)^{-1} \mathbf{z}_{*i}\right)^2 \frac{\left(Z_{\mathrm{L}_A} - Z_{\mathrm{L}_B}\right)}{\left(Z_{\mathrm{L}_A} + Z_{\mathrm{ant_i}}\right)\left(Z_{\mathrm{L}_B} + Z_{\mathrm{ant_i}}\right)} \tag{A.43}$$

For a common MST scenario, it is reasonable to consider that $\Delta Z_{\mathrm{in}_{\mathrm{rdr}}}$ is much smaller that Z_{in} and Z_{o}. As such, $\Delta Z_{\mathrm{in}_{\mathrm{rdr}}}$ can be related to $\Delta\rho_{\mathrm{rdr}}$ using (A.19) as:

$$\Delta\rho_{\mathrm{rdr}} = \frac{2Z_{\mathrm{o}}\Delta Z_{\mathrm{in}_{\mathrm{rdr}}}}{\left(Z_{\mathrm{in}_{\mathrm{rdr}}}^{A} + Z_{\mathrm{o}}\right)\left(Z_{\mathrm{in}_{\mathrm{rdr}}}^{B} + Z_{\mathrm{o}}\right)} \approx \frac{2Z_{\mathrm{o}}}{\left(Z_{\mathrm{in}_{\mathrm{rdr}}} + Z_{\mathrm{o}}\right)^2} \Delta Z_{\mathrm{in}_0} \tag{A.44}$$

Both S-Parameter and Z-parameter formulation have obtained a final expression involving the input impedance from port i, $Z_{\mathrm{ant_i}}$. It must be noted that the definition of this value is different for each formulation, since the loading conditions in both formulation for reader's port is different: in S-parameters it has been assumed $Z_g = Z_{\mathrm{o}}$, whilst for the Z-formulation the contributions has been neglected, which is effectively equivalent to an open circuit. However provided that the coupling between probes and self-coupling is much larger than the coupling with the reader, as expected, they are essentially equivalent.

A.5.3 Comments on the coupling error term

The coupling effects between the different elements of the array will determine the error in the measurements, however, a special note must be taken in what parameters are used to quantify this coupling and error. For instance, when Z-parameters are used in an array, the term Z_{0i} is assumed to be the parameter of interest (proportional to the field E), however, this is only valid if Z_{0i} does not change in the presence of the array, which according to its definition requires that the extra elements with an open-circuit as load do not affect the element i. This would be the case of an array of minimum scattering antennas, such as dipoles, but for other antennas such as slots, the definition of Z_{0i} wouldn't be constant, and in this case the formulation should be referred to $Y-$parameters that in the case of the slot remains constant.

B

Appendix B

RFID communication protocol

This appendix presents the most important aspects of the communication with UHF RFID tags as defined by the standard ISO 18000-6C (based in EPC Global RFID protocol [91]) which is one of the most commonly used UHF RFID protocols.

Due to local regulations, the frequency bands and power limits of UHF RFID change with the location as presented in Table B.1.

	Frequency [MHz]	Maximum power [W]	Regulation
Europe	868	2 ERP (3.3EIRP)	ETSI EN-300-220, EN-300-440 and EN-302-228
	915-921	4 EIRP	ETSI TR 102-649-2 (Under study)
USA	902-928	4 EIRP	FCC Part 15.247
Japan	952-954	4 EIRP (licensed)	Band Operative until March 31 2018
	952-954	0.02 EIRP (unlicensed)	www.soumu.go.jp
	915-928	0.25 EIRP	From July 25th 2012
Australia	918-926	4 EIRP	Radiocommunications (Low Interference Potential Devices) Class License 2000, Variation notice 1

Table B.1: Frequencies and maximum power levels of RFID for each operating zone.

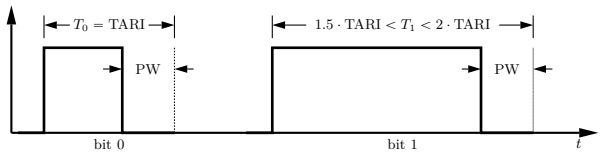

Figure B.1: Shape and duration for bits 0 and 1 as encoded by the reader. TARI is an important quantity since it will determine the maximum rate and the modulation response. It can be between 6.5 µs and 25 µs

B.1 Modulation and Encoding

The communication between reader and tag is defined as half-duplex, where the reader acts as the master, and it is the one that initiates the communication, to which the RFID tag responds accordingly before going back silent.
Modulation of the downlink, from the reader to the tag, can be in either double sideband amplitude shift keying (DSB-ASK), single sideband amplitude shift keying (SSB-ASK) or phase reversal amplitude shift keying (PR-ASK) with appropriate timings as shown in [91]. The modulating frequency is not fixed and can vary from 40 kHz to 160 kHz. Independently of the modulation, the downlink data is encoded with PIE, in which the symbols or bits 0 and 1 are encoded with a combination of high and low level pulses with different duration (see Fig. B.1). The duration of the symbol 0 is in part responsible for the data-rate and frequency of the uplink.
On the other end, the modulating frequency for the up-link is in the range from 40 kHz to 640 kHz. As opposed to the down-link, the frequency of modulation is fixed by the reader when the communication is established. Its value depends on some of the information encoded in the *QUERY* command (which will be introduced next), and the duration of signaling elements at its header. The modulation for the uplink is ASK, PSK, or a combination of both, and depends entirely of the tag. On the other hand, the encoding which is FM0 baseband or Miller encoding [91], is decided by the reader within the *QUERY* command.

B.2 Transmission cycle

When the reader is transmitting in an environment where multiple RFID tags are present, there is a high risk of collision between different tags that try to access the uplink simultaneously. Although the reader can issue a command that pre-selects a subset of the RFID tags, or even a single tag, in most of the application cases the identity of the tags is unknown beforehand and therefore it is necessary an anti-collision mechanism.
In the case of RFID tags this is solved, similarly as in ALOHA system, by the introduction of a compulsory acknowledge as well as the use of random tokens to start the communication. A time diagram on RFID communication is presented in Fig. B.2, with the different stages where the communication might be:

1. The reader pre-selects a subset of tags that fulfill a specific condition, for instance the manufacturers ID, by issuing the *SELECT* command. Tags that fulfill the condition encoded within the command mark themselves as selected and continue the round.

2. The reader sends a *QUERY* command to start the communication with the first RFID tag that answers it. Among other things the *QUERY* command establishes the encoding that the tag must use when responding, as well as establishing the modulation frequency of the response. Within the *QUERY* command a number (Q) between 0 and 15 is transmitted to the tags.
3. After receiving the *QUERY* command any tag previously selected uses the value Q to initialize an internal counter (C) with a random number between 0 and $2^Q - 1$. This counter will act as a token to allow transmission.
4. Any tag whose counter C reaches zero is allowed to respond to the *QUERY* command by sending a 16-bit random number that identifies *uniquely* the transaction; any other tag remains silent waiting until C is zero.
5. At this stage, if at least one tag has answered, there are two possibilities:
   (a) Only one tag responds the *QUERY* command to which the reader must acknowledge within the appropriate timing. This establishes a link between reader and tag that allows the exchange of information. After the communication is finished the tag singles itself out and no longer consider itself selected.
   (b) Two or more tags answer the initial *QUERY* at the same time, producing a collision to which the reader is unable to acknowledge. Upon no reception of acknowledge from the reader within the required timing, the tags that have answered the *QUERY* command reset their internal counter with a new random number between $2^Q - 1$.
6. After the communication round with a specific tag is complete, or after a waiting period if no communication has been established (due to collision or because no tag reached 0 in the internal counter), the reader sends a *QUERY_REP* command to try to start a new round.
7. Upon reception of the *QUERY_REP* command, selected tags decrease their internal counter and the cycle goes back to 4 and repeats until all tags have answered.

B.3 RFID Protocol Implementation

In this thesis most of the measurements concerning RFID tags use conventional laboratory instrumentation, namely a spectrum analyzer (Rohde & Schwarz FSL-6) to capture the response coming from the tag and a vector signal generator (Rohde & Schwarz SMJ100A) to modulate the interrogating signals. With this equipment is not possible to comply with the tight timing requirements of the RFID protocol that would allow a full communication with the tag; in particular the demodulation and acknowledgment of the RN16 coming from the tag is not possible in real-time due to the latency between the instrumentation and the computer. However, by properly modulating a *SELECT* command to single out a specific tag, and capturing the RN16 code that comes as a response to the *QUERY* command, the electromagnetic information of the RFID tag can be captured, as will be seen in chapters 3 and 4. Note that in the case of multiple tags present, it is required the knowledge of the ID of each tag to be able to isolate each separately to differentiate the responses.

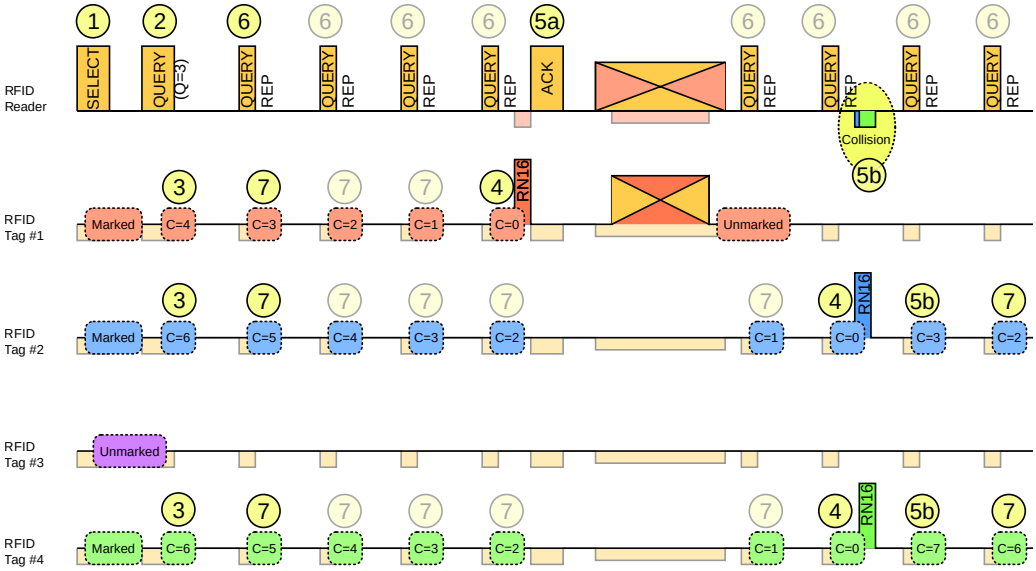

Figure B.2: Graphical representation of the RFID transmission cycle. The numbers represent the step/state produced at each instant

B.3.1 Experimental identification of the RFID codes without a complete reader

If no RFID reader is available, and the equipment is not capable of processing and generating an interactive response with the proper timings as established by the RFID protocol, only an exhaustive search can be used to determine the RFID IDs of the tags under study. Two different sequences of commands can be used to obtain the IDs in these conditions. On the one hand, the command *SELECT* can single out each and all the possible IDs consecutively while setting Q=0 in the *QUERY* command. This ensures that if the code being singled out is of one of the RFID tags being tested, it will answer with RN16 after the *QUERY* command. By capturing the response (or lack of response) the presence of a tag with this code can be detected. This must be repeated for all the possible codes (or code portions if a mask is used) to detect them. Due to the length of possible codes, this exhaustive search can take a long while, although this time can be shorten by progressively masking out the IDs, that is identifying it bit by bit.

An alternative approach is to make use of the measurement cycle of Fig. B.2. In this case although the transmitter is unable to respect the timings to generate the proper ACK using the RN16 transmitted by the tag, it is possible to use a fake ACK for a fixed code, and issue a READ code just afterwards requesting the ID. By capturing the response to the READ command, the ID of the tag will be obtained. Since RN16 consists of 16 bits, there will be a total of 65536 possible combinations, but unlike the previous method, this one could interrogate multiple tags at the same time, since collision would not be a problem since only the tag that has issued the same code of the ACK will respond.

However, when interrogating tags initialized by the manufacturer, it is quite common that they come pre-initialized with a consecutive sequence of IDs, so that by identifying the

first with either method, it is easy to determine the code of the subsequent tags.
The identification of the tags was implemented using software defined radio, although the details of the implementation are out of the scope of the thesis, and will not be included.

C

Appendix C

Non-linear input impedance of a rectifying circuitry

This appendix tries to derive an expression that can be of use to understand the non-linear behavior that should be expected in an RFID IC. It must be noted that each RFID IC may use a different configuration, for instance MOS diode-connected transistors, that directly affect the final behavior of the input impedance of the rectifier. A proper characterization of the impedance can be done experimentally as done in chapters 3 and 4

C.1 Rectifying circuitry

The rectifying circuitry can be viewed as a charge pump module, based on Dickson multi-stage rectifier [84], which is a voltage multiplier rectifier. Fig. C.1 shows two rectifiers with a different number of stages. The ratio between the output DC voltage to the input RF voltage is approximately proportional to the number of diodes, $2N$ with N the number of stages, although the load current and the threshold voltage of the diodes will limit the total output voltage [123]:

$$V_o = \left(V_g \cdot \frac{C_c}{C_c + C_s} - V_d \right) \cdot 2N - \frac{I_L \cdot 2N}{(C_c + C_s) \cdot f} \tag{C.1}$$

where C_c are the coupling capacitors, C_s the stray capacitance of the diodes (parallel capacitance to the diode), N the number of stages, f the frequency and V_g, V_o and V_d the input, output and threshold voltage respectively. It must be taken into account that V_d is not a constant but depends on the actual current going through the diode so this

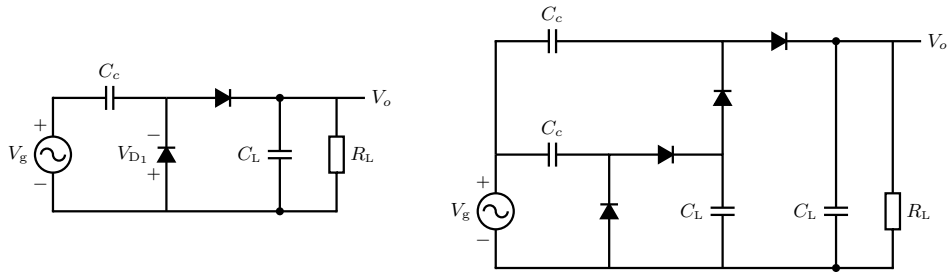

(a) Single stage (2×) **(b)** Double stage (4×)

Figure C.1: Configuration of a charge pump rectifier. (a) presents a voltage double, consisting of a single stage, and (b) is a 4x multiplier with 2 stages

is just an approximated expression that might not be suitable for extremely low input powers, where the threshold is less well-defined. At UHF frequencies the second term is usually negligible for the levels of operation.
The selection of the diodes determines in great measure the efficiency of the power harvesting; in particular low threshold voltage [85] and high saturation current [124] allow greater output voltage for low power. Schottky diodes are among the best options to improve efficiency of the system [90] , although they require special fabrication processes and might not be suitable in CMOS processes. Another option is the use of diode-connected MOSFET transistors [85], since they can be integrated in the CMOS fabrication processes, reducing manufacturing costs, although its efficiency can be worse due to the channel resistance and threshold voltages.
To determine the input impedance of the rectifier it is necessary to introduce the I-V curve of the diode in the analysis:

$$i_d = I_S \cdot \left(e^{\frac{v_d}{nV_T}} - 1 \right) \tag{C.2}$$

where I_s is the saturation current of the diode, V_d is the voltage in the diode terminals, n is the ideality factor, and $V_T = \frac{kT}{e}$ is the thermal voltage (about 25.8mV at 300K) where k is Boltzmann constant, e the electron charge and T the temperature. However, for real diodes, additional components must be taken into account, such as series resistance, junction capacitance and more complex models. Fig. C.2 presents a linearization of the

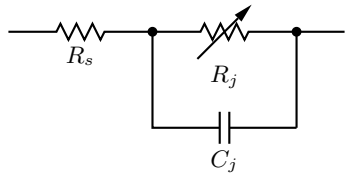

Figure C.2: Equivalent linear circuit of a Schottky diode

diode with the junction capacitance (C_j), the series resistance (R_s) and the junction resistance (R_j) whose value will depend on the biasing point of the diode. These extra components will need to be taken into account to obtain an accurate description of the rectifier input impedance.

Taking the previous into account, the analysis of the input impedance of the rectifier is divided in two steps, the first obtains a theoretical expression for an ideal rectifier without losses nor parasitic effects, and the second validates the expression and conclusions through circuit simulations for both ideal and realistic diodes.

C.2 Ideal Rectifier

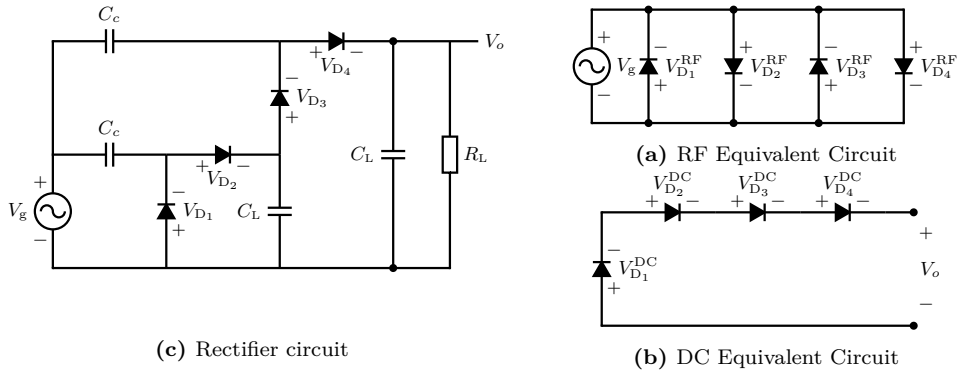

(c) Rectifier circuit

(a) RF Equivalent Circuit

(b) DC Equivalent Circuit

Figure C.3: Equivalent circuit of the rectifier under steady state. (a) High frequency equivalent, the capacitors become shortcircuits and the 2N diodes are in parallel. (b) DC equivalent, the capacitors do not let current go through, and the diodes are in series.

Provided that the capacitors in the rectifier are well-dimensioned, for steady state, it is reasonable to consider that the rectifier presents the following equivalent circuits for RF and DC:

- For RF signal, the input and output capacitors are short-circuited, see Fig. C.3a. The RF voltage at each diode is therefore $V_d^{RF} = \pm V_g$, with all the diodes in parallel (the sign depending on the orientation of the diode).
- For the DC component, the capacitors are open circuits, see Fig. C.3b. In this case the diodes are connected in series, and assuming the same characteristics for all of them, the DC voltage at each diode is equally divided $V_d^{DC} = -\frac{V_o}{2N}$.

As such the biasing conditions of the diodes in steady state become:

$$v_d = -\frac{V_o}{2N} \pm V_g \cos(2\pi f t) \tag{C.3}$$

Therefore the RF input impedance of a 2N-stage rectifier consists of the parallel of 2N diodes with a DC bias of $V_{d_1}^{DC}$, and therefore it will be a parallel of the junction resistance obtained through (C.2) using the steady state biasing conditions of (C.3),

$$i_d = I_s \cdot \left(e^{-\frac{V_o}{2N \cdot n V_T} \pm \frac{V_g}{n V_T} \cos(2\pi f t)} - 1 \right) \tag{C.4}$$

Due to the exponential, although v_g consisted of a single tone, the current consists of a set of harmonics. The exponential in I_d can be expanded using the modified Bessel function

expansion [125]:

$$e^{x\cos(2\pi ft)} = B_0(x) + 2\sum_{i=1}^{\infty} B_i(x)\cos(2\pi ift) \tag{C.5}$$

and taking into consideration that $B_i(-x) = (-1)^i \cdot B_i(x)$, the current for each frequency harmonic is:

$$\begin{aligned}
I_{DC} \to i = 0, \qquad & I_s \cdot \left[B_0\left(\frac{V_g}{n\cdot V_T}\right)\cdot e^{-\frac{V_o}{2N\cdot nV_T}} - 1\right] = I_L \\
I(f_1) \to i = 1, \quad & \pm 2I_s \cdot B_1\left(\frac{V_g}{n\cdot V_T}\right)\cdot e^{-\frac{V_o}{2N\cdot nV_T}} = \pm 2\left(I_L + I_s\right)\frac{B_1\left(\frac{V_g}{n\cdot V_T}\right)}{B_0\left(\frac{V_g}{n\cdot V_T}\right)}
\end{aligned} \tag{C.6}$$

$$I(2f_1) \to i = 2, \qquad 2I_s \cdot B_2\left(\frac{V_g}{n\cdot V_T}\right)\cdot e^{-\frac{V_o}{2N\cdot nV_T}} = 2\left(I_L + I_s\right)\frac{B_2\left(\frac{V_g}{n\cdot V_T}\right)}{B_0\left(\frac{V_g}{n\cdot V_T}\right)} \tag{C.7}$$

and the diode equivalent resistance (R_j) at the operating frequency:

$$\hat{R}_j(V_g, V_o) = \frac{\pm V_g}{I_{RF}} = \frac{V_g}{2I_s B_1\left(\frac{V_g}{nV_T}\right)\cdot e^{-\frac{V_o}{2N\cdot nV_T}}} \tag{C.8}$$

and the output voltage can be obtained, developing (C.6) as:

$$V_o = 2N\cdot nV_T \cdot \ln\left(B_o\left(\frac{V_g}{nV_T}\right)\right) - 2N\cdot \underbrace{nV_T\cdot\ln\left(\frac{I_L}{I_s}+1\right)}_{\text{DC Voltage drop in 1 diode}} \tag{C.9}$$

which at large voltage is equivalent to (C.1). Equation (C.8) is clearly dependent on the load conditions, through (C.9), as well as on the input RF power.

C.2.1 Diode equivalent resistance for a given load current

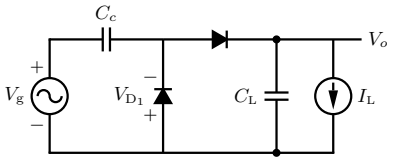

Figure C.4: The load is assumed to consume a constant current, therefore it is represented by a current source

Under the assumption that the rectifying stage of the RFID IC is followed by a series regulator, such as a low-quiescent current LDO [88] and provided that the output voltage is above the minimum required voltage, the current consumption of the load can be

assumed as constant. As such, the load can be substituted by a current source for the analysis, see Fig. C.4. With this hypothesis $\hat{R}_j$ becomes:

$$\hat{R}_j = \frac{V_g}{2 \cdot (I_s + I_L)} \cdot \frac{B_0\left(\frac{V_g}{nV_T}\right)}{B_1\left(\frac{V_g}{nV_T}\right)} \tag{C.10}$$

Which can be evaluated for the asymptotic cases of small input voltage and large input voltage.

C.2.1.1 Asymptotic case. Low input voltage

When the argument of the Bessel function $\frac{V_g}{nV_T}$ is close to 0 (which corresponds to a small input voltage V_g), the modified Bessel functions are approximated as:

$$B_0(x) \approx 1 \tag{C.11}$$

$$B_1(x) \approx \frac{x}{2} \tag{C.12}$$

which after introducing in (C.10) gives an equivalent resistance

$$\hat{R}_j = \frac{nV_T}{I_s + I_L} \tag{C.13}$$

that corresponds to the equivalent resistance in the small-signal model of a biased diode. However, it can be shown that for an operative RFID IC, the input voltage will be too large for the previous approximation, and thus we will never truly detect this asymptotic resistance. In fact, the minimum V_g can be obtained setting $V_o = 0V$ and the output current at I_L, resulting in the relation of the Bessel function as:

$$B_0\left(\frac{V_g}{nV_T}\right) = 1 + \frac{I_L}{I_s} \tag{C.14}$$

Therefore this asymptotic case although numerically correct, will not appear in an RFID IC under conventional operation mode, although as will be shown later, it will be of importance when an analysis having two tones is considered in section C.6.

C.2.1.2 Asymptotic case. Large input voltage

Similarly to the previous section, the modified Bessel function can be approximated for large arguments as:

$$\begin{aligned} B_0(x) &\approx \frac{e^x}{\sqrt{2\pi x}} \sum_{p=0}^{\infty} \frac{\prod_{i=0}^{p}(2i-1)^2}{p!(8x)^p} \\ B_1(x) &\approx \frac{e^x}{\sqrt{2\pi x}} \left(1 + \sum_{p=1}^{\infty} \frac{\prod_{i=1}^{p}(4-(2i-1)^2)}{p!(8x)^p}\right) \end{aligned} \tag{C.15}$$

and considering only the first term of the series and introducing it in (C.10), it is possible to obtain an expression for the junction resistance as:

$$\hat{R}_j = \frac{V_g}{2 \cdot (I_s + I_L)} \cdot \underbrace{\frac{8\frac{V_g}{nV_T} + 1}{8\frac{V_g}{nV_T} - 3}}_{\approx 1} \tag{C.16}$$

which results in an impedance that depends in V_g as well as I_L in agreement with [123].

C.2.2 Diode equivalent resistance for a given output voltage

For the sake of completeness the case of a given output voltage, independent of the load is analyzed. This would be the case of a rectifier followed by a regulator that adds a parallel load to increase the current consumption to keep the output voltage at a given value [88]: In this case, the asymptotic expressions becomes:

C.2.2.1 Small input voltage

Making use of (C.12) and (C.8) the equivalent resistance is:

$$\hat{R}_j = \frac{n \cdot V_T}{I_s} \cdot e^{\frac{V_o}{2N \cdot nV_T}} \tag{C.17}$$

Although mathematically the expression allows for any desired output voltage, similarly to to the case of a given output current, the output current must be positive, to ensure that the rectifier is acting as a supply. This establishes a minimum supply voltage:

$$B_o\left(\frac{V_g}{nV_T}\right) \geq e^{\frac{V_o}{2N \cdot nV_T}} \tag{C.18}$$

C.2.2.2 Large input voltage

Similarly, when the input voltage is large, the junction resistance of the diode becomes:

$$\hat{R}_j = 4\frac{V_g^2\sqrt{2\pi V_g}}{I_s \cdot nV_T\sqrt{nV_T}\left(\frac{8V_g}{nV_T} - 3\right)} e^{\frac{V_o}{2N \cdot nV_T} - \frac{V_g}{nV_t}} \tag{C.19}$$

C.3 Non-ideal diode rectifier

In the previous section an ideal diode without any parasitic element has bee considered, however to obtain the equivalent input impedance these parasitic elements (R_s and C_j, among others for a complete diode model) must be taken into account. The complete analysis taking into account the different parasitic elements will not be carried out in this thesis, and instead will be using numerical simulations and harmonic balance using Agilent ADS [126]. However, a first analytical approximation will be carried out assuming that the parasitic elements do not greatly modify the biasing conditions of the diode, so that the junction resistance will not change, and the parasitic elements can be added

Parameters			Parameters		
Saturation Current	I_s	3 µA	Non-ideality	n	1.06
Series Resistance	R_s	25 Ω	Junction Voltage	V_j	0.35 V
Energy Gap	E_G	0.68eV	Grading coefficient	M	0.5
Saturation current Temperature Exponent	XTI	2	Zero-bias Junction Capacitance	C_{jo}	0.18 pF
Reverse breakdown Voltage	B_v	3.8 V	Breakdown Current	I_{BV}	300 µA

Table C.1: SPICE parameters of HSMS-285x diodes [127]

a-posteriori. In this case, the junction capacitance for reverse biased diodes is obtained through the zeros-bias junction capacitance (C_{jo}) as:

$$C_j = C_{jo} \cdot \frac{1}{\left(1 - \frac{V_{bias}}{V_j}\right)^M} = C_{jo} \cdot \frac{1}{\left(1 - \frac{V_o}{2N \cdot V_j}\right)^M} \tag{C.20}$$

where V_j, the junction voltage, is a characteristic of the diode.
Finally the input impedance of the rectifier of N-stages with an input capacitor C_c becomes:

$$Z_{\text{in}}(f) = \frac{1}{2N} \cdot \underbrace{\left(R_s + \frac{1}{R_j^{-1} + j2\pi f C_j} \right)}_{Z_f(f)} - \frac{j}{2N\pi f C_c} \tag{C.21}$$

C.4 Validation of the theoretical models with SPICE simulations

In order to validate the model, a rectifier circuit has been simulated using Agilent ADS simulation package [126]. The diodes for the simulations are based on zero bias Schottky Detector diodes by Avago Technlogies, HSMS-285x [127], whose most important spice parameters are summarized in table C.1. It must be noted that in this model, the parasitic effects that arise from the packaging of the diode have not considered.

C.4.1 Rectifier with ideal diodes

Initially the diode model used considers only the three two initial parameters from table C.1 to remove all parasitic behavior and it is compared with the derived expression for a fixed load current. The simulated circuit consists of a double stage rectifier as shown in Fig. C.1b, where the load has been switched to a current sink of value I_L and where the capacitors have a value of $C_s = 100\,\text{pF}$ and $C_L = 100\,\text{pF}$. The equivalent resistance for the double stage circuit is presented in Fig. C.5 for a set of different output currents and supply voltages. The dependence of the equivalent resistance of the diode with both the DC output load current and the input voltage are shown in the figure. For really low currents, below the saturation current I_s, the impedance is basically constant for a given V_g but as for larger values it becomes dependent on both parameters.

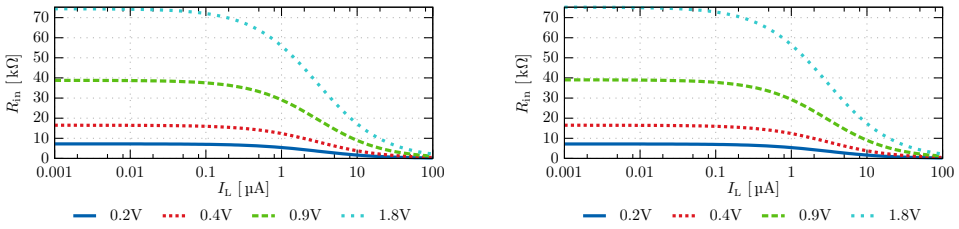

(a) Double stage simulation **(b)** Double stage asymptotic approximation

Figure C.5: Comparison of the input resistance of the rectifier of Fig. C.1b between the simulation (a) and the approximated expressions (b) for a diode that only specifies saturation current and non-ideality factor

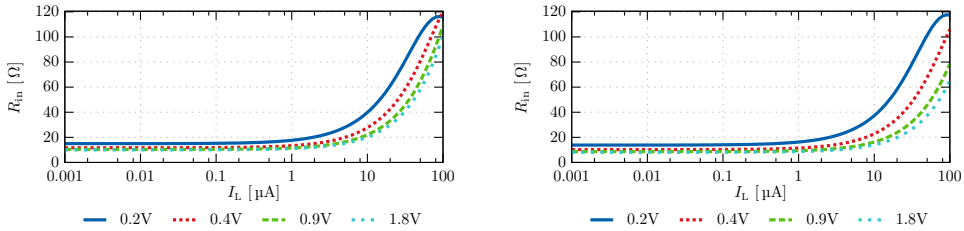

(a) Double stage simulation **(b)** Double stage asymptotic approximation

Figure C.6: Comparison of the input resistance of the rectifier of Fig. C.1b between the simulation (a) and the approximated expressions (b) for a real diode that makes use of all the diode parameters defined in Table C.1

C.4.2 Rectifier with non-ideal diodes

A rectifier with an ideal diode without parasitic effects showed a good agreement between analytical prediction and the simulation results; a new set of simulation is carried in this section with the complete model for the diode. This will impact the performance of the expression versus the simulation results in several ways:

- The output voltage and current are now limited by the breakdown limits, which is not taken into account by the analytical expressions.
- The capacitance is strongly dependent on the biasing voltage. In the expression (C.20) the ideal DC biasing voltage is assumed, however, it has been shown from the simulation that this is not accurate. A correcting factor is applied for this deviation, as explained next.

Figs. C.6 and C.7 present the resistance and reactance of the input impedance of the rectifier using the expressions and the approximated formulas. The analytical expressions still prove useful for determining the behavior of the impedance and the dependence with the incident voltage and the load currents of the system, however the reactance present a larger deviation (explained by the simplistic approximation used in the analytical expressions), however a better estimation can be obtained using a correction factor of 0.74 to correct a deviation observed in the junction capacitance with respect to the simulation,

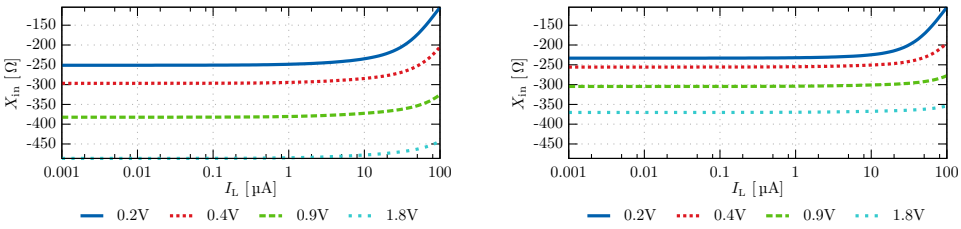

(a) Double stage simulation

(b) Double stage asymptotic approximation

Figure C.7: Comparison of the input reactance of the rectifier of Fig. C.1b between the simulation (a) and the approximated expressions (b) for a real diode that makes use of all the diode parameters defined in Table C.1

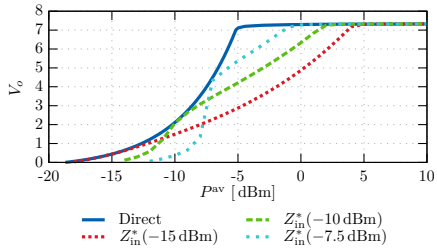

Figure C.8: Output voltage from the rectifier for different antenna impedances versus available power.

so that (C.20) becomes for this rectifier (the correction has been applied in Fig. C.7):

$$C_j = \frac{C_{jo}}{\left(1 - 0.74\frac{V_o}{2N \cdot V_j}\right)^M} \tag{C.22}$$

C.5 Generator influence in the input impedance

Up until now the input voltage to the rectifier has been applied directly to its input terminals, but in a real application the generator will have a given impedance. This input impedance will affect the input voltage at the feeding points of the rectifier, which will be unknown. Moreover, the voltage at the feeding points will consist of a main tone at the frequency of interest plus a series of harmonics, which if they were sufficiently large could lead to inaccuracies of the input impedance. This section presents a series of simulations to evaluate the effect of introducing a generator input impedance in the predicted performance and non-linear behavior of the rectifier.

First of all Fig. C.8 presents the output voltage of a double stage rectifier in terms of the available power at the generator when the current output load is 30 μA. The different curves correspond to a different generator impedance which corresponds to the conjugate of the input impedance of the rectifier at a different power level. For comparison purposes the direct connection output voltage has been plotted, although since P^{av} cannot be computed, the delivered power has been force to be $P^{in} = P^{av}$, equivalent to a perfect

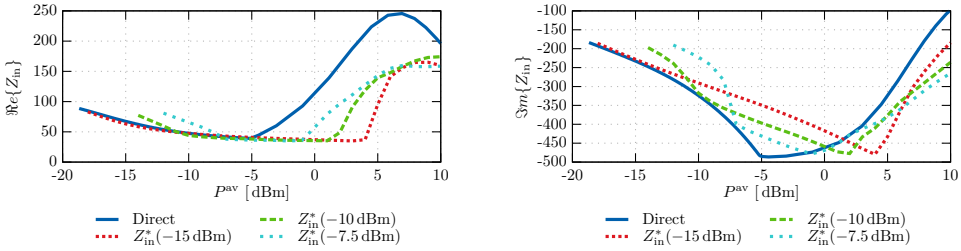

(a) Resistance **(b)** Reactance

Figure C.9: Input impedance of the rectifier versus available power for different generator impedances.

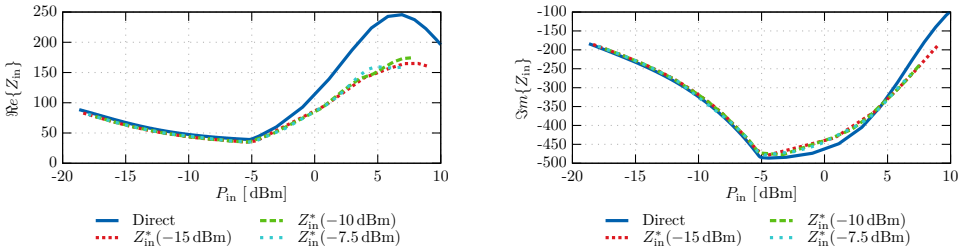

(a) Resistance **(b)** Reactance

Figure C.10: Input impedance of the rectifier versus delivered power for different generator impedances.

match at all power levels. Similarly Fig. C.9 shows the input impedance for the same circuits.

From the figures it can be concluded that the behavior of the rectifier seems different for each generator impedance, and as such the determination of the optimum input impedance will depend of the actual voltage divider configuration. However, it can be observed that whenever P^{av} reaches the value of conjugate matching of one of the generators (ensuring that $P^{in} = P^{av}$), the output voltage, and the input impedance is the same as that of the direct connection of a voltage source to the rectifier.

This clearly implies that the adequate parameter to use in the X-axis is not the P^{av} of the generator but rather the delivered power to the rectifier. As such, Fig. C.10 presents once again the input impedance of the rectifier (as in Fig. C.9), but plotted against the delivered power to the rectifier. All the different curves now overlap each other, until the point of saturation of the rectifier (approximately -5 dBm of delivered power for this simulations).

The fact that below the saturation point the different generators give basically the same input impedance implies that the harmonics at the input of the rectifier are having a negligible effect on the input impedance, however, after the saturation point is reached (which is in fact not considered in the previous theoretical analysis), this hypothesis is no longer true, and the harmonics become important which is what makes the direct connection curve be so different as the rest.

C.6 Rectifier behavior with two simultaneous tones

In the previous section a rectifier circuitry has been theoretically analyzed when the input signal consists of a single frequency; when the input signal consists of a more complex signal, for instance two different tones, the previous analysis is no longer valid, since the operation point of the diode will depend on the power associated to both signals. This section presents the expected behavior of the input impedance of the rectifier when a signal with 2 different frequencies is used to feed it. The procedure is similar to the development followed in the previous section. Taking as reference the charge pump of Fig. C.4, the input signal becomes $v_g = v_{g_1} + v_{g_2}$:

$$v_{g_1} = V_{g_1} \cos(2\pi f_1 t + \phi_1) \tag{C.23}$$
$$v_{g_2} = V_{g_2} \cos(2\pi f_2 t + \phi_2) \tag{C.24}$$

where an arbitrary phase independent for each frequency has been considered. Under the same asymptotic assumptions of the preceding section, the steady stage voltage between the terminals of a diode v_d:

$$v_d = -\frac{V_o}{2N} \pm (V_{g_1} \cos(2\pi f_1 t + \phi_1) + V_{g_2} \cos(2\pi f_2 t + \phi_2)) \tag{C.25}$$

Due to the non-linear behavior of the diode the presence of a tone generates multiple harmonics of the tone; in this case since the input signal corresponds to two frequencies, there will be a set of mixed harmonics whose amplitude generally depend on both $V_{g_{1,2}}$:

$$\begin{aligned} i_d =& I_s \cdot \left(e^{-\frac{V_o}{2N \cdot n V_T}} \left\{ B_0(\beta_1) + 2\sum_{p=1}^{\infty} B_p(\beta_1) \cos\left(p\left(2\pi f_1 t + \phi_1\right)\right) \right\} \cdot \right. \\ & \left. \left\{ B_0(\beta_2) + 2\sum_{q=1}^{\infty} B_q(\beta_2) \cos\left(q\left(2\pi f_2 t + \phi_2\right)\right) \right\} - 1 \right) \end{aligned} \tag{C.26}$$

where $\beta_i = \pm\frac{V_{g_i}}{nV_T}$ is used for compactness of the expression. Rearranging (C.26) in the set of mixed harmonics $f = pf_1 \pm qf_2$, and looking only at the frequencies of interest, f_1, f_2, the expression for the current phasors become:

$$\begin{aligned} I(f_1) = 2 \cdot I_s \cdot e^{-\frac{V_o}{2N \cdot n V_T}} \cdot \Bigg[& B_1(\beta_1) B_0(\beta_2) e^{j\phi_1} + \\ & 2\sum_{p=1}^{\infty} B_p(\beta_1) e^{jp\phi_1} \left[B_{q_1}(\beta_2) e^{-jq_1\phi_2} + B_{q_2}(\beta_2) e^{-jq_2\phi_2} \right] \Bigg] \\ I(f_2) = 2 \cdot I_s \cdot e^{-\frac{V_o}{2N \cdot n V_T}} \cdot \Bigg[& B_0(\beta_1) B_1(\beta_2) e^{j\phi_2} + \\ & 2\sum_{q=1}^{\infty} B_q(\beta_2) e^{jq\phi_2} \left[B_{p_1}(\beta_1) e^{jp_1\phi_1} + B_{p_2}(\beta_1) e^{jp_2\phi_1} \right] \Bigg] \end{aligned} \tag{C.27}$$

where p and q must ensure that the following conditions are fulfilled:

$$\begin{aligned} q_{1,2} =& \frac{f_1}{f_2}(p \pm 1) > 0, \quad q_{1,2} \in \mathbb{Z} \\ p_{1,2} =& \frac{f_2}{f_1}(q \pm 1) > 0, \quad p_{1,2} \in \mathbb{Z} \end{aligned} \tag{C.28}$$

For frequencies that are not multiples of each other, equation (C.28) guarantees that at least one of the values p or q is much greater than 1. Since $B_i(x) \to 0$ for $i \gg 1$, the series in (C.27) can be neglected and the dynamic resistance of the diode is:

$$\hat{R}_j(f_1) = \frac{\pm V_{g_1}}{I(f_1)} = \frac{\pm V_{g_1}}{2I_s \cdot e^{-\frac{V_o}{2N \cdot nV_T}} \cdot B_1(\pm\beta_1) B_0(\pm\beta_2)} = \frac{V_{g_1}}{2(I_s + I_L)} \frac{B_0(\beta_1)}{B_1(\beta_1)} \tag{C.29}$$

$$\hat{R}_j(f_2) = \frac{\pm V_{g_2}}{I(f_2)} = \frac{\pm V_{g_2}}{2I_s \cdot e^{-\frac{V_o}{2N \cdot nV_T}} \cdot B_0(\pm\beta_1) B_1(\pm\beta_2)} = \frac{V_{g_2}}{2(I_s + I_L)} \frac{B_0(\beta_2)}{B_1(\beta_2)} \tag{C.30}$$

where I_L is the DC current that goes through the diode and is equal to:

$$I_L \approx I_s \left[e^{-\frac{V_o}{2N \cdot nV_T}} B_0(\beta_1) B_0(\beta_2) - 1 \right] \tag{C.31}$$

C.6.1 Asymptotic behavior of the input impedance

In the previous section two opposite conditions, a small and a large input voltage, were analyzed to see that the approximated solution only made sense for large arguments, otherwise biasing conditions where not fulfilled for a given load current. For this case, a particularly interesting case is when one of the tones (f_2) presents a small amplitude while the other (f_1) is large enough to supply the current and biasing required by the rectifier.

Assuming $V_{g_1} \gg V_{g_2}$ and $V_{g_2} < nV_T$, the Bessel function can be approximated as in (C.12) and the output voltage takes the same expression as in (C.9) with V_{g_2} instead of V_g, and the input impedance at f_2 becomes:

$$\hat{R}_j(f_2) = \frac{nV_T}{I_s + I_L} \tag{C.32}$$

which equals the asymptotic expression found in (C.13), and the small signal equivalent model for a diode. As such, it is independent of the input voltage V_{g_2} and only depends on the bias point established by the load current. Similarly input impedance at f_1 becomes insensitive to changes of V_{g_2} as:

$$\hat{R}_j(f_1) = \frac{-V_{g_1}}{I(f_1)} = \frac{V_{g_1}}{2(I_L + I_s)} \frac{B_0\left(\frac{V_{g_1}}{nV_T}\right)}{B_1\left(\frac{V_{g_1}}{nV_T}\right)} \tag{C.33}$$

Although for a single input tone the approximation of $R_j(f_2)$ would not have been possible, since the required output current could not be achieved for low input voltages, in this case, since the tone at frequency f_1 is capable of establishing the biasing point (and providing the required current), this is a acceptable solution.

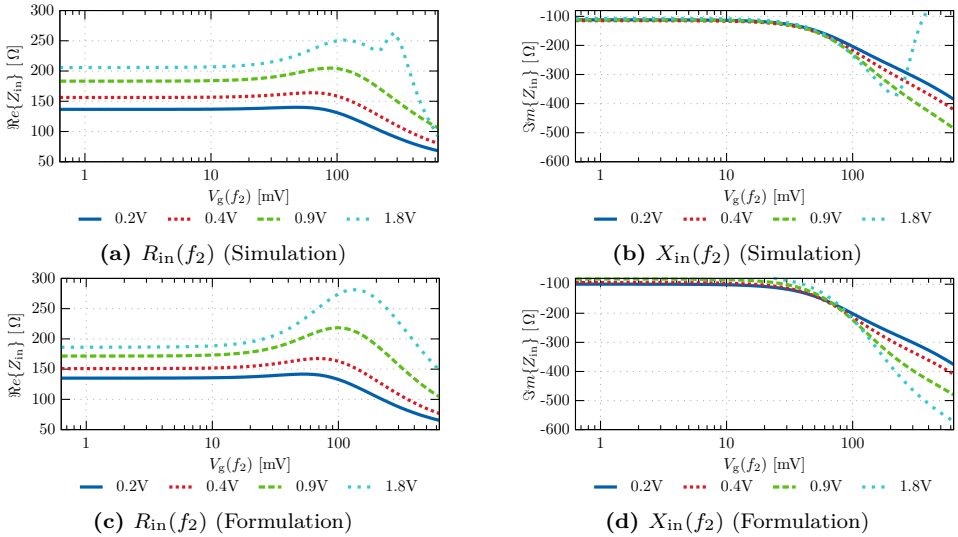

(a) $R_{\text{in}}(f_2)$ (Simulation)

(b) $X_{\text{in}}(f_2)$ (Simulation)

(c) $R_{\text{in}}(f_2)$ (Formulation)

(d) $X_{\text{in}}(f_2)$ (Formulation)

Figure C.11: Input impedance variation for a 2-stage rectifier with a voltage source directly connected

Simulations for an ideal diode show that the analytic expression predicts the behavior of R_j as with the rectifier with only 1 input tone. However, when parasitic effects, such as the junction capacitance are taken into account, $R_j(f_2)$ becomes dependent on the input voltage at frequency f_1, due to the dependence with the biasing point.
Fig. C.11, presents the results for the input impedance at frequency f_2 when the 2 stage rectifier is excited using two tones, $f_1 = 1\,\text{GHz}$ and $f_2 = 868\,\text{MHz}$, where the same criteria for the junction capacitance of the previous section has been applied (eq. (C.22) for C_j). The predicted behavior is consistent with the results of the simulation, except for simultaneously large values of input voltage at both frequencies. In particular, it can be seen that for a given available power $\text{V}_g(f_1)$, the input impedance at the frequency f_2, $Z_{\text{in}}(f_2)$, is basically constant for low values of $\text{V}_g(f_2)$, although it changes if $\text{V}_g(f_1)$ varies.
Finally Fig. C.12 presents the input impedance of the same rectifier in the presence of a generator whose impedance is $Z_g = 48 + j327\,\Omega$, corresponding to the conjugate matched of the rectifier input impedance at $f_1 = 1\,\text{GHz}$ for a power level of $-10\,\text{dBm}$. The different curves corresponds to different $P^{\text{av}}(f_1)$ without changing the generator input impedance.. The figure shows that the rectifier input impedance at f_2, $Z_{\text{in}}(f_2)$, remains constant as long as the power is smaller than $P^{\text{av}}(f_1)$. The values of $P^{\text{av}}(f_2)$ at which the impedance starts changing, showing a variation of around 5% are shown in Table C.2, which summarizes the values of input impedance for the each available power.

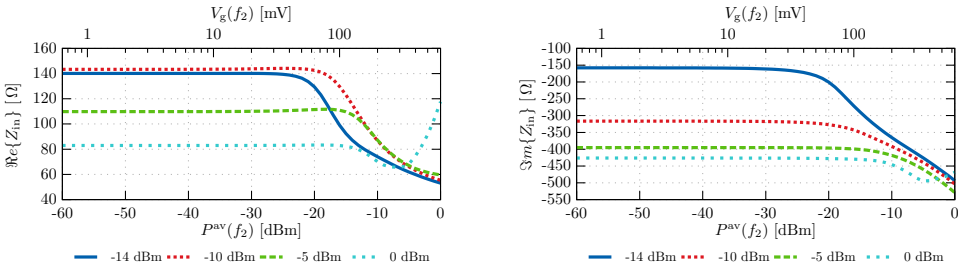

(a) Resistance at $f_2 = 868\,\text{MHz}$ **(b)** Reactance at $f_2 = 868\,\text{MHz}$

Figure C.12: Input impedance at f_2 for the 2-stage rectifier connected to a generator with $Z_g = 48 + j327\,\Omega$ and using different $P^{av}(f_1)$.

$P^{av}(1\,\text{GHz})$ [dBm]	V_o [V]	$Z_{in}(1\,\text{GHz})$ [Ω]	$Z_{in}(868\,\text{MHz})$ [Ω]	$P^{av}_{th\ 5\%}(868\,\text{MHz})$ [dBm]
−14	0.1	$77.3 - j197.3$	$140.1 - j157.9$	−25
−10	2.0	$44.0 - j317.0^{\square}$	$143.4 - j316.5$	−18
−5	4.2	$37.9 - j396.2$	$109.8 - j395.0$	−11
0	6.3	$35.2 - j458.3$	$82.95 - j426.2$	−10

Table C.2: Key parameters observed in the 2-stage rectifier with two input tones at frequencies 868 MHz and 1 GHz: $P^{av}_{th\ 5\%}(868\,\text{MHz})$ represents the limit in the available power level at the antenna to have a variation on the input impedance lower than a 5%. The ($^{\square}$) marks the input impedance to which the antenna is conjugate matched.

D

Appendix D

Uncertainty of the multi-load MST

This appendix develops the expression for the multi-load MST introducing Gaussian noise in the measurement of ρ_{rdr}, in order to evaluate the uncertainty in the estimation of Z_{ant}.

D.1 Uncertainty formulation

In conventional MST, the backscattered signal by the MST probe is proportional to $\Delta\tilde{\rho}_{\text{L}_{A,B}}$, as such in order to minimize the uncertainty of the measurement with a given probe, the requirement was the maximization of $\Delta\tilde{\rho}_{\text{L}_{A,B}}$.

For the multi-load MST formulation, there are three different loads involved in the isolation of Z_{ant}, and as such the optimum selection is not so direct. It is possible to use a first glance analysis, and consider that we now have two different sets of conventional MST signals, and as such it seems reasonable that we must maximize simultaneously $\Delta\tilde{\rho}_{\text{L}_{A,B}}$ and $\Delta\tilde{\rho}_{\text{L}_{A,C}}$. However, since the previous selection of the pairs of loads is arbitrary, the goal will be to simultaneously maximize $\Delta\tilde{\rho}_{\text{L}_{A,B}}$, $\Delta\tilde{\rho}_{\text{L}_{A,C}}$ and $\Delta\tilde{\rho}_{\text{L}_{B,C}}$. This mutual maximization of the distance implies that the loads must be in the outer circle of the Smith chart with an angular separation of 120 °.

This section will formally derive the uncertainty of the measurement of Z_{ant} in terms of the generic loads $Z_{\text{L}_{A,B,C}}$, in a more general expression to what can be found in [113] for a specific set of loads (shortcircuit, open circuit and resistive load), to obtain a design criteria to minimize the uncertainty.

The starting point is adding noise to equation (5.8):

$$\begin{bmatrix} 1 & Z_{\mathrm{L}_A} & -\left(\rho^A_{\mathrm{rdr}}+n^A\right) \\ 1 & Z_{\mathrm{L}_B} & -\left(\rho^B_{\mathrm{rdr}}+n^B\right) \\ 1 & Z_{\mathrm{L}_C} & -\left(\rho^C_{\mathrm{rdr}}+n^C\right) \end{bmatrix} \begin{bmatrix} Z_{tr}+\rho_{\mathrm{und}}Z_{\mathrm{ant}} \\ \rho_{\mathrm{und}} \\ Z_{\mathrm{ant}} \end{bmatrix} = \begin{bmatrix} \left(\rho^A_{\mathrm{rdr}}+n^A\right)Z_{\mathrm{L}_A} \\ \left(\rho^B_{\mathrm{rdr}}+n^B\right)Z_{\mathrm{L}_B} \\ \left(\rho^C_{\mathrm{rdr}}+n^C\right)Z_{\mathrm{L}_C} \end{bmatrix} \tag{D.1}$$

where n^i is additive white Gaussian noise (AWGN) noise with a power σ_N^2 which is observed in the measurement of ρ_{rdr}. It must be noted how the presence of noise is simultaneously in both sides of the equation, also being present in the matrix $\mathbf{N}$.
Developing the linear system, and isolating the term Z_{ant}, the expression for the estimated $\hat{Z}_{\mathrm{ant}}$ becomes:

$$\hat{Z}_{\mathrm{ant}} = \frac{Z_{\mathrm{ant}} + \frac{C}{Z_{tr}} \cdot \left[\frac{Z_{\mathrm{L}_A} n^A}{\Delta Z_{\mathrm{L}_{B,A}} \Delta Z_{\mathrm{L}_{A,C}}} + \frac{Z_{\mathrm{L}_B} n^B}{\Delta Z_{\mathrm{L}_{C,B}} \Delta Z_{\mathrm{L}_{B,A}}} + \frac{Z_{\mathrm{L}_C} n^C}{\Delta Z_{\mathrm{L}_{A,C}} \Delta Z_{\mathrm{L}_{C,B}}} \right]}{1 - \frac{C}{Z_{tr}} \cdot \left[\frac{n^A}{\Delta Z_{\mathrm{L}_{B,A}} \Delta Z_{\mathrm{L}_{A,C}}} + \frac{n^B}{\Delta Z_{\mathrm{L}_{C,B}} \Delta Z_{\mathrm{L}_{B,A}}} + \frac{n^C}{\Delta Z_{\mathrm{L}_{A,C}} \Delta Z_{\mathrm{L}_{C,B}}} \right]} \tag{D.2}$$

where $\Delta Z_{\mathrm{L}_{i,j}} = Z_{\mathrm{L}_i} - Z_{\mathrm{L}_j}$ and $C = (Z_{\mathrm{ant}} + Z_{\mathrm{L}_A})(Z_{\mathrm{ant}} + Z_{\mathrm{L}_B})(Z_{\mathrm{ant}} + Z_{\mathrm{L}_C})$. If the noise is low, in comparison to Z_{tr}, the denominator can be approximated by the Taylor series $\frac{1}{1-x} \approx 1 + x$, and neglecting second order noise terms, the expression becomes:

$$\hat{Z}_{\mathrm{ant}} = Z_{\mathrm{ant}} + \frac{C}{Z_{tr}} \cdot \left[n^A \frac{(Z_{\mathrm{L}_A} + Z_{\mathrm{ant}})}{\Delta Z_{\mathrm{L}_{B,A}} \Delta Z_{\mathrm{L}_{A,C}}} + n^B \frac{(Z_{\mathrm{L}_B} + Z_{\mathrm{ant}})}{\Delta Z_{\mathrm{L}_{C,B}} \Delta Z_{\mathrm{L}_{B,A}}} + n^C \frac{(Z_{\mathrm{L}_C} + Z_{\mathrm{ant}})}{\Delta Z_{\mathrm{L}_{A,C}} \Delta Z_{\mathrm{L}_{C,B}}} \right] \tag{D.3}$$

which taking into account the definition of $\Delta\tilde{\rho}_{\mathrm{L}_{B,A}} = \frac{2R_{\mathrm{ant}} \cdot \Delta Z_{\mathrm{L}_{B,A}}}{(Z_{\mathrm{ant}} + Z_{\mathrm{L}_A})(Z_{\mathrm{ant}} + Z_{\mathrm{L}_B})}$ becomes:

$$\hat{Z}_{\mathrm{ant}} = Z_{\mathrm{ant}} + \frac{4R_{\mathrm{ant}}^2}{Z_{tr}} \cdot \left[\frac{n^A}{\Delta\tilde{\rho}_{\mathrm{L}_{A,B}} \cdot \Delta\tilde{\rho}_{\mathrm{L}_{C,A}}} + \frac{n^B}{\Delta\tilde{\rho}_{\mathrm{L}_{B,C}} \cdot \Delta\tilde{\rho}_{\mathrm{L}_{A,B}}} + \frac{n^C}{\Delta\tilde{\rho}_{\mathrm{L}_{C,A}} \cdot \Delta\tilde{\rho}_{\mathrm{L}_{B,C}}} \right] \tag{D.4}$$

From (D.4) it shows that the estimator is unbiased, and its variance is:

$$\sigma^2 Z_{\mathrm{ant}} = \sigma_N^2 \frac{16R_{\mathrm{ant}}^4}{|Z_{tr}|^2} \underbrace{\left[\frac{1}{\left|\Delta\tilde{\rho}_{\mathrm{L}_{A,B}} \Delta\tilde{\rho}_{\mathrm{L}_{C,A}}\right|^2} + \frac{1}{\left|\Delta\tilde{\rho}_{\mathrm{L}_{B,C}} \Delta\tilde{\rho}_{\mathrm{L}_{A,B}}\right|^2} + \frac{1}{\left|\Delta\tilde{\rho}_{\mathrm{L}_{C,A}} \Delta\tilde{\rho}_{\mathrm{L}_{B,C}}\right|^2} \right]}_{M_{\mathrm{A,B,C}}} \tag{D.5}$$

This shows that the uncertainty of the estimation will depends on the attenuation due to the scenario, and the distance in a Smith chart representation of the 3 loads.

D.2 Uncertainty minimization

If we compute the gradient of $M_{A,B,C}$ in terms of the three $|\Delta\tilde{\rho}_{\mathrm{L}_{i,j}}|^2$, it shows that $M_{A,B,C}$ is a strictly monotonically decreasing function in the domain of positive values, as such there is no local minimum that can be used as the optimum load. However, since $|\Delta\tilde{\rho}_{\mathrm{L}}|$ is bounded an absolute minimum (or minima) can be found using the Lagrangian. The condition to be used in the Lagrangian is related to the limits that $|\Delta\tilde{\rho}_{\mathrm{L}}|$ can take. Fig. D.1a presents different possible values for $|\Delta\tilde{\rho}_{\mathrm{L}}|$, which depend on the relative position of the different $\tilde{\rho}_{\mathrm{L}}$, and as such it can be seen that $0 \leq \Delta\tilde{\rho}_{\mathrm{L}_{i,j}} \leq 2$. However, this constraint

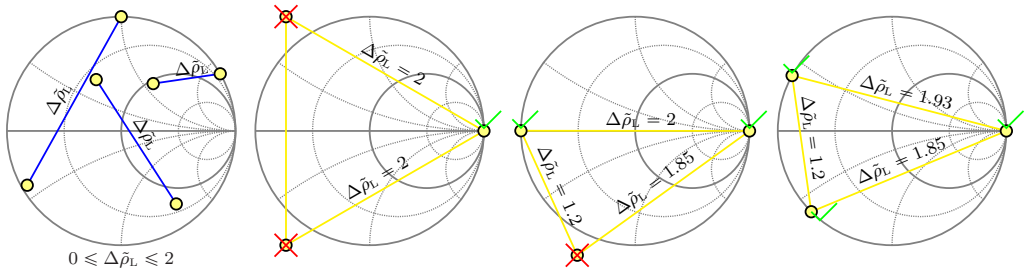

(a) Valid $\Delta\tilde{\rho}_L$ **(b)** Valid $\Delta\tilde{\rho}_L$ result into invalid $\tilde{\rho}_L$ **(c)** Constraint

Figure D.1: (a) presents possible choices of $\tilde{\rho}_L$ which result in $\Delta\tilde{\rho}_L$ values upper bounded by 2, however this constraint may result in acceptable configurations (b). The constraint (c) is that the triangle must be circumscribed in a circle of radius 1.

is not sufficiently strict, since it allows combinations that go out of the Smith chart (see Fig. D.1b), which would lead to a wrong minimization result. A more strict condition is to ensure that the triangle formed by the different loads $\tilde{\rho}_{L_{A,B,C}}$ can be circumscribed by the outer circle of the Smith chart, that is the radius of the circumscribing circle R_C must be below unity. From geometry, R_C can be related to the side lengths of the triangle $\alpha = |\Delta\tilde{\rho}_{L_{B,A}}|$, $\beta = |\Delta\tilde{\rho}_{L_{C,B}}|$ and $\gamma = |\Delta\tilde{\rho}_{L_{A,C}}|$ as:

$$R_C^2 = \frac{(\alpha\beta\gamma)^2}{2\left[(\alpha\beta)^2 + (\beta\gamma)^2 + (\alpha\gamma)^2\right] - \alpha^4 - \beta^4 - \gamma^4} \tag{D.6}$$

With this condition, the Lagrangian becomes

$$L = M_{\mathrm{A,B,C}} - \zeta\left((\alpha\beta\gamma)^2 + \alpha^4 + \beta^4 + \gamma^4 - 2\left[(\alpha\beta)^2 + (\beta\gamma)^2 + (\alpha\gamma)^2\right]\right) \tag{D.7}$$

The solution for the Lagrangian is $\alpha = \beta = \gamma = \sqrt{3}$, which corresponds to the anticipated position of $\tilde{\rho}_{L_{A,B,C}}$ in the outer circle of the Smith chart forming an angle of 120 ° between each other. When this conditions is fulfilled, the uncertainty becomes:

$$\sigma_{Z_{\mathrm{ant}}} = \sigma_N^2 \frac{16R_{\mathrm{ant}}^4}{3|Z_{tr}|^2} \tag{D.8}$$

E

Appendix E

Research on new materials for small antennas

This appendix presents part of the work developed during this thesis which consisted in the research and experimental characterization of new materials that could be used as building block of the RFID antennas, and which presented a high potential to miniaturization[1].

E.1 Carbon nanotubes

The first study that was carried out was the experimental characterization of carbon nanotubes (CNTs). A CNT consists of a seamless cylindrical graphene sheet, with diameters that go from the 0.7nm to 10nm, and lengths of a few micrometers, [128], with some reports on nanotubes up to some millimeters of length, [129]. Such high aspect ratio, $10^4 - 10^5$, allows to consider carbon nanotubes as 1D nanostructure, therefore only allowing conduction in one direction; figure E.1 presents a virtual representation of the nanotube, where the characteristic honeycomb structural lattice of the carbon atoms can be observed.

E.1.1 Why carbon nanotubes?

The interest in characterizing CNT is to experimentally analyze their behavior as antennas, and its correspondence with the existing models that predict resonant lengths much smaller than conventional metals. This behavior arises from the fact that conductivity in

[1] The following sections contains portions, sometimes verbatim, of the publication [JA5] of the author.

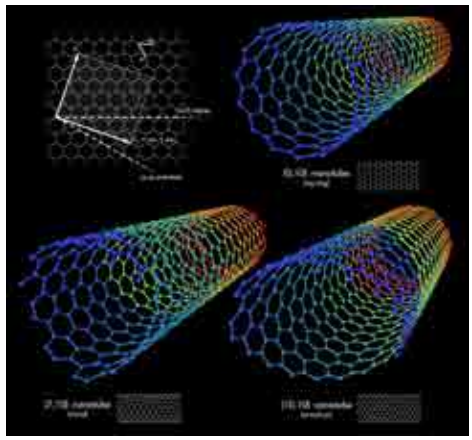

Figure E.1: Zig-zag, chiral and armchair carbon nanotube representation. ©Michael Ströck / CC-BY-SA-3.0

carbon nanotubes is a complex quantity, which arises from the inability of the electrons to move keeping the phase of an incident electrical field. This is a common effect seen in superconductors as well as metals close to the plasma frequency (usually near optical frequencies). .
The practical consequence of this imaginary term for antennas was shown in [130, 131]: the transmission line model used for instance to analyze a dipole antenna and shown in Fig. E.2 adds new reactive elements (L_K, C_q) to the conventional magnetic inductance (L_M) and electrostatic capacitance (C_{es}). C_q is the quantum capacitance and accounts for the extra energy required to introduce 1 electron in the carbon nanotube, having a similar value to C_{eq} [132]; on the other hand, L_k is the kinetic inductance which as previously mentioned, comes from the inertia of the electrons and the delay in following the incident electric field; its value is several order of magnitude greater than L_M. As

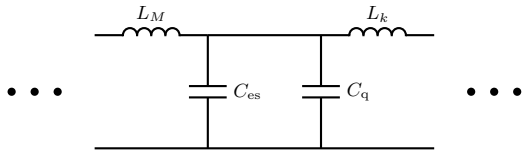

Figure E.2: Transmission model of the carbon nanotube at microwave frequencies [132]. It can be observed the existence of two different sets of reactive elements, the conventional L_M and C_{es}, and an additional set L_K and C_q which take into account the quantum effects in the nanotube.

a consequence, the phase velocity is much smaller than in air, which eventually would translate in resonant lengths (L_{CNT}) between 50 to 100 times smaller than the wavelength in free-space. It must be noted that the theoretical model establishes a cut-off frequency around 50 GHz for the resonances to start to appear, but although the difference with RFID frequencies is large, it could still be thought of to operate at higher frequencies with RFID-like sensors operating for instance at millimeter wave frequencies.
The characterization of the CNT was planned as a 2-step process.

(a) Si wafer with the electrodes and the grown nanotubes

(b) Detail of one of the electrodes

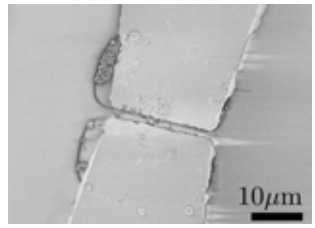

(c) SEM image of a contact with 3 carbon nanotubes

Figure E.3: Wafer with the different electrodes that were fabricated for the characterization of the nanotubes. The small gap corresponds to the expected nanotubes length according to the manufacturing process, with values of $2, 5, 7, 10, 15\,\mu m$. Similarly, the CPW were designed for use with $100\,\mu m$ pitch on-wafer probes, with straight electrodes as well as tapered electrodes (down to a central line of $20\,\mu m$) to reduce the parasitic capacitance where designed.

1. Initially the response of a nanotube interconnection was to be tested by placing CNTs in a gap in the central electrode of a CPW. Using a TRL calibration the response between of the CNT could be obtained and characterized.

2. The second stage consisted in measuring using an external antenna 2 *monopole* version of a CNT antenna, which had been placed *protruding* from the central electrode of a CPW antenna.

Fig. E.3 presents a picture of the electrodes that were designed and fabricated in collaboration with the Centre Nacional de Microelectrònica (CNM). However it must be noted that due to manufacturing difficulties (such as the length of the grown nanotubes), and the intrinsic parasitic effects between the electrodes, there was no relevant outcome from the measurements that could be used to extract experimental conclusions on the viability of CNTs as antenna bodies.
In spite of this, it must be noted that due the predicted ratio between length of the resonant CNTs and the free-space wavelength (between 50-100), the radiation resistance will be extremely small, which results in a extremely small efficiency for antennas. This can be alleviated if arrays (or bundles) of carbon nanotubes are used [133]. However, when multiple carbon nanotubes are closely spaced in a parallel configuration and sharing the excitation, as in CNT bundles, the effect of the kinetic inductance is progressively reduced, which results in longer resonant lengths than isolated CNT [133, 134].
Figs. E.4 and E.5 present the resonances that infinite arrays of carbon nanotube antennas would present depending on the separation between elements, and it clearly shows a shift towards higher frequencies for the same physical length of the nanotubes as they are more closely spaced.

E.2 Graphene

Graphene is the second material which has been characterized during the development of this thesis. The research on graphene resulted from a direct continuation of the trials with

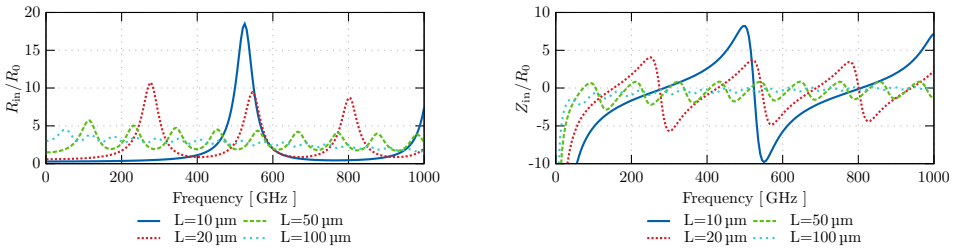

(a) Resistance **(b)** Reactance

Figure E.4: Normalized impedance for nanotube of lengths between 10 µm and 100 µm ($R_o = 12.8\,\mathrm{k}\Omega$), with a radius of 2.7 nm. It can be observed how for the 100 µm the first damped *resonance* occurs almost at 50 GHz, although the imaginary part cannot reach the 0 reactance; alternatively the nanotube of length 10 µm has a resonance at 280 GHz, corresponding to a reduction factor of 50 GHz with respect to a conventional wire (non-plasmonic) of the same dimensions.

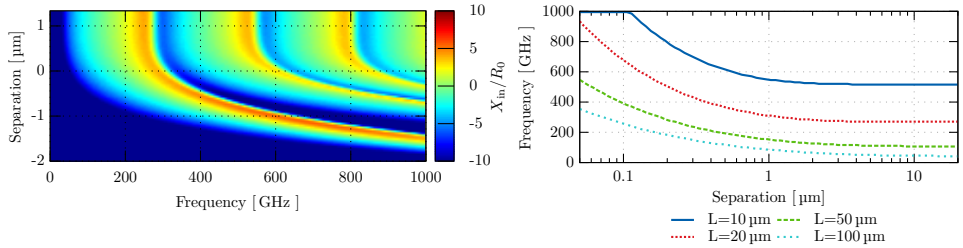

(a) Resistance for the nanotube of length 20 µm **(b)** Variation of the resonant frequency.

Figure E.5: (a) Shows the evolution of the resistance for a 2D array of nanotubes of 20 µm of length. The maximum of the resonance is shifted upwards as the separation between the nanotubes decreases. (b) presents the value of the resistance peak (1st anti-resonance) as the separation between nanotubes changes.

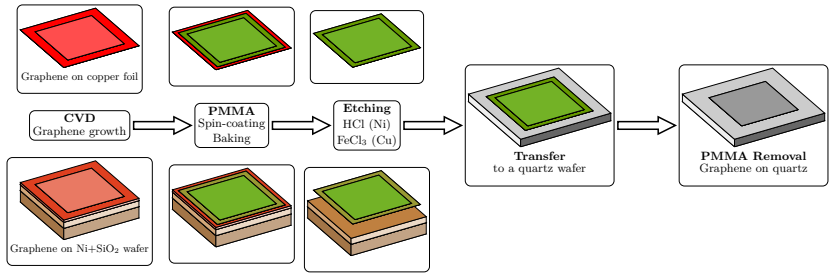

Figure E.6: Block diagram summarizing the transfer procedure of graphene from the metallic support to a quartz wafer.

carbon nanotube and was initiated during an international stay at the Univesity of California, Irvine (UCI) Nanotechnology group led by Professor Peter J. Burke. Graphene is a sheet of carbon atoms placed in a honeycomb lattice (which when rolled over themselves conforms carbon nanotubes). Due to the atomic structure, it has very good mechanical properties [135] as well as electronic properties [136].
One of the most interesting properties of graphene is the universal conductivity up to optical frequencies. However, due to scattering and chemical doping this behavior is cut-off at low frequencies, where a Drude-like behavior appears [137]. Due to the thickness of the material (atomically thin), in spite that the conductivity at optical frequencies is not negligible, graphene allows about 97% of the light through. This along with a variation of conductivity at low frequencies could allow the fabrication of *transparent* (optically speaking) antennas. Moreover, the electronic structure of graphene predicts that the conductivity at low frequencies can be changed with the adequate voltage biasing of the graphene sample, which could be exploited to develop an alternative MST modulation changing the complete antenna properties instead of simply the load.
The characterization that was carried out has measured the conductivity multi-layer (conformed by multiple graphene layers stacked on top of each other with low interaction between layers) and single-layer graphene at low frequencies without any external biasing. Specifically, the measurements were carried out using transmission measurements through the graphene sample in a waveguide setup at X-band (8-12 GHz), and a free-space optics approach in W-band (75-110 GHz).

E.2.1 Graphene samples preparation

As previously mentioned, two different kind of samples were measured, multi-layer and single-layer samples, and each of them where obtained by chemical vapor deposition (CVD) on a different metallic substrate: multi-layer samples were grown on top of a nickel wafer and single-layer samples ere grown on top of a copper foil.
The metallic substrate where graphene is grown is incompatible with a transmission measurement, since it will completely block the transmission, and similarly it would short-circuit a reflection measurement. The graphene samples were transferred to a quartz substrate using the procedure summarized in Fig. E.6:

1. The graphene sample is protected with a thin layer of polymethyl methacrylate (PMMA) spin coated on top of it and baked at 170 °C.

(a) Multi-layer

(b) Single layer

Figure E.7: Samples of (a) multi-layer and (b) single layer graphene. The dashed red frames mark the region occupied by graphene, where the multi-layer samples can be easily spotted thanks to the higher attenuation at optical frequencies versus the single layer sample.

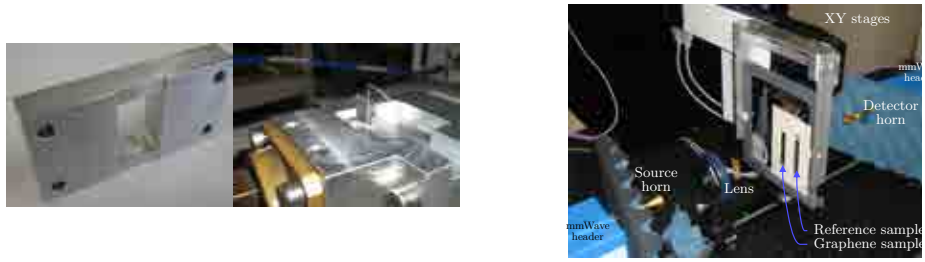

(a) X-band

(b) W-band

Figure E.8: Experimental setup for the measurements at X-band (a) and W-band (b). A thru transition for an X-band waveguide has been mechanized to create a small slit to deposit the quartz sample without disturbing the current or field lines, and ensuring appropriate interaction between the waveguide mode and the sample.

2. The metallic layer is etched using HCl (for Ni) or $FeCl_3$ (for Cu) until the PMMA and graphene float on top of the etchant.
3. The samples are cleansed in deionized water.
4. The samples are placed on top of a quartz wafer and are coated again with a new layer of PMMA to stabilize the removal of PMMA.
5. Finally the PMMA is removed from the graphene with an acetone bath

The samples consisted in rectangular pieces of quartz with the smaller size compatible with the smaller side of an X-band waveguide (1.27 mm) shown in Fig. E.7. This figure shows clearly the difference between multi-layer and single-layer samples, since multi-layer samples have a higher attenuation (absorption) at optical frequencies, while single layer should allow 97.7% of light through [138].

E.2.2 Sheet conductance measurement

Fig. E.8 presents two pictures of the setup for the measurement of the graphene samples at the different frequency bands. At X-band the samples were introduced in a waveguide

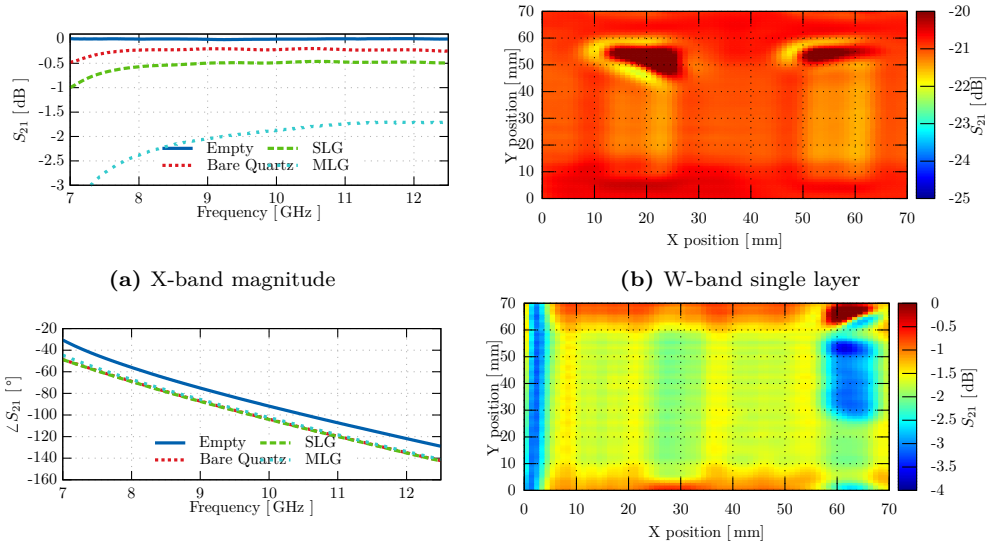

(a) X-band magnitude

(b) W-band single layer

(c) X-band phase

(d) W-band multi-layer

Figure E.9: S_{21} of the graphene samples in the X and W-bands experimental setups. For the W-band measurements, the 2D scan at the frequency of 90 GHz is shown, with the reference sample (right) and the graphene sample (left)..

with a small slit on the side that allowed to introduce and remove the sample without disturbing the current distribution of the samples. At W-band the samples were placed on a frame and measurements were carried out using two focusing lenses.
The measurement is based on the transmission equation through a multi-layer structure [139], consisting of an extremely thin layer of graphene on top of a thick layer of quartz and surrounded by air. The relevant quantities for the measurement are the permittivity of each layer and its thickness; it can be shown that since the graphene layer is extremely small (ideally atomic) it can be modeled as a sheet impedance $Z_G = {}^1/_{\sigma_G^{3D} d_G} = {}^1/_{\sigma_G}$. The transmission equation is then equivalent to transmission through a thin film [140]:

$$\tau = \frac{2}{\left(2 + \frac{Z_o}{Z_G}\right)\cos(k_Q d_Q) + j\left(\frac{Z_o}{Z_Q} + \frac{Z_Q}{Z_o} + \frac{Z_Q}{Z_G}\right)\sin(k_Q d_Q)} \tag{E.1}$$

where Z_o,Z_Q is the wave impedance of the propagating mode in free-space and quartz respectively, k_Q is the wavenumber of the mode in the quartz and d_Q is the thickness of the quartz sample. It must be noted that the mode for X-band corresponds to the TE_{10} of the waveguide.
A reference sample of quartz without graphene on top was used to determine the unknown parameters to isolate Z_G in (E.1). Fig. E.9 presents the measured S_{21} of the measurement of the samples in both frequency bands. In W-band, the use of a XY-linear stage allows to scan the whole sample which makes the region covered by the samples extremely noticeable. Finally Fig. E.10 presents the values of the retrieved sheet conductance using expression (E.1) and the measurements of the reference quartz sample.
Although there is not yet a comprehensive theory of the conductivity model for multi-

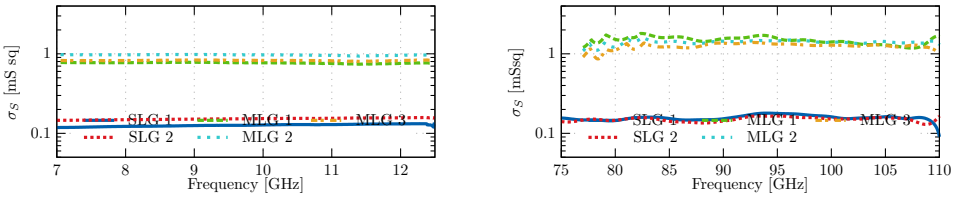

(a) X-band **(b)** W-band

Figure E.10: Conductivity obtained after processing the S_{21} of the samples and the reference measurement of bare quartz using (E.1).

layer graphene, it is expected to shown low coupling between the layers, so that it can be assumed that each layer behaves independently of the others, effectively resulting in a parallel configuration of the layers. This is qualitatively confirmed in the measurements where the multi-layer samples (which have between 4-6 layers [JA5]) present a conductivity 5-10 times larger than single layer graphene.
The results that are observed in these experimental measurements are in agreement (in the order of magnitude) with the results obtained in experiments with similar graphene samples [141].

F

Appendix F
Algebra

This appendix summarizes known algebra methodologies that are convenient for some of the calculations performed within this thesis.

F.1 Inversion of a perturbed matrix

Let $\mathbf{A}$ be a non-singular square matrix of dimensions $N \times N$ with inverse $\mathbf{B}$, and $\mathbf{D}$ a perturbing matrix which is added to $\mathbf{A}$ and which only has element (i, j) different from zeros:

$$\mathbf{C} = \mathbf{A} + \mathbf{D} \tag{F.1}$$

then, the inverse of C is found through the Sherman-Morrison formula [142] as:

$$\mathbf{C}^{-1} = \mathbf{B} - \mathbf{b}_i \left(\mathbf{b}^\intercal\right)_j^\intercal \frac{D_{ij}}{1 + D_{ij} B_{ij}} \tag{F.2}$$

where $\mathbf{b}_i$ stands for the i-column of $\mathbf{B}$ and $\left(\mathbf{b}^\intercal\right)_j^\intercal$ for the j-row of $\mathbf{B}$.

F.2 Inversion of a partitioned matrix

Let $\mathbf{A}$ be a non-singular $N \times N$ square matrix, partitioned in 4 different matrices:

$$\mathbf{A} = \begin{pmatrix} \mathbf{A}_{00} & \mathbf{A}_{01} \\ \mathbf{A}_{10} & \mathbf{A}_{11} \end{pmatrix} \tag{F.3}$$

being $\mathbf{A}_{00}$ and $\mathbf{A}_{11}$ square matrices, and $\mathbf{A_{01}}$ and $\mathbf{A_{10}}$ to vertical and horizontal shaped matrices. Provided that $\mathbf{A}_{00}$ and $\mathbf{A}_{11}$ are non-singular, the inverse matrix $\mathbf{B} = \mathbf{A}^{-1}$ will

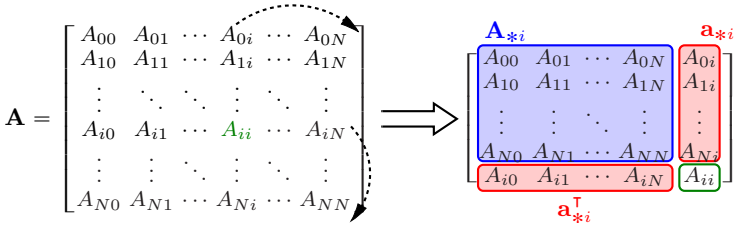

Figure F.1: Re-organization of matrix **A** used to apply partitioned inversion.

be:

$$\mathbf{B}_{00} = \left(\mathbf{A}_{00} - \mathbf{A}_{01}\mathbf{A}_{11}^{-1}\mathbf{A}_{10}\right)^{-1} \tag{F.4}$$

$$\mathbf{B}_{01} = -\mathbf{A}_{00}^{-1}\mathbf{A}_{01}\left(\mathbf{A}_{11} - \mathbf{A}_{10}\mathbf{A}_{00}^{-1}\mathbf{A}_{01}\right)^{-1} \tag{F.5}$$

$$\mathbf{B}_{11} = \left(\mathbf{A}_{11} - \mathbf{A}_{10}\mathbf{A}_{00}^{-1}\mathbf{A}_{01}\right)^{-1} \tag{F.6}$$

$$\mathbf{B}_{10} = -\mathbf{A}_{11}^{-1}\mathbf{A}_{10}\left(\mathbf{A}_{00} - \mathbf{A}_{01}\mathbf{A}_{11}^{-1}\mathbf{A}_{10}\right)^{-1} \tag{F.7}$$

For a symmetric matrix A, the inversion can be computed with multiple partitioned configuration. Of special interest (for some developments in this thesis) is when one of the main partitioned matrices correspond to a single element ii. In this case the matrix can be subdivided in a set of 3 matrices which re-arrange the elements, see Fig. F.1:

- $\mathbf{A}_{*i}$ is the resulting matrix when the i row and i column are removed from $\mathbf{A}$.
- A_{ii} is the i-element of the diagonal of $\mathbf{A}$.
- $\mathbf{a}_{*i}$ is the vector formed by the i-column of $\mathbf{A}$ without row i.

The sub-matrices can be used to obtain their equivalent $\mathbf{B}$ sub-matrices, to finally obtain $\mathbf{B} = \mathbf{A}^{-1}$:

$$\mathbf{B}_{*i} = \left(\mathbf{A}_{*i} - \mathbf{a}_{*i}A_{ii}^{-1}\mathbf{a}_{*i}^{\intercal}\right)^{-1} \tag{F.8}$$

$$B_{ii} = \left(A_{ii} - \mathbf{a}_{*i}^{\intercal}\mathbf{A}_{*i}^{-1}\mathbf{a}_{*i}\right)^{-1} \tag{F.9}$$

$$\mathbf{b}_{*i} = -\mathbf{A}_{*i}^{-1}\mathbf{a}_{*i}B_{ii} \tag{F.10}$$

$$\mathbf{b}_{*i}^{\intercal} = -A_{ii}^{-1}\mathbf{a}_{*i}^{\intercal}\mathbf{B}_{*i} \tag{F.11}$$

Nomenclature

Latin Letters

a	Power wave incident upon a given port	
A^{eff}	Effective area of an antenna	m^2
b	Power wave reflected on a given port (or received at a given port)	
B_i	Modified Bessel function of order i	
C	Capacitor	F
C_i^Z, C_i^S	Coupling coefficients using the Z-parameters formulation in MST arrays	
$\vec{E}$	Electric field	V/m
$\vec{e}_m$	E-field distribution of a mode m in a waveguide	V/m
e_{mis}	Impedance matching factor between two devices, usually an antenna and the load/generator connected at the port	
f	Frequency	Hz
G	Gain of an antenna	
$\vec{H}$	Magnetic field	A/m
$\vec{h}_m$	H-field distribution of a mode m in a waveguide	V/m
I	Electric current	A
i_d	Instantaneous current going through the diode	A
I_s	Saturation current	A
k	Wavenumber	m^{-1}
L	Physical length	m
LF	Load factor between an antenna and a given load	
L_{inc}	Normalized incident field distribution	
M	Mutual coupling between two conductors	
ME	Modulation efficiency for an antenna and a set of loads.	
$\mathbf{N}$	Matrix to be inverted to solve the multi-load sensing equation	
n	Non-linearity of the diode	
$\hat{n}$	Vector normal to a surface	
n^i	Reflection coefficient AWGN noise received in the state i	
P_a	Power associated to the incident wave a	W
P^{av}	Available power at the antenna or generator. It is the maximum power that can be transferred to a given load, achieved for the conjugate matching load	W

P_b	Power associated to the reflected wave b	W
P_{bs}	Backscattered power by an RFID/MST device received by the reader	W
P_{L}	Power delivered to load Z_{L}	W
ρ	Reflection coefficient	
r	Distance	m
R_{ant}	Resistance of the probe's antenna	Ω
R_j	Juntion resistance of the diode	Ω
R_s	Series resistance of the diode	Ω
S	Power density associated with a radiated/scattered field	W/m^2
S_{ij}	S-parameter between ports i and j	
t_d	Thickness of the dielectric	m
V	Voltage	V
v_d	Instantaneous voltage at the diode terminals	V
V_g	Amplitude of the voltage of the generator at the operating frequency	V
v_g	Instantaneous voltage of the generator	V
V_o	Output voltage of the rectifier	Ω
V^{OC}	Voltage at the antenna ports when it is left as an open circuit	V
V_T	Thermal voltage	V
W	Physical width	m
X_{ant}	Reactance of the probe's antenna	Ω
Z_{ant}	Input impedance of the antenna	Ω
Z_g	Generator's impedance	Ω
Z_{SC}	Input impedance of an RFID IC while at the short-circuiting mode	Ω
Z_{scav}	Input impedance of an RFID IC while at the scavenging operation mode	Ω
Z_{ij}	Z-parameter between ports i and j	
Z_{in}	Input impedance	Ω
Z_{L}	Input impedance of a load. Primary it refers to the load attached to a probe antenna (MST/RFID)	Ω
Z_{o}	Characteristic impedance used as reference. Usually $50\,\Omega$	Ω
Z_{tr}	Trasnfer impedance, which accounts for the coupling between a reader and probe antenna, $Z_{tr} = \frac{\left(V_{\text{ant}}^{OC}\right)^2}{2P_a}$	Ω

Greek Letters

α	Proportionality factor between two quantities	
β	Thermistor material constant	K
η	Wave impedance	Ω
λ	Wavelength	m
ψ	Generic physical quantity to be sensed, e.g. temperature, humidity, etc.	
$\tilde{\rho}$	Complex reflection coefficient	
σ	Radar cross section of an antenna or a scatterer	m^2
ρ_g	Generator's reflection coefficient, normalized with Z_{o}	
ρ_{in}	Input reflection coefficient	

$\tilde{\rho}_{\text{L}}$	Complex reflection coefficient, usually with respect the antenna impedance Z_{ant}, $\tilde{\rho}_{\text{L}} = \frac{Z_{\text{L}} - Z_{\text{ant}}^*}{Z_{\text{L}} + Z_{\text{ant}}}$	
Σ	Volume for the integral	
σ_N	Standard deviation of the noise	
$\sigma_{Z_{\text{ant}}}$	Standard deviation of the estimation of Z_{ant}	Ω
τ	Transmission coefficient between two different ports of a multi-port device. Equivalent to the term S_{ij}	

Superscripts

DC	Relative to a direct current quantity
OC	Relative to an open circuit termination

Subscripts

A, B, C, D	Referring to a specific load state
AM	Relative to the antenna mode scattering
ant	Relative to the antenna
inc	Relative to an incident field
prb	Relative to the scattering of the probe, usually including structural and antenna modes
rdr	Relative to the external transmitting/receiving antenna, usually called the reader
Rx	Receiver
SC	Relative to an short-circuited termination
scav	Relative to the scavenging state of the RFID
SM	Relative to the structural scattering
Tx	Transmitter
und	Refers to a term that while present it does not contain the information requested

List of Acronyms

AC Alternating current

AM Antenna mode

ASK Amplitude shift keying

AWGN Additive white Gaussian noise

Agilent Agilent Technologies

AUT Antenna under test

CDMA Code division multiple access

CNM Centre Nacional de Microelectrònica

CNT Carbon nanotube

CPW Coplanar waveguide

CVD Chemical vapor deposition

CW Continuous wave

DC Direct current

DSB-ASK Double sideband amplitude shift keying

EEPROM Electrically erasable programmable read only memory

EIRP Equivalent isotropically radiated power

EM Electromagnetic

EMC Electromagnetic compatibility

ERP Effective radiated power

GCPW Grounded coplanar waveguide

HFSS High frequency structural simulator

IC Integrated circuit

IFBW IF bandwidth

LDO Low-drop out

LF Load factor

LOS Line of sight

ME Modulation efficiency

MEMS Micro electromechanical systems

MST Modulated scatterer technique

MoM Method of moments

VNA Vector network analyzer

NDE Non destructive evaluation

NTC Negative temperature coefficient

OCR Optical character recognition

PC Personal computer

PIC Programmable integrated circuit

PIE Pulse-interval encoding

PIN Positive-intrinsic-negative

PMMA Polymethyl methacrylate

PNA Personal vector network analyzer

PR-ASK Phase reversal amplitude shift keying

PSK Phase shift keying

PSO Particle swarm optimization

PTC Positive temperature coefficient

RCS Radar cross section

RF Radio frequency

RFID Radio frequency identification

R&S Rohde & Schwarz

SAR Specific absorption ratio

SAW Surface acoustic wave

SEM Scanning electron microscope

SM Structural mode

SMA Sub-miniature version A connector

SNR Signal to noise ratio

SP4T Single pole four throw

SPDT Single pole double throw

SRF Self resonant frequency

SSB-ASK Single sideband amplitude shift keying

TARI Type a reference interval

TRL Thru-reflect-line

UCI Univesity of California, Irvine

UHF Ultra high frequency

USB Universal serial bus

UWB Ultra wideband

WISP Wireless identification and sensing platform

XTI Saturation current temperature exponent

List of Figures

List of Tables

Bibliography

[1] K. Finkenzeller, *RFID Handbook. Fundamentals and Applications in Contactless Smart Cards and Identification*, 2nd ed. John Wiley & Sons, Inc., 2003. (Cited on pages 3, 13, and 43.)

[2] S. Preradovic and N. Karmakar, "Chipless RFID: Bar code of the future," *IEEE Microwave Magazine*, vol. 11, no. 7, pp. 87 –97, dec. 2010. (Cited on page 4.)

[3] A. L. Cullen and J. C. Parr, "A new perturbation method for measuring microwave fields in free space," *Proceedings of the IEE-Part B: Radio and Electronic Engineering*, vol. 102, no. 6, pp. 836–844, 1955. (Cited on page 5.)

[4] J. H. Richmond, "A modulated scattering technique for measurement of field distributions," *IRE Transactions on Microwave Theory and Techniques*, vol. 3, no. 4, pp. 13–15, 1955. (Cited on pages 5 and 13.)

[5] G. Hygate and J. Nye, "Measuring microwave fields directly with an optically modulated scatterer," *Measurement Science and Technology*, vol. 1, no. 8, p. 703, 1990. (Cited on pages 5 and 60.)

[6] J. F. Nye and W. Liang, "Theory and measurement of the field of a pyramidal horn," *IEEE Transactions on Antennas and Propagation*, vol. 44, no. 11, pp. 1488–1498, 1996. (Cited on pages 5 and 54.)

[7] J. F. Nye, W. Liang, and G. Hygate, "Mapping a diffraction field close to an obstacle," *IEEE Transactions on Electromagnetic Compatibility*, vol. 37, no. 2, pp. 288–292, 1995. (Cited on page 5.)

[8] J.-C. Bolomey and F. E. Gardiol, *Engineering Applications of the Modulated Scatterer Technique*, A. House, Ed. Artech House, 2001. (Cited on pages 5, 13, 16, 60, and 76.)

[9] J.-C. Bolomey, B. Cown, G. Fine, L. Jofre, M. Mostafavi, D. Picard, J. Estrada, P. Friederich, and F. Cain, "Rapid near-field antenna testing via arrays of modulated scattering probes," *IEEE Transactions on Antennas and Propagation*, vol. 36, no. 6, pp. 804–814, 1988. (Cited on page 5.)

[10] Satimo, "Stargate 64." [Online]. Available: www.satimo.com (Cited on page 5.)

[11] J. C. Bolomey, A. Izadnegahdar, L. Jofre, C. Pichot, G. Peronnet, and M. Solaimani, "Microwave diffraction tomography for biomedical applications," *IEEE Transactions on Microwave Theory and Techniques*, vol. 30, no. 11, pp. 1998–2000, 1982. (Cited on page 5.)

[12] M. T. Ghasr, M. A. Abou-Khousa, S. Kharkovsky, R. Zoughi, and D. Pommerenke, "Portable real-time microwave camera at 24 GHz," *IEEE Transactions on Antennas and Propagation*, vol. 60, no. 2, pp. 1114–1125, 2012. (Cited on pages 5 and 54.)

[13] A. Joisel, K. J. Bois, A. D. Benally, J.-C. Bolomey, and R. Zoughi, "Embedded modulating dipole scattering for near-field microwave inspection of concrete: preliminary investigations," *Proc. SPIE 3752, Subsurface Sensors and Applications*, pp. 208–214, 1999. [Online]. Available: +http://dx.doi.org/10.1117/12.365700 (Cited on pages 5 and 54.)

[14] D. Hughes and R. Zoughi, "A novel method for determination of dielectric properties of materials using a combined embedded modulated scattering and near-field microwave techniques-part I: forward model," *IEEE Transactions on Instrumentation and Measurement*, vol. 54, no. 6, pp. 2389–2397, 2005. (Cited on pages 5 and 88.)

[15] Y. Jia, M. Heiss, Q. Fu, and N. A. Gay, "A prototype RFID humidity sensor for built environment monitoring," in *Proc. and 2008 Int Education Technology and Training Workshop Geoscience and Remote Sensing. ETT and GRS 2008. Int. Workshop*, vol. 2, 2008, pp. 496–499. (Cited on pages 5, 8, and 88.)

[16] K. M. Donnell, M. A. Abou-Khousa, M. Belayneh, and R. Zoughi, "Dual-loaded modulated dipole scatterer as an embedded sensor," *IEEE Transactions on Instrumentation and Measurement*, vol. 60, no. 5, pp. 1884–1892, 2011. (Cited on pages 5 and 95.)

[17] J. Ko, C. Lu, M. Srivastava, J. Stankovic, A. Terzis, and M. Welsh, "Wireless sensor networks for healthcare," *Proceedings of the IEEE*, vol. 98, no. 11, pp. 1947 –1960, nov. 2010. (Cited on page 6.)

[18] N. Xu, S. Rangwala, K. K. Chintalapudi, D. Ganesan, A. Broad, R. Govindan, and D. Estrin, "A wireless sensor network for structural monitoring," in *Proceedings of the 2nd international conference on Embedded networked sensor systems*, ser. SenSys '04. New York, NY, USA: ACM, 2004, pp. 13–24. [Online]. Available: http://doi.acm.org/10.1145/1031495.1031498 (Cited on page 6.)

[19] J. P. Lynch, Y. Wang, K. J. Loh, J.-H. Yi, and C.-B. Yun, "Performance monitoring of the Geumdang bridge using a dense network of high-resolution wireless sensors," *Smart Materials and Structures*, vol. 15, no. 6, p. 1561, 2006. [Online]. Available: http://stacks.iop.org/0964-1726/15/i=6/a=008 (Cited on page 6.)

[20] C. Oliveira and G. Gonçalves, "Environmental monitoring services and wireless sensor networks applied on urban spaces," in *Proc. IEEE Int Automation Quality and Testing Robotics (AQTR) Conf*, vol. 3, 2010, pp. 1–6. (Cited on page 6.)

[21] P. B. Gibbons, B. Karp, Y. Ke, S. Nath, and S. Seshan, "IrisNet: an architecture for a worldwide sensor web," *IEEE Pervasive Computing*, vol. 2, no. 4, pp. 22–33, 2003. (Cited on page 6.)

[22] U. Lee, B. Zhou, M. Gerla, E. Magistretti, P. Bellavista, and A. Corradi, "Mobeyes: smart mobs for urban monitoring with a vehicular sensor network," *IEEE Wireless Communications Magazine*, vol. 13, no. 5, pp. 52–57, 2006. (Cited on page 6.)

[23] D. Dondi, A. Bertacchini, D. Brunelli, L. Larcher, and L. Benini, "Modeling and optimization of a solar energy harvester system for self-powered wireless sensor networks," *IEEE Transactions on Industrial Electronics*, vol. 55, no. 7, pp. 2759–2766, 2008. (Cited on page 6.)

[24] F. Simjee and P. H. Chou, "Everlast: Long-life, supercapacitor-operated wireless sensor node," in *Proc. Int. Symp. ISLPED'06 Low Power Electronics and Design*, 2006, pp. 197–202. (Cited on page 6.)

[25] H. Chu, G. Wu, J. Chen, and Y. Zhao, "Study and simulation of semi-active RFID tags using piezoelectric power supply for mobile process temperature sensing," in *Proc. IEEE Int Cyber Technology in Automation, Control, and Intelligent Systems (CYBER) Conf*, 2011, pp. 38–42. (Cited on page 6.)

[26] D. J. de Villiers, S. Kaplan, and R. H. Wilkinson, "Energy harvesting for a condition monitoring mote," in *Proc. 34th Annual Conf. of IEEE Industrial Electronics IECON 2008*, 2008, pp. 2161–2166. (Cited on page 6.)

[27] V. Leonov, T. Torfs, P. Fiorini, and C. Van Hoof, "Thermoelectric converters of human warmth for self-powered wireless sensor nodes," *Sensors Journal, IEEE*, vol. 7, no. 5, pp. 650 –657, may 2007. (Cited on page 6.)

[28] M. Philipose, J. Smith, B. Jiang, A. Mamishev, S. Roy, and K. Sundara-Rajan, "Battery-free wireless identification and sensing," *IEEE Pervasive Computing*, vol. 4, no. 1, pp. 37–45, 2005. (Cited on page 6.)

[29] A. Pohl, "A review of wireless SAW sensors," *IEEE Transactions on Ultrasonics, Ferroelectrics, and Frequency Control*, vol. 47, no. 2, pp. 317–332, 2000. (Cited on pages 6, 7, and 171.)

[30] D. Girbau, A. Ramos, A. Lazaro, S. Rima, and R. Villarino, "Passive wireless temperature sensor based on time-coded UWB chipless RFID tags," *IEEE Transactions on Microwave Theory and Techniques*, vol. PP, no. 99, pp. 1 –10, 2012. (Cited on pages 7 and 171.)

[31] X. Q. Bao, W. Burkhard, V. V. Varadan, and V. K. Varadan, "SAW temperature sensor and remote reading system," in *Proc. IEEE 1987 Ultrasonics Symp*, 1987, pp. 583–586. (Cited on page 7.)

[32] L. M. Reindl and I. M. Shrena, "Wireless measurement of temperature using surface acoustic waves sensors," *IEEE Transactions on Ultrasonics, Ferroelectrics, and Frequency Control*, vol. 51, no. 11, pp. 1457–1463, 2004. (Cited on page 7.)

[33] S. Schuster, S. Scheiblhofer, L. Reindl, and A. Stelzer, "Performance evaluation of algorithms for SAW-based temperature measurement," *IEEE Transactions on Ultrasonics, Ferroelectrics, and Frequency Control*, vol. 53, no. 6, pp. 1177–1185, 2006. (Cited on page 7.)

[34] R. Fachberger, G. Bruckner, R. Hauser, and L. Reindl, "Wireless SAW based high-temperature measurement systems," in *International Frequency Control Symposium and Exposition, 2006 IEEE*, june 2006, pp. 358 –367. (Cited on page 7.)

[35] D. Chen, J. Ding, L. Du, G. Liu, and J. He, "A wireless thin contact stress sensor based on surface acoustic wave resonator in ZnO/Si structure," in *Instrumentation, Measurement, Computer, Communication and Control, 2011 First International Conference on*, oct. 2011, pp. 50 –53. (Cited on page 7.)

[36] R. Taziev, "Stress, temperature and pressure behavior of SAW on langasite plates," in *Frequency Control Symposium and PDA Exhibition, 2001. Proceedings of the 2001 IEEE International*, 2001, pp. 227 –234. (Cited on page 7.)

[37] W.-E. Bulst, G. Fischerauer, and L. Reindl, "State of the art in wireless sensing with surface acoustic waves," *IEEE Transactions on Industrial Electronics*, vol. 48, no. 2, pp. 265–271, 2001. (Cited on page 7.)

[38] C. Occhiuzzi, A. Rida, G. Marrocco, and M. Tentzeris, "RFID passive gas sensor integrating carbon nanotubes," *IEEE Transactions on Microwave Theory and Techniques*, vol. 59, no. 10, pp. 2674–2684, 2011. (Cited on pages 8, 26, and 89.)

[39] C. Occhiuzzi, C. Paggi, and G. Marrocco, "Passive RFID strain-sensor based on meander-line antennas," *IEEE Transactions on Antennas and Propagation*, vol. 59, no. 12, pp. 4836–4840, 2011. (Cited on pages 8, 89, and 90.)

[40] A. Sample, D. Yeager, P. Powledge, A. Mamishev, and J. Smith, "Design of an RFID-based battery-free programmable sensing platform," *IEEE Transactions on Instrumentation and Measurement*, vol. 57, no. 11, pp. 2608 –2615, nov. 2008. (Cited on pages 8 and 9.)

[41] G. Marrocco, L. Mattioni, and C. Calabrese, "Multiport sensor RFIDs for wireless passive sensing of objects- basic theory and early results," *IEEE Transactions on Antennas and Propagation*, vol. 56, no. 8, pp. 2691–2702, 2008. (Cited on pages 8 and 95.)

[42] R. Bhattacharyya, C. Floerkemeier, and S. Sarma, "Low-cost, ubiquitous RFID-tag-antenna-based sensing," *Proceedings of the IEEE*, vol. 98, no. 9, pp. 1593–1600, 2010. (Cited on pages 8 and 90.)

[43] S. Caizzone, C. Occhiuzzi, and G. Marrocco, "Multi-chip RFID antenna integrating shape-memory alloys for detection of thermal thresholds," *IEEE Transactions on Antennas and Propagation*, vol. 59, no. 7, pp. 2488–2494, 2011. (Cited on pages 8 and 93.)

[44] J. Gao, J. Sidén, and H. Nilsson, "Printed temperature sensors for passive RFID tags," in *Progress in Electromagnetics Research Symposium Proceedings, Xi'an*. Wiley, 2010. (Cited on page 8.)

[45] J. Gao, J. Siden, and H.-E. Nilsson, "Printed electromagnetic coupler with an embedded moisture sensor for ordinary passive RFID tags," *IEEE Electron Device Letters*, vol. 32, no. 12, pp. 1767–1769, 2011. (Cited on pages 8 and 90.)

[46] Z. Tan, R. Daamen, A. Humbert, K. Souri, Y. Chae, Y. V. Ponomarev, and M. A. P. Pertijs, "A 1.8v 11μw cmos smart humidity sensor for RFID sensing applications," in *Proc. IEEE Asian Solid State Circuits Conf. (A-SSCC)*, 2011, pp. 105–108. (Cited on page 8.)

[47] H. Reinisch, M. Wiessflecker, S. Gruber, H. Unterassinger, G. Hofer, M. Klamminger, W. Pribyl, and G. Holweg, "A multifrequency passive sensing tag with on-chip temperature sensor and off-chip sensor interface using EPC HF and UHF RFID technology," *IEEE Journal of Solid-State Circuits*, vol. 46, no. 12, pp. 3075–3088, 2011. (Cited on pages 8 and 9.)

[48] F. Gasco, P. Feraboli, J. Braun, J. Smith, P. Stickler, and L. DeOto, "Wireless strain measurement for structural testing and health monitoring of carbon fiber composites," *Composites Part A: Applied Science and Manufacturing*, vol. 42, no. 9, pp. 1263 – 1274, 2011. [Online]. Available: http://www.sciencedirect.com/science/article/pii/S1359835X1100145X (Cited on page 9.)

[49] L.-Y. Chen, L.-H. Mao, and X.-Z. Huang, "Design and analysis of a low power passive UHF RFID transponder IC," *Analog Integrated Circuits and Signal Processing*, vol. 66, pp. 61–66, 2011, 10.1007/s10470-010-9521-5. [Online]. Available: http://dx.doi.org/10.1007/s10470-010-9521-5 (Cited on page 9.)

[50] K. Kurokawa, "Power waves and the scattering matrix," *IEEE Transactions on Microwave Theory and Techniques*, vol. 13, no. 2, pp. 194–202, 1965. (Cited on pages 12, 17, and 19.)

[51] R. Green, "Scattering from conjugate-matched antennas," *IEEE Transactions on Antennas and Propagation*, vol. 14, no. 1, pp. 17–21, 1966. (Cited on page 13.)

[52] R. Hansen, "Relationships between antennas as scatterers and as radiators," *Proceedings of the IEEE*, vol. 77, no. 5, pp. 659–662, 1989. (Cited on page 13.)

[53] H. Memarzadeh-Tehran, J.-J. Laurin, and R. Kashyap, "Optically modulated probe for precision near-field measurements," *IEEE Transactions on Instrumentation and Measurement*, vol. 59, no. 10, pp. 2755–2762, 2010. (Cited on pages 13, 35, and 60.)

[54] C.-C. Yen, A. Gutierrez, D. Veeramani, and D. van der Weide, "Radar cross-section analysis of backscattering RFID tags," *IEEE Antennas and Wireless Propagation Letters*, vol. 6, pp. 279–281, 2007. [Online]. Available: http://ieeexplore.ieee.org/stampPDF/getPDF.jsp?tp=&arnumber=4260976 (Cited on pages 14 and 32.)

[55] P. Nikitin, K. Rao, and R. Martinez, "Differential RCS of RFID tag," *Electronics Letters*, vol. 43, no. 8, pp. 431–432, 12 2007. (Cited on pages 14, 15, 18, and 19.)

[56] R. Harrington, "Electromagnetic scattering by antennas," *IEEE Transactions on Antennas and Propagation*, vol. 11, no. 5, pp. 595–596, 1963. (Cited on pages 15 and 17.)

[57] D. M. Pozar, *Microwave engineering*, 2nd ed. John Wiley & Sons, Inc, 2004. (Cited on pages 16, 70, 120, and 122.)

[58] J.-C. Bolomey and F. Gardiol, "Optimization of passive RFID tag antennas," in *Proc. IEEE Antennas and Propagation Society International Symposium AP-S 2008*. APS 2008, 2008, pp. 1–4. (Cited on page 17.)

[59] R. F. Harrington, "Field measurements using active scatterers (correspondence)," *IEEE Transactions on Microwave Theory and Techniques*, vol. 11, no. 5, pp. 454–455, 1963. (Cited on page 17.)

[60] R. Harrington, "Theory of loaded scatterers," *IEE Proc.*, vol. 111, no. 4, pp. 617–623, 1964. (Cited on page 17.)

[61] K. Penttila, M. Keskilammi, L. Sydanheimo, and M. Kivikoski, "Radar cross-section analysis for passive RFID systems," *Microwaves, Antennas and Propagation, IEE Proceedings* -, vol. 153, no. 1, pp. 103–109, 2006. (Cited on page 18.)

[62] P. Nikitin and K. Rao, "Theory and measurement of backscattering from RFID tags," *IEEE Antennas and Propagation Magazine*, vol. 48, no. 6, pp. 212–218, Dec. 2006. (Cited on pages 18 and 51.)

[63] L. Mats, J. Cain, and M. Mickle, "A method for the remote measurement of the effective area of passive RFID tag antenna," in *Antenna Measurement Techniques Association 29th Annual Symposium (AMTA 2007)*. St. Louis, MO, USA: AMTA, November 2007, pp. 405–408. (Cited on page 18.)

[64] K. Rao, P. Nikitin, and S. Lam, "Antenna design for UHF RFID tags: a review and a practical application," *IEEE Transactions on Antennas and Propagation*, vol. 53, no. 12, pp. 3870–3876, Dec. 2005. (Cited on pages 27 and 28.)

[65] S. Serkan Basat, S. Bhattacharya, L. Yang, A. Rida, M. Tentzeris, and J. Laskar, "Design of a novel high-efficiency UHF RFID antenna on flexible LCP substrate with high read-range capability," in *Proc. IEEE Antennas and Propagation Society International Symposium 2006*, 2006, pp. 1031–1034. (Cited on pages 27 and 51.)

[66] *Higgs™-2 EPC Class 1 Gen 2 RFID Tag IC. Datasheet*, Alien Tech. (Cited on pages 27, 36, 46, 48, and 51.)

[67] H. Son, J. Yeo, G. Choi, and C. Pyo, "A low-cost, wideband antenna for passive RFID tags mountable on metallic surfaces," *Antennas and Propagation Society International Symposium 2006, IEEE*, pp. 1019–1022, July 2006. (Cited on pages 27 and 51.)

[68] P. Nikitin, S. Lam, and K. Rao, "Low cost silver ink RFID tag antennas," *Antennas and Propagation Society International Symposium, 2005 IEEE*, vol. 2B, pp. 353–356 vol. 2B, July 2005. (Cited on pages 27 and 51.)

[69] G. Marrocco, "The art of UHF RFID antenna design: impedance-matching and size-reduction techniques," *IEEE Antennas and Propagation Magazine*, vol. 50, no. 1, pp. 66–79, 2008. (Cited on pages 27 and 30.)

[70] *ALN-9540 Squiggle*, Alien Technology. [Online]. Available: http://www.falkensecurenetworks.com/PDFs/DS_ALN_9540_Squiggle_tag.pdf (Cited on page 28.)

[71] S.-L. Chen and R. Mittra, "Indirect coupling method for RFID tag antenna design," *Electronics Letters*, vol. 46, no. 1, pp. 8–10, 2010. (Cited on page 28.)

[72] C. Balanis, *Antenna Theory. Analysis and Design*, 2nd ed. John Wiley & Sons, Inc., 1997. (Cited on pages 27, 29, and 30.)

[73] C.-T. Tai, "Theory of terminated monopole," *IEEE Transactions on Antennas and Propagation*, vol. 32, no. 4, pp. 408–410, 1984. (Cited on pages 27 and 29.)

[74] K. R. Demarest and D. D. Deavours, "Limitations of the Uda model for T-match antennas," vol. 113, pp. 1–15, 2011. (Cited on page 27.)

[75] H.-W. Son and C.-S. Pyo, "Design of RFID tag antennas using an inductively coupled feed," *Electronics Letters*, vol. 41, no. 18, pp. 994–996, 2005. (Cited on page 31.)

[76] M. M. Masud, "Design of miniature rfid sensors for electromagnetic field measurements," 2008. [Online]. Available: http://hdl.handle.net/2099.1/5422 (Cited on page 31.)

[77] *UCODE EPC G2 TSSOP8 Package Specification*, Rev. 1.1 ed., Philips, August 30 2005. (Cited on pages 31 and 41.)

[78] L. Yang, A. Rida, R. Vyas, and M. M. Tentzeris, "RFID tag and RF structures on a paper substrate using inkjet-printing technology," *IEEE Transactions on Microwave Theory and Techniques*, vol. 55, no. 12, pp. 2894–2901, 2007. (Cited on page 32.)

[79] A. K. Skrivervik, J.-F. Zurcher, O. Staub, and J. R. Mosig, "Pcs antenna design: the challenge of miniaturization," *IEEE Antennas and Propagation Magazine*, vol. 43, no. 4, pp. 12–27, 2001. (Cited on page 33.)

[80] R. Meys and F. Janssens, "Measuring the impedance of balanced antennas by an s-parameter method," *IEEE Antennas and Propagation Magazine*, vol. 40, no. 6, pp. 62 –65, dec 1998. (Cited on page 33.)

[81] NXP Semiconductors, *BAP1321-03 Silicon PIN diode*, NXP Semiconductors. [Online]. Available: http://www.nxp.com/documents/data_sheet/BAP1321-03.pdf (Cited on page 35.)

[82] Y. Yao, J. Wu, Y. Shi, and F. F. Dai, "A fully integrated 900-MHz passive RFID transponder front end with novel zero-threshold RF–DC rectifier," *IEEE Transactions on Industrial Electronics*, vol. 56, no. 7, pp. 2317–2325, 2009. (Cited on page 41.)

[83] A. Ashry and K. Sharaf, "Ultra low power UHF RFID tag in 0.13μm CMOS," in *Proc. Internatonal Conf. Microelectronics ICM 2007*, 2007, pp. 283–286. (Cited on page 41.)

[84] G. De Vita and G. Iannaccone, "Design criteria for the RF section of UHF and microwave passive rfid transponders," *IEEE Transactions on Microwave Theory and Techniques*, vol. 53, no. 9, pp. 2978–2990, 2005. (Cited on pages 41, 42, and 135.)

[85] A. Shameli, A. Safarian, A. Rofougaran, M. Rofougaran, and F. De Flaviis, "Power harvester design for passive UHF RFID tag using a voltage boosting technique," *IEEE Transactions on Microwave Theory and Techniques*, vol. 55, no. 6, pp. 1089–1097, 2007. (Cited on pages 42 and 136.)

[86] J. F. Dickson, "On-chip high-voltage generation in mnos integrated circuits using an improved voltage multiplier technique," *IEEE Journal of Solid-State Circuits*, vol. 11, no. 3, pp. 374–378, 1976. (Cited on page 42.)

[87] G. K. Balachandran and R. E. Barnett, "A 110 nA voltage regulator system with dynamic bandwidth boosting for RFID systems," *IEEE Journal of Solid-State Circuits*, vol. 41, no. 9, pp. 2019–2028, 2006. (Cited on pages 42 and 43.)

[88] J. Heidrich, D. Brenk, J. Essel, M. Heinrich, M. Jung, G. Hofer, G. Holweg, R. Weigel, and G. Fischer, "Design of a low-power voltage regulator for RFID applications," in *Proc. IEEE Region 8 Int Computational Technologies in Electrical and Electronics Engineering (SIBIRCON) Conf*, 2010, pp. 552–557. (Cited on pages 43, 138, and 140.)

[89] G. De Vita and G. Iannaccone, "Ultra-low-power series voltage regulator for passive RFID transponders with subthreshold logic," *Electronics Letters*, vol. 42, no. 23, pp. 1350–1351, 2006. (Cited on page 43.)

[90] U. Karthaus and M. Fischer, "Fully integrated passive UHF RFID transponder IC with 16.7-μW minimum RF input power," *IEEE Journal of Solid-State Circuits*, vol. 38, no. 10, pp. 1602–1608, 2003. (Cited on pages 43, 44, and 136.)

[91] EPCGlobal, *EPC Radio-Frequency Identity Protocols Class-1 Generation-2 UHF RFID Protocol for Communications at 860 MHz – 960 MHz*, January 2005. (Cited on pages 44, 129, and 130.)

[92] P. V. Nikitin, K. V. S. Rao, R. Martinez, and S. F. Lam, "Sensitivity and impedance measurements of UHF RFID chips," *IEEE Transactions on Microwave Theory and Techniques*, vol. 57, no. 5, pp. 1297–1302, 2009. (Cited on page 45.)

[93] L. Mayer and A. Scholtz, "Sensitivity and impedance measurements on UHF RFID transponder chips," in *International EURASIP Workshop on RFID Technology, Vienna, Austria*, 2007. (Cited on page 45.)

[94] M. Daiki, H.Chaabane, E. Perret, S. Tedjini, and T.Aguili, "RFID chip impedance measurement for UHF tag design," in *Progress in Electromagnetics Research Symposium (PIERS)*, Marrakesh, Morocco, Mar 20-23 2011, pp. 679–680. (Cited on page 45.)

[95] *ALN-9529 Squiggle SQ*, Alien Technology. [Online]. Available: http://www.epcsolutionsinc.com.tw/DS_ALN_9529-SQ.pdf (Cited on page 64.)

[96] J. Rius, C. Pichot, L. Jofre, J.-C. Bolomey, N. Joachimowicz, A. Broquetas, and M. Ferrando, "Planar and cylindrical active microwave temperature imaging: numerical simulations," *IEEE Transactions on Medical Imaging*, vol. 11, no. 4, pp. 457–469, 1992. (Cited on page 75.)

[97] R. F. Harrington, *Time-Harmonic Electromagnetic Fields*, 2nd ed. Wiley-IEEE Press, Aug. 2001. (Cited on page 76.)

[98] M. Guardiola, "Anàlisi i implementació de tècniques de formació d'imatge i localització," July 2008. [Online]. Available: http://hdl.handle.net/2099.1/5422 (Cited on page 78.)

[99] G. M. Rebeiz, *RF MEMS: theory, design, and technology*, J. Wiley and Sons, Eds. John Wiley and Sons, 2003. (Cited on pages 79 and 177.)

[100] H. G. Schantz, "Planar elliptical element ultra-wideband dipole antennas," in *Proc. IEEE Antennas and Propagation Society Int. Symp*, vol. 3, 2002. (Cited on page 80.)

[101] T. Yang, S.-Y. Suh, R. Nealy, W. A. Davis, and W. L. Stutzman, "Compact antennas for UWB applications," *IEEE Aerospace and Electronics Systems Magazine*, vol. 19, no. 5, pp. 16–20, 2004. (Cited on page 80.)

[102] J. Rius, J. Parron, A. Heldring, J. Tamayo, and E. Ubeda, "Fast iterative solution of integral equations with method of moments and matrix decomposition algorithm - singular value decomposition," *IEEE Transactions on Antennas and Propagation*, vol. 56, no. 8, pp. 2314–2324, aug. 2008. (Cited on page 82.)

[103] G. Marrocco and D. Scarana, "Permittivity passive RFID sensor for non-cooperating objects," in *Proc. Second European Conference on Antennas and Propagation EuCAP 2007*, 2007, pp. 1–4. (Cited on page 88.)

[104] G. Deschamps, "Impedance of an antenna in a conducting medium," *IRE Transactions on Antennas and Propagation*, vol. 10, no. 5, pp. 648–650, 1962. (Cited on page 89.)

[105] H. Wheeler, "The radiansphere around a small antenna," *Proceedings of the IRE*, vol. 47, no. 8, pp. 1325 –1331, aug. 1959. (Cited on page 89.)

[106] A. Kraszewski, M. A. Stuchly, and S. S. Stuchly, "ANA calibration method for measurements of dielectric properties," *IEEE Transactions on Instrumentation and Measurement*, vol. 32, no. 2, pp. 385–387, 1983. (Cited on page 89.)

[107] D. Hughes and R. Zoughi, "A novel method for determination of dielectric properties of materials using a combined embedded modulated scattering and near-field microwave techniques-part II: dielectric property recalculation," *IEEE Transactions on Instrumentation and Measurement*, vol. 54, no. 6, pp. 2398–2401, 2005. (Cited on page 89.)

[108] M. Yvanoff and J. Venkataraman, "A feasibility study of tissue characterization using LC sensors," *IEEE Transactions on Antennas and Propagation*, vol. 57, no. 4, pp. 885–893, 2009. (Cited on page 89.)

[109] A. R. von Hippel, *Dielectric Materials and Applications*, A. R. V. Hippel, Ed. The M.I.T. Press, 1954. (Cited on page 89.)

[110] S. Caizzone and G. Marrocco, "RFID grids: Part II—experimentations," *IEEE Transactions on Antennas and Propagation*, vol. 59, no. 8, pp. 2896–2904, 2011. (Cited on pages 90 and 95.)

[111] I. E. Commission, *Industrial platinum resistance thermometers and platinum temperature sensors*, International Electrotechnical Commission Std. IEC 60 751. (Cited on page 92.)

[112] G. Marrocco, "RFID grids: Part I—electromagnetic theory," *IEEE Transactions on Antennas and Propagation*, vol. 59, no. 3, pp. 1019–1026, 2011. (Cited on page 94.)

[113] J. T. Mayhan, A. R. Dion, and A. J. Simmons, "A technique for measuring antenna drive port impedance using backscatter data," *IEEE Transactions on Antennas and Propagation*, vol. 42, no. 4, pp. 526–533, 1994. (Cited on pages 95 and 149.)

[114] P. Pursula, D. Sandstrom, and K. Jaakkola, "Backscattering-Based measurement of reactive antenna input impedance," *IEEE Transactions on Antennas and Propagation*, vol. 56, no. 2, pp. 469–474, 2008. (Cited on page 95.)

[115] B. Monsalve, S. Blanch, J. Romeu, and L. Jofre, "A contact-less small antenna characterization through impedance modulation," in *Antennas and Propagation, 2009. EuCAP 2009. 3rd European Conference on*, March 2009, pp. 696–698. (Cited on page 95.)

[116] R. Gold, "Optimal binary sequences for spread spectrum multiplexing (corresp.)," *IEEE Transactions on Information Theory*, vol. 13, no. 4, pp. 619–621, 1967. (Cited on page 108.)

[117] I. E. Commission, *Degrees of protection provided by enclosures (IP Code)*, International Electrotechnical Commission Std. IEC 60 529, 2001. (Cited on page 108.)

[118] U. Kang and K. D. Wise, "A high-speed capacitive humidity sensor with on-chip thermal reset," *IEEE Transactions on Electron Devices*, vol. 47, no. 4, pp. 702–710, 2000. (Cited on page 113.)

[119] M. J. Lesho and N. F. S. Jr., "Adhesion of polymer films to oxidized silicon and its effect on performance of a conductometric ph sensor," *Sensors and Actuators B: Chemical*, vol. 37, no. 1–2, pp. 61–66, 1996. [Online]. Available: http://www.sciencedirect.com/science/article/pii/S092540059780072X (Cited on page 113.)

[120] X. Huang, S. Li, J. Schultz, Q. Wang, and Q. Lin, "A capacitively based MEMS affinity glucose sensor," in *Solid-State Sensors, Actuators and Microsystems Conference, 2009. TRANSDUCERS 2009. International*, june 2009, pp. 1457 –1460. (Cited on page 113.)

[121] J.-C. Bolomey, E. Roubine, S. Drabowitch, and C. Ancona, *Antennes.* Paris: Masson et Cie., Éditeurs, 1977, v; Conté: 1. Introduction générale / E. Roubine, J.Ch. Bolomey. 2. Applications / S. Drabowitch, C. Ancona. (Cited on page 120.)

[122] D. Kuester, D. Novotny, J. Guerrieri, A. Ibrahim, and Z. Popovic, "Simple test and modeling of rfid tag backscatter," *Microwave Theory and Techniques, IEEE Transactions on*, vol. 60, no. 7, pp. 2248 –2258, july 2012. (Cited on page 124.)

[123] R. E. Barnett, J. Liu, and S. Lazar, "A RF to DC voltage conversion model for multi-stage rectifiers in uhf rfid transponders," *IEEE Journal of Solid-State Circuits*, vol. 44, no. 2, pp. 354–370, 2009. (Cited on pages 135 and 140.)

[124] A. Technologies, *Designing the Virtual Battery*, Agilent Technologies, application Note 1088. (Cited on page 136.)

[125] G. B. Arfken and H. J. Weber, *Mathematical Methods for Physicists, Sixth Edition: A Comprehensive Guide*, 6th ed. Academic Press, June 2005. (Cited on page 138.)

[126] Agilent Technologies, "Advanced design system 2011 (ADS)." (Cited on pages 140 and 141.)

[127] AVAGO Technologies, *HSMS-285x Series. Surface Mount Zero Bias Schottky Detector Diodes*, AVAGO Technologies. (Cited on pages 141 and 177.)

[128] R. Saito, G. Dresselhaus, and M. Dresselhaus, *Physical Properties of Carbon Nanotubes*, 1st ed. Imperial College Press, 1998. (Cited on page 153.)

[129] S. Li, Z. Yu, C. Rutherglen, and P. Burke, "Electrical properties of 0.4 cm long single-walled carbon nanotubes," *Nano Letters*, vol. 4, no. 10, pp. 2003–2007, 2004. [Online]. Available: http://pubs3.acs.org/acs/journals/doilookup?in_doi=10.1021/nl048687z (Cited on page 153.)

[130] G. Hanson, "Current on an infinitely-long carbon nanotube antenna excited by a gap generator," *IEEE Transactions on Antennas and Propagation*, vol. 54, no. 1, pp. 76–81, 2006. (Cited on page 154.)

[131] P. Burke, S. Li, and Z. Yu, "Quantitative theory of nanowire and nanotube antenna performance," *IEEE Transactions on Nanotechnology*, vol. 5, no. 4, pp. 314–334, 2006. (Cited on page 154.)

[132] P. Burke, "Luttinger liquid theory as a model of the gigahertz electrical properties of carbon nanotubes," *IEEE Transactions on Nanotechnology*, vol. 1, no. 3, pp. 129–144, 2002. (Cited on page 154.)

[133] S. Choi and K. Sarabandi, "Performance assessment of bundled carbon nanotube for antenna applications at terahertz frequencies and higher," *IEEE Transactions on Antennas and Propagation*, vol. 59, no. 3, pp. 802–809, 2011. (Cited on page 155.)

[134] G. W. Hanson, S. McKernan, and D. Wang, "Analysis of large planar arrays of single-wall carbon nanotubes," *IEEE Transactions on Microwave Theory and Techniques*, vol. 59, no. 10, pp. 2758–2768, 2011. (Cited on page 155.)

[135] C. Lee, X. Wei, J. W. Kysar, and J. Hone, "Measurement of the elastic properties and intrinsic strength of monolayer graphene," *Science*, vol. 321, no. 5887, pp. 385–388, 2008. [Online]. Available: http://www.sciencemag.org/content/321/5887/385.abstract (Cited on page 157.)

[136] S. K. Banerjee, L. F. Register, E. Tutuc, D. Basu, S. Kim, D. Reddy, and A. H. MacDonald, "Graphene for cmos and beyond cmos applications," *Proceedings of the IEEE*, vol. 98, no. 12, pp. 2032–2046, 2010. (Cited on page 157.)

[137] V. P. Gusynin, S. G. Sharapov, and J. P. Carbotte, "On the universal ac optical background in graphene," *New Journal of Physics*, vol. 11, no. 9, p. 095013, Sep. 2009. [Online]. Available: http://iopscience.iop.org/1367-2630/11/9/095013 (Cited on page 157.)

[138] R. R. Nair, P. Blake, A. N. Grigorenko, K. S. Novoselov, T. J. Booth, T. Stauber, N. M. R. Peres, and A. K. Geim, "Fine structure constant defines visual transparency of graphene." *Science (New York, N.Y.)*, vol. 320, no. 5881, p. 1308, 2008. [Online]. Available: http://www.sciencemag.org/cgi/content/abstract/320/5881/1308 (Cited on page 158.)

[139] C. A. Balanis, *Advanced Engineering Electromagnetics*. John Wiley & Sons, 1989. (Cited on page 159.)

[140] N. M. Rugheimer, A. Lehoczky, and C. V. Briscoe, "Microwave transmission- and reflection-coefficient ratios of thin superconducting films," *Phys. Rev.*, vol. 154, pp. 414–421, Feb 1967. [Online]. Available: http://link.aps.org/doi/10.1103/PhysRev.154.414 (Cited on page 159.)

[141] J. S. Gómez-Díaz, J. Perruisseau-Carrier, P. Sharma, and A. Ionescu, "Non-contact characterization of graphene surface impedance at micro and millimeter waves," *Journal of Applied Physics*, vol. 111, no. 11, p. 114908, 2012. [Online]. Available: http://link.aip.org/link/?JAP/111/114908/1 (Cited on page 160.)

[142] J. Sherman and W. J. Morrison, "Adjustment of an inverse matrix corresponding to a change in one element of a given matrix," *The Annals of Mathematical Statistics*, vol. 21, no. 1, pp. pp. 124–127, 1950. [Online]. Available: http://www.jstor.org/stable/2236561 (Cited on page 161.)

List of Publications

Journals articles

[JA1] D. Rodrigo, J. Romeu, **S. Capdevila**, and L. Jofre, "A figure-of-merit for pattern reconfigurable antennas," *Antennas and Propagation, IEEE Transactions on*, vol. Accepted for publication, no. 99, pp. 1–6, 2013.

[JA2] **S. Capdevila**, L. Jofre, J. Romeu, and J. Bolomey, "Multi-loaded modulated scatterer technique for sensing applications," *IEEE Transactions on Instrumentation and Measurement*, vol. 62 (Tentative). Accepted for publication, no. 7, pp. 1–12, July 2013. (Cited on page 88.)

[JA3] **S. Capdevila**, L. Jofre, J. Romeu, and J. C. Bolomey, "Efficient parametric characterization of the dynamic performance of an RFID IC," *IEEE Microwave and Wireless Components Letters*, vol. 22, no. 8, pp. 436–438, 2012. (Cited on pages 45 and 48.)

[JA4] M. Guardiola, **S. Capdevila**, J. Romeu, and L. Jofre, "3-d microwave magnitude combined tomography for breast cancer detection using realistic breast models," *Antennas and Wireless Propagation Letters, IEEE*, vol. 11, pp. 1548 –1551, 2012.

[JA5] N. Rouhi, **S. Capdevila**, D. Jain, K. Zand, Y. Wang, E. Brown, L. Jofre, and P. Burke, "Terahertz graphene optics," *Nano Research*, vol. 5, pp. 667–678, 2012. [Online]. Available: http://dx.doi.org/10.1007/s12274-012-0251-0 (Cited on pages 153 and 160.)

[JA6] M. Guardiola, L. Jofre, **S. Capdevila**, S. Blanch, and J. Romeu, "3D UWB magnitude-combined tomographic imaging for biomedical applications. algorithm validation," *Radioengineering*, vol. 20, no. 2, p. 367, 2011. (Cited on page 75.)

[JA7] J. C. Bolomey, **S. Capdevila**, L. Jofre, and J. Romeu, "Electromagnetic modeling of RFID-modulated scattering mechanism. Application to tag performance evaluation," *Proceedings of the IEEE*, vol. 98, no. 9, pp. 1555–1569, 2010. (Cited on page 11.)

[JA8] **S. Capdevila**, L. Jofre, J.-C. Bolomey, and J. Romeu, "RFID multiprobe impedance-based sensors," *IEEE Transactions on Instrumentation and Measurement*, vol. 59, no. 12, pp. 3093–3101, 2010. (Cited on pages 88, 89, and 95.)

[JA9] R. Serrano, **S. Capdevila**, A. Aguasca, J. Romeu, and L. Jofre, "Multiport multiband decoupling optimization for miniature antennas," *Radioengineering*, vol. 18, 2009.

Conference Articles

[CA1] **S. Capdevila**, J. Romeu, L. Jofre, and J. Bolomey, "Design of a small MST probe for EM-field measurements and sensing applications," in *Antennas and Propagation Society International Symposium (APSURSI), 2012 IEEE*, july 2012, pp. 1 –2.

[CA2] M. Masud and **S. Capdevila**, "UHF bowtie RFID antenna with resistive and inductive stubs," in *Antennas and Propagation Society International Symposium (APSURSI), 2012 IEEE*, july 2012, pp. 1 –2.

[CA3] **S. Capdevila**, G. Roqueta, M. Guardiola, L. Jofre, J. Romeu, and J. Bolomey, "Water infiltration detection in civil engineering structures using RFID," in *Antennas and Propagation (EUCAP), 2012 6th European Conference on.* IEEE, Mar. 2012, pp. 2505–2509.

[CA4] M. Guardiola, L. Jofre, **S. Capdevila**, and J. Romeu, "UWB brain differential imaging capabilities," in *Antennas and Propagation (EUCAP), 2012 6th European Conference on.* IEEE, Mar. 2012, pp. 1780–1783.

[CA5] M. Guardiola, G. Roqueta, **S. Capdevila**, J. Romeu, and L. Jofre, "Semi-embedded RFID sensor networks for imaging applications," in *Proceedings of the 5th International Conference on Electromagnetic Near-field Characterization and Imaging (ICONIC)*, Rouen, France, Nov. 2011, pp. 1–4, nov. 30-Dec. 2. (Cited on page 195.)

[CA6] **S. Capdevila**, L. Jofre, J. Romeu, and J. Bolomey, "Passive RFID based sensing," in *RFID-Technologies and Applications (RFID-TA), 2011 IEEE International Conference on.* IEEE, Sep. 2011, pp. 507–512.

[CA7] J. Bolomey, **S. Capdevila**, L. Jofre, and S. Tedjini, "Sensitivity analysis for wireless dielectric reflectometry with modulated scatterers," in *General Assembly and Scientific Symposium, 2011 XXXth URSI.* IEEE, Aug. 2011, pp. 1–4.

[CA8] N. Rouhi, D. Jain, **S. Capdevila**, L. Jofre, E. Brown, and P. Burke, "Broadband conductivity of graphene from DC to THz," in *Nanotechnology (IEEE-NANO), 2011 11th IEEE Conference on.* IEEE, Aug. 2011, pp. 1205–1207.

[CA9] L. Jofre, J. Romeu, **S. Capdevila**, J. Abril, E. Nova, and M. Alonso, "The "challenging" world of terahertz radiation and imaging," in *Antennas and Propagation (EUCAP), Proceedings of the 5th European Conference on*, Apr. 2011, pp. 3470–3475.

[CA10] L. Jofre, R. Serrano, and **S. Capdevila**, "The small antenna concept. from microwaves to optical frequencies," in *Antennas and Propagation (EUCAP), Proceedings of the 5th European Conference on*, Apr. 2011, pp. 3707–3711.

[CA11] M. Guardiola, L. Jofre, F. Gedda, **S. Capdevila**, J. Romeu, and S. Blanch, "3D arrayed microwave tomographic system for medical imaging," in *Wireless Information Technology and Systems (ICWITS), 2010 IEEE International Conference on*, Sep. 2010, pp. 1 –4, 28 2010-sept. 3.

[CA12] B. Izquierdo, J. Alonso, **S. Capdevila**, and J. Romeu, "A combined spectral-parabolic equation approach for propagation prediction in tunnels," in *Antennas and Propagation Society International Symposium (APSURSI), 2010 IEEE*. IEEE, Jul. 2010, pp. 1–4.

[CA13] J. Abril, E. Nova, **S. Capdevila**, A. Broquetas, F. Torres, and L. Jofre, "Active and passive THz systems for short-range imaging applications," in *Antennas and Propagation (EuCAP), 2010 Proceedings of the Fourth European Conference on*. IEEE, Apr. 2010, pp. 1–4.

[CA14] **S. Capdevila**, L. Jofre, J. Romeu, and J. Bolomey, "RFID array sensing," in *Antennas and Propagation (EuCAP), 2010 Proceedings of the Fourth European Conference on*. IEEE, Apr. 2010, pp. 1–5.

[CA15] M. Guardiola, L. Jofre, **S. Capdevila**, S. Blanch, and J. Romeu, "Toward 3D UWB tomographie imaging system for breast tumor detection," in *Antennas and Propagation (EuCAP), 2010 Proceedings of the Fourth European Conference on*. IEEE, Apr. 2010, pp. 1–5.

[CA16] E. Nova, J. Abril, M. Guardiola, **S. Capdevila**, A. Broquetas, J. Romeu, and L. Jofre, "Terahertz subsurface imaging system," in *Antennas and Propagation (EuCAP), 2010 Proceedings of the Fourth European Conference on*. IEEE, Apr. 2010, pp. 1–5.

[CA17] M. Guardiola, **S. Capdevila**, S. Blanch, J. Romeu, and L. Jofre, "UWB high-contrast robust tomographic imaging for medical applications," in *Electromagnetics in Advanced Applications, 2009. ICEAA'09. International Conference on*. IEEE, Sep. 2009, pp. 560–563.

[CA18] J. Alonso, B. Izquierdo, **S. Capdevila**, and J. Romeu, "Preliminar propagation and MIMO experiments in train tunnels at 5.8 GHz," in *Antennas and Propagation Society International Symposium, 2009. APSURSI '09. IEEE*. IEEE, Jun. 2009, pp. 1–4.

[CA19] **S. Capdevila**, L. Jofre, J.-C. Bolomey, and J. Romeu, "RFID array probe for EM–field measurements," in *Antennas and Propagation Society International Symposium, 2009. APSURSI '09. IEEE*, Jun. 2009. (Cited on page 195.)

[CA20] L. Jofre, **S. Capdevila**, J. Romeu, and J.-C. Bolomey, "Near field RFID sensing and imaging," in *Proceedings of the 4th International Conference on Electromagnetic Near-Field Characterization and Imaging*, Jun. 2009, pp. 1–4, june 24-26.

[CA21] **S. Capdevila**, M. M. Masud, R. Serrano, A. Aguasca, S. Blanch, J. Romeu, , J.-C. Bolomey, and L. Jofre, "RFID based probes for EM–field measurements," in *Antennas and Propagation (EuCAP), 2009 Proceedings of the Third European Conference on*, Mar. 2009. (Cited on page 31.)

[CA22] M. Guardiola, **S. Capdevila**, and L. Jofre, "UWB bifocusing tomography for breast tumor detection," in *Antennas and Propagation (EuCAP), 2009 Proceedings of the Third European Conference on*, Mar. 2009, pp. 1855 –1859.

[CA23] R. Serrano, **S. Capdevila**, A. Aguasca, J. Romeu, and L. Jofre, "Multiport multiband coupling minimization for miniature antenna," in *Antennas and Propagation (EuCAP), 2009 Proceedings of the Third European Conference on*, Mar. 2009.

[CA24] J. C. Bolomey, L. Jofre, and **S. Capdevila**, "Reciprocity-based formulation of RFID tag response in arbitrary environments," in *Internation Symposium on Antennas and Propagation (ISAP 08)*, Oct. 2008. (Cited on page 17.)

[CA25] J. Alonso, **S. Capdevila**, B. Izquierdo, and J. Romeu, "Propagation measurements and simulations in tunnel environment at 5.8 GHz," in *Antennas and Propagation Society International Symposium, 2008. AP-S 2008. IEEE.* IEEE, Jul. 2008, pp. 1–4.

[CA26] **S. Capdevila**, M. Jofre, J. Rodriguez, M. Guardiola, A. Papio, F. De Flaviis, and L. Jofre, "UWB MST MEMS-based near-field imaging system," in *Proc. IEEE Antennas and Propagation Society International Symposium AP-S 2008*, Jul. 2008, pp. 1–4.

[CA27] **S. Capdevila**, R. Serrano, A. Aguasca, S. Blanch, J. Romeu, and L. Jofre, "RFID-based flexible low-cost EM field probe," in *Proc. IEEE Antennas and Propagation Society International Symposium AP-S 2008*, Jul. 2008, pp. 1–4. (Cited on page 195.)

[CA28] R. Serrano, **S. Capdevila**, D. Nyberg, J. Romeu, and L. Jofre, "Port balance, efficiency and correlation impact evaluation for MIMO compact multiantenna systems," in *Antennas and Propagation Society International Symposium, 2008. AP-S 2008. IEEE*, Jul. 2008, pp. 1 –4.

[CA29] R. Serrano, A. Diallo, **S. Capdevila**, S. Blanch, J. Romeu, C. Luxey, P. Le Thuc, R. Staraj, and L. Jofre, "Optimal multiantenna structures for maximum capacity in wireless compact systems," in *The European Conference on Antennas and Propagation: EuCAP 2007*, ser. ESA Special Publication, nov 2007.

[CA30] **S. Capdevila**, J. Pérez, M. Jofre, N. Ferrer-Anglada, A. Aguasca, S. Blanch, J. Romeu, and L. Jofre, "Microwave characterization of a CNT bucky paper transmission line," in *Trends in Nanotechnology 2007*, San Sebastian, Spain, Sep. 2007.

[CA31] B. Izquierdo, **S. Capdevila**, L. Jofre, and J. Romeu, "Evaluation of MIMO capacity in train tunnels," in *Antennas and Propagation International Symposium, 2007 IEEE*, Jun. 2007, pp. 1365–1368, 9-15 June.

[CA32] R. Serrano, M. Alonso, **S. Capdevila**, S. Blanch, J. Romeu, and L. Jofre, "Miniature multiantenna for optimal capacity in wireless microsystems," in *The European Conference on Antennas and Propagation: EuCAP 2006*, ser. ESA Special Publication, vol. 626, Oct. 2006.

[CA33] **S. Capdevila**, L. Jofre, A. Cardama, S. Blanch, J. Romeu, and G. Roqueta, "Gap fillers coverage prediction at S frequency band," in *XXI Simpósium Nacional de la Unión Científica de Radio (URSI 2006)*, Sep. 2006, pp. 1365–1368.

[CA34] R. Serrano, I. Cairo, **S. Capdevila**, S. Blanch, A. Aguasca, J. Romeu, and L. Jofre, "Miniature antenna as optimal load for high efficiency integrated active UHF microsystems," in *Radar Conference, 2006. EuRAD 2006. 3rd European*, Sep. 2006, pp. 68–71.

[CA35] R. Serrano, S. Blanch, **S. Capdevila**, J. Romeu, and L. Jofre, "Evaluation of stand-alone RFID miniature antennas using MST principle," in *2006 IEEE Antennas and Propagation Society Internation Symposium*, ser. ESA Special Publication, Jul. 2006.

Awards and Mentions

Part of the work developed during this thesis has lead to the following mentions at international conferences:

- First student Prize at the *5th International Conference on Electromagnetic Near-Field Characterization and Imaging (ICONIC 2011)* held in Rounen, France in December 2011 for the paper "Semi-embedded RFID sensor networks for imaging applications" [CA5]

- Honorable Mention at the Student Paper Contest of the *Antennas and Propagation Society International Symposium, 2009. APSURSI '09. IEEE* held in Charleston, USA in June 2009 for the paper "RFID array probe for EM-field measurements" [CA19]

- Finalist at the Student Paper Contest of the *Antennas and Propagation Society International Symposium, 2008. APSURSI '08. IEEE* held in San Diego, USA in July 2008 for the paper "RFID-Based Flexible Low-Cost EM Field Probe" [CA27]

Master Thesis Supervised

During the development of this thesis, two master thesis have been supervised:

- Muhammad Mubeen Masud, "Design of miniature RFID sensors for electromagnetic field measurements", Master Thesis, Universitat Politècnica de Catalunya (UPC), September 2008

- Marta Guardiola Garcia, "Anàlisi i implementació de tècniques de formació d'imatge i localització", Master Thesis, Universitat Politècnica de Catalunya (UPC), July 2008

Participation in R&D Projects

CONSOLIDER CSD2008-68 CONSOLIDER project CSD2008-68 entitled "Terahertz Technology for Electromagnetic and Sensing Applications (TERANSENSE)" From 2008 to 2013.

CICYT TEC2010-20841-C04-02 Supported by the Spanish Interministerial Comission on Science and Technology (CICYT) under project TEC2010-20841-C04-02 entitled "Design, Simulation and Measurement of Millimetre Wave Antennas for Communication and Imaging". From 2010 to 2012.

FPU Fellowship Supported by the Formación de Profesorado Universitario (FPU) Fellowship program from the Spanish Ministerio de Educación y Ciencia (MEC). May 2007 - November 2010.

JCM Technology. "Design and optimization of a radio transmitter at 125 kHz". Analysis and optimization of a radio controlled system at 125 kHz for increased range coverage up to 6 m. May 2009 - February 2010

CICYT TEC2007-66698-C04-01 Supported by the Spanish Interministerial Comission on Science and Technology (CICYT) under project TEC2007-66698-C04-01 entitled "Sistemas Multiantenas Reconfigurables para Comunicaciones y Sensores". From 2007 to 2009.

Baolab. "Superdirective miniature rotating antennes". Analysis of rotating structures for the development of super-directive antennas. January 2006 - December 2006